

Final Report

A320 Auxiliary Propulsion and Power Unit

by

DSE Group 21

Students:	Daniel Cisneros Acevedo	4657349
	Tom van Cranenburgh	4647645
	Joaquin Exalto	4647882
	Luuk Halsema	4659953
	Bob van der Heijden	4643631
	Yoram Hoogterp	4293746
	Eliisabet Jahilo	4679024
	Antonio Machado Jorge	4768915
	Yair Naäman	4675088
	Martin van Schie	4648366
	Manouk van der Zwan	4654196
	Tutor:	Dr. Arvind Gangoli Rao
Coaches:	Dr. ir. Maurice Hoogreef	FPP
	Ir. Tijmen Pollack	C&S



Nomenclature

Abbreviations

APPU	Auxiliary Power and Propulsion Unit
APU	Auxiliary Power Unit
ATC	Air Traffic Control
BLI	Boundary Layer Ingestion
CC	Combustion Chamber
CCH ₂	Cryogenically compressed hydrogen
CFD	Computational Fluid Dynamics
CG	Centre of Gravity
CVP	Cold Vacuum Pressure
EI	Emissions Index
EIS	Entry Into Service
EPNL	Effective Perceived Noise Level
FAA	Federal Aviation Administration
FBS	Functional Breakdown Structure
FFD	Functional Flow Diagram
FH	Flight Hour
GH ₂	Gaseous hydrogen
HP	High Pressure
LH ₂	Liquid hydrogen
LHV	Lower Heating Value
LP	Low Pressure
LTO	Landing and Take Off
MLI	Multi-layer Insulation
MLW	Maximum Landing Weight
MPL	Maximum Payload Weight
MTOW	Maximum Take Off Weight
OEW	Operating Empty Weight
PD	Positive Displacement
ROC	Rate Of Climb
SL	Sea Level
SM	Safety Margin
TRL	Technology Readiness Level

TSFC Thrust Specific Fuel Consumption [g/Ns]

WBT Warm Boundary Temperature

Symbols

α_{kero}	Kerosene consumption velocity correction	[-]
$\bar{x}_{a.c.}$	Longitudinal aerodynamic centre position	[m]
$\bar{x}_{c.g.}$	Longitudinal centre of gravity position	[m]
$\bar{x}_{n.p.}$	Longitudinal neutral point position	[m]
Δx	Section of the heat exchanger	[m]
\dot{m}	Mass flow	[kg/s]
\dot{q}	Heat transfer	[W]
ϵ	Downwash angle	[°]
η_{gen}	Generator efficiency	[%]
η_{prop}	Propeller efficiency	[%]
η_{pro}	Profit margin	[-]
η_{th}	Engine thermal efficiency	[%]
$\frac{V_h}{V_\infty}$	Horizontal tail velocity ratio	[-]
γ	Acceleration	[m/s ²]
γ	Flight path angle	[°]
ρ	Air density	[kg/m ³]
ρ_0	Sea level air density	[kg/m ³]
σ_f	Failure stress	[MPa]
σ_w	Hoop stress	[Pa]
σ_{xx}	Normal stress over x-plane	[MPa]
σ_{yy}	Normal stress over y-plane	[MPa]
σ_Y	Tensile strength	[MPa]
σ_{zz}	Normal stress over z-plane	[MPa]
τ_{xy}	Shear stress in xy-plane	[MPa]
τ_{yz}	Shear stress in yz-plane	[MPa]
τ_{zx}	Shear stress in zx-plane	[MPa]
a	Acceleration	[m/s ²]
A_c	Cylinder surface area	[m ²]
A_s	Sphere surface area	[m ²]
c	Mean aerodynamic chord	[m]

C_D	Drag coefficient	[-]	L/D	Lift-to-Drag ratio	[-]
C_L	Lift coefficient	[-]	l_h	Horizontal ail arm	[m]
C_{ACQ}	Acquisition Cost	[USD]	l_v	Vertical tail arm	[m]
C_{DISP}	Disposal Cost	[USD]	L_{cyl}	Length cylinder	[m]
$C_{L\alpha_h}$	Tail lift curve slope	[-]	LCC	Life Cycle Cost	[USD]
$C_{L\alpha_{A-h}}$	Tailless aircraft curve lift slope	[-]	m	Aircraft mass	[kg]
C_{MAN}	Manufacturing Cost	[USD]	$N_{program}$	Aircraft program size	[-]
C_{OPS}	Operational Cost	[USD]	p	Pressure	[Pa]
C_{RDTE}	Research, Development, Test and Evaluation Cost	[USD]	P_{0max}	Sea level maximum power output	[W]
CEF	Cost Escalation Factor	[-]	P_{max}	Maximum power output	[W]
D	Aerodynamic drag	[N]	$p_{venting}$	Venting pressure	[Pa]
d	Diameter	[m]	q	Heat flow	[W]
d_o	Outer diameter, $d_o = 2 \cdot r$	[m]	r	Radius	[m]
DOC	Direct Operational Cost	[USD/blhr]	r_a	Radius artificial shell	[m]
DOC_{depr}	DOC of depreciation	[USD]	r_o	Outer tank radius	[m]
DOC_{flt}	DOC of flying	[USD]	R_{th}	Thermal resistance	[K/W]
DOC_{maint}	DOC of maintenance	[USD]	R_{blann}	Annual flight distance	[nm]
DOC_{other}	Other DOC, consisting of fees,taxes, insurance and financial cost		ROI	Return On Investment	[-]
E_1	Tensile modulus in axial direction	[MPa]	S	Wing surface area	[m ²]
E_1	Tensile modulus of an isotropic material	[MPa]	S_h	Horizontal tail surface area	[m ²]
E_2	Tensile modulus in tangential direction	[MPa]	T	Thrust	[N]
f_{rad}	Radiation correction factor	[-]	t	Thickness	[m]
h	Altitude	[m]	T_{air}	Air temperature	[°C]
h_i	Internal heat transfer coefficient	[W/m ² K]	T_{H2}	Hydrogen temperature	[°C]
h_o	External heat transfer coefficient	[W/m ² K]	UA	Heat flux of heat exchanger	[W/m ²]
h_{exit}	Height of exit spout measured from datum	[m]	V_t	Tank volume	[m ³]
h_{fin}	Fin heat transfer coefficient	[J/m ² sK]	V_∞	Freestream velocity	[m/s]
h_i	Inner heat transfer coefficient	[J/m ² sK]	V_{TAS}	True air speed	[m/s]
h_o	Outer heat transfer coefficient	[J/m ² sK]	W	Aircraft weight	[N]
$h_{surface}$	Height of surface measured from datum	[m]	w	Mass-specific energy density	[J/kg]
IOC	Indirect Operational Cost	[USD/blhr]	S_h	Wing surface	[m ²]
k	Thermal conductivity	[W/mK]	V_{mca}	Minimum control speed in the air	[m/s]
k_e	Effective thermal conductivity	[W/mK]	V_{mcg}	Minimum control speed on the ground	[m/s]
K_t	Stress concentration factor	[-]	V_R	Rotation speed at take-off	[m/s]
L	Aerodynamic lift	[N]	V_{S_1}	Stall speed in landing configuration	[m/s]

Executive Overview

The increasing demand for sustainable aircraft solutions has encouraged the development of non-CO₂ emitting aircraft designs. Currently, a number of theoretically successful designs have been created by parties such as the Massachusetts Institute of Technology, National Aeronautics and Space Administration, and The Technical University of Delft. Unfortunately, these radical aircraft redesigns are too risky to conceive, requiring massive amounts of investment and research. Since growth of the global aviation industry will only persist if aircraft greenhouse gas emissions are reduced, airlines have been looking for more fuel efficient aircraft, and the demand for green solutions has skyrocketed¹. Thus, in this study the A320appu is proposed in an effort to significantly decrease the environmental footprint of aviation while limiting the risks and cost that accompany novel designs. This is done through a conversion of the A320neo to use a hybrid, multi-fuel power and propulsion system. By replacing the traditional kerosene Auxiliary Power Unit (APU) with a hydrogen engine and an aft mounted, boundary layer ingesting propulsor, the design will enter the narrow-body market as an intermediate step between current generation kerosene-powered aircraft and more distant radical redesigns, like the Flying V² or the Aurora D8³. The APU is thus adapted into an Auxiliary Power and Propulsion Unit (APPU). This single aisle, short-medium haul airliner was specifically chosen for this conversion because aircraft of this class are expected to comprise 80% of all aircraft sales by 2038. The reconfigured A320neo, coined the A320appu, shall provide an economically feasible and green alternative. It shall be the first advance towards normalising hydrogen within the aviation industry.

The challenges of designing the A320appu are to maintain low development costs, integrating the cutting edge subsystem and reassessing aircraft parameters such as the stability and controllability or range. Moreover the Operating Empty Weight (OEW) increases because of the added subsystems, and as the A320appu is designed for the same Maximum Take-off Weight (MTOW), the available payload decreases. The A320appu is designed such that the increase of the OEW is minimised, while maximising the integrability by limiting the amount of changes to the A320neo. Furthermore, significant reduction of the CO₂ emissions and local pollution have to be ensured, while providing similar performance to the A320neo. To achieve the aforementioned points, four main changes to the A320neo are proposed below and thereafter discussed in more detail.

First of all, to convert the APU to the APPU the engine needs to be enlarged to provide power for the propulsive system. The placement of this larger engine is decided to be at the same location as the current APU, mostly because of the proximity to the propeller which makes the transfer of power easier. Secondly, a propeller needs to be added to the back of the fuselage to ensure efficient use of BLI. Thirdly a hydrogen fuel tank was placed in the aft cargo compartment and lastly a T-tail configuration is used for the empennage to ensure the boundary layer is less distorted before reaching the propeller.

The APPU turboshaft engine is designed to provide power and bleed air to aircraft subsystems throughout the mission, and in addition to this, provide propulsive power. To aid the engine design, a typical mission of the A320neo from Amsterdam to Lisbon is simulated. The simulation addressed climb, cruise and descent, omitting the LTO phase. This resulted in preliminary fuel consumption values, as well as the required power of the APPU. The power was iterated with respect to propeller design and propeller required shaft power in various phases. The engine performs at a 36% thermal efficiency in cruise, with a hydrogen fuel consumption of 0.0845 kg/kWh. The final sea-level shaft power output of the engine is 3550 kW. With an approximate figure for output power, the engine was sized in GasTurb [62]. Maximising thermal efficiency, input parameters of the program were optimised. This allows for iteration with the mission simulation, given accurate values of fuel consumption. Additionally, it was verified that the engine could provide sufficient power on kerosene as well as hydrogen.

The geometric sizing of the turboshaft was determined from GasTurb, and the mass estimated from statistics, resulting in a total engine mass of 410 kg. This was followed by the design of the gearbox, which needed to allow for variable RPM of the APPU propeller. Furthermore, the engine and propeller shaft are at an angle, which required the inclusion of a universal joint. The total mass of the gearbox and torque converter is approximately 300 kg. Knowing the required inlet flow of the engine, the S-duct was sized, and the flow properties in the duct quantified. After this, the engine exhaust was discussed, with a centrifugal exhaust chosen due

¹<https://www.airbus.com/aircraft/market/global-market-forecast.html>, retrieved on 23-04-2020.

²<https://www.tudelft.nl/en/ae/flying-v/>, retrieved on 30-06-2020.

³https://www.nasa.gov/topics/aeronautics/features/future_airplanes.html, retrieved on 30-06-2020.

to space limitations. Furthermore, a safety analysis was completed, including an estimation of empennage impact probabilities. Finally, a sensitivity analysis of the mission simulation was done to show the impact of changing cruise altitude, mission distance and operational empty weight on the design of the APPU and its fuel consumption.

The propeller design was a challenging tasks as the different flight envelopes required the propeller to perform at varying altitudes. By using the propeller simulation software CRotor, the propeller performance could be evaluated in different configurations. Unfortunately, the boundary layer ingestion (BLI) efficiency gain could not be assessed by this software. Due to this limitation, the BLI gain was evaluated through a theoretical approach. Albeit, this approach might not fully encompass the gain, a preliminary assessment estimated the gain to be around 200 kW. Eventually, by using a contra-rotating, variable RPM, variable pitch three-bladed propeller, the required propulsive efficiency could be met. By use of CFD software the boundary layer thickness was quantified. Together with tip-back angle constraint a maximum diameter was determined. As, initially, this diameter did not allow for a high enough efficiency, it was decided to increase the diameter and bypass the tip-back angle by stopping the propeller during take-off and landing. By allowing the propeller to stop, at the exact right angle, during these flight envelopes, the tip-back angle was increased since the vertical distance from the propeller hub to the ground was decreased. This solution is visualised in Figure 1. The ultimate propeller design properties are displayed in Table 1 for both the forward and aft propeller.

Table 1: Propeller geometrical characteristics

Variable	Forward propeller	Aft propeller
Number of blades [-]	3	3
Radius [m]	1.75	1.75
RPM 5-11 km [-]	1 000	1 000
RPM 0-4 km [-]	1 400	1 400
Efficiency [%]	80	92.6

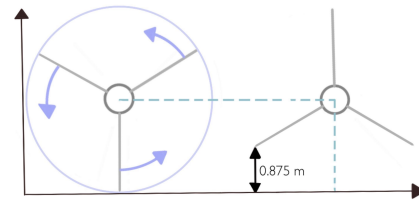


Figure 1: Propeller configuration on the right used to bypass maximum propeller diameter

To store the hydrogen fuel for the APPU a cryogenic tank has been designed to fit in the aft cargo hold. Gaseous hydrogen proved to be unfeasible due to larger tank volume and mass, leading to usage of liquid hydrogen instead. It is required that the tank has enough capacity to store 400 kg of hydrogen at an ambient temperature of 45°C for 48 hours without boil-off. That is to say, the venting pressure should not be reached before the 48 hours. Subsequently, one of the bigger challenges is to design and find the appropriate materials for an insulation system such as foam, Aerogel, and multilayer insulation (MLI). Besides thermal analysis, the cryogenic tank was also designed to withstand the pressure difference between the inner and the outer layer. This analysis is part of the mechanical design. According to the numerical model the two analyses resulted in the tank as shown in Figure 2. Furthermore, the tank has a 30.5 mm thick wall that consists of aluminium, Aerogel, multilayer insulation (MLI), and Carbon Fibre Reinforced Polymer (CFRP). Additionally, it has a boil-off time of 52.8 hours and is able to withstand at least 60,000 cycles before failure due to crack formation. Then, the mass of the tank was found to be 288 kg. Lastly, the fuel distribution system was also designed. This includes the design of the fuel lines, pump selection, and the heat exchanger. The fuel storage and distribution system resulted in a total mass of 499 kg.

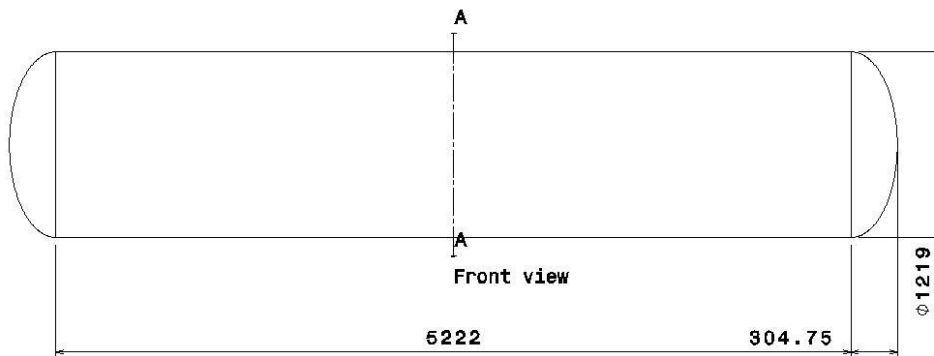


Figure 2: The dimensions of the hydrogen tank.

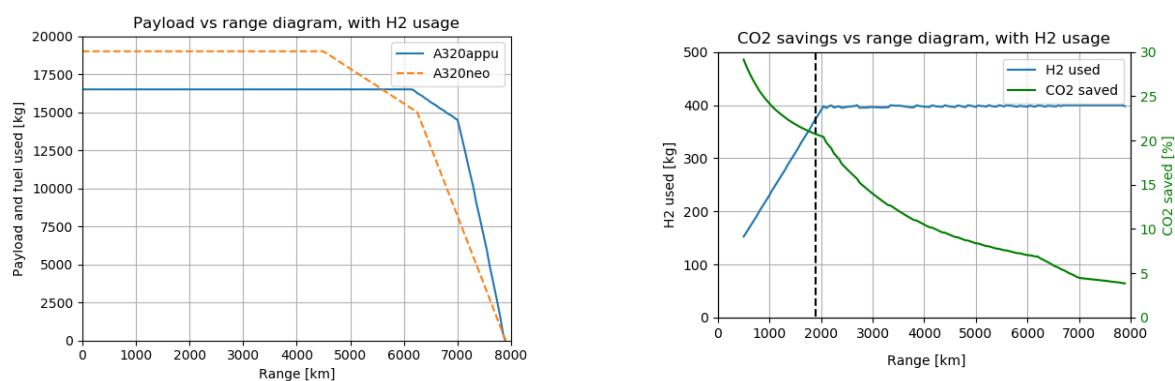
The empennage was decided to be adapted to a T-tail to ensure proficient use of the boundary layer by the propeller. The main purpose of the empennage is to provide sufficient stability and control to the aircraft. This changing configuration means that the design of the tail needs to be reassessed. In addition, the added subsystems shift the centre of gravity of the plane and this needs to be taken into account. Thus, a new centre of gravity range for the A320appu is proposed and thereafter the horizontal tail is sized by means of the following six criteria:

- Stick-fixed cruise
- Short period eigenmotion
- Recovery from deep stall
- Rotation at take-off
- Trimming at approach
- Trimming at stalling conditions

Furthermore the vertical tail is sized by looking at the required yawing moment to counteract engine failure during take-off and cruise. The analysis results in a surface area of approximately 37 m^2 for the horizontal tail and 25 m^2 for the vertical tail. Lastly a preliminary look is taken at the structural aspect of the T-tail by considering a static load case on the tail and the response to vibrations by the tail. This did not yet lead to an initial design for the structural elements in the tail as the used method could not be validated yet. More investigation into this topic is needed at later design stages.

Next to the design of the four subsystems, an analysis of the aircraft as a whole is performed. To start, the performance is assessed by looking at conventional performance metrics (e.g. range or take-off distance). Then the improvement from a sustainability point of view, is looked at. Furthermore, the operations and logistics is discussed and lastly a cost estimation is performed.

It is important that the A320appu maintains the same performance characteristics as the A320neo. Therefore, first, the payload-range was assessed, using a similar simulation as the engine design. This analysis resulted in a harmonic range, a maximum fuel range and a ferry range of $6\,150 \text{ km}$, $7\,000 \text{ km}$ and $7\,870 \text{ km}$ respectively. These ranges are valid when the APPU engine only runs on hydrogen. If it were to run on kerosene, the ranges are slightly extended, most importantly to a harmonic range of $6\,700 \text{ km}$. Figure 3 graphically displays the payload-range on the left. The right graph shows in the green line the percentage of CO_2 that is saved for a certain range. Manoeuvrability and take-off and landing performance was also qualitatively addressed. Climb, turning and take-off performance were determined to be equal or better for the A320appu, as the MTOW is kept the same at 79 tons, while there is the same or more thrust available. The landing distance is increased however, because, due to the added mass of the APPU systems, the MLW was increased by almost two tons. This increase turned out to be only 3.31% however, well within the requirement.



(a) Payload-range diagram for the A320appu with hydrogen usage

(b) CO_2 savings-range diagram for the A320appu with hydrogen usage

Figure 3: Payload-range and CO_2 savings-range diagrams for the A320appu with hydrogen usage

This project revolves around the goal of lowering the greenhouse gas emissions of the A320. CO_2 emissions are covered by Figure 3, but LTO cycle emissions are of importance for the local environment as well. NO_x , unburnt hydrocarbons and CO emissions were analysed for both the A320neo and A320appu. According to this analysis, the A320appu emits 63.4% less LTO emissions on average, better than the 50% requirement. Furthermore, noise levels from the complete A320neo, the APPU propeller and the APPU engine were quantified. The APPU noise was added to the A320neo noise, as the A320appu essentially is the A320neo with the APPU system added to it. This addition only increases the noise level by 0.93%, well within the requirement of a maximum 5% increase.

A new aircraft with a new fuel raises questions regarding the operations and logistics, which is thus evaluated. The logistics of the supply of hydrogen is as follows. The airport storage tank trucks will be supplied with

hydrogen by trucks coming in from nearby liquefaction plants. When an aircraft needs to be refuelled, a small fuelling tank will be filled and driven to the gate to refill the hydrogen tank. Subsequently, the refuelling is then done with the use of a dispenser and the fuelling time of the hydrogen tank is estimated to be 14 minutes, which falls within the fuelling time of the kerosene tank of 16 minutes. As both tanks can be fuelled simultaneously, this means that the turnaround time will not increase. Furthermore, the evacuation plan of the A320appu was assessed and determined to be similar to the A320neo. The final discussed aspect is the ground operations after re-servicing which will be performed solely by the APPU. The pushback is done by reversing the pitch of the propeller and when the aircraft in the right position the pitch is changed to a forward thrust position. The aircraft will then taxi to the runway with using only the APPU and turn on the main engines 5 minutes before take-off to warm-up the engines.

Whenever a new aircraft is designed, an initial cost estimation has to be performed to assess the economic viability of the aircraft. In this cost estimation the manufacturing and hence the acquisition price of the aircraft is determined. This acquisition price is then a function of the manufacturing, profit and R&D cost. For the A320appu, the acquisition cost of the aircraft is determined to be 116 million dollars, based on a 50% profit margin. After having performed an extensive market analysis and outlook, the aircraft program size is determined to be 3 900 aircraft. In total, the A320appu's aircraft program profit is expected to be roughly 154 billion dollars, which results in a Return On Investment (ROI) of 149% for the aircraft manufacturer (Airbus).

When looking at the aircraft cost from the airliner's perspective, the operational cost is the most important cost related variable. First, the operational cost of a single-aisle narrow-body aircraft (similar to the A320neo) is determined using the method as described in Roskam [54]. These values, were then validated using statistical data to make sure the method is accurate. For a normal A320neo, the operational cost per block hour is equal to roughly 4 608\$. By adding the APPU system to the aircraft configuration, the operational cost per block hour is expected to increase to 5 128\$ per block hour for a non-H₂ configuration, and to 5 450\$ per block hour for an H₂ configuration. The total Life Cycle Cost (LCC) of the A320appu per aircraft is equal to 442 million \$, where the operational cost are almost two thirds of the LCC.

All in all, the A320appu - being the successor to the A320neo - features four fully redesigned subsystems. The traditional APU has been replaced with a hydrogen turbine powering all subsystems and a contra-rotating propeller at the aft of the fuselage. An additional tank is integrated into the aft cargo hold to safely store the liquid hydrogen. Just as importantly, the empennage configuration has been changed to a T-tail configuration to facilitate the ingestion of the fuselage boundary layer by the aft propeller. Further analyses on the aircraft as a whole have been performed to conclude that the A320appu performs similarly to the A320neo while reducing the CO₂ emissions by 20% and the local emissions by over 50%. The combination of significantly reducing the environmental impact while still introducing limited changes to the A320neo is a favourable trait for the A320appu: it makes the aircraft a prime contender to cover the transition period between the current airliner offerings and the next generation, fully sustainable aircraft.



Figure 4: The A320appu

Contents

Nomenclature	iii
Executive Overview	iv
1 Introduction	1
2 Problem Statement and Proposed Solutions	2
2.1 Problem analysis	2
2.2 Proposed solution	2
2.3 Requirements	4
3 Baseline Design	6
3.1 Initial design choices	6
3.2 Engine configuration choice	7
3.3 Tank design choices	8
I Preliminary Analyses	11
4 Market Analysis	12
4.1 Market outlook	12
4.2 Market size and breakdown	12
5 Sustainable Development Strategy	16
5.1 Aviation climate impact prospects	16
5.2 Current technologies	17
5.3 Hydrogen production	18
5.4 General costs	18
6 Functional Analysis	19
6.1 Functional Flow Diagram	19
6.2 Functional Breakdown Structure	19
7 Technical Risk Assessment	23
II Subsystem Design	26
8 Engine Design	27
8.1 Requirements	27
8.2 Subsystem power and bleed	27
8.3 Mission analysis	28
8.4 Engine design	31
8.5 Engine mass estimation	34
8.6 Drivetrain	35
8.7 Engine inlet and exhaust	36
8.8 Safety analysis	39
8.9 Mission Sensitivity analysis	41
8.10 Recommendations	43
9 Propeller Design	44
9.1 Requirements	44
9.2 Boundary layer theory	44
9.3 Propeller design	46
9.4 BLI performance gain	49
9.5 Additional propeller mechanisms	51
9.6 Structural integrity of the propeller	52
9.7 Conclusion	60
9.8 Recommendations	61

10 Fuel System Design	62
10.1 Numerical model	62
10.2 Input data	63
10.3 Thermal design	63
10.4 Mechanical design	68
10.5 Geometry	73
10.6 Fuel distribution system	74
10.7 Sensitivity analysis	80
10.8 Verification and validation	81
10.9 Conclusion	85
10.10 Recommendations	86
11 Empennage Design	87
11.1 Requirements	87
11.2 CG estimations	87
11.3 Required horizontal stabiliser surface area	88
11.4 Wing group placement	90
11.5 Horizontal stabiliser geometry	91
11.6 Required vertical stabiliser surface area	92
11.7 Vertical stabiliser geometry	94
11.8 Structural considerations	95
11.9 Verification and validation	100
11.10 Conclusion	101
11.11 Recommendations	101
III A320appu Analyses	103
12 Complete Aircraft Performance Analysis	104
12.1 Requirements	104
12.2 Performance analysis	104
12.3 Electrical block diagram	109
12.4 Hardware-Software block diagram	109
13 Sustainability Analysis	110
13.1 Requirements	110
13.2 LTO analysis	110
13.3 Noise	112
14 Operations and Logistics Concept Description	113
14.1 Liquid hydrogen operations & logistics	113
14.2 Airport operations and logistics	115
15 RAMS Characteristics	118
15.1 Safety	118
15.2 Maintainability	120
15.3 Reliability and availability	122
16 Cost Estimation	123
16.1 Research, Development, Test and Evaluation Cost Estimation	123
16.2 Acquisition Cost Estimation	124
16.3 Operational Cost Estimation	126
16.4 Disposal Cost Estimation	127
16.5 Life Cycle Cost	128
16.6 Profit and Return On Investment Estimations	128
17 Project Outlook	129
17.1 Entry into service	129
17.2 Project Gantt chart	130
17.3 Manufacturing, Assembly, Integration plan	132
18 Conclusion	133
A Technical Drawings of the A320appu	135
Bibliography	137

Introduction

Due to the increasing social and economic pressure, the world's dependency on fossil fuels and the global greenhouse gas emissions are issues that must be addressed. The aviation industry significantly contributes to the increase of greenhouse gases in the atmosphere and is dependent on carbon fuels. Forecasts anticipate aircraft to be responsible for 25% of all emitted greenhouse gases in the near future [26]. Due to the aforementioned reasons, it is necessary for the aviation industry to adapt. The development of future aviation begins with reductions in emissions. In the search for carbon neutral aircraft, a variety of different concepts were conceived. These drastically altered designs are, theoretically, able to eliminate any environmental drawbacks. However, excessively modifying aircraft architecture may not be economically feasible for aircraft manufacturers and pose many questions. Evidently, aircraft should undergo significant adjustments to become sustainable. A suitable approach is through incremental improvements of conventional aircraft configurations. Iterating on aircraft like the A320neo will reduce expenses allowing for a profitable aircraft design. This incremental improvement calls for the need of a hybrid aircraft design, which will be realised by installing an Auxiliary Power and Propulsion Unit (APPU) providing power, as well as a fraction of the total thrust, during flight.

On the Airbus A320neo, the Auxiliary Power Unit is a unit placed in the tail cone of the aircraft that provides power for the aircraft's electrical systems. It utilises fuel from the main fuel tanks and through a small turbine engine generates power for the aircraft on the ground. An APPU will be a larger device able to provide more power and also propulsion, providing a fraction of the aircraft's total thrust. The APPU will operate both on ground and during flight to provide power to subsystems of the aircraft. For instance, the APPU could be able to take over ground mission operations, such as exiting the gate position and the taxi phase. Moreover, the APPU will be designed to enable both kerosene and hydrogen as fuel to ease the transition from kerosene to hydrogen.

The purpose of this report is to provide the final design for all A320appu subsystems. The design choices are mainly driven by predetermined design parameters. These same requirements provide constraints within which the subsystems need to perform. A number of simulation software are used to perform design analyses. The purpose of this design phase is to motivate design choices and provide technical specifications for each subsystem.

The structure of the report is as follows: Firstly, [chapter 2](#) describes the problem in more detail. Additionally, the proposed solution is presented. Thereafter, [chapter 3](#) present a baseline design and the associated fundamental design choices. As economic viability is essential for a successful design, [chapter 4](#) presents a market analysis. Afterwards, [chapter 5](#) focuses on maintaining a sustainable development strategy. Subsequently, [chapter 6](#) presents the Functional Flow Diagram (FFD) and Functional Breakdown Structure (FBS). Since risks are associated with any engineering project, these should be well documented. The severity and likeliness of the most important technical risks are summarised in [chapter 7](#). After defining all engineering project formalities, the design chapters are initiated by engine design in [chapter 8](#). The engine design is followed by the propeller design in [chapter 9](#). As hydrogen will be used as a fuel, a specialised tank should be designed which is assessed in [chapter 10](#). Eventually, [chapter 11](#) concludes the design phase by describing the updated empennage configuration. Following the design phase, aircraft performance can be evaluated in [chapter 12](#). To ensure the sustainability requirements are met by the A320appu, [chapter 13](#) provides a sustainability analysis. As hydrogen imposes difficulties regarding operations and logistics, these are analysed in [chapter 14](#). Following the information provided on performance, subsystem design and operations, reliability, availability, maintainability and safety analyses are performed in [chapter 15](#). Eventually, a cost estimation can be performed in [chapter 16](#). For future research, the project outlook and recommendations are described in [chapter 17](#). Ultimately, the report is concluded by a conclusion providing an overview of the entire project and outcome in [chapter 18](#).

Problem Statement and Proposed Solutions

This chapter aims to summarise information on the problem that is assessed. First, the motivation to conduct the A320appu design is presented. Additionally, the proposed solution is described, namely the reconfiguration of the Auxiliary Power Unit to an Auxiliary Power and Propulsion Unit. This includes the rationale behind the most important concepts to be integrated in the conversion, namely introducing Boundary Layer Ingestion and the use of hydrogen as a fuel. From this, a list of requirements was generated and included in the final section.

2.1. Problem analysis

The Airbus A320neo Auxiliary Power and Propulsion Unit (APPU) project evolves around designing a hybrid single-aisle aircraft, the A320appu, using a combination of hydrogen and kerosene as fuel. The motivation to realise this design is caused by the increasing amount of greenhouse gas emissions due to aviation. This is summarised in the Mission Need Statement and Project Objective Statement.

Mission Need Statement - Design an Auxiliary Power and Propulsion Unit integrated in a single aisle passenger aircraft that will decrease the environmental impact of this class of aircraft.

Project Objective Statement - Design and integrate an Auxiliary Power and Propulsion Unit for a single-aisle passenger aircraft using boundary layer ingestion and multi-fuel, in 10 weeks by 11 students.

Two fundamental engineering concepts will be used in the A320appu design: Boundary Layer Ingestion and the use of hydrogen as a fuel. BLI can be utilised to obtain a significant propulsive efficiency gain and thus lower fuel consumption. Relevant theory on these concepts is discussed prior to examining design concepts as they are vital for the success of the design and influence other system choices.

Ultimately, to ensure an economically feasible design and decrease the development time of the design, making few changes to the A320neo structure is beneficial. Substantially redesigning the A320neo will increase development cost which discourages manufacturers to realise the design.

2.2. Proposed solution

The proposed solution is a reconfigured Airbus A320neo. The aircraft will contain an Auxiliary Power and Propulsion Unit which can utilise either hydrogen or kerosene as fuel. The APPU system powers a propeller located at the aft of the fuselage to enable ingestion of the boundary layer formed on the fuselage. Importantly, the aft propeller will generate a fraction of the total thrust, reducing the thrust produced by the main, kerosene-fuelled, engines. This allows for a goal of twenty percent reduction in greenhouse gas emissions for a typical mission. Additionally, a requirement on reducing the Landing and Take-off cycle (LTO) emissions by 50% is set. Use of the APPU for thrust reversing and taxi helps achieve this goal. Finally, the APPU will provide power to components such as the air-conditioning system, emergency power and starting power throughout the entire flight.

2.2.1. Boundary Layer Ingestion

Boundary Layer Ingestion potentially provides a significant propulsive efficiency gain. In essence, this efficiency gain is due to the propeller taking in energised air present in the boundary layer and wake of the fuselage. By locating the propeller at the aft of the fuselage it will perform in the wake or boundary layer of the aircraft. Also, the slower moving air introduces a second efficiency gain.

Equations (2.1) and (2.2) show the difference for a propulsive situation without and with BLI respectively. In the equations $\dot{E}_{\text{body, wake}}$ is the body wake energy flow, $\dot{E}_{\text{kinetic energy}}$ the kinetic energy imparted to the flow by

the propeller, T the thrust, V_∞ the free-stream velocity, and $\dot{E}_{\text{propulsor, wake}}$ the propulsor wake power.

$$\dot{E}_{\text{kinetic energy}} = TV_\infty + \dot{E}_{\text{propulsor, wake}} \quad (2.1)$$

$$\dot{E}_{\text{body, wake}} + \dot{E}_{\text{kinetic energy}} = TV_\infty + \dot{E}_{\text{propulsor, wake}} \quad (2.2)$$

Assuming that the thrust, freestream velocity and propulsor wake power remain constant between equations (2.1) and (2.2), a comparison can be performed. Since the right side of the equations remains unchanged, the same applies for the left side. Additionally, $\dot{E}_{\text{body, wake}}$ is a positive number. Ultimately, $\dot{E}_{\text{kinetic energy}}$, or the shaft power, will decrease. To summarise, wake-energy is used which means that the shaft power can be decreased for the same thrust output.

$$\eta_{\text{prop}} = \frac{TV_\infty}{P_{\text{shaft}}} \quad (2.3)$$

Following this rationale, BLI provides the same thrust for a lower shaft power input. Hence, as P_{shaft} decreases in equation (2.3), the propulsive efficiency increases. Figure 2.1 provides a visual presentation of a propeller configured in a BLI setting.

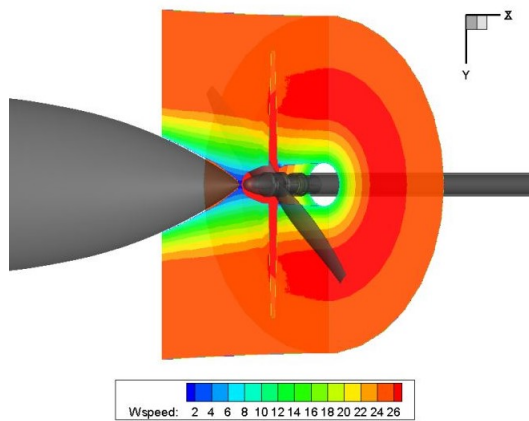


Figure 2.1: A visual representation of BLI [44]

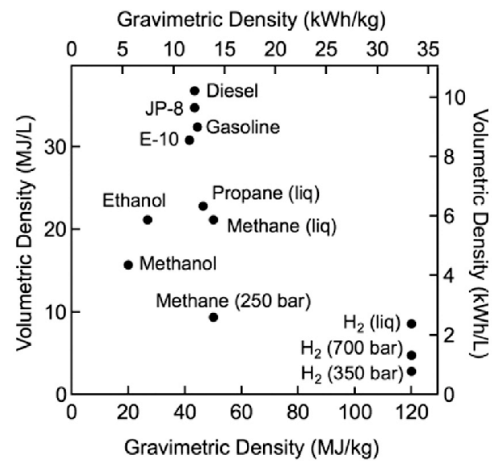


Figure 2.2: Mass and volumetric densities (lower heating value) plotted for multiple energy sources [68]

This theory has been applied to real-life experiments and has shown promising potential [44]. A propulsive system in which BLI is adapted is beneficial to propulsive efficiency, this is why the concept is to be implemented in the A320appu design.

2.2.2. Hydrogen as a fuel source

As introduced in section 2.1, the A320appu shall be a hybrid aircraft, using a combination of hydrogen and kerosene. Figure 2.2 contains volumetric and mass-specific energy densities for various fuels that allows for a performance comparison. Fossil fuels contain a high amount of energy per litre but less per kilogram. Batteries perform poorly both in volumetric and mass-specific energy density. Hydrogen and liquid hydrogen both contain a high amount of energy per kilogram. However, the volumetric density is low which creates challenges in storage. Both batteries and hydrogen are emission-neutral energy sources. Batteries are neglected as an energy source due to their poor performance in both volumetric and mass density. Hydrogen has been elected as the primary APPU fuel source due to its beneficial mass density over kerosene. However, the challenge imposed by hydrogen's volumetric density is yet to be overcome.

2.3. Requirements

The requirements for the A320appu are stated below. These were determined for the design to be successful and are used in this design phase to support the choices for design options.

Flight Mechanics and Performance

- FMP-User-01:** The aircraft shall have the same range as the Airbus A320neo WV055.
- FMP-User-01.1:** The aircraft range at maximum payload and maximum take-off weight shall be 4500 *km*.
- FMP-User-01.2:** The aircraft range at maximum fuel and maximum take-off weight shall be 6250 *km*.
- FMP-User-01.3:** The aircraft ferry range shall be 7900 *km*.
- FMP-User-02:** The aircraft shall have the capacity to transport at least 150 passengers.
- FMP-Sys-03:** The cruise mach number of the aircraft shall not decrease by more than 5% from the cruise mach number of the Airbus A320neo WV055.
- FMP-Sys-04:** The cruise altitude of the aircraft shall not differ by more than 10% from the cruise altitude of the Airbus A320neo WV055.
- FMP-Sys-05:** The landing distance of the aircraft shall not increase more than 5% from the total landing distance of the Airbus A320neo WV055 at the same weight and altitude.
- FMP-Sys-06:** The take-off distance of the aircraft shall not increase more than 5% from the total take-off distance of the Airbus A320neo WV055 at the maximum take-off weight and altitude.
- FMP-Sys-07:** The climb angle during initial climb of the aircraft shall not decrease by more than 5% from the climb angle of the Airbus A320neo WV055 at the maximum take-off weight and altitude.
- FMP-Sys-08:** The climb rate during initial climb of the aircraft shall not decrease by more than 5% from the climb rate of the Airbus A320neo WV055 at the maximum takeoff weight and altitude.
- FMP-Sys-09:** The aircraft shall passively be statically and dynamically stable.

Power Generation

- POW-Sys-10:** The minimum power of the APPU shall be sufficient to power non-essential subsystems continuously during normal operations.
- POW-Sys-11:** The APPU system shall provide sufficient power to essential subsystems in emergency conditions.
- POW-Sys-12:** The main engines shall be used as a backup system to provide power to essential subsystems.
- POW-Sys-13:** The APPU shall be able to provide power for the main engine start-up.
- POW-Sys-14:** The APPU turbine shall drive the generator at all times.

APPU Propulsion

- PROP-User-15:** The A320appu aircraft shall be able to use H2 as well as kerosene.
- PROP-Sys-16:** The APPU turbine shall be able to power the propeller at all times.
- PROP-Sys-17:** The APPU shall be able to provide sufficient thrust reversing to reverse an aircraft from stationary position out of its gate position.
- PROP-Sys-18:** The Boundary Layer Ingestion shall increase energy efficiency.
- PROP-Sys-19:** The aircraft shall have means to limit damage to the propeller caused by a ground strike.
- PROP-Sys-20:** The APPU shall be able to operate using either hydrogen or kerosine.

Fuel Tank and Distribution

- FTD-Sys-21:** The amount of energy stored in H2 shall not exceed 15% of the energy content in kerosene.
- FTD-Sys-22:** The hydrogen tank shall be able to be drained in equal or less amount of minutes as the kerosene tanks.
- FTD-Sys-23:** The H2 tank shall have a storage of fuel that stores fuel for 48 hours without boil-off at an ambient temperature of 45°C.

Sustainability

- SUST-User-24:** The CO2 emission should be at least 20% lower than A320neo for a typical mission.
- SUST-User-25:** The NOx, CO, unburnt hydrocarbon, and soot emissions for the LTO cycle should be reduced by at least 50% when compared to A320neo for a typical mission.
- SUST-Sys-26:** The noise pollution of the renewed aircraft shall not exceed the noise emissions of the A320neo by more than 5%.

Operations and Safety

- OPS-User-27:** The entry in service of the aircraft shall be in 2035.
- OPS-User-28:** The total development cost of the aircraft shall not exceed 5 billion euros.
- OPS-Sys-29:** The aircraft hydrogen refuelling system shall be safe to operate.
- OPS-Sys-30:** The aircraft hydrogen storage system shall be safely separated from the passenger cabin.
- OPS-Sys-31:** The fuel tank(s) shall fit inside the A320neo fuselage.
- OPS-Sys-32:** The aircraft APPU subsystem shall not affect passenger evacuation .
- OPS-Sys-33:** The propeller shall not cause considerable risk or danger for ground crew.
- OPS-Sys-34:** The APPU propeller shall have sufficient ground clearance during mission.
- OPS-Sys-35:** The operation procedures of the APPU shall be compatible with the Airfield procedures.
- OPS-Sys-36:** The aircraft shall be able to make use of the same airport gates as an A320neo.
- OPS-Sys-37:** The turn-around time shall not be more than 10% greater than the A320neo.
- OPS-Sys-38:** The aircraft cg shall not exceed the tip-over limit after that APPU has been integrated.
- OPS-Sys-39:** The aircraft shall be safe during all flight operations.

Regulations

- REG-Sys-40:** The aircraft shall comply with CS 25 safety regulations.
- REG-Sys-40.1:** The Auxiliary Power Unit shall comply with CS 25 subsection J: 'AUXILIARY POWER UNIT INSTALLATION'.
- REG-Sys-40.2:** The aircraft shall comply with the CS 25 regulations regarding manoeuvrability.
- REG-Sys-41:** The aircraft shall comply with airport regulations.

Baseline Design

The design process for redesigning the A320neo to the A320appu commences with exploring all various possibilities and making the first fundamental changes. These changes concern the use of a propeller aft of the fuselage and the use of a T-tail configuration. Furthermore trade-offs are performed for two primary APPU subsystems: the tank and the engine.

3.1. Initial design choices

Some fundamental choices were completed in the very first stages of the design. This section describes the rationale for choosing a propeller at the back of the fuselage and a T-tail configuration.

3.1.1. Propeller placement

Usage of Boundary Layer Ingestion can be examined for use of propeller air intake. As explained in [subsection 2.2.1](#), it can increase the propulsive efficiency of a propeller. To obtain this efficiency increase the propeller should be placed such that the boundary layer flows as undisturbed as possible to the intake of the propeller. There are two possibilities that ensure the intake of boundary layer air for a propeller: placing it behind or near the fuselage or placing it behind the wing. Placing the propeller behind the main wing has not been adopted as an option because of the increase in weight since multiple propellers would be required to ensure enough boundary layer intake and ensure lateral symmetry. Additionally, structural limitations were also considered - the wing would need to be redesigned in order to carry the extra weight. Finally, delivering power to the propeller would be a challenge since usually the APU is placed in the tail cone. The fuselage is surrounded by a well established and stable boundary layer, which makes the aft of the fuselage a favourable placement.

3.1.2. Tail configurations

The reason for examining the current tail of the A320neo in combination with the aft propeller is that the conventional horizontal tail surface will interfere with the flow taken in by the propeller, significantly decreasing the effect of Boundary Layer Ingestion. Furthermore, multiple APPU-elements will be configured in the tail cone which further motivates a redesign of the empennage. Thus other configuration options have to be examined. Initially, non-feasible options or options that cannot yet be developed were removed. The primary tail configurations that remained, were the conventional tail, T-tail and cruciform tail. The main factors influencing the choice of the tail configuration were compatibility with boundary layer ingestion of the propeller, complexity, weight, similarity to A320neo, drag, and elevator and rudder effectiveness. Following, the best options were summarised and a trade-off was executed to find the best choice based on a number of criteria. In [Table 3.1](#) an overview of the remaining options are listed together with their most significant benefits and drawbacks.

Table 3.1: Overview of the benefits and drawbacks of different tail configurations [50]

Configuration	Benefits	Drawbacks
Conventional	<p>Elevators at low air speeds are more effective if the engine thrust air is blowing over the elevator, this is only significant at lower speeds</p> <p>Lowest structural strength required</p>	<p>Interference with propeller air intake</p> <p>Distorted flow over the horizontal tail plane as a result of engine exit flow, wing wake and wing vortices</p>
T-tail	<p>Free stream air allows for a smaller required area because of a higher effectiveness of the control surfaces</p> <p>End plate effect, no vortices are produced at the edge of a vertical tail, increasing the effectiveness of the vertical stabiliser and rudder, reducing its size</p> <p>The horizontal tailplane is out of the wing wake, downwash, vortices and exhaust from the main engines, allowing for high effectiveness of elevator</p>	<p>A stronger and thus heavier tail structure is required as more loads need to be carried, the bending moment produced by the horizontal stabiliser needs to be transferred through the structure</p> <p>In deep stall, T-tail aircraft often have pitching moment instability</p>
Cruciform	<p>Advantages of both the conventional and T-tail configuration</p> <p>Flutter is not as much of a problem as with a T-tail</p>	<p>Decreases effective aspect ratio of the vertical tail</p> <p>Interference with propeller and wake</p>

All in all, comparing the various options, the T-tail configuration shows the most suitable configuration for the A320appu design. With it come challenges related to providing sufficient structural integrity to support the higher placed horizontal stabiliser and elevator, as well as not increasing the mass of the empennage to the extent that other large design changes have to be made to the aircraft. Moreover, after the first APPU and hydrogen tank design has been completed the empennage will have to be redesigned to make sure the horizontal and vertical tail are large enough to ensure the stability and controllability of the aircraft.

3.2. Engine configuration choice

Three concepts for the engine configuration were suggested, which are shown in [Figure 3.1](#). These concepts varied in their engine placement. As discussed in [section 3.1](#), the location of the propulsor and the empennage configuration are the same for all concepts. The drawings are not to scale, with sizes exaggerated for legibility.

Concept 1 has the engine in the tail cone similar to the APU in the A320neo, with an S-duct that has an inlet in the vertical stabiliser, placed some distance from the fuselage to prevent boundary layer to flow into the duct. A generator is included for the generation of subsystem power, but this is far smaller than the generators required for the other concepts. The S-duct introduces some minor pressure losses, but has been employed in civil aircraft before. This concept is one of the easiest to integrate, as the current A320neo APU sits similarly in the tail cone of the aircraft.

Concept 2 has two engines, one on each wing tip. Electric generators and motors are used to transfer the power from these engines to the propeller, as well as generating subsystem power. The use of two engines instead of one, as well as two generators and a motor, leads to this concept being heavier and more complex, accounting also for wires and connections throughout the aircraft to the tail cone. Wingtip engines have been explored, but are uncommon in aircraft and unseen in modern civil aviation. Their effects on the wing of the aircraft may be difficult to quantify.

The third concept has the engine in the vertical stabiliser, with its inlet at the same location as the inlet of the S-duct in Concept 1. This omits the need for designing an S-duct, but the engine now needs to include a generator and motor for driving the aft propeller. Furthermore, the engine placement may require considerable redesign of the tail.

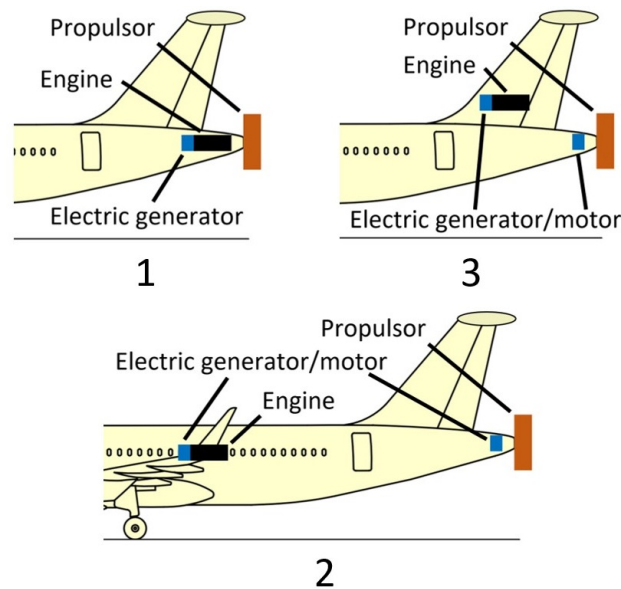


Figure 3.1: Concepts for engine placement.

Ultimately, Concept 1 fared the best in the trade-off. This was a result of its smaller and therefore lighter generators and because it required the simplest changes to the existing A320neo - only an increase in the auxiliary engine size and an addition of an S duct was necessary. [25].

3.3. Tank design choices

The three main design choices are the tank placement, geometry, and either liquid or gaseous hydrogen. The following options were explored for tank placement: using the cargo hold, reducing passenger rows and extending the fuselage. Furthermore, different geometries were considered depending on the placement.

3.3.1. Hydrogen storage method choices

Current technology allows for three different options to store hydrogen. Compressed gaseous hydrogen, cryogenic compressed hydrogen, and liquid hydrogen. Table Table 3.2 shows a summary of important properties regarding each type.

Table 3.2: Hydrogen storage properties [51]

Type of hydrogen	Volumetric density [MJ/L]	Temperature [K]	Pressure [bar]
GH ₂	4.9	293	700
LH ₂	5.4	20	1-1.5
CCH ₂	4.0	40-80	300

Cryogenic compressed and gaseous hydrogen have the advantage that they do not need to be as heavily thermally regulated. However, it can be seen that liquid hydrogen contains the most energy per volume, which is a very large advantage as volume is the limiting factor when trying to integrate the tank. These advantages of liquid hydrogen off-set the disadvantage of extra complexity and mass of a cooling system. Therefore liquid hydrogen is going to be used in all design options.

3.3.2. Possible tank solutions

The goal of the design is to implement the APPU into the already existing A320neo architecture minimising the changes to the overall structure and performance of the aircraft. Therefore, when looking at the tank location, it is important to investigate the different storage locations that may be used. In this section, different storage locations are examined.

Solution 1: cargo space

The first and most evident solution is to store the hydrogen in the cargo bay. However, airliners use this space to store luggage or cargo. First, the cargo hold of the A320neo is assumed to be a perfect trapezoidal shape. Thereafter, different geometries have been created to fit in the trapezoid. The objective is to make effective use

of the available space. Only cylindrical and elliptical shapes are considered in order to stay within the stress ranges and prevent the need of highly reinforced tanks. Four different configurations are shown in Figure 3.2 as an option for fitting the hydrogen tanks.

Placing a hydrogen tank in the cargo hold will decrease the available space for luggage. The decrease in cargo space should therefore be as small as possible. Since tank 2 and tank 4 use most of the area it was concluded that these offer the best solution in terms of volume. Due to their high geometric efficiencies they can carry more hydrogen for the same amount of cargo volume. However, in order to reach the requirement on boil-off time only tank 3 is feasible and is therefore chosen in the end.

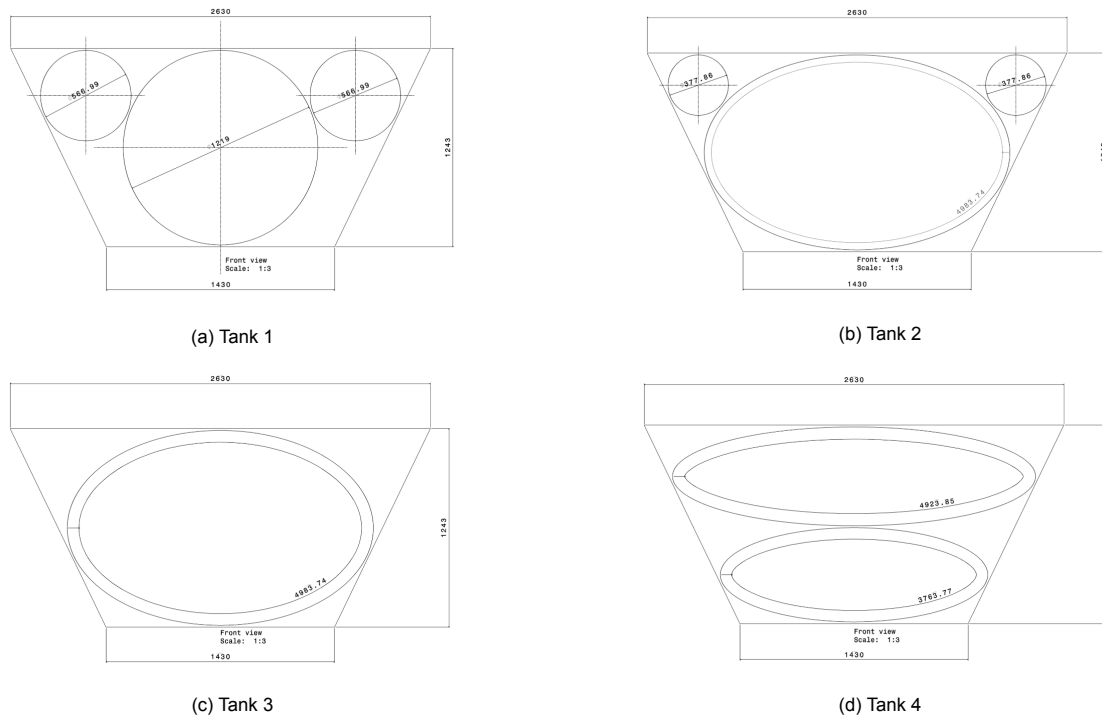


Figure 3.2: Various geometries for the hydrogen tank in the cargo hold.

Solution 2: reduce passengers rows & extend fuselage

In this section the option to reduce the number of passenger rows or extend the fuselage is investigated. Both options open up additional space in the back of the cabin to place a hydrogen tank. That is, behind the end of the cabin.

A first impression of a possible design is visualised in Figure 3.3. Here, it can be seen that the tank starts cylindrical and ends with a conical shape. The conical shape is in particularly interesting since it can fit better in the tail cone.

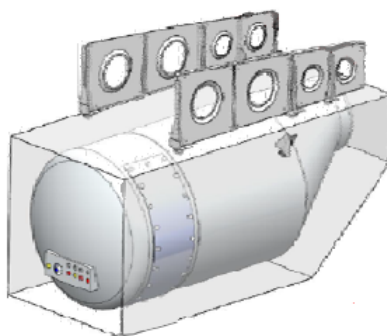


Figure 3.3: Tank concept by Air Liquide [11]

If passenger rows are removed, volume is gained behind the cabin in case it is moved forward. The A320appu has a minimum requirement of 150 passengers and therefore a maximum of 5 rows may be removed before

exceeding the limit. It was determined that enough volume could be gained after removing 3 rows for a conical tank and 4 rows for the cylindrical one. In both cases, the space is over designed by 30%. The reason that the cylindrical option was also investigated is that it is less complex and more technologically ready than a conical tank. However, an additional row must be removed because it is less efficient in occupying space which is bad for profits.

Another solution for hydrogen storage is to extend the fuselage. This option is rather complex as it adds a significant amount of mass to the operational empty weight and alters the current geometry resulting in additional redesign considerations of the aircraft. Nevertheless, this option is investigated and discussed in this section. Similarly, the volume gained by extending the fuselage is estimated as a truncated cone. The cabin is maintained at a fixed position with respect to the nose. The aft diameter of the cone is fixed to the original diameter at the end of the cabin. An extension of 2 m using a cone poses the best solution. Again, one could use a cylindrical tank for which the fuselage must be extended by 3 m. The mass of the hydrogen tank itself is not much different from the row reducing option. However, extra structural mass from extending the fuselage has not been taken into account. Thus, in terms of mass and complexity, row reducing is a better solution to place the hydrogen tank.

3.3.3. Trade-off

In the end it was decided to place the tank in the aft cargo compartment. The most important reasons are the proximity to the engine and that the value of cargo space is less than the value of seats. Furthermore, a cylindrical tank was chosen in order to comply to the boil-off requirements. More information on this trade-off can be found in previous reports [25].

3.3.4. Conclusion

All in all, it was decided to place the propeller at the aft of the fuselage and use a T-tail configuration to allow efficient use of BLI. Furthermore, the engine is placed in the tail cone to minimise weight and the amount of required changes to the A320neo. Lastly, the tank is placed in the aft cargo hold to minimise operational profit and complexity.



Preliminary Analyses

Market Analysis

Since the A320appu design will be based on the Airbus A320neo, it was assumed that both would compete in the same market. The market analysis will therefore examine the features of the single-aisle, short to medium-range aircraft sector. This market is dominated by Boeing and Airbus, with the dyad controlling over 90% of the market share¹. Due to their near negligible contribution, the remaining manufacturers will be omitted from the analysis. The analysis will cover the market outlook, market size and breakdown, competition and finally all these aspects will be applied to form an initial business strategy.

4.1. Market outlook

In the past decades, aircraft manufacturers have mainly focused on decreasing greenhouse gas emissions caused by aircraft. Strict regulations regarding local pollution around airports the aviation industry is motivated to limit greenhouse gas emissions. Additionally, as the general public is becoming more aware of global warming and its disadvantages, the aviation industry is pressured to decrease the amount of polluting emissions during the entire flight envelope. Since aircraft have to be sustainable with respect to the environment, social factors and economic influences, a green solution has to have relatively low development, production and operating cost. The difficulties provide an opportunity to create a green and profitable aircraft. Airline such as easyJet and Quantas are already implementing carbon offset strategies which means that soon the entire industry will be focused on reducing emissions. Together with the increasingly popular small, such as the A320neo, aircraft, the A320appu provides a sustainable design to profit from the aforementioned trends.

4.2. Market size and breakdown

The global market size is an important parameter in the market analysis to be able to identify the largest potential customers. By identifying these customers the business strategy can be altered and fitted to their needs. To determine the most prominent sectors in aviation the current number of aircraft and the anticipated growth is analysed. Following this analysis, numbers representing the demand for narrow-body aircraft like the A320neo are presented. Only commercial and freighter aircraft are considered since private-jet consumers, usually, do not consider the A320 segment.

The Global Market

The total number of aircraft and anticipated growth are assessed both globally and for certain regions. The anticipated growth is established by use of a forecast presented by Airbus. These numbers are discussed for each region to establish a deeper understanding of the global markets and their potential value.

Table 4.1: 20 year aircraft forecast

Region	Start Fleet 2019	End Fleet 2038	Percentile change
Africa	670	1 660	248
Asia-Pacific	7 441	20 009	268.9
CIS	1 022	1 870	183.0
Europe	5 141	9 271	180.3
Latin America	1 459	2 995	205.3
Middle East	1 355	3 524	260.1
North America	5 593	8 354	149.4
World	22 682	47 684	210.23

¹<https://bit.ly/2YA8T97>, retrieved on 22-04-2020

All numbers and data presented in this subsection have been collected from Airbus' Global Market Forecast². Eventually, possible crises and the ongoing Covid-19 crisis will be discussed. Table 4.1 predict aviation to grow significantly over the next 20 years. The former table solely displays the passenger aircraft growth, where the latter details the growth of passenger and freighter aircraft. With a total percentile change of more than 200%, aviation is expected to support a substantially larger audience by 2038. These tables show no data about the number of aircraft to be substituted, only the number of new aircraft. This effect causes the actual number of aircraft to be manufactured by 2038 to be higher as retired aircraft will have to be replaced. Estimations show that by 2038, 14 210 aircraft will be replaced. Ultimately, the increase in freighter aircraft numbers is partly realised by converting old passenger aircraft. The total number of aircraft to be converted by 2038 is estimated at 1 631. The two aforementioned effects cause the total aircraft demand over the next 20 years to be estimated at 39 210 units.

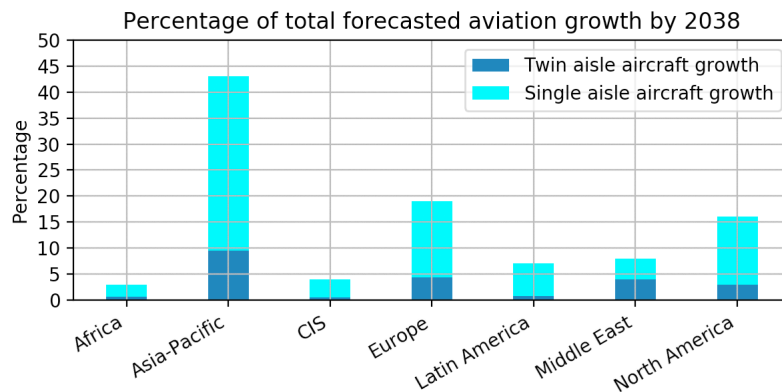


Figure 4.1: Breakdown of global growth into continental growth

As Figure 4.1 depicts that the demand for narrow-body aircraft, like the A320neo, will rise significantly. This demand is global even though it differs per continent. From previously detailed table and figure it is obvious that the Asia-Pacific market will experience the largest percentile and absolute growth. Europe and North America will still contribute a significant portion of the aviation industry growth and the CIS (Commonwealth of Independent States), Middle-East, Africa and Latin-America will expand their fleet with mainly smaller aircraft types like the A320neo.

Main Focus

Currently Europe and America possess the largest aircraft fleet worldwide. However, forecasts show that Asia-Pacific will significantly expand their fleet and exceed Europe and America in aircraft-fleet size. Africa, the Middle-East, the CIS and Latin America and the Caribbean currently contain a small portion of the aviation market. Nonetheless, these regions show noticeable potential to evolve their economy. Subsequently, the demand for aircraft will increase.

To conclude, the business strategy should primarily be focused on the Asia-Pacific region due to its anticipated growth. America and Europe are also expected to be substantially profitable. Therefore, intensive market research should be performed for the three aforementioned regions. The most important conclusion that can be drawn from the market analysis is the expected growing economies that have a persistent demand for aircraft are expected to grow, giving more assurance for future demand of the A320neo.

Assessing Crises

Crisis analysis is rather important due to the current Covid-19 outbreak. Global crises cause the economy to shrink in almost all sectors worldwide. The aviation industry also experiences a recession during a global crisis, affecting the use of aircraft, the demand for future aircraft and the development of new types.

Figure 4.2 shows the Revenue Passenger Kilometre (RPK) per year since 1978. The Revenue Passenger Kilometres per year displays the kilometres travelled by paying passengers. This directly correlates to the growth of the aviation industry. This graph details two important phenomena; the aviation sector is experiencing a rapid growth and; the aviation industry is almost completely resilient to crises. Events such as 9/11, the outbreak of the SARS virus or the financial crisis of 2008, which all had a significant impact on the global economy, merely cause wrinkles in Figure 4.2.

²<https://bit.ly/2VjOsv9>, retrieved on 23-04-2020

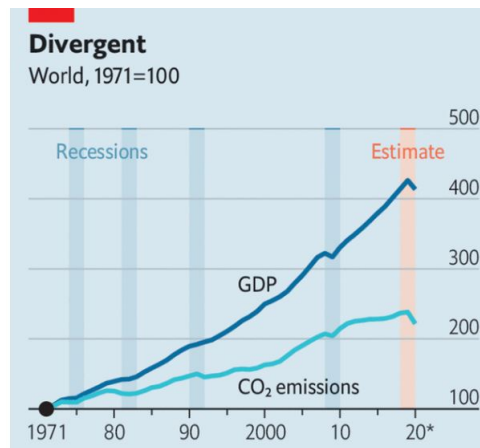


Figure 4.2: The global GDP and Carbon-dioxide emissions monitored over a certain time-span⁴

Furthermore, as apparent from looking at [Figure 4.2](#), also carbon-dioxide emissions will be relatively untouched by the current Covid-19 crisis. Additionally, crises might introduce incentives for airlines to increase sustainability since carbon-dioxide taxes are a renowned manner to repay government debts. Given the aforementioned information, it can be concluded that the aviation industry will relatively quickly recover from the Covid-19 crisis. Due to this expectation the Covid-19 crisis will not be assessed any further or taken into account for the current business strategy.

4.2.1. Competition

Examining the Boeing and Airbus fleet, the A320appu's main competitors can be specified: the Boeing 737 MAX and the Airbus A320 family, including the A320neo. The analysis will be focused on figures from around 2015, which unfortunately means they will be to some degree outdated. The reason for this is that recent events have greatly disturbed the aviation industry. Since the start of the millennium, Boeing and Airbus have been engaged in cut-throat competition with both parties oscillating between 45-55% market share. Only until recently has this battle shown signs of slowing down. With the 737 MAX groundings, the duopoly disintegrated with Airbus swiftly gaining ground. This, paired with the Covid-19 pandemic, have strongly disturbed a very stable and fast-growing market. The market outlook for 2035, the A320appu's planned entry-into-service year, is uncertain at this time. For this reason, this analysis will take into account the market outlooks for 2020 made during the end of 2019⁵. Freak occurrences such as the record-low oil prices will be forgone in the analysis.

Porter's Five Forces Analysis

Following examining the market as a whole, a more technical analysis is performed to examine the performance of various aircraft types. For this analysis Porter's Five Forces framework was chosen to analyse the level of competition.

Threat of new entrants - The threat of new entrants refers to the possibility of new manufacturers entering the market and detracting from the A320appu's sales. As mentioned in [section 4.1](#), the single aisle market has been dominated by Airbus and Boeing over the past decades. Few new competitors have been able to gain significant market share as a result of Airbus and Boeing's aggressive 'competitive' and 'destroyer' pricing strategies, restraining most competition between the duopoly. This means Airbus and Boeing aim to lower the prices of their fleets to the point where other manufacturers cannot compete and then match the prices to each other to avoid a price war as this would ultimately be detrimental for both parties. With this in mind, it is unlikely that new entrant will be a threat to the A320appu, especially given the barriers of entry of this market, such as tight regulation.

Threat of substitute products - This entails competitors developing new aircraft with similar features, namely partial hydrogen propulsion or equivalent. The APPU is the main selling point of this aircraft and consequently, if competitors start offering something similar, then the A320appu will naturally lose some buyers. Currently, there seem to be few potential substitutes for the A320appu, as none of Airbus's competitors have shown serious investment into the development of sustainability-focused designs.

Rivalry among existing competitors - The most immediate competition comes from the Boeing 737 MAX; the A220 and its variants, and the A320 family. Since the 737 MAX is no longer a viable product for airlines this

⁴<https://econ.st/38178F2>, retrieved on 15-06-2020

⁵<https://bit.ly/383DBud>, retrieved on 23-04-2020

means the A320appu will be competing similar Airbus aircraft, including its predecessor the A320neo. While this cannibalisation will not be detrimental for Airbus, it may negatively affect the sales of the A320appu. Its performance will largely depend on the chosen pricing strategy. The higher the price, the lower the sales. Despite the current generation of the 737 MAX being grounded, it is likely that Boeing is either developing a new and improved (i.e: safe) generation, or will release a new reliable version, since the 737 MAX was a very popular product prior to the accidents. So while it may seem logical to disregard the 737 MAX as a direct competitor, this should not be done because, for one, it was one of the best selling aircraft in the world, meaning it is a good example of what the market demands, and second, because a similar iteration from Boeing will likely enter the market soon.

Bargaining power of suppliers - The suppliers in the aircraft market have the power to change the price and quality of their products to their benefit. Airbus is very dependent on its suppliers for production, for example, most jet engines are bought from GE, Safran and Rolls Royce. Without insider information it is hard to determine how the power is distributed in these relationships.

Bargaining power of buyers - This is similar to the point above however it relates to buyers, i.e: airlines. Since there is such vicious competition in this market, the buyers are in an advantageous position and will always have strong bargaining power as they can relatively easily switch from Airbus to Boeing. Unless there is collusion between the two manufacturers, the customer will always be the priority.

Technical Performance

In Table 4.2, information relevant to the A320appu's competitors is presented. From this table it can be seen that the A320appu's MTOW should be around 90 tonnes to match that of the competition and thus for it to compete with these aircraft. Matching some of its main performance parameters indicates that there currently is a demand for this aircraft and will likely not change in the future, and it ensures that the A320appu will compete with the listed aircraft, giving the team and the stakeholders an overview of the market the design will enter. Therefore, the passenger capacity should be between 160 and 190; the range around 3 700 nautical miles (at maximum payload) and it should cost no more than US\$120M. All of the values stated were slightly above the average of the competitor pool. For generation of functions and requirements, performance and price of the aircraft this will be investigated extensively.

Table 4.2: Overview of competitor features⁶

Type	MTOW [tonnes]	Pax	Range [nmi]	List price [USD]
A220-100	60.8	100-120	2 950	79.5M
A220-300	67.6	120-150	3 350	89.5M
A319neo	75.5	120-150	3 700	101.5M
737 MAX-7	80.3	138-153	3 850	96.0M
A320neo	79.0	150-180	3 400	110.6M
737 MAX-8	82.2	162-178	3 550	117.1M
737 MAX-9	88.3	178-193	3 550	120.2M
A321neo	97.0	180-220	4 000	129.5M

Designing an aircraft with similar performance characteristics and similar price will ensure that the A320appu enters the market with the listed aircraft as competitors. For generation of functions and requirements, performance and price of the aircraft above will be looked into extensively.

Sustainability

Across both manufacturers, sustainability is a major focus, with both parties setting ambitious goals to reduce waste, water and emissions. As mentioned earlier, there are also regulations that in the future restrict aircraft design choices and forces manufacturers to reduce emissions of their aircraft. This paired with the A320appu's emphasis on emissions reductions means that special consideration should be taken throughout the development of this aircraft to ensure that it is in at the very least line with the rest of the market in terms of sustainability, and has reduced greenhouse gas emissions compared to current competing aircraft.

⁶<https://bit.ly/3eFrNRB>, retrieved on 27-04-2020

Sustainable Development Strategy

As the demand for air travel increases, more emphasis is laid on sustainable development in aviation. Sustainability is often regarded from an environmental standpoint by looking at emissions and climate change. However, when sustainable measures are taken, one has to not only consider environmental but also social and economic aspects. These aspects should be incorporated with every decision.

5.1. Aviation climate impact prospects

Over the last decades, carbon-emissions per passenger have decreased greatly due to the development of more efficient aircraft. Nevertheless, current trends show that the amount of kilograms of CO₂ will increase over the years if the industry does not change. As shown in Figure 5.1, even with efficiency improvements of 2% per year, the emissions are expected to double to 1.5-2B tons by 2050 according to Air Transport Acting Group (ATAG) and International Air Transport Association (IATA) [19]. It becomes clear that a substantial amount of money has to be invested in researching and developing new technologies in order to achieve a 50% CO₂ reduction compared to 2005. These projections have driven companies to fund new projects and are a prime motivation for the development of the A320appu project.

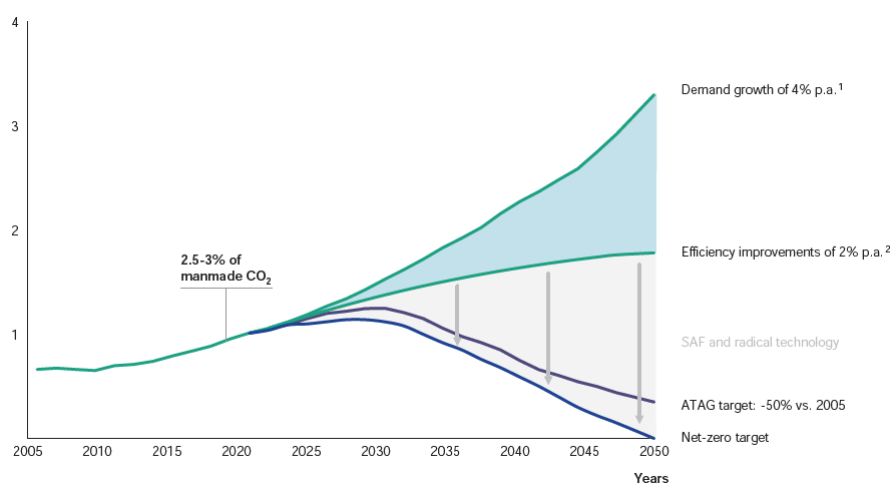
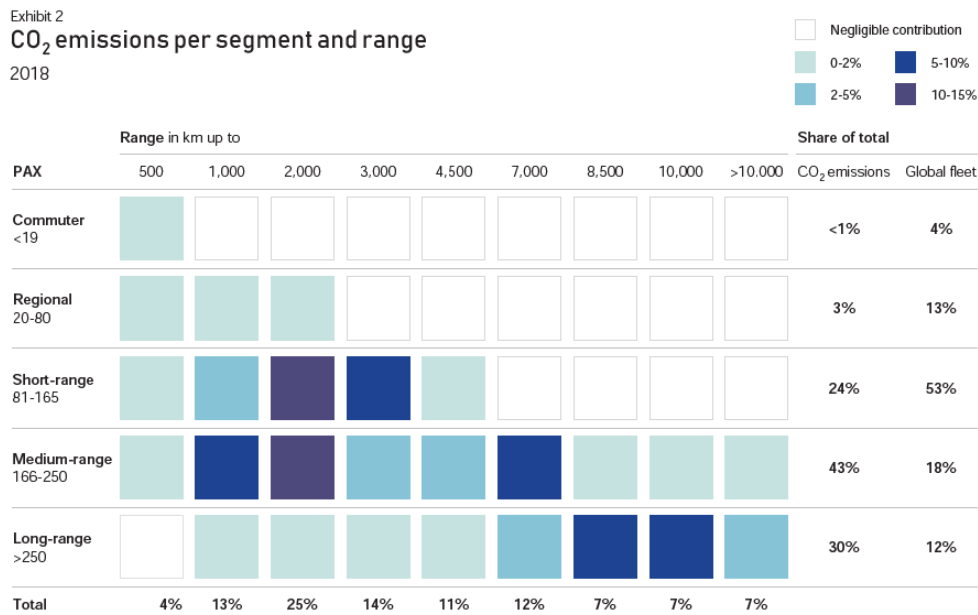


Figure 5.1: Aviation CO₂ emission projections in gigatons [19].

5.1.1. Targeting the right market

It is, undoubtedly, beneficial to focus company resources and financial support on impactful sustainable solutions. Furthermore, time is of the essence when dealing with the world's environmental crisis. Sustainability projects should target sectors which show financial potential within a reasonable schedule. Approximately two-thirds of CO₂ emissions originate from short- and medium-range aircraft. These flights contain less than 165 or 250 passengers, respectively. According to a DiiOMI database and ICCT report from 2018 [19], 70% of total aircraft are of this type. Therefore, this indicates that the best course of action is the development of new, and more sustainable technologies for this niche.

Figure 5.2: CO₂ emissions per aircraft type [19].

5.1.2. Measuring climate impact

Climate impact is often evaluated in CO₂ emissions only. However, greenhouse gasses (GHGs) such as NO_x, CO, methane, and soot also have impact on the environment. Their life time is also of great importance because some GHGs remain for longer duration in the atmosphere. Therefore, the Global Warming Equivalent (GWE) is used to measure the total impact expressed in CO₂ equivalent emissions. The Global Warming Potential (GWP) relates the impact of each greenhouse gas to the impact that a certain amount of CO₂ would have. For example, 1 kg of methane would have equal consequences as 25 kg CO₂ which includes the time it remains in the atmosphere. Therefore, the GWP of methane in Equation 5.1 is 25¹ with a, b, and c in kg.

$$\text{GWE} = a \cdot \text{GWP}_{\text{CO}_2} + b \cdot \text{GWP}_{\text{CH}_4} + c \cdot \text{GWP}_{\text{N}_2\text{O}} \quad (5.1)$$

5.2. Current technologies

Sustainable fuels and/or new propulsion technologies are often looked at for the design of sustainable aircraft. A number of technologies are listed below and discussed [19].

- Biofuels from waste and biomass may be used to extract energy. A main advantage is that infrastructure and aircraft do not have to be changed radically in design. However, due to large use of water and land this option quickly becomes a controversial topic since a significant amount of the world's population does not even have access to these basic needs.
- Fuels synthesised from hydrogen and CO₂ are another option. Here, only electricity is needed for production. However, the use of synthetic fuels only have limited effect on improving sustainability.
- Electric powered aircraft has also been looked into in other projects. Here, the main challenge lies in the low gravimetric densities of batteries which make them unsuitable as main power source. A big leap in battery technology is required for which cannot be waited for.
- Hydrogen fuel and propulsion show promising solutions for sustainable aviation, but also have their own challenges. Even though hydrogen has roughly a 3 times higher gravimetric density than kerosene, its lower volumetric density forms difficult problems in finding the necessary volume within an aircraft. Also, besides redesigning aircraft, airport infrastructure must be changed as well.

The main focus of the A320appu project is to create a hybrid hydrogen successor of the A320neo. The hybrid concept allows time for other airports to update their infrastructure in order to obtain a smooth and sustainable transition. By implementing minimum changes the A320appu has a low entry into service and also offers a more sustainable solution for short to medium range aircraft which are the biggest polluting type of aircraft in the industry as explained in subsection 5.1.1.

¹<https://bit.ly/38eSWIN> retrieved 27-05-2020

5.3. Hydrogen production

How sustainable using hydrogen is depends on the way it is produced. 97% of global hydrogen production is done through steam reforming [40]. This is a process which in itself produces GHGs. However, there are certainly other less common ways to produce hydrogen such as electrolysis of water or biogas reforming. In any case, the Hydrogen Production Pathway (HPP) will directly influence the cost, practicability, and how green the alternative fuel is [24].

5.3.1. Steam reforming

Steam reforming is by far the most common method to produce hydrogen. In essence, it is the reaction of natural gas, which typically consists 95% of methane (CH_4), with steam (H_2O). Besides hydrogen, this process also produces carbon dioxide and carbon monoxide. In the book of L. García, *Compendium of Hydrogen Energy*, it is explained that this method consists of four main steps: desulfurization, reforming, water gas shift (WGS) reaction, and H_2 purification [35]. For the WGS reaction in Equation 5.2 it can be seen quickly that it produces CO_2 which categorises steam reforming as a non-renewable method of hydrogen production.



5.3.2. Hydrogen vs. Kerosene

In the paper of C. Koroneos et al., *Advantages of the use of hydrogen fuel as compared to kerosene* [40], the environmental impact of kerosene and hydrogen have been studied through life cycle assessment (LCA). Here, the life cycle of hydrogen is balanced against kerosene which includes extraction, transportation, refining processes, distribution, and combustion in jet engines [40]. Furthermore, besides steam reforming, this paper analysed the effects that different renewable hydrogen production methods had on the environment such as photovoltaics; solar thermal energy; wind and hydro power, and biomass. In Figure 5.3a this can be seen relatively. Even if hydrogen is produced through a non-renewable method it would be more sustainable than using kerosene. The impact could be even bigger if renewable methods would be used instead.

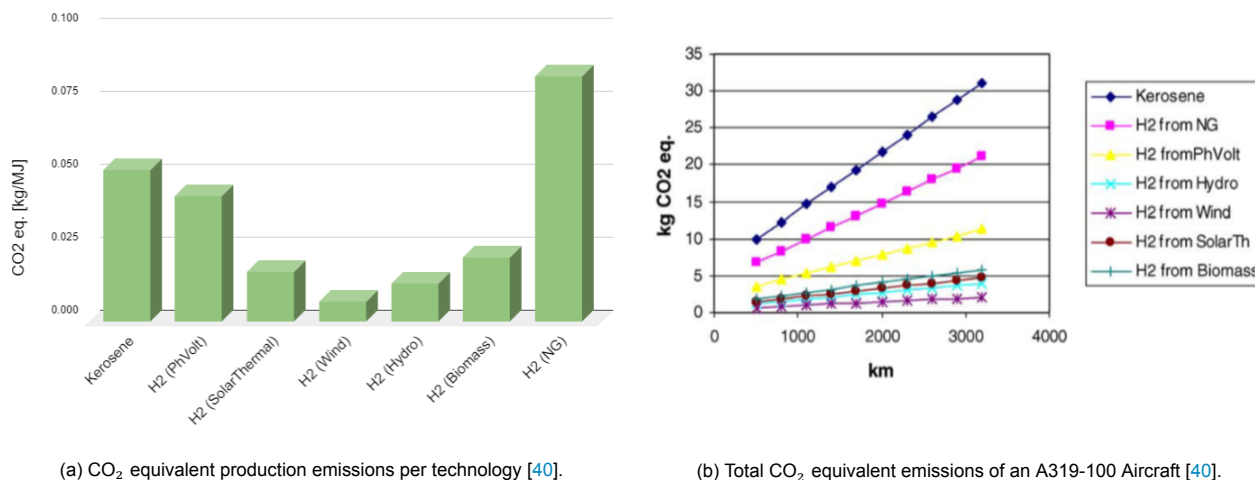


Figure 5.3: CO_2 equivalent emissions in production and in total.

5.4. General costs

As mentioned in section 5.1 the economical factor of sustainability has to be considered as well. Energy, maintenance, crew, and other costs add up to the total costs of the aircraft during its life time. In terms of energy, the production of hydrogen is currently more expensive than that of kerosene. Also, if the operational empty weight of the aircraft increases it would require more energy to move. Furthermore, a hybrid design may be more complex due to the distribution system and cryogenic tank. Consequently, maintenance costs are expected to rise because highly skilled engineers are required to assess the condition of the system. Also, due to stricter regulations more checks need to be performed. Lastly, the turnaround times must be considered as well since an increase leads to less potential flights. Therefore, operational processes such as refueling must be compared to current refueling times. Any aircraft manufacturer has to address these costs since it influences the sustainability of an airliner long term.

Functional Analysis

To accurately design the subsystems of the A320appu determining all the functions the aircraft must be able to perform is an important step in the design phase. The functional analysis of the A320appu will be illustrated by making use of a functional flow diagram in [section 6.1](#). This flow diagram shows the operations of the A320appu throughout the mission. It is divided into three phases; pre-mission, mission and post mission and shows the necessary steps that are needed to be taken. The steps are mainly focused on the APPU system as this has been added to the current operating A320neo. This flow is elaborated on in the functional breakdown structure in [section 6.2](#).

6.1. Functional Flow Diagram

Several explanations are required to explain the flow and reasoning behind the flow. The pre-flight operations flow first needs to know whether the aircraft is connected to grid power. On several airports the gate is able to provide electrical power and pre-conditioned air to the aircraft, whereas in other ground positions the APPU is required to run to provide the electrical power to the aircraft. Block number one, 'Start APPU' is therefore only required if the APPU had been switched off due to the aircraft being connected to ground power and cabin air supply, or if it is turned off after its previous mission. Furthermore, other pre-flight operations that are dependant on the weather conditions and the airport infrastructure are highlighted under function 2.6 and 2.7. The specific functions related to these are elaborated further upon in the FBS.

The separate functional green box 'APPU' is applicable in the taxi and all mission phases and explains the fuel feed to the APPU engine and when the APPU power and propulsion system are running. Power to the aircraft's systems is provided in all flight phases from the moment the unit is running. The propeller and thus the gear box function during the taxi, climb, cruise and descent and not during take-off and landing procedures. For each of these phases shaft power is provided, after which the gear box setting determines the RPM delivered to the propeller hub. In combination with adjusted blade pitch the required thrust for each of these phases can be delivered. To be able to carry out all missions successfully and efficiently, the APPU engine will use the hydrogen fuel system as input up until a certain amount of hydrogen is left in the fuel tank. The amount that is left indicates the amount of hydrogen needed for the final taxi phase with a small contingency. This is done to reduce the LTO emissions significantly, which was an important requirement. Moreover the design is able to do this as in flight the engine will be able to switch from hydrogen to kerosene fuel feed if needed.

6.2. Functional Breakdown Structure

The functional breakdown structure provides more insight in the sub functions that are to be performed in parallel of those represented in the FFD. For instance, the refuelling processes for both kerosene and hydrogen are expanded upon with more functions in steps 2.4 and 2.5 respectively of [Figure 6.3](#).

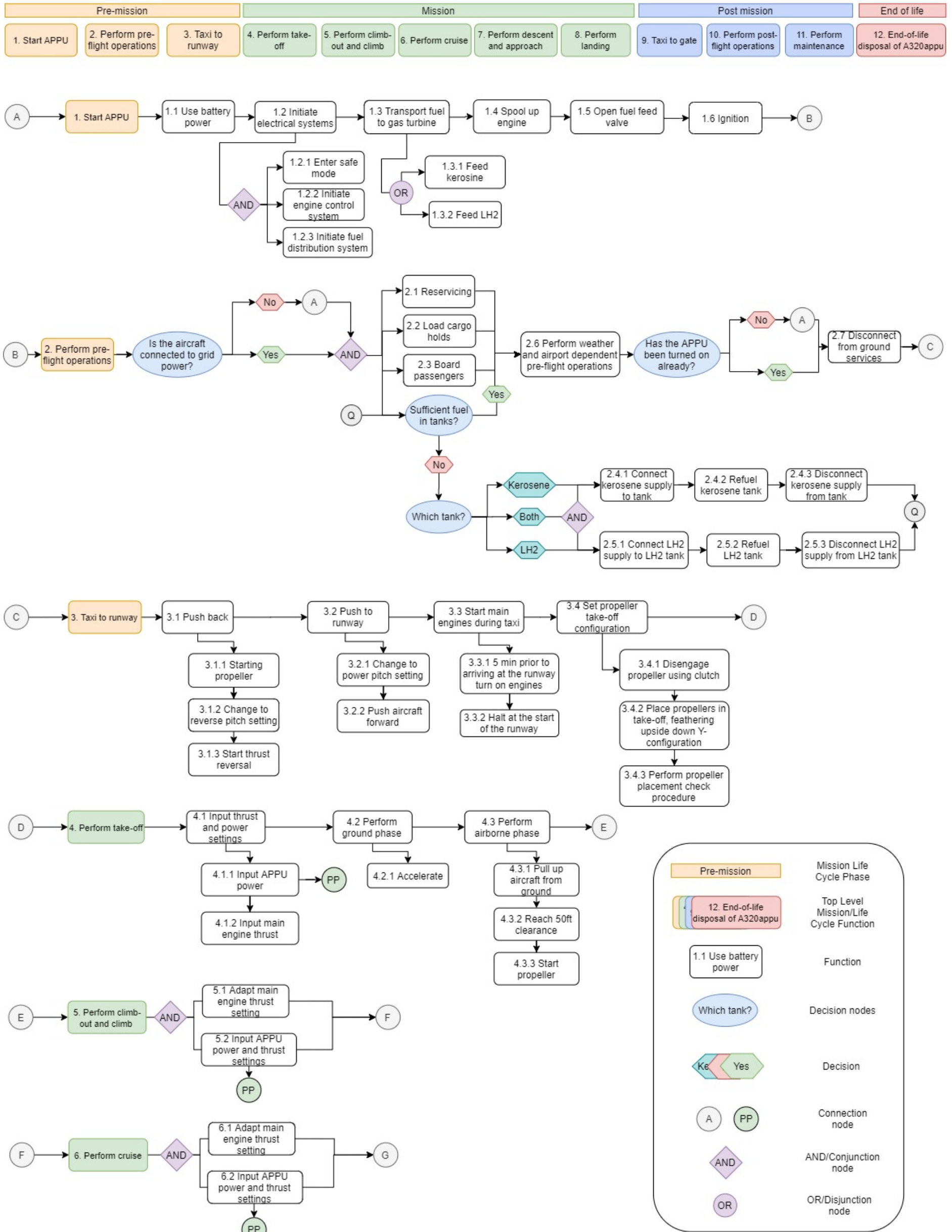


Figure 6.1: Functional flow diagram part I

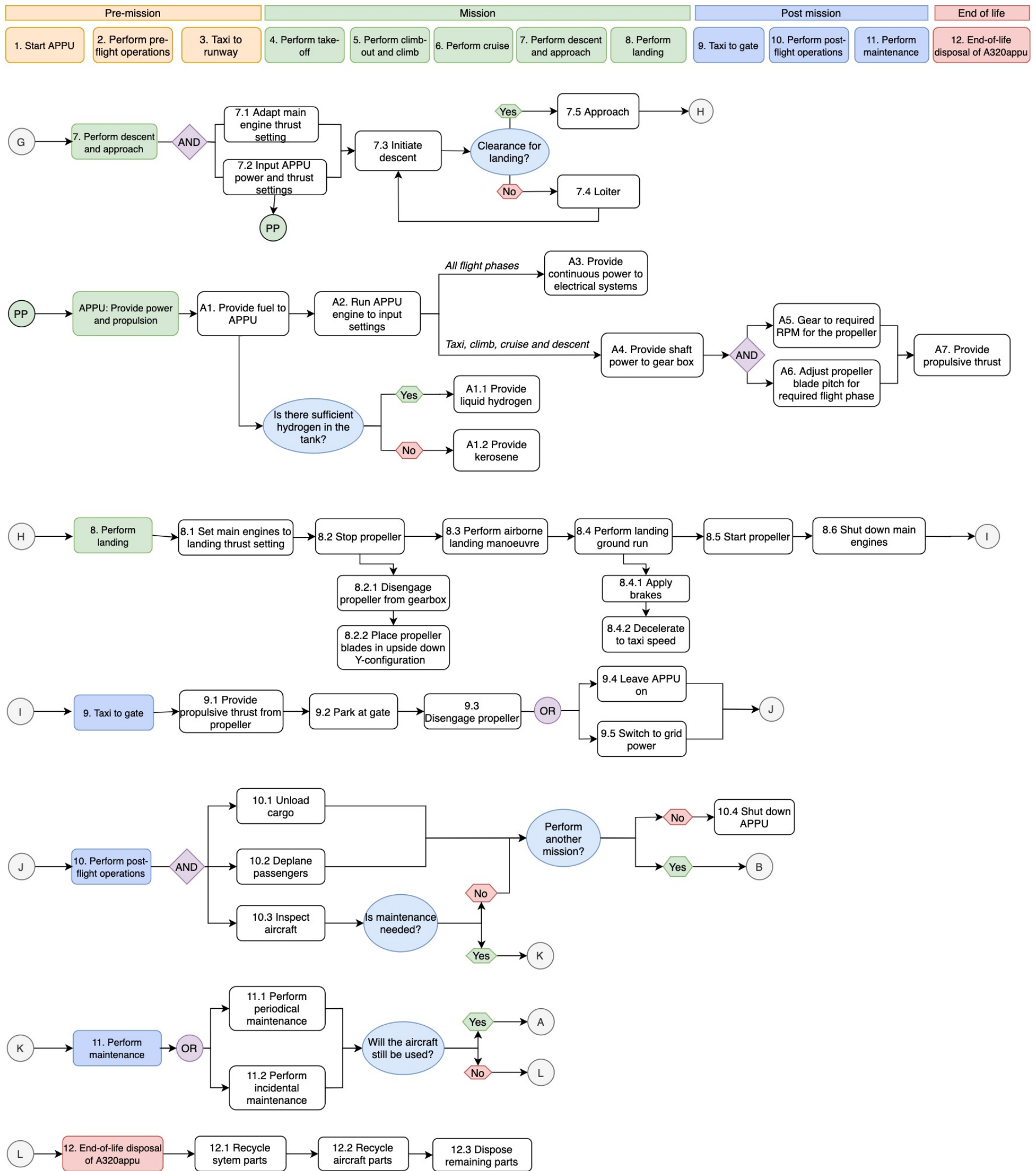


Figure 6.2: Functional flow diagram part II

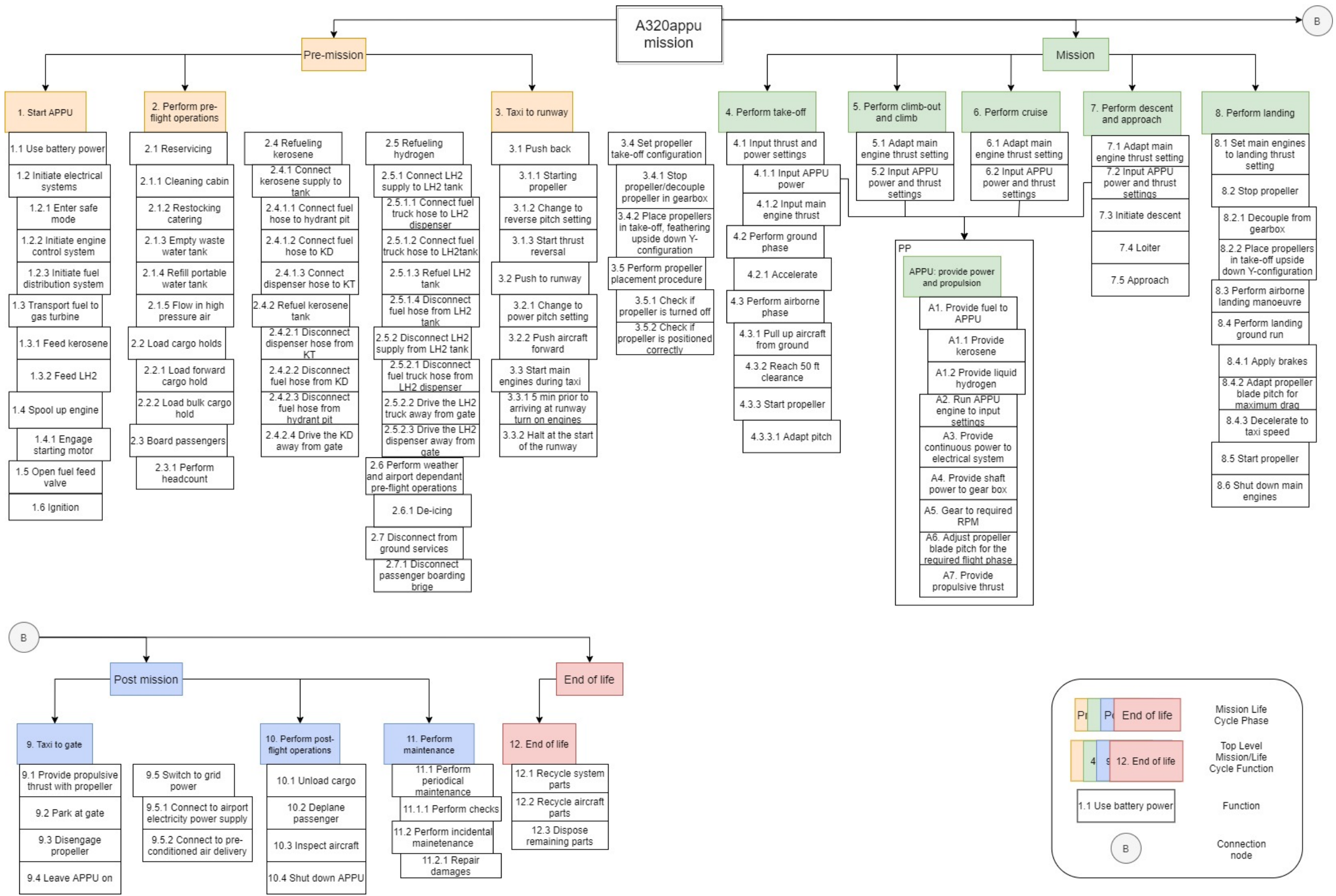


Figure 6.3: Functional Breakdown Structure

Technical Risk Assessment

During operation there are a variety of hazards involved with handling the A320appu, many of which put the crew and passengers at risk. In this chapter, the most relevant risks are identified and assessed, in order to ensure the safety of the aircraft in practical scenarios. A strategy to mitigate and contain these risks is illustrated in the contingency plan. Furthermore, throughout the design process, these risks are taken into account and where necessary, the contingency plan is expanded upon.

The risks are organised into the following categories:

- OP - Operational
- EF - Engine failure
- HT - Hydrogen tank
- FP - Flight performance
- PR - Propeller

Once organised into their respective categories, each risk is assigned a corresponding *probability* and *impact*. [Table 7.1](#) lists each risk and describes the consequences if these were to become a reality. Furthermore, a mitigation strategy is determined to either lower their probability and or lower their impact if they were to happen. The probability and impact are scaled from one to five and are detailed below. The change in either criterion as a result of the contingency plan can be seen in the last two columns of [Table 7.1](#). The updated probability and impact values can be visualised in [Figure 7.2](#).

Probability

1. Unlikely
2. Seldom
3. Occasional
4. Likely
5. Definite

Impact

1. Insignificant
2. Minor
3. Moderate
4. Critical
5. Catastrophic

Initial risk analysis matrix

[Table 7.1](#) covers the identification, assessment and analysis of the risks. The assessment is done by making use of the scale shown above and it is performed by analysing the consequences of the particular risk. A summary of the probability and impact of the initial risks can be seen in [Figure 7.1](#), where the vertical axis shows the probability of the event happening and the horizontal axis the impact.

Risk handling

The goal of risk handling is to decrease the probability and the impact of undesirable events. Generally, decreasing the probability can be done by mitigation and decreasing the impact by contingency. The third column of [Table 7.1](#) shows the implemented mitigation and/or contingency plan, the consequences of the plan and the effect of plan on the assessment. The updated values can be found in [Figure 7.2](#).

The numbers in the final columns of [Table 7.1](#) represent the probability before and after the mitigation strategy and the impact before and after the contingency plan respectively.

Table 7.1: Risk analysis, including mitigation strategies and contingency plans

Number	Risk	Consequence	Mitigation Strategy or Contingency Plan	Probability	Impact
OP-01	The \$5 billion development cost budget is exceeded	The project will require more financial investment which may not be guaranteed	Keep an overview of development costs of sections and minimise amount of changes in regard to the A320neo	2 / 1	3 / 3
OP-02	The aircraft is not ready to enter into service in 2030	The plane will enter into service later, possibly at the same time as fully hydrogen powered aircraft enter service	In the design phase, minimise the changes that have to be made to multiple subsystems to reduce total development time	2 / 1	2 / 2
OP-03	Unable to fly and perform missions due to missing hydrogen infrastructures	No optimal use of the benefits of the aircraft can be made	Negotiate with manufacturers or airports to produce hydrogen	4 / 2	4 / 4
OP-04	Passenger perception of LH2 as a fuel is poor	No consumer demand for flying with the A320appu	Determine new safety procedures and inform passengers	2 / 1	3 / 3
OP-05	Refueling takes significantly longer than current aircraft kerosene refueling	Longer turn-around time and thus less likely that airlines will buy the aircraft	Optimise ground operations to minimise turn around time	3 / 2	3 / 2
OP-06	The aircraft does not comply with the CS25 regulations	Safety and other regulations are not met and the aircraft is not permitted to fly	Avoid large design changes since the A320neo is already compliant	2 / 1	5 / 5
EF-01	APPU engine underperforms when running on kerosene	Emissions reductions will be significantly lower	Chose an engine that compromises between hydrogen and kerosene performance	3 / 2	4 / 3
EF-02	Uncontained engine failure has a high probability of hitting important systems	Catastrophic failure during flight operations and major failure during ground operations	The engine should be placed such that there is a minimal chance to hit important parts	1 / 1	5 / 3
HT-01	Helium leaks in the hydrogen conduit	The hydrogen will either mix with the helium, stopping the combustion process in the engine, or it will leak into the fuselage	Include reinforcements in the fuel line design	2 / 1	4 / 3
HT-02	Hydrogen boil off causes a higher venting pressure than anticipated	Hydrogen tanks cannot maintain the hydrogen at the desired conditions	Design tank with safety margins	4 / 4	4 / 2
HT-03	Passive cooling is insufficient for 48h of safe storage	The product becomes less viable as its safety decreases	Inclusion of additional cooling system or heavy insulation	3 / 2	3 / 3
HT-04	The passenger and/or cargo capacity has to be further reduced to accommodate the LH2 tanks	The competitiveness of the A320appu in the market falls	Perform additional fuel tank trade off to minimise the impact on other subsystems and cabin size	2 / 1	4 / 4
HT-05	Overly conservative contingency margins lead to oversized fuel tanks and thus a lack of optimisation	If the fuel tanks/propeller/engine are too large, potential weight savings are lost	Perform multiple iterations during the design process to avoid overdesigning systems	5 / 3	3 / 3
HT-06	Hydrogen diffusion drains tanks faster than anticipated	The mass of hydrogen will gradually decrease throughout the flight, decreasing range	Investigate tank designs that circumvent this issue and implement a solution	1 / 1	2 / 1
FP-01	New empennage configuration does not support significant flight controllability	The aircraft cannot be easily controlled	Perform a comprehensive analysis on the new empennage configuration	3 / 1	5 / 5
FP-02	Landing gear does not support the weight distribution and causes the aircraft to tip back	Aircraft tips back and cannot take-off	Redesign the landing gear accordingly	4 / 2	5 / 5
FP-03	Tailstrike at take-off or landing	Damage to the propeller	Design the propeller intake such that there is enough clearance between it and the ground	3 / 1	4 / 4
FP-04	Center of gravity position too far aft after the APPU integration to provide stability	The A320appu's longitudinal stability will deteriorate	Use lightweight materials in the aft section or move fuel tanks forward. Empennage can be designed to overcome this issue	3 / 1	4 / 4
FP-05	The vertical tail encounters flutter/divergence because of the t-tail configuration	The tail will fail and the aircraft is compromised	Modal analysis of the empennage should be performed to assess vibrations	3 / 2	5 / 5
PR-01	Low speed propulsive efficiency is too low to provide enough thrust for the LTO cycle	Emissions requirements are not met as the propeller needs more thrust, and thus more fuel flow, impacting the entire design	Use more comprehensive tools for blade design	3 / 1	3 / 3
PR-02	Ground debris is sucked into the propeller	Blade damage or failure of the propeller	Place the propeller such that there is enough clearance between it and the ground	2 / 1	4 / 4
PR-03	Loading from propeller to fuselage causes too much stress	Structural failure of the empennage and tail cone	Employ the use of high strength materials or sound structural design	3 / 1	5 / 5
PR-04	Propeller blades failing and striking the empennage	The structural integrity of the propeller might not be sufficient leading to severe damage of the aft propulsion system and the empennage control surfaces	The structural integrity of the propeller should be assessed with a large safety margin	2 / 1	4 / 4
PR-05	The propeller stopping mechanism fails propeller hits the ground during take-off and/or landing	The propeller breaks	Introduce back up stopping mechanism	2 / 1	4 / 4

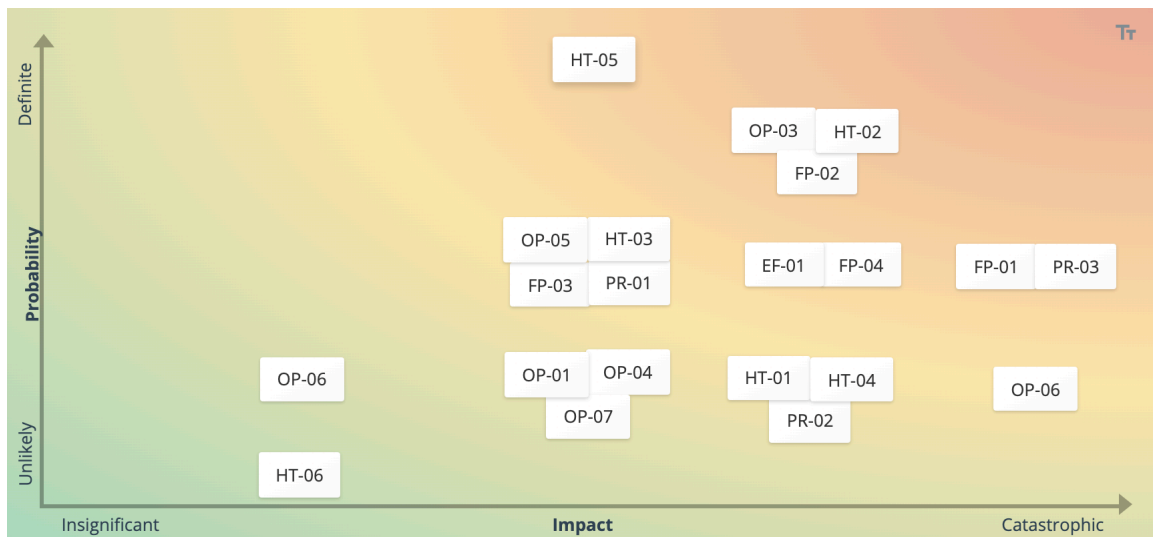


Figure 7.1: Risk analysis matrix prior to mitigation and contingency plan

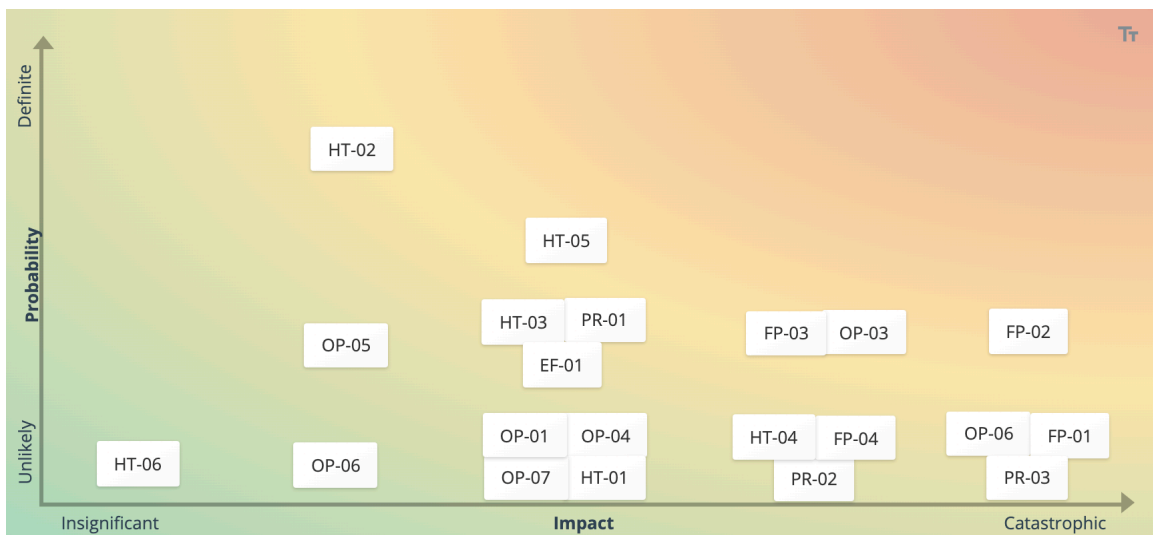
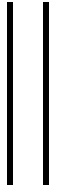


Figure 7.2: Updated risk analysis matrix

Conclusion

This analysis will be used alongside the requirements throughout the design of the subsystems. By addressing the pertinent risks throughout this process, the safety of the aircraft can be directly implemented into the design; this avoids considering safety as an afterthought. Current mitigation strategies and contingency plans may be expanded upon throughout the report in the event that they are not sufficient or are not compatible with other design features and requirements.



Subsystem Design



Engine Design

The APPU engine needs to be sized up from the A320neo APU, as the engine has to provide propulsive power as well as subsystem power. This involves a design of the turboshaft engine, as well as the design of a reconfigured inlet duct. Firstly, the requirements applicable to the engine design are stated in [section 8.1](#). Next, in [section 8.2](#), one of the major functions of the APPU is quantified, the power and bleed air off-take. After that the engine is scaled by performing a detailed mission analysis in [section 8.3](#), which is followed by the actual design of the turboshaft engine in [section 8.4](#) and the mass estimation in [section 8.5](#). Then, the drivetrain is discussed in [section 8.6](#) and the engine inlet and exhaust in [section 8.7](#). The safety risks of placing an engine close to such a critical component as the empennage are assessed in [section 8.8](#). To shed light on what influences the design and fuel usage of the APPU engine, a sensitivity analysis is performed in [section 8.9](#). This chapter is concluded by recommendations for future design stages in [section 8.10](#).

8.1. Requirements

The requirements have been determined before in the Baseline Report as described in [chapter 3](#). This section states the requirements relevant for engine design and mission analysis.

- POW-Sys-10:** The minimum power of the APPU shall be sufficient to power non-essential subsystems continuously during normal operations.
- POW-Sys-11:** The APPU system shall provide sufficient power to essential subsystems in emergency conditions.
- POW-Sys-12.01:** The main engines shall be used as a backup system to provide power to essential subsystems.
- POW-Sys-13:** The APPU shall be able to provide power for the main engine start-up.
- POW-Sys-14:** The turbine shall drive the generator at all times.
- PROP-User-15:** The A320appu aircraft shall be able to use H₂ as well as kerosene.
- PROP-Sys-16:** The turbine shall power the propeller at all times.
- PROP-Sys-17:** The APPU shall be able to provide sufficient thrust reversing to reverse an aircraft from stationary position out of its gate position.
- PROP-Sys-18:** The Boundary Layer Ingestion shall increase energy efficiency.
- PROP-Sys-19:** The aircraft shall have means to limit damage to the propeller caused by a ground strike.
- PROP-Sys-20:** The APPU shall be able to operate using either hydrogen or kerosene.
- SUST-User-24:** The CO₂ emission should be at least 20% lower than A320neo for a typical mission.
- SUST-User-25:** The NO_x, CO, unburnt hydrocarbon and soot emission for the LTO cycle should be reduced by at least 50% when compared to A320neo for a typical mission.
- SUST-Sys-26:** The noise pollution of the renewed aircraft shall not exceed the noise emissions of the A320neo by more than 5%.
- OPS-Sys-32:** The aircraft APPU subsystem shall not affect passenger evacuation .

8.2. Subsystem power and bleed

The secondary power and bleed air requirements for the A320appu will not be different from the A320neo. Therefore, it is assumed that the power consumption of aircraft systems for the A320appu will be the same as the A320neo. In the A320neo there are three different power sources by three generators; the two main engines and the APU. The APU also serves as a backup power system for the aircraft. However, for this design

the two main engines will function as a backup system instead. Assuming the A320neo uses the same APU system, this design choice should not create any problems since the APU system of the A320neo is capable of providing similar electrical power compared to the main engines [66]. The main engines are normally started using power from the APU. As will be shown later, the APPU is more powerful, hence is also able to power the main engine start-up. Concerning bleed air, the maximum bleed air per phase from the main engines is taken as the requirement, except with it now being taken from the APPU engine. To ensure functioning of the secondary power systems, the required power and bleed air mass flow, shown in Table 8.1, has to be delivered by the new APPU. All power values were calculated by adding all the individual subsystems power demands during the different flight phases [60]. The maximum bleed air values were also sourced from [60].

Table 8.1: Shaft power off-take and bleed air mass flow for the Airbus A320 during different flight phases [60]

Flight phase	Required shaft power off-take [kW]	Maximum bleed air mass-flow [kg/s]
Taxi-out	206.41	0.667
Take-off (to 1 500 ft)	101.14	1.042
Climb (to 31 000 ft)	234.5	1.018
Cruise (in 31 000 ft)	281.6	0.667
Descent (to 1 500 ft)	244.5	0.761
Landing	107.36	0.906
Taxi in	206.41	0.667

8.3. Mission analysis

In order to get an accurate and detailed estimation of the required thrust from the APPU system and required hydrogen tank capacity, a typical mission was analysed. This mission is a flight from Amsterdam to Lisbon, and spans around 1 900 km. Flight data was retrieved, and the average was taken to be the original flight profile. However, to aid in the design of the propeller, the cruise altitude was lowered to a constant 36 000 ft. At this lower altitude, and thus higher density, the propeller is better able to provide the thrust required with sufficient efficiency. The values which were used in the simulation are shown in Table 8.2 and Table 8.3. In this section, the simulation that was used to analyse this mission is further explained. First by explaining the main principle and stating the used inputs and assumptions. Later the different flight phases are elaborated upon. Next, the fuel flows are explained, after which some manual iteration is performed. Finally, the results are given.

Table 8.2: Flight phases and their characteristics of the AMS - LIS flight¹

Flight segment	Time in minutes	H_b [ft]	H_e [ft]	V_b [kts]	V_e [kts]
Climb	17	3 000	36 000	238.5	449
Cruise	114	36 000	36 000	449	453
Descent	21	36 000	3 000	453	231

8.3.1. Inputs and assumptions

The analysis consists of a simulation. The principle of this simulation is as follows: it has the weight, altitude and velocity, calculates the lift and drag with it and adds the acceleration, climb rate and power for subsystems. This results in a thrust and power, both from the APPU and from the main engines. This then gives the required fuel flows for the power and thrust, which is multiplied with the time step. The resulting fuel burnt is subtracted from the weight, and the program continues with to the next time step with the updated weight, altitude and velocity. To get the right amount of APPU contribution, the simulation is run for multiple APPU contributions. The contribution is increased each time, until 20% CO₂ is saved with respect to the A320neo. In this value the savings from the LTO cycle are also taken into account.

¹<https://www.flightradar24.com/>, retrieved on 06-05-2020.

Table 8.3: Input variables

Variable	A320neo	A320appu	Units
OEW	44 300	45 320	[kg]
Hydrogen mass	-	400	[kg]
Kerosine mass	6 500	5 500	[kg]
Payload mass	19 000	16 500	[kg]
Kerosene burned in LTO	650	250	[kg]
Boundary layer velocity	N.A.	0.80 V_∞	[m/s]
Generator efficiency.		0.96	[-]
Hydrogen LHV		120 * 10 ⁶	[J/kg]
TSFC Kerosene		8.5-14.8	[g/kNs]
Subsystem power (climb)		234 500	[W]
Subsystem power (cruise)		281 600	[W]
Subsystem power (descent)		244 500	[W]

8.3.2. Climb phase

The climb phase introduces a number of changes: the altitude increases gradually and thus the air density decreases, the flight speed increases, and significant thrust is required in order to climb. During the climb phase it was assumed that the rate of climb (ROC) is constant. The ROC was calculated by dividing the altitude increase over the time necessary for the climb envelope. This resulted in an ROC of 9.86 m/s for the defined mission. The power required for this can easily be calculated, and by dividing this by the velocity the thrust required for climbing is achieved. This is shown in Equation 8.1.

$$T_{ROC} = \frac{ROC \cdot W}{V_{TAS}} \quad (8.1)$$

In Equation 8.1, W is the weight of the aircraft. The velocity profile of the mission was acquired by linearly interpolating the velocity values in the different phases. The acceleration is assumed to be constant, and calculated by dividing the total velocity increase by the time. This resulted in an average acceleration of 0.106 m/s². The thrust required for this acceleration can be calculated using Equation 8.2, a variation of Newton's first law.

$$T_{acc} = m \cdot a \quad (8.2)$$

The lift coefficient C_L is calculated at every time increment as well. First, the density ρ is calculated according to the International Standard Atmosphere (ISA). At every instance the weight, and thus lift, ρ and the velocity are known, and the wing surface area S is a given constant. Using these variables and Equation 8.3 the C_L is calculated.

$$C_L = \frac{2 \cdot L}{\rho \cdot V_{TAS}^2 \cdot S} \quad (8.3)$$

A relation was used to calculate the drag coefficient C_D as a function of C_L , and is shown in Equation 8.4.

$$C_D = 0.027 - 0.0287 \cdot C_L + 0.068 \cdot C_L^2 \quad (8.4)$$

Now that both C_L and C_D are known at all times, the lift to drag ratio (L/D) can be calculated, and this is used to calculate the drag. Thus, drag at every point results from the lift calculation. Now the thrust and power required for gaining altitude, accelerating and to overcome drag are known. Adding these together gives the total required thrust, as shown in Equation 8.5.

$$T_{tot} = T_{ROC} + T_{acc} + T_D \quad (8.5)$$

It was determined that the APPU would be utilised fully during the climb phase. As will be explained in chapter 9, the APPU system is limited by the thrust it can generate during the climb.

8.3.3. Cruise phase

As with the climb phase, the altitude and velocity are linearly interpolated in order to obtain the ROC and acceleration. The different parts of the thrust are also calculated in a similar manner to the climb. The thrust the APPU produces was calculated in an iterative process. The APPU thrust was increased with 0.5% every iteration, and the loop continued until 20% kerosene was saved during the whole mission, so including the LTO

cycle. Once 20% would be saved, the program gives the kerosene usage, the hydrogen usage, and the fraction of the thrust the APPU takes over.

8.3.4. Descent phase

In contrast to the climb phase, during the descent phase a constant flight path angle, γ , is used. This is in order to keep the 'thrust' provided by descending as constant as possible. γ is calculated by first integrating the velocity with respect to the time during the descent phase, in order to achieve the distance flown. With the horizontal and vertical distances travelled known, γ is obtained using [Equation 8.6](#). For the current mission this gives a γ of 3° .

$$\gamma = \arctan \frac{\text{vertical distance}}{\text{horizontal distance}} \quad (8.6)$$

Knowing γ and the velocity, the ROC can be calculated. With the weight the power gained by descending can be obtained. Now the thrust gained by descending can be calculated by dividing by the velocity. In short this can be done with [Equation 8.7](#).

$$T_{des} = W * \sin(\gamma) \quad (8.7)$$

The aircraft also decelerates. The deceleration is linearly interpolated, just like the acceleration in [subsection 8.3.2](#). The thrust for this is also calculated in the same manner as in the climb phase.

Now all thrust contributions are known, and it was found that in the current flight profile there is excess thrust throughout the descent phase. Because of this the main engines are idling, and for the APPU this opened the door to something completely new: regenerative 'braking'. Here the propulsor of the APPU system acts as a wind turbine, extracting power from the air in order to drive a shaft. This power can then be used to power the generator and thus the aircraft subsystems, saving some hydrogen. If this concept was not used, some energy would have had to be wasted by flying less optimally as well, increasing overall fuel usages.

8.3.5. Fuel usage

For all time increments the thrust and power output of the engines and the APPU are known. The thrust specific fuel consumption (TSFC) of the main engines under static conditions at sea level is 8.5 g/kNs , and during cruise equals 14.8 g/kNs . This is linearly interpolated, dependent on the altitude. The main engine fuel flow is then calculated with [Equation 8.8](#).

$$\dot{m}_{kero} = (TSFC_0 + \alpha_{kero} * h) * T_{main} \quad (8.8)$$

The APPU fuel flow is calculated differently, as it is a turboshaft engine and thus has a power specific fuel consumption rather than a TSFC. Instead of calculating a power specific fuel consumption, the fuel flow is calculated directly using the thermal efficiency shown in [Table 8.3](#). The mass flow is then obtained using [Equation 8.9](#).

$$\dot{m}_{H2} = \frac{P}{w * \eta_{th}} \quad (8.9)$$

where w is the lower heating value (LHV) of hydrogen, which is 120 MJ/kg . A maximum fuel flow of 0.095 kg/s is found throughout the flight. The total fuel usage is calculated by multiplying all fuel flows by the time increment, and summing them all together.

8.3.6. Manual iteration

The program was manually iterated as well. Only one thing was iterated in this process: the maximum sea level power capacity of the APPU engine. A more powerful engine is heavier, and thus it is desired to have an engine that is just powerful enough to fulfil the requirements in order to keep it as light weight as possible. In the simulation code it was possible to change the APPU sea level maximum power output. This value was tweaked in such a way that the engine would be running close to maximum during the majority of the mission. [Figure 8.1](#) shows the power output of the APPU in the left graph. The right graph shows what fraction of the engine's total power is used. These graphs are for an engine with a sea level power capacity of 10 MW . It can be seen that during the cruise the APPU is running only at roughly 15 percent of its maximum power. This means that for the majority of the flight the APPU is not utilised to its full potential and thus is over-designed.

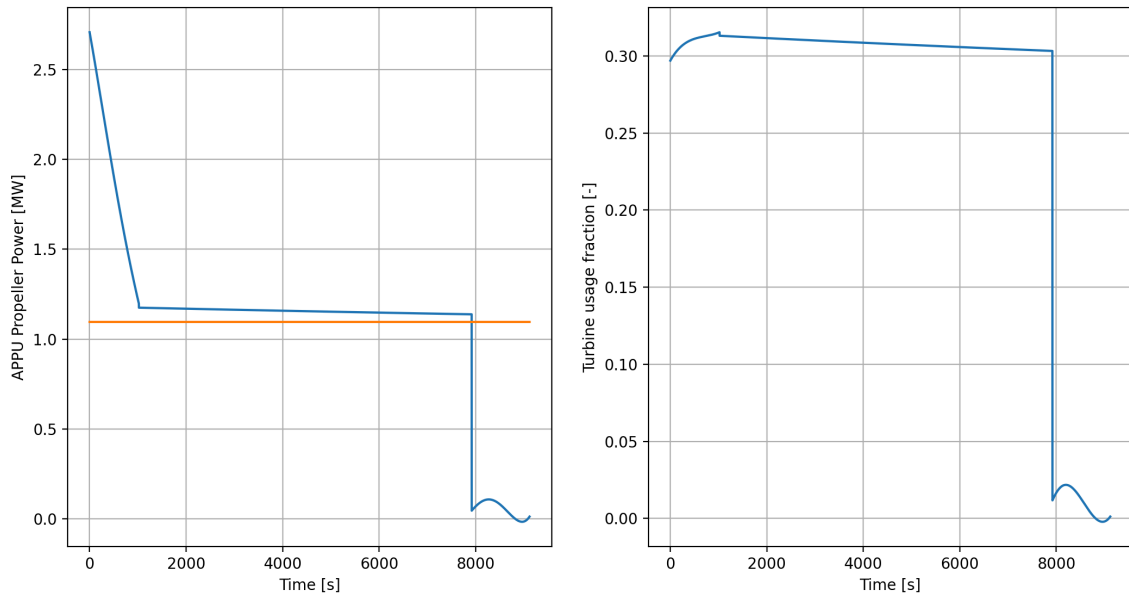


Figure 8.1: APPU power output and fraction of maximum power output for an over-designed engine (10 MW)

Figure 8.2 shows the power output and the fraction of the potential as well, but now for when the engine is sized optimally for this particular mission. It can be seen that for the whole flight, except the descent, the engine runs at or between roughly 98% and 100% of its maximum. Here the engine thus is optimally sized.

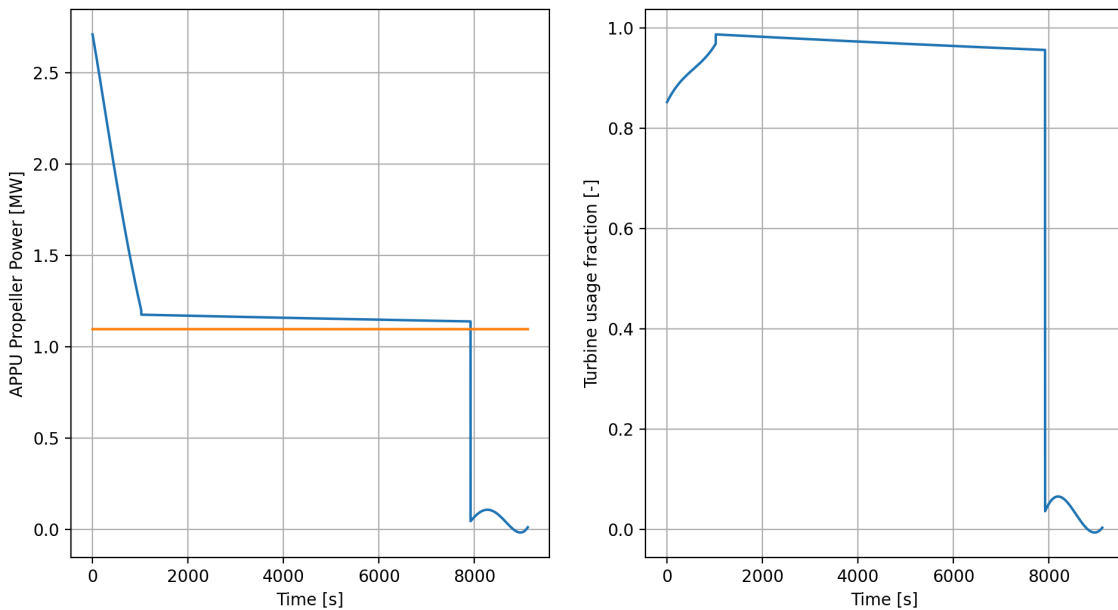


Figure 8.2: APPU power output and fraction of maximum power output for an optimal engine (3.65 MW)

It has to be noted that during the cruise the absolute power output also differs significantly. This is due to the fact that a more powerful APPU takes over more work during the climb, and thus saves more kerosene there. This results in the APPU having to provide less of the thrust during cruise in order to just meet the requirement of 20% CO₂ savings. This effect was known during the manual iterations, making it more difficult to find the optimal power.

8.4. Engine design

Detailed design of the engine was completed in GasTurb 12 [62]. The sea-level power determined in subsection 8.3.6 was taken as a guideline, but the power requirements throughout the mission were considered to ensure the designed engine was providing enough power at various altitudes and velocities.

8.4.1. Choice of configuration

GasTurb offers various engine configurations for design. A double-boosted turboshaft engine with the booster on the high-pressure spool was chosen. The design allows for high overall pressure ratios and thus improved performance with lower fuel consumption. Furthermore, this configuration on GasTurb features a radial compressor as well as a reverse-flow combustion chamber, both of which are present on the PW150, a turboshaft engine with a similar power output to the APPU. Given the lack of expertise in detailed engine design, drawing inspiration from existing and similarly sized engines was deemed useful as a point of verification.

8.4.2. Design points

Inputs of altitude and Mach number were used to determine the performance of the designed turboshaft in various flight phases. Certain points of the simulation were taken into consideration: climb at the end of LTO and cruise. The descent phase is not considered as the power required is significantly lower than in other phases, as seen in [Figure 8.2](#). The simulation does not tackle LTO, so this was omitted. This can further be justified as in take-off, the APPU only provides subsystem power and the propeller is turned on in the air, which the end of LTO condition is deemed sufficient to represent. In taxi, aside from subsystems the propulsive power is significantly lower than in flight, and in landing the APPU propeller is similarly stationary. While thrust reversal is a possibility, it is not a design condition as there is no strict requirement on the reverse thrust of propulsive power required in that phase. Thus, the designed engine can be considered to provide reverse thrust to its capacity at sea-level, but this is not at present designed in a detailed manner. The shaft power of the APPU was provided, which was converted to engine required power by use of a 92% gearbox efficiency and a 10% safety factor. The required APPU power and flight conditions in climb+out and cruise are given in [Table 8.4](#).

Table 8.4: Mission points at which engine design was considered

Mission points	Altitude [m]	Mach [-]	APPU propulsive power required [kW]
End of LTO (climb-out)	924	0.365	3 740
Cruise	10 973	0.785	1 400

8.4.3. Engine parameter optimisation

Many of the input parameters to GasTurb were kept similar as the demo data in the programme due to lack of expertise and insight. This includes various component efficiencies of the engine, interduct pressure ratios, the spool speed and design parameters of compressors. These were kept constant, or in some cases these were increased by incremental amounts to account for new developments in technology. The parameters that have significant effect on the design and were considered were the inlet corrected (with respect to standard sea level conditions) flow, pressure ratios of the two boosters and the compressor, and the burner exit temperature. GasTurb's optimisation function was employed to determine an optimal design. A constraint was set on the power required to design for the correct power. The bounds of varying the parameters were taken from values seen in existing designs; these ranges and the optimisation parameters are given in [Table 8.5](#). GasTurb allows for the input of bleed air off-take and power off-take for powering subsystems. This was implemented from [Table 8.1](#) for the different design points. The design power was the cruise power. However, this means that the APPU engine is undersized in climb, as climb-out requires high power due to having to accelerate as well as climb. On the contrary, designing for climb-out would lead to a 28% over-design in the engine power at cruise, leading to a roughly 20% increase in weight. As cruise is the primary design and use case for the APPU propeller, the engine is optimised for this phase. Additionally, the power estimate for climb is overestimated, as the wake contribution has not been taken into account in the phase.

Table 8.5: Optimisation ranges and constraints

Variable	Value	
	Min.	Max.
Inlet corrected flow [kg/s]	13	20
LP booster pressure ratio [-]	1.5	2.5
HP booster pressure ratio [-]	1.5	2.5
HP compressor pressure ratio [-]	7	10
Burner exit temperature [K]	1 400	1 600
APPU propulsive power [kW]	3 800	

Table 8.6: Optimised input variables

Variable	Value
Inlet corrected flow [kg/s]	14.68
LP booster pressure ratio [-]	1.54
HP booster pressure ratio [-]	2.20
HP compressor pressure ratio [-]	8.88
Burner exit temperature [K]	1 580

The figure of merit chosen for the optimisation was thermal efficiency. Maximising thermal efficiency optimises the engine design as it leads to a lower power-specific fuel consumption in the APPU. The results of running the optimisation are given in [Table 8.6](#). The engine design was run for both climb-out and cruise, as well as

sea-level conditions to obtain a sea-level power. The resulting engine performance metrics are highlighted in [Table 8.7](#). Here, the power requirement determined from [subsection 8.3.6](#) is stated as required power, and the engine's produced power as delivered power. This highlights that climb-out is the design case but that cruise power is still only slightly over-designed.

Table 8.7: Optimised engine's performance

Flight condition	Propulsive power required [kW]	Delivered power [kW]	Thermal efficiency [-]
Sea level	-	3 550	0.33
Climb-out	3 800	3 250	0.32
Cruise	1 400	1 400	0.36

8.4.4. Engine sizing

GasTurb provides geometry of the designed engine, as shown in [Figure 8.3](#). The geometry is excluding the inlet duct, gearbox and precise exhaust geometry.

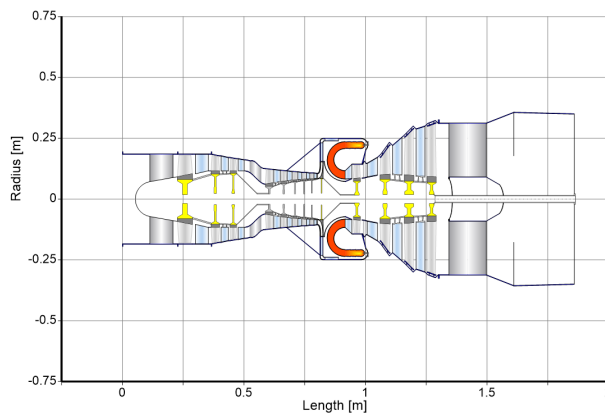


Figure 8.3: Geometry of the designed engine

Table 8.8: Input variables

Total length [m]	1.5
Maximum diameter [m]	0.66
Inlet diameter [m]	0.4

Some of the important geometric parameters are highlighted in [Figure 8.3](#). The total length of the engine is taken excluding the exhaust cone, as the geometry of the exhaust is different than the GasTurb model, as discussed in [section 8.7](#).

8.4.5. Kerosene usage in the turboshaft

Considering **PROP-User-15**, the APPU engine should be able to run on kerosene as well as hydrogen as a fuel. Thus far, the engine has been designed for hydrogen usage, and this is the desired optimal condition. Still, the engine as optimised in GasTurb was simulated with kerosene by changing the input fuel in the program. The total power of the engine, its fuel consumption and thermal efficiency were investigated for both kerosene and hydrogen. The results are given in [Table 8.9](#).

Table 8.9: Engine power with kerosene and hydrogen

Flight condition	Propulsive power [kW]		Specific fuel consumption [kg/kWh]		Thermal efficiency [-]	
	H ₂	Kerosene	H ₂	Kerosene	H ₂	Kerosene
Climb-out	3 240	3 500	0.0927	0.2580	0.32	0.31
Cruise	1 400	1 516	0.0845	0.2382	0.36	0.35

As seen, the engine is capable of supplying enough, and more, power at the given flight conditions when operating on kerosene. There is a slight loss in thermal efficiency, and fuel consumption is higher, explained by the higher mass-specific energy of hydrogen over kerosene. This analysis is deemed sufficient to show the engine can perform and provide the required power with both kerosene and hydrogen as a fuel.

8.4.6. Summary of engine characteristics

The summarised performance of the engine is given in Table 8.10. Here, the total power is presented, taking into account the power for subsystems required.

Table 8.10: Summary of engine performance

Parameter	Flight condition	
	Sea level	Cruise
Total power [kW]	3 550	1 400
Total pressure ratio [-]	29.81	
Thermal efficiency [%]	33	36
Specific fuel consumption [kg/kWh]	0.0902	0.0845

8.5. Engine mass estimation

In order to estimate the engine mass, the power and mass of several existing turboshaft and turboprop engines have been collected. Using this data an equation was fitted for the engine mass as a function of the output power. Table 8.11 shows the engines and their details used for this analysis. These particular engines were used because they are all quite recently developed engines (2000 first run or later). The best fitting equation for this data is Equation 8.10.

$$m = 3.4772 * x^{0.5691} \quad (8.10)$$

where x is the power output in kW and m is the mass in kg . The error was smaller for a polynomial, but it was not chosen due to the fact that at a certain point an engine would get lighter for more power output. This is unrealistic, and hence the power relation was used.

Table 8.11: Engine data on existing turboshaft and turboprop engines [61][8]

Engine	Power output [kW]	Mass [kg]	Power density [kW/kg]
RR500 ²	354	102	3.47
H80	597	180	3.32
Arriel	738	111	6.64
CTS800	1 193	170	7.01
Ardiden	1 491	205	7.27
Makila	1 641	279	5.88
RM322	1 939	228	8.49
T700-CT7	1 939	204	9.49
TV7-117VM	2 088	360	5.80
GE38	5 593	502	11.15

Generator mass

Electric generators have a power density of roughly 13 kW/kg [39]. The cruise condition is used as the limit condition to design the generator, as the power off-take for subsystems is highest then at 281.6 kW , given in Table 8.1. Taking a generator efficiency of 96%, the generator mass is determined.

Final engine mass

The engine mass as calculated by Equation 8.10 and the generator mass determined are given in

Table 8.12: Engine weight breakdown

Turboshaft engine mass [kg]	379
Generator mass [kg]	31
Total mass [kg]	410

²<https://bit.ly/31iF0pf> retrieved on 18-05-2020.

8.6. Drivetrain

The coupling of engine and propeller will be realised by use of a number of mechanisms. This section aims to describe the necessary systems and associated considerations. Since the propeller and engine are slightly inclined to each other, a universal joint is necessary which converts the torque over an angle. Furthermore, a clutch to decouple the engine from the gearbox and propeller is necessary. Figure 8.4 illustrates the steps to couple the engine to the propeller.

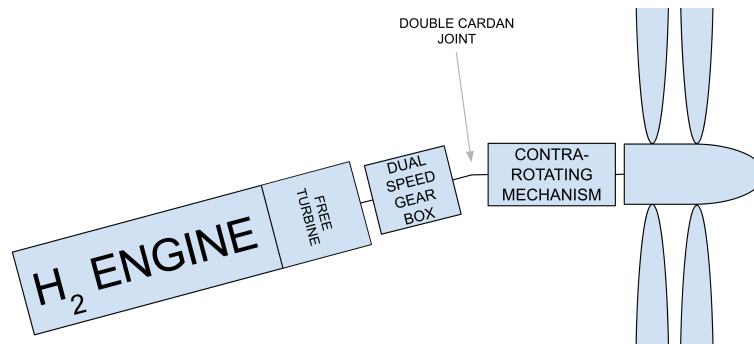


Figure 8.4: Structural overview of the engine-propeller coupling system

8.6.1. Gearbox

As will be described further in chapter 9, a number of support systems were implemented to ensure the propeller operates at maximum efficiency. Relevant to this chapter is the use of variable RPM, which means that a gearbox with multiple speeds has to be incorporated in the design. The greatest challenge surrounding this component is its reliability. Gearboxes in turboprops or turboprop engines are usually confined to one reduction gear due to the high weight, cost and poor reliability, that are not overcome by the increased efficiency. With an input shaft speed of 28,000 RPM, and a reduction ratio of roughly 30:1, designing a gearbox which operates in these conditions can be challenging.

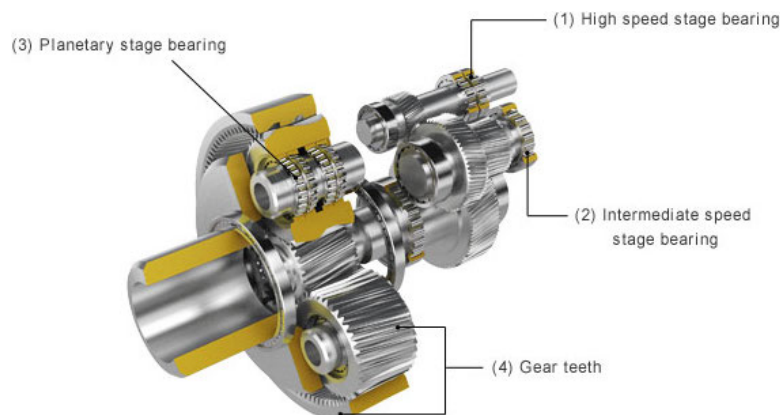


Figure 8.5: Schematic overview of a wind turbine gearbox².

Taking into account the scope and schedule of the project, a full design of the gearbox was deemed unnecessary. Rather, the drivetrain will use an adapted wind turbine gearbox with inverted gear ratios. Such transmissions are specifically designed to convert the high torque power of the rotor to the high RPM power of the electrical motor, while ensuring great reliability. Given that these gearboxes are tailored to the needs of wind turbines, a few modifications need to be made.

Gearbox modifications

Since the weight of the drivetrain was not accounted for in previous design stages, its mass budget is very limited. As a result, it is imperative that its weight is kept to a minimum, and consequently lightweight materials will be employed in its construction. Such efficiency losses were also not accounted for during the design of the engine which once again draws importance towards the efficiency of the gearbox and that this remains as high as possible. With this in mind, the use of inline helical gears is suggested. Due to new propeller requirements, the gearbox must also allow for two gear stages - one with a reduction ratio of 20:1 and another with 28:1. Finally, given the tight operating conditions, it is likely that heat generation will prove to be a challenge and so

²<https://bit.ly/388iven>, retrieved on 20-06-2020

preemptively, a cooling solution will be designed. The following upgrades will be implemented in a future report. A brake system, present inside of the propeller assembly, allows the output shaft of the torque converter, and all connected shafts, to be slowed down for the gear shifts to take place. This system is further described in [subsection 9.5.1](#).

Decoupling mechanism

Typically, engine need a decoupling mechanism such as a clutch or torque converter to allow for gear changes while the engine continues running. This is especially important for the A320appu since the subsystems still require power during these short periods, and it is necessary that the life of the gearbox is extended as much as possible. To fulfil this role, the gearbox will be directly connected to the free turbine in the hydrogen engine, since this will act as a fluid coupling.

8.6.2. Universal joint

A universal joint, or U-joint, is a coupling connection which allows two rotating axes to be inclined relative to one another. The gearbox and propeller are, as mentioned earlier, at an angle of roughly 14° to each other. A double Cardan joint, displayed in [Figure 8.6](#) is preferred over a conventional U-joint. The rationale behind this choice is elaborated on later. A second design choice to be made is whether to place the joint before or after the gearbox. Essentially, this choice is a trade off between either exerting high RPM or high torque on the U-joint. Generally, wear and fatigue are significant on joints, and higher RPM introduces more significant fatigue loads [18]. Due to this, the high torque configuration is chosen and the joint is placed between the gearbox and the propeller.



Figure 8.6: Double Cardan joint⁵



Figure 8.7: Conventional U-joint⁵

A major drawback associated with the less complex, conventional U-joint is the irregular output speed. Even if the input shaft rotates at a constant speed, the output shaft rotational velocity will vary. This effect causes vibrations and wear on the joint. The varying output RPM is essentially caused by in- and output shaft rotational planes being inclined. As the propeller-gearbox coupling requires a 14 degree inclination, an inconsistent output RPM will be present. This can be resolved by using a double Cardan shaft. The slightly more complex joint equals out the varying output RPM and therefore provides a higher efficiency. More specifically, it is estimated to be 98.8% at 1500 RPM [17]. As the Cardan joint will operate at a maximum of 1400 RPM and a minimum of 1000 RPM, the mechanical efficiency can be estimated to be slightly higher at 99%. Ultimately, the mass of the double Cardan joint is considered negligible compared to the torque converter and gearbox.

8.6.3. Drivetrain performance

As the drivetrain has been chosen, the total efficiency of this system can be calculated. By multiplying all efficiencies the total efficiency can be obtained. An overview of the subsystem and total drivetrain efficiency and masses has been given in [Table 8.13](#). The masses are a preliminary estimation and could benefit from a more in depth research.

Table 8.13: Overview of mass and efficiency estimation of the drivetrain system

System	Mass [kg]	Efficiency [%]
Gearbox	250	99.5
Double Cardan joint	-	99.8
Total	300	99.3

8.7. Engine inlet and exhaust

As a result of the mass flow and efficiency requirements of the engine, as well as its unconventional mounting angle, further investigation was required for the inlet and exhaust design.

⁵<https://grabcad.com/library/tag/u-joint>, retrieved on 17-06-2020

8.7.1. S duct motivation

The current APU of the A320neo has a ram air inlet placed on the bottom of the tail cone, which can be opened and closed freely by the pilot. While such a solution would satisfy the mass flow required by the engine, it would do so by ingesting boundary layer air. This slower air has a lower total pressure which harms the efficiency of the jet engine [43]. It is also preferable that the engine doesn't ingest the fuselage boundary layer because the velocity gradients require the use of specialised compressor blades. With this in mind, the inlet had to be placed somewhere in free-stream air. The preferred solution was an S duct similar to that of the Lockheed L1011, as shown in Figure 8.9.



Figure 8.8: A320neo APU inlet⁷



Figure 8.9: Lockheed L1011 S duct⁸

The S duct inlet is mounted on the leading edge of the vertical stabiliser, with a clearance of 41 cm from the bottom of the inlet to the fuselage to avoid ingesting the boundary layer which forms over the surface. This number was obtained from the CFD analysis in section 9.2. Horizontally, it spans roughly 4 m from the vertical stabiliser leading edge to the engine intake near the bottom of the tail cone; vertically, it spans 2.5 m. The full specifications can be seen in Figure 8.10.

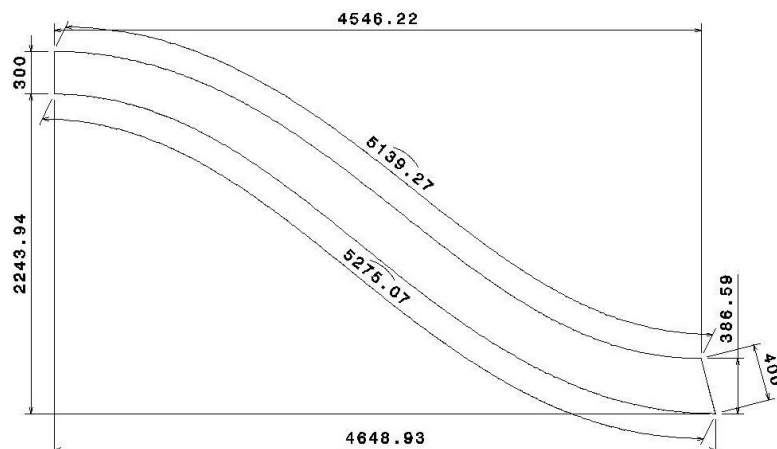


Figure 8.10: Schematic overview of the S duct

The design was heavily inspired by the L1011 since it proved to be a successful design. The L1011 engineers limited "the curve of the S-duct to less than a quarter of the radius of the engine intake diameter" [58] to minimise pressure losses, but this was not possible in this design due to the small intake diameter and relatively long length. High Reynolds number flows in thin, slender tubes tend to lead to the formation of a thick boundary layer [41]. The S duct also serves to slow the incoming free-stream air to more manageable speeds for the engine. The engine requires a maximum mass airflow of 6 kg/s. Using the mass flow rate equation - see Equation 8.11 - with a free-stream velocity of 230 m/s (Mach 0.78 at 11 km), this yields a diameter of 0.3 m. The end of the S duct has a diameter of 0.4 m which is the diameter of the engine. A bell intake was not included in the analysis, which means any intake phenomena are ignored and the intake is considered to have 100% efficiency.

$$\dot{m} = \rho \cdot A \cdot V \quad (8.11)$$

The diffusive effect and boundary layer were modelled using CFD.

⁷<https://bit.ly/3dIsjwY>, retrieved on 19-06-2020

⁸<https://bit.ly/2VifxyE>, retrieved on 19-06-2020

8.7.2. Numerical analysis

A numerical analysis was done on the S duct to model the boundary layer inside the duct and the diffusive effect of the diverging diameter. The software in question is the latest version of SIMULIA⁹. The duct was modelled in CATIA¹⁰ and the geometry was exported into a physics simulation. Compressible flow was enabled with the SST $k-\omega$ turbulence model. A hexahedron-dominant mesh was used with around 250,000 elements. An inlet velocity of 230 m/s was set with a temperature of 216.65K. The operating pressure and temperature were set to 22 632.1 Pa and 216.65K respectively; the corresponding values for 11 km altitude. The walls of the duct were set to be adiabatic and have no slip. The outlet was set to have a zero gauge pressure, as suggested in the user manual. The Mach number contour plots can be seen in Figure 8.11 and Figure 8.12.

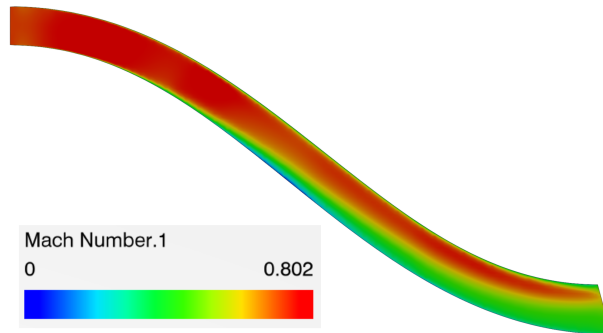


Figure 8.11: Cutaway side view of S duct in SIMULIA

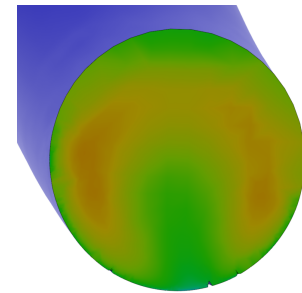


Figure 8.12: Exit view of S duct in SIMULIA

In Figure 8.11, a fast flowing region can be observed near the inlet of the duct. The air is approximately at Mach 0.78 and slowly accelerates as the boundary layer forms and constricts the area of the duct. The region of highest speed is the dark red area in the first bend, with a maximum Mach number of 0.81. Half way through the duct, the boundary layer separates and becomes increasingly thick. Beyond this point, the duct diverges faster than the boundary layer thickens, allowing the airflow to slow down. The exhaust is shown in Figure 8.12. On the bottom, the circular boundary layer can be seen. A second boundary layer starts forming on the top of the duct near the exit. While not very clear from the picture, there is a boundary layer all around the surface of the duct, although this is much thinner than the others - with a finer mesh this would become more apparent. The average velocity and temperature are 178 m/s and 225.9K, respectively across this area, and therefore the average Mach number is 0.59.

Comparison to experiment data

The results were compared to the paper *Numerical simulations for high offset intake diffuser flows* by T.M. Berens, A.-L. Delot, M. Chevalier and J. van Muijden at the NLR, Amsterdam [12]. The same phenomena occurred for a comparable duct size, albeit with a shorter length. In both scenarios: a thick, circular boundary layer formed on the bottom of the duct, which becomes more pronounced towards the exit. The airflow accelerates near the first bend, and a second, thick boundary layer on the top of the duct near the exit - these are illustrated in Figure 8.16 and Figure 8.17. Due to the similarities with the NLR paper, the analysis was deemed sufficiently accurate. An average total pressure of 26 834 Pa is obtained for the exhaust area. Using Equation 8.12, the total pressure of the free-stream air is calculated to be 32 357 Pa yielding an efficiency of 83.2%. The NLR efficiency was roughly 96%. In a future report, the design will be optimised with the possible use of vortex inducers inside the duct to increase the efficiency.

$$\begin{aligned}
 p_{total} &= p_{static} + p_{dynamic} \\
 &= p_{static} + \frac{1}{2} \cdot \rho \cdot V^2 \\
 &= 22632.1 + \frac{1}{2} \cdot 0.363918 \cdot 230^2 = 32357 \text{ Pa}
 \end{aligned}
 \tag{8.12}$$

⁹<https://bit.ly/3dySHZN>, retrieved on 19-06-2020

¹⁰<https://bit.ly/2VocuFj>, retrieved on 19-06-2020

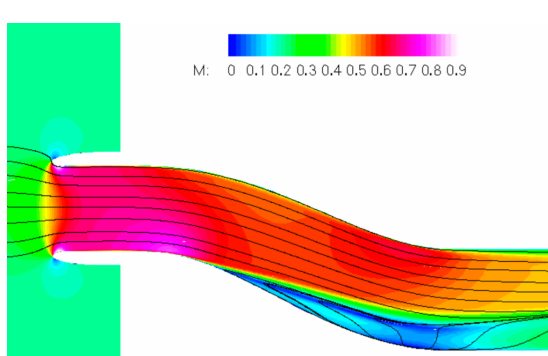


Figure 8.13: NLR paper results - duct side cross section

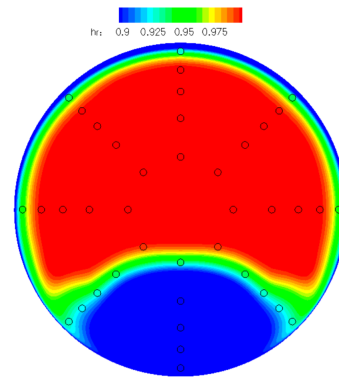


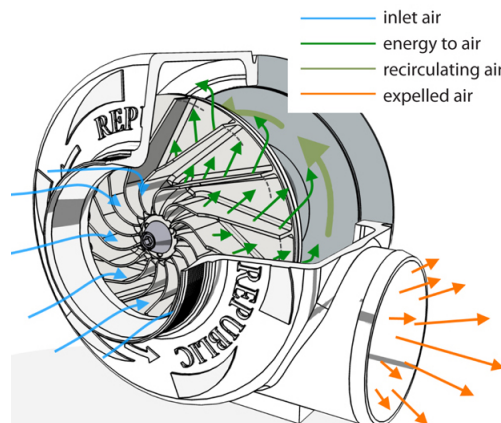
Figure 8.14: NLR paper results - duct exit cross section

Ideally, the duct would be modelled with an bell shaped intake and with non-adiabatic walls however, this was not possible due to the various constraints such as time, computational horsepower and the CFD programme itself.

8.7.3. Engine exhaust

With the inclusion of a contra-rotating propeller at the aft of the fuselage, little space is left for the exhaust. Commercial airliners typically have the exhaust in this location, but in order for this to be implemented into the A320appu, the exhaust would have to pass through the propeller shaft. With the inclusion of a contra-rotating gearbox and a variable pitch mechanism, this was deemed unfeasible. The alternative location was the current APU's inlet: under the tail-cone - refer to Figure 8.8. Given the space constraints due to the drivetrain, a centrifugal exhaust will be used.

The exhaust shroud will be mounted around the low pressure turbine and redirect the flow outwards towards into the free-stream air at the bottom of the fuselage. The effect on the boundary layer and the propeller will be neglected in this report due to the relatively low mass flow rate. The thermal energy is expected to diffuse greatly by the time it reaches the propeller blades, but still needs to be addressed especially if the propeller are made from composites. Consequently, the use of heat resistant coatings will be explored in a future report.

Figure 8.15: Centrifugal fan using a similar concept to that used in the APPU exhaust¹¹

A numerical analysis was not applied to the exhaust since its efficiency is not relevant. The engine simulation yielded an exit velocity of 105 m/s and a density of 0.119 kg/m^3 . Using Equation 8.11 once again, it can be inferred that an exit area of 0.472 m^2 is required. The exhaust will be rectangular, and the length will have to be equal or greater to the LP turbine length (0.75 m) since it will encase it. With this in mind, the final dimensions will be $0.75 \times 0.63 \text{ m}$.

8.8. Safety analysis

Since the APPU engine is a turboshaft, it can have the same safety measures, such as automatic shutdowns if limits are reached or exceeded. Risk **EF-02** refers to uncontained engine failure and is addressed in this section.

¹¹<https://bit.ly/2NKmsN7>, retrieved on 19-06-2020

For containment of failed parts the same measures could be taken as well in terms of thickness. However, this protection should be placed specifically for this engine placement. The engine is located in the tail cone right under the vertical stabiliser. If a rotating engine part were to break loose and escape the engine housing, the tail should be protected from it. This can be done by increasing the strength of the engine housing or by applying measures that will deflect the debris away from the tail. Increasing the engine housing strength is desirable from a safety perspective, as then also non critical parts are protected and the damage is limited to the engine itself. However, this will drastically increase the mass of the engine. Engine parts that are flying off can be large and thus heavy, and have a high velocity. This makes them high energy projectiles, which are hard to stop. A protective shield which deflects these projectiles away from the tail can be lighter, both because it does not have to cover 360° , and because it does not have to stop a projectile. However, these deflected projectiles (or projectiles that are not directed at the tail in the first place) will still damage the tail cone, weakening its structure. This would help address risk **EF-02**.

8.8.1. Impact probability calculations

In order to quantify the risks and decide what measures have to be used, an analysis has to be done about the risk of a certain part getting hit in case of an uncontained engine failure. A distinction is made between the fan, the compressor and the turbine. Since this chapter is about a turboshaft engine itself only, there is no fan and thus the fan is not included. A further distinction is made between the disk, the blades and the rim of the rotors.

Assumptions

A few assumptions are made in this analysis. The largest one is that the engine is modelled as a point in the fuselage, not as a cylinder. This means that all debris originates from the same location, while in reality turbine debris comes from further back than compressor debris. The debris itself is also seen as point masses. In reality the pieces flying off can have quite a significant size, resulting in larger probabilities of hitting something. Furthermore, some of the data used is quite dated. From before 1989 to be exact. Engines have become more reliable since then. However, in this analysis only the conditional probabilities are used, rendering it irrelevant what the probability of an uncontained engine failure is in the first place. Lastly, the probability of an uncontained part colliding with the pressure vessel or propeller is considered negligible since empirical data¹ shows that the trajectory paths are limited. Thus, when placing the engine as shown in Figure 8.16, the empennage is assumed to be the only critical system that can be hit as that is the only large system that is within blast range of the engine. Colliding with smaller systems such as the (hydrogen) fuel lines, hydraulics, is considered negligible for now, as the exact placement is not known yet.

Analysis

Radially, engine parts can fly off in any direction. Only for a fraction of the circumference parts will hit the empennage. The chance of an impact is calculated for the vertical and horizontal stabiliser separately. The spread angle for the horizontal stabiliser is not including the tips. These are deemed to not be critical, because if these tips are hit, the aircraft is still very much able to safely land. The spread angles of the vertical and horizontal stabiliser are determined to be 32° and 80° respectively. These angles are graphically shown in Figure 8.16 as well.

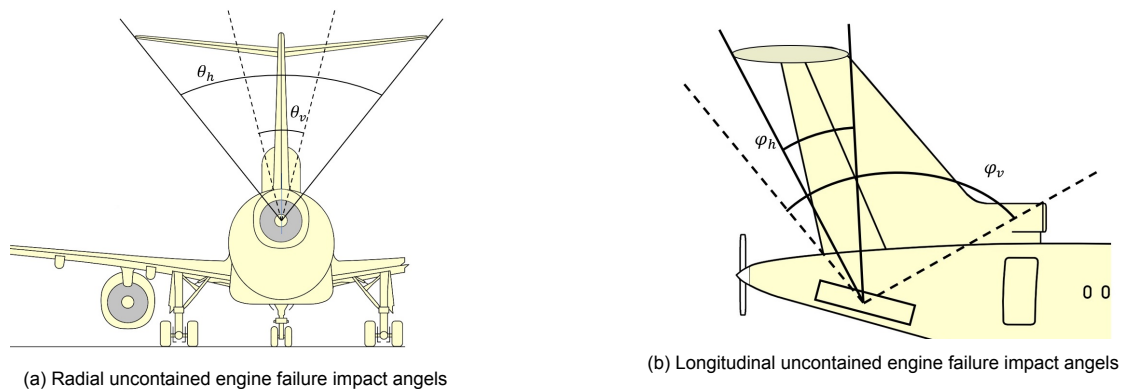


Figure 8.16: Payload-range and CO₂ savings-range diagrams for the A320appu without hydrogen usage

In the plane of rotation the debris also has spread angles, meaning it can fly either forwards or backwards. It depends on the part of the engine how large these angles are. They are all shown in Table 8.14. First, the

¹<http://www.tc.faa.gov/its/worldpac/techrpt/AR99-11.pdf>

probabilities are calculated for when it is known what engine part fails. It is desired later to also know what the probability is of the empennage getting hit if it is not yet known what type of failure it is. The reports AIR4003 and AIR4770 by the FAA/SEA² give numbers on what part of the engine escaped the engine housing for a number of uncontained engine failures. These are also shown in Table 8.14. Based on these statistics, it can be derived what the chance is that a certain part escapes in the event of an uncontained engine failure. This is also shown in the table.

Table 8.14: Longitudinal debris spread angles, w.r.t. the rotation plane

Uncontained part	Forward angle [°]	Rearward angle [°]	Number of failures	Fraction of total
Compressor disk	5	-5	32	0.169
Compressor blade	15	-15	4	0.0211
Compressor rim	15	0	13	0.0688
Turbine disk	5	-5	39	0.206
Turbine blade	20	-55	83	0.439
Turbine rim	0	-30	18	0.0952
Total			189	1

With all angles known, the possibility of impact can be calculated per part. This means that in the event of a particular engine part flying out of the engine, what is the chance of either the vertical or the horizontal tail being hit? This can be done using Equation 8.13.

$$P(\text{Stabiliser being hit} \mid \text{Uncontained part}_i) = \left(\frac{\phi_{i\text{-overlap}}}{\phi_{i\text{-spread-angle}}} \right) * \left(\frac{\theta_{i\text{-overlap}}}{\theta_{i\text{-spread-angle}}} \right) \quad (8.13)$$

Here ϕ are the longitudinal spread angles and θ are the radial spread angles. $\phi_{i\text{-overlap}}$ and $\theta_{i\text{-overlap}}$ represent the parts where the spread angles coincide with the empennage. These are divided by the total spread angles to get the probability of the empennage getting hit. This is done for the vertical and horizontal stabiliser separately. The calculated probabilities per part can now be multiplied by the probabilities shown before in Table 8.14. This gives, for when there is an uncontained engine failure, the probability that a certain part hits either the vertical or horizontal tail. These can be summed, resulting in the probability of either part of the empennage being hit in the event of an uncontained engine failure. The probability of a general empennage hit was also calculated. All calculations are the same, except that the trajectories where some debris would hit both the vertical and horizontal stabiliser are not accounted for twice. All resulting probabilities are shown in Table 8.15.

Table 8.15: Probabilities of the empennage being hit in the event of an uncontained engine failure

Uncontained part	P(Vertical stabiliser impact)	P(Horizontal stabiliser impact) [%]	P(Empennage impact) [%]
Compressor disk	1.5	3.8	3.7
Compressor blade	0.18	0.39	0.42
Compressor rim	0.61	1.0	1.2
Turbine disk	1.8	4.6	4.6
Turbine blade	2.7	5.2	5.8
Turbine rim	0.85	2.1	2.1
Total	7.7	17.1	17.9

8.9. Mission Sensitivity analysis

Two important outputs from the simulation are the required APPU percentage and the fuel consumption of the APPU. The APPU percentage relates to the total power it produces, and fuel consumption is important to determine environmental impact and size the hydrogen tank. A sensitivity analysis is performed on these two outputs, considering the effect of changing some variables on them. The variables considered are the cruise altitude of the mission, mission distance and operational empty weight. Each variable is varied in a range of 10% decrease to 10% increase.

²<http://www.tc.faa.gov/its/worldpac/techrpt/AR99-11.pdf> retrieved on 03-06-2020

8.9.1. Sensitivity on cruise altitude

The sensitivity of APPU percentage and fuel consumption to cruise altitude is shown in Figure 8.17.

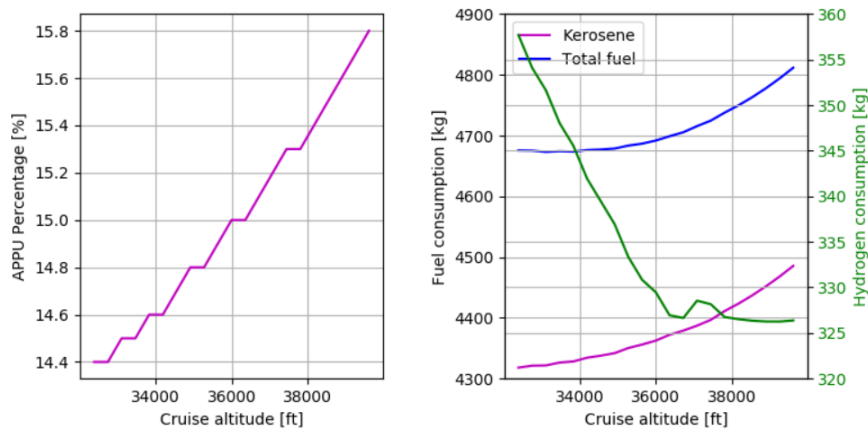


Figure 8.17: Sensitivity of APPU percentage and fuel consumption on cruise altitude

APPU percentage increases with increasing cruise altitude, with the increase seemingly growing in magnitude with altitude increase. There is an overall variation from 14.4% to 15.8%, which is around a 5% variation in value around the central value. The fuel consumption shows a less simple relationship, with hydrogen consumption dropping, while the kerosene consumption, and thus total consumption, go up over the same period. Hydrogen consumption varies around 10% overall, with kerosene and overall consumption varying less than 4% through the investigated range.

8.9.2. Sensitivity on mission distance

Similarly to cruise altitude, varying mission distance increases the APPU percentage, this time varying in a slightly higher range of 6%. The kerosene and hydrogen consumption both increase in a linear manner with mission distance, which is expected as the APPU simply needs to be powered for longer. The increase in hydrogen is around 15% in either direction and the total fuel and kerosene around 10% in either direction. It is good to note that the hydrogen tank volume is not breached with a 10% increase in mission distance, and when extrapolating perhaps even a mission of 15% higher mission length would be possible with a full hydrogen tank. This is all due to contingency taken into account when designing the hydrogen tank.

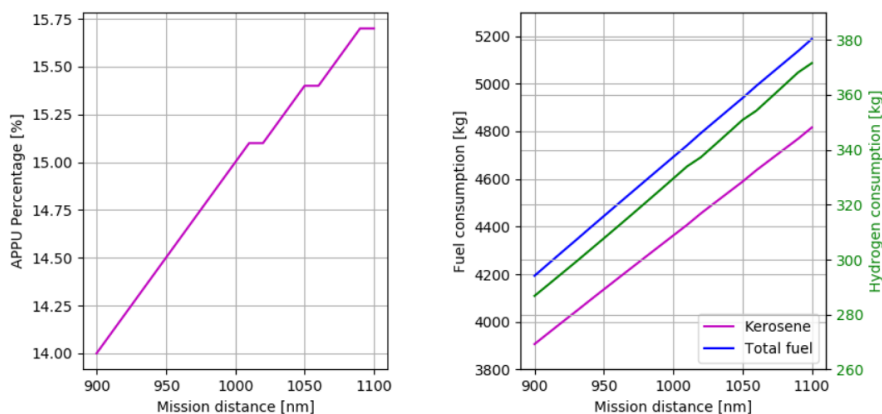


Figure 8.18: Sensitivity of APPU percentage and fuel consumption on mission distance

8.9.3. Sensitivity on operational empty weight

Again, there is a roughly linear increase in APPU percentage with operational empty weight, varying about 4% in either direction of the original value. Kerosene and hydrogen consumption increase in a linear manner as the aircraft is heavier and thus requires more thrust, and more fuel. Hydrogen consumption varies about 5% in either direction, with kerosene and total consumption varying about 3%. An increase of 10% in OEW does not lead to the hydrogen tank reaching its cap, with there still being contingency.

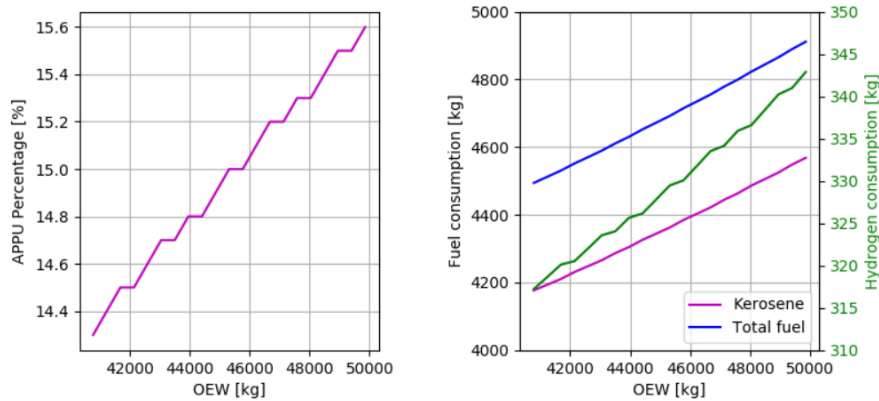


Figure 8.19: Sensitivity of APPU percentage and fuel consumption on operational empty weight

8.10. Recommendations

On longer flights, when the 400 kg limit of H₂ capacity is reached, it could be worth while to investigate the use of simultaneous H₂ and kerosene burn as a mixture. This way, the engine emits less CO₂ throughout the whole flight instead of only the part where H₂ is available. As was discussed in [subsection 8.3.4](#), no thrust is required from any of the engines in descent. There was excess power due to the descent, which allows regenerative braking. However, this is not a very efficient process. There are major power losses in the propeller. It would be more efficient to fly the descent in such a way that there is never power or thrust required, and there is never excess power. This way the APPU has to generate the power required for subsystems, but this is more efficient than regenerative braking. Additionally, the descent can be initiated earlier, shortening the cruise and thus saving some fuel there.

Another possible improvement is initiating the descent much earlier, in such a way that the main engines will still run idle, but the APPU runs at maximum power. In this case kerosene is saved because the period where the main engines produce thrust, and thus use more fuel, is shorter. This way more savings could be achieved without needing to increase the engine of the APPU. However, both these flight paths will be difficult to execute in practice because of air traffic control (ATC). ATC has to manage many aircraft, and probably cannot accommodate such descent profiles.

Propeller Design

This chapter aims to describe the propeller design process. This is based on the requirements which are repeated below. The design revolves around the boundary layer which forms on the A320 fuselage, and as such this is modelled in SIMULIA. Subsequently, the design of the propeller is specified and analysed numerically using CROTOR. Additionally, a structural analysis tool is developed. The chapter is finalised by verifying and validating the results, drawing conclusions and lastly providing recommendations for future design stages.

9.1. Requirements

The requirements which impose constraints on the propeller designed are listed below.

- FMP-Sys-03:** The cruise mach number of the aircraft shall not decrease by more than 5% from the cruise mach number of the Airbus A320neo WV055.
- FMP-Sys-04:** The cruise altitude of the aircraft shall not differ by more than 10% from the cruise mach number of the Airbus A320neo WV055.
- PROP-Sys-17:** The APPU shall be able to provide sufficient thrust reversing to reverse an aircraft from stationary position out of its gate position.
- PROP-Sys-18:** The Boundary Layer Ingestion shall increase energy efficiency.
- PROP-Sys-19:** The aircraft shall have means to limit damage to the propeller caused by a ground strike.
- SUST-Sys-26:** The noise pollution of the renewed aircraft shall not exceed the noise emissions of the A320neo by more than 5%.
- OPS-Sys-33:** The propeller shall not cause considerable risk or danger for ground crew.
- OPS-Sys-34:** The APPU propeller shall have sufficient ground clearance during mission.
- OPS-Sys-38:** The aircraft cg shall not exceed the tip-over limit after that APPU has been integrated.
- OPS-Sys-39:** The aircraft shall be safe during all flight operations.
- REG-Sys-40:** The aircraft shall comply with CS 25 safety regulations.
- REG-Sys-41:** The aircraft shall comply with airport regulations.

9.2. Boundary layer theory

Boundary Layer Ingestion provides a significant efficiency gain. To quantify this efficiency gain, the boundary layer properties need to be evaluated. These boundary layer properties are assessed by use of computational fluid dynamics (CFD) software. Ultimately, this software is bench-marked against *Engineering Sciences Data Unit* (ESDU) papers [57]. These papers are endorsed and supplied by the Royal Aeronautical Society.

9.2.1. Numerical analysis

The physics scenario used in [subsection 8.7.2](#) was adapted to the fuselage of the A320neo. The CAD geometry was obtained from existing sources and imported into SIMULIA. An initial analysis included the A320neo fuselage in full detail, including wings, empennage, engines and small elements on the fuselage surface such as Pitot tubes. The model can be seen in [Figure 9.1](#), and its wake in [Figure 9.2](#).

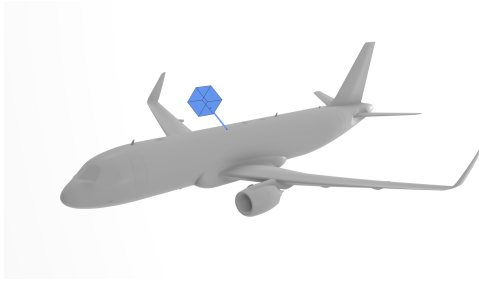
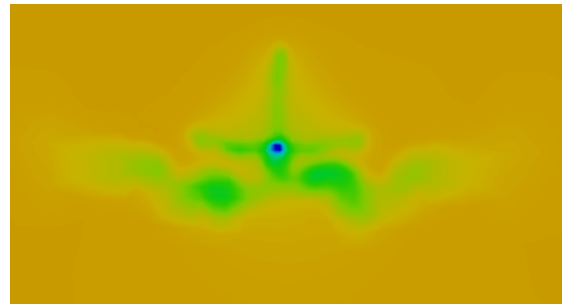
Figure 9.1: Full detail CAD model of the A320neo¹

Figure 9.2: Mach number colour plot for A320neo wake

While this analysis was accurate, the wake from the fuselage was not clear as it was combined with flow from the wings and empennage. Since the propeller is specifically targeting the wake of the fuselage, the model was simplified to only include the fuselage. This gave much clearer results on the velocity profile of the wake and boundary layer across the surface, which can be seen in Figure 9.3 and Figure 9.4. The ambient conditions were identical to the duct analysis with a pressure of 22 632.1 Pa and temperature of 216.65K. The fluid domain was significantly larger than the model itself to allow the use of free-stream boundary conditions at the inlet and sides of the fluid section. Because of this larger domain, a finer mesh with additional boundary layers was used, as otherwise the resolution of the results would be insufficient; the mesh consisted of around 700,000 elements. The analysis was also performed for a number of other flight stages such as climb-out and take-off. Once again, a pressure outlet was used with a gauge pressure of 0 Pa, and the turbulence model was the SST $k-\omega$.

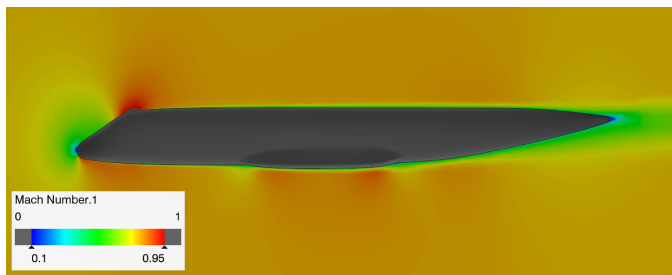


Figure 9.3: Cutaway side-view of Mach number colour plot for A320neo fuselage

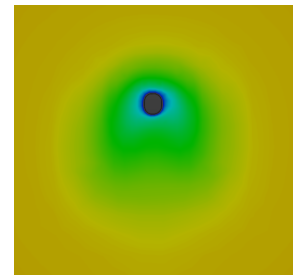


Figure 9.4: Rear view of Mach number colour plot for A320neo fuselage

From this data, the boundary layer profile can be obtained. As a result of the upwards taper of the tail-cone, and as can be seen from Figure 9.4, the boundary layer is asymmetric; it is much thicker on the bottom of the fuselage. For the propeller analysis, it was assumed that intake velocity was equal to the speed present at the tip section of the blade in the boundary layer velocity profile. For this we looked at the velocity profile on the lower fuselage section. Examining Figure 9.6, at a radial position of 1.75 the velocity is around 175 m/s and this is the inlet velocity used in the propeller analysis. The profile for the top and bottom can be seen in Figure 9.5 and Figure 9.6, respectively. By excluding the vertical stabiliser, it was also possible to compare the results with existing literature.

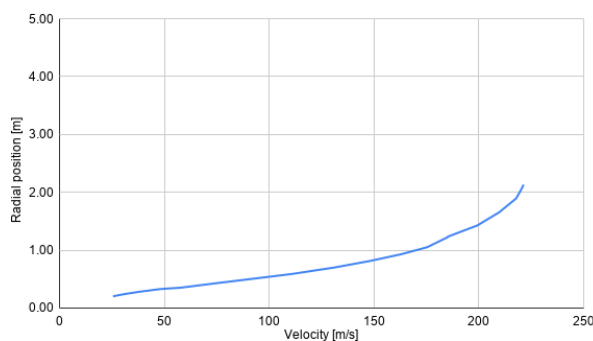


Figure 9.5: Radial boundary layer velocity profile - upper fuselage surface

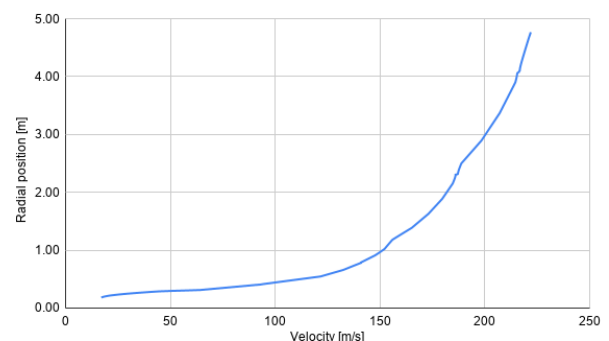


Figure 9.6: Radial boundary layer velocity profile - lower fuselage surface

¹https://grabcad.com/library?page=1&time=all_time&sort=recent&query=a320, retrieved on 22-06-2020

9.2.2. CFD verification

As aforementioned, the CFD results were compared with the values obtained from ESDU papers. Unfortunately, validation of the results was not possible since the manufacturing and testing of a real size duct was not possible. The paper used is ESDU 72019: *The influence of body geometry and flow condition on axisymmetric boundary layer at sub-critical Mach number* [57]. These papers should provide a solid basis for comparison since essentially the same parameters are calculated. As the title might reveal, the paper discusses the boundary layer profile along a certain body geometry. Figure 9.7 visualises the boundary layer and its growing thickness as one progresses along the geometry length. For an axisymmetric fuselage with a similar length-diameter ratio, nose cone radius and tail-cone proportions to the A320neo, the boundary layer thickness is roughly 2.4 m. Here, the thickness is the radial distance from the tail-cone end at which the velocity is 99% that of free-stream air. The CFD returned an average thickness of 3.1 m. While there is almost a 30% difference, this is deemed acceptable due to the empirical nature of the estimations and their inherent error as well as due to the differences in geometry which are not accounted for in the paper. Figure 9.7 shows the dimensions which were relevant to the analysis. In an ideal scenario, various turbulence models would be assessed and compared, and a small scale experiment would be conducted to fully validate the results.

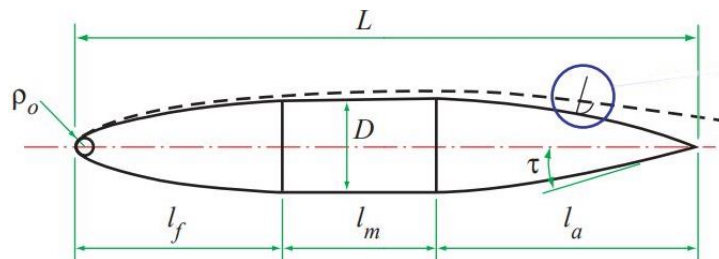


Figure 9.7: Relevant geometry for boundary layer thickness estimation [57]

The geometry was validated using the technical drawings provided on Airbus' website². Given the tight schedule, only a basic grid independence test was conducted. Similarly, concerning the choice of turbulence model, no analysis was done to assess its accuracy, rather, the NLR paper was used for this purpose [12]. Ultimately, the SST $k-\omega$ model was chosen due to its superior boundary layer estimation method.

9.3. Propeller design

Following the requirements and Boundary Layer theory, the propeller design can be initiated. Firstly, the performance parameters are discussed. Following this, the CRotor simulation software is elaborated upon. This section is concluded with the propeller overview and propeller mass estimation. The propeller design is optimised for cruise conditions. The A320appu will spend the largest amount of time in cruise. Consequently, propeller performance should be optimised for this condition. However, also climb-out performance was considered during the design since this flight phase requires substantially large amounts of thrust.

9.3.1. Propeller performance

In order to achieve the requirements set in section 9.1, analysing the performance influencing parameters is of importance. The baseline constraints of propeller performance are documented in section 8.3. During the design process, the following variables were considered:

- **Number of blades** - This has an effect on the efficiency-advance ratio curve. Increasing the number of blades will decrease the efficiency due to more disturbances in the flow while increasing the thrust density
- **Variable pitch** - This allows the angle of attack of the propeller blades to be changed during flight. With this, the system can optimise its performance during various flight phases.
- **Blade twist** - This also changes the angle of attack the blade sees except it is fixed during flight and varies along the radius.
- **Blade airfoil** - Since the local speed changes along the radius of the blade, each section needs an airfoil that is optimised for its corresponding Mach number. Successful optimisation decreases the drag of the propeller.
- **Rotations per minute** - The rotational speed of the propeller affects the advance ratio and the blade tip Mach number.

²<https://bit.ly/2CW4xRr>

9.3.2. Airfoil analysis software

As multiple airfoil configurations have been compared, detailed aerodynamic data was necessary. This airfoil data was analysed in XFLR5³, which provides an environment in which airfoils can be analysed. As CRotor accounts for 3D aerodynamic effects, a 2D analysis has been performed in XFLR5. The chosen Reynolds number for each airfoil was dependent on the blade section at which the airfoil would be applied. These Reynolds numbers varied from $Re = 0.25 - 1.22 \cdot 10^6$. As the CRotor authors recommended and included the MH-airfoil family, this set of airfoils was used to determine the airfoil distribution along the blade. By iteratively refining the propeller blade and applying more airfoils, and the data obtained through XFLR5, a significantly optimised design could be found.

9.3.3. Propeller simulation software

The propeller design was realised by use of a propeller simulation software. The designated software is CRotor⁴. CRotor is an upgraded version of CRotor which supplements features with which the optimum C_L distribution can be found. Also, a contra-rotating propeller system can be evaluated. Ultimately, the programme calculates slipstream velocities and accounts for induced propeller drag. The programme requires the following inputs:

- Airfoil aerodynamic data
- Number of blades
- Propeller tip radius
- Propeller hub radius
- Propeller power or thrust output
- Advance ratio or RPM
- Airspeed
- Altitude

Following the analysis, the programme outputs a rather large number of values. The most important ones for the current propeller design are:

- Propeller efficiency
- Propeller blade pitch
- Produced thrust
- C_L distribution

The outputs provide meaningful data which was leading in the propeller design process. The design phase was an iterative process in which design parameters such as RPM, the implemented airfoils and propeller radius, were altered to eventually achieve a successful design.

Table 9.1: An overview of all required aerodynamic parameters, together with the default values, for an example symmetric airfoil, in CRotor and CRotor

Aerodynamic property	Value	Blade section property	Value
Zero-lift α	0 [degrees]	$dC_D/d(C_L^2)$	0.0040 [-]
r/R	0.00 [-]	Reference Reynolds number	2 000 000 [-]
$dC_L/d\alpha$	6.28 [rad ⁻¹]	Reference Reynolds number	2 000 000 [-]
$dC_L/d\alpha$ at stall	0.1 [-]	Reynolds scaling exponent	-0.20 [-]
Maximum C_L	2.00 [-]	C_M	-0.1 [-]
Minimum C_L	-1.50 [-]	M_{crit}	0.62 [-]
Minimum C_d	0.0070 [-]	C_L a minimum	0.150 [-]
C_L increment to stall	0.20 [-]		

Aerodynamic input parameters

As mentioned earlier, CRotor allows the user to define airfoils at distinct spanwise locations along the blade. The CRotor⁵ module within CRotor provides an environment in which the blade section properties can be adjusted. Important to notice is that when multiple airfoil sections are defined, linear interpolation is used to define the aerodynamic properties in between the sections. Table 9.1 provides an overview of all required aerodynamic parameters. The zero-lift α , maximum- minimum- C_L , $dC_L/d\alpha$ and $dC_L/d\alpha$ at stall and C_L increment to stall are used to determine the lift parabola. Consequently, the aforementioned parameters have a rather important role in determining the propeller blade pitch. By using a certain blade pitch, the angle of attack, α , can be altered. Additionally, Prandtl-Glauert corrections are applied to compensate for compressibility effects. The equation for the Prandtl-Glauert correction is given below in Equation 9.1⁶ with $c_{l,0}$ being the incompressible lift coefficient.

$$C_l = \frac{C_{l,0}}{\sqrt{1 - M_\infty^2}} \quad (9.1)$$

³<http://www.xflr5.tech/xflr5.htm>, retrieved on 05-06-2020

⁴<http://www.esotec.org/sw/crotor.html>, retrieved on 01-06-2020

⁵<http://web.mit.edu/drela/Public/web/CRotor/>, retrieved on 25-05-2020

⁶http://www.ae.metu.edu.tr/~ae342/recitation_2.pdf, retrieved on 18-06-2020

The *Minimum* C_d , C_L for *minimum* C_d and the $\frac{dC_D}{d(C_L^2)}$ determine the quadratic drag dependence on C_L . This drag is afterwards scaled by a Reynolds number scaling based on the *Reference Reynolds number* and the *Reynolds scaling exponent* which is elaborated upon later. The quadratic relation between C_L and C_D is given in equation Equation 9.2.

$$C_D = (C_{D,0} + b \cdot (C_{L,0} - C_L)^2) \cdot \left(\frac{\text{True } Re}{\text{Reference } Re} \right)^f \quad (9.2)$$

In Equation 9.2, the b is determined by the quadratic C_D coefficient, or $dC_D d(C_L^2)$. The f is the Reynolds number scaling exponent. The latter is determined by the actual Reynolds number by use of a predefined table. Furthermore, some more miscellaneous parameters are: The r/R describes the spanwise position along the blade at which the described airfoil is utilised. The C_m describes the moment coefficient, used to calculate the aerodynamic twist. Finally, the M_{crit} gives a constraint for at which induced Mach number supersonic effects, such as wave drag and shockwaves, will occur.

9.3.4. Propeller simulation software limitations

As CRotor does not include all effects experienced by a BLI-propeller, some limitations should be considered whilst using the programme. Firstly, CRotor uses a constant velocity input. In reality the Boundary Layer Ingestion propeller will experience a velocity profile. Consecutively, the second limitation can be deduced: the actual propeller system will have a higher efficiency. BLI significantly increases efficiency, as is elaborated on later in section 9.4. Also, a constant velocity input might cause propeller blade sections to stall as the actual experienced velocity is lower. The angle of attack of a propeller section is caused by the rotational and incoming velocity. If the incoming velocity is lower than expected, the angle of attack could change and exceed the airfoil stall angle. Furthermore, CRotor was not created to analyse propellers which perform near transonic airspeeds. Compressibility effects are largely neglected which is a significant limitations. Additionally, the software does not account for the air inflow being turbulent. Lastly, for both propellers, radii is assumed to be constant. This assumption is adopted due to the limited scope and resources associated with the propeller design.

9.3.5. Propeller overview

Following the propeller analysis, a propeller design is established. To ensure the thrust requirements could be met a contra-rotating propeller system was generated. Additional features such as variable RPM and variable propeller blade pitch are applied to increase efficiency. The design requires some additional subsystems which are elaborated on later in section 9.5. The propeller characteristics for cruise conditions are displayed in Table 9.2 and the propeller airfoils are summarised in Table 9.3. The design choices summarised in aforementioned tables provided the highest efficiency whilst still meeting all requirements and constraints. The cruise phase of the flight envelope is considered since the propeller design was driven by these circumstances.

Table 9.2: The forward propeller characteristics

Variable	Forward propeller	Aft propeller
Number of blades [-]	3	3
Radius [m]	1.75	1.75 *
RPM 4-11 km [-]	1 000	1 000
RPM 0-4 km [-]	1 400	1 400
Shaft power [kW]	620	620
Thrust [kN]	2.83	3.28
Torque [kNm]	5.92	5.92
Tip mach number [-]	0.856	0.860
Efficiency [%]	80	92.6

*In future design phases, this radius will be decreased relative to the forward propeller to avoid excessive aerodynamic interference

Table 9.3: The airfoil distribution along the propeller blade in spanwise direction

r/R	Airfoil
0.000 - 0.274	MH112mod
0.274 - 0.400	MH113mod
0.400 - 0.580	MH114mod
0.580 - 0.770	MH115mod
0.770 - 0.988	MH117mod
0.988 - 1.00	MH120mod

Table 9.2 indicates the usage of two different RPM settings. The rationale behind choosing a variable RPM propeller is explained by considering the climb-out requirements. The propeller is designed for cruise conditions. Nonetheless, it should be able to output a ≈ 26 kN of thrust during climb-out. To achieve this thrust, the propeller will perform at a higher RPM in between 0 and four kilometres altitude. As established in Table 9.2, the propeller radius is 1.75 m. This radius is larger than allowed by the tip back angle constraints. This challenge is assessed by stopping the propeller during the take-off- and landing-phase in which the tip-back angle would cause a problem. By stopping the propellers at the exact correct attitude, the maximum allowed

tip-back angle is increased. This solution is visualised in Figure 9.8. The additional clearance of 0.875 m, can be calculated by subtracting $\sin 30$ multiplied with the propeller radius from the original propeller radius, $1.75 - 1.75 \cdot \sin 30 = 0.875 \text{ m}$.

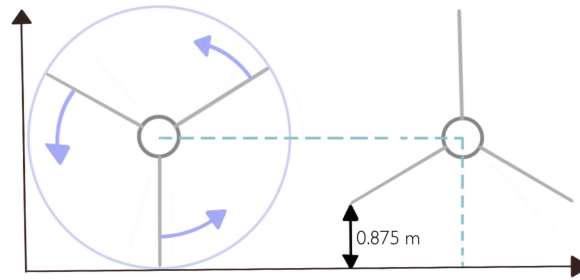


Figure 9.8: Visualisation of moment the propeller is stopped to create a larger tip-back angle

9.3.6. Propeller mass estimation

The propeller mass estimation is performed by using empirical relations. These are paired with a 17% weight penalty due to the contra-rotating mechanism⁷. The propeller weight regression used is the adjusted Torenbeek equation based on statistical data [67]. This regression is given in Equation 9.3. However, Equation 9.3 accounts for aluminium systems. As the propeller blades will consist of carbon fibre composites, which is elaborated on in section 9.6, a second correction factor is applied. Additionally, it is assumed that the propeller hub and mechanism are mainly composed of carbon fibre composites. The correction factor to account for a composite structure is given by $\frac{\rho_{\text{carbon fibre}}}{\rho_{\text{aluminium}}}$. The density of carbon fibre is $1\,600 \text{ kg/m}^3$ and the density for aluminium is $2\,710 \text{ kg/m}^3$ ⁸.

$$\begin{aligned} m_{\text{propeller}} &= 1.1[D_p \cdot P_{\text{max}} \cdot \sqrt{B}]^{0.52} \\ &= 1.1[(1.75 \cdot 2) \cdot 3956000 \cdot \sqrt{6}]^{0.52} \\ &= 249.6 \text{ kg} \end{aligned} \quad (9.3)$$

$$m_{\text{propeller}} = 249.58 \cdot \frac{1600}{2710} \cdot 1.17 = 172.4 \text{ kg} \quad (9.4)$$

Given Equation 9.3 and the data supplied by Table 9.2, the propeller mass can be estimated to be 249.58 kg. Applying the correction factor for the carbon fibre and contra-rotating mechanism gives a mass of 172.4 kg. This will be the final propeller mass, which includes the hub and mechanisms located in the hub such as the variable pitch system.

9.4. BLI performance gain

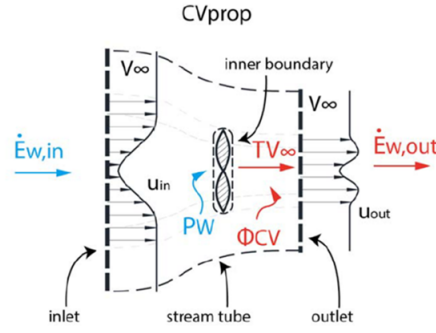
Boundary layer ingestion provides benefits in two manners. Both are discussed to determine the overall performance gain:

1. The slower moving velocity present in the boundary layer along the fuselage is the velocity that the propeller ingests, which is beneficial
2. Energy present in the wake is recycled and provides the same thrust output for a lower shaft power input

The first characteristic of the BLI is partly taken into account in the CRotor analysis by not ingesting the free stream velocity but 75% of the free stream velocity. According to the computational fluid dynamics analysis represented in section 9.2, the velocity at a radial position of 1.75 m from the fuselage, where the tip blades will be, encounter a velocity equal to 0.75 times the free stream velocity. However, CRotor limits the analysis to a single velocity input. Therefore, the value for the velocity inlet is recalculated to account for the slower moving air entering the propeller. The second performance gain of BLI can be numerically analysed to some extent. Examining the power balance of a propeller in the wake of a fuselage for a two-dimensional control volume propeller in Figure 9.9, the energies present prior and aft are visible.

⁷<https://www.rcgroups.com/forums/showatt.php?attachmentid=2815700>, retrieved on 17-06-2020

⁸http://www.performance-composites.com/carbonfibre/mechanicalproperties_2.asp, retrieved on 17-06-2020



$$\dot{E}_{w,in} + P_W = TV_{\infty} + \dot{E}_{w,out} + \Phi_{CV}$$

Figure 9.9: Power balance [44]

In the power balance, the P_w represents the shaft power input. ϕ_{CV} is the viscous energy present in the boundary layer and can be considered negligible in the analysis. From the propeller design, shaft power inputs have been determined together with the achieved thrust values for various flight phases. In determining the performance gain due to re-energising the wake energy, the incoming wake energy $\dot{E}_{w,in}$ is to be determined together with the outward wake energy, $\dot{E}_{w,out}$. In the wake energy calculations to determine the BLI efficiency gain, the analysis was limited to cruise altitude and velocity only as this is the most critical phase to examine the gain due to BLI. Therefore the following values for density and free stream velocity are used:

$$\rho = 0.364 \text{ kg/m}^3 \quad V_{\infty} = 225 \text{ m/s}$$

The incoming wake energy flow can then be calculated as follows for a control volume over an area.

$$\dot{E}_{w,k} = \iint_{tp} \rho u \cdot \frac{1}{2} (u - V_{\infty})^2 dS \quad (9.5)$$

To examine this with a list of various incoming velocities u as input for certain radial positions the equation is transformed to a sum of around 200 y intervals, to ensure an accurate value of the wake energy. This discretisation of Equation 9.5 results in Equation 9.6.

$$E_{w,body} = \sum_{r=0}^{1.75} \rho u_r \frac{1}{2} (u_r - V_{\infty})^2 (dy)_r \cdot 2\pi \cdot y_r \quad (9.6)$$

The results are shown in Table 9.4.

Table 9.4: Power balance calculations results

	Power in [kW]		Power out [kW]
P_w	1 143.3	$T \cdot V_{\infty}$	1 342
$\dot{E}_{w,in}$	1 326.7	$\dot{E}_{w,out}$	1 129
Total in	2 470.0	Total out	2 470.0

When calculating the wake energies and setting the thrust the propeller is to produce, it is determined that the shaft power input required is 1143.32 kW. This is due to the difference in wake energy in and out, $E_{w,out}$ is equal to 198 kW. The wake energy into the propeller is relatively high compared to the aft energy. The calculated required input shaft power is less power than the initial 1 240 kW calculated in the propeller design. To determine the reliability of the numbers achieved from the wake energy calculations using the integral method, one can look at the total drag of the fuselage, which consists of both the boundary layer energy and the wake energy. The wake energy is expected to be around 15% of the total fuselage drag [44]. Equation Equation 9.7 shows the balance of the drag and its components: the viscous dissipation over the boundary layer, which represents the profile drag mostly, and the wake energy.

$$D \times V_{\infty} = \Phi_{BL} + E_{w,body} = \int_{tp} \rho u \frac{1}{2} (V_{\infty}^2 - u^2) dy + \int_{tp} \rho u \frac{1}{2} (u - V_{\infty})^2 dy \quad (9.7)$$

The wake energy inlet in the right side of Equation 9.7 has been calculated in the previous step. The boundary layer energy is calculated using the first part of the right hand side of the equation. From this it can be determined what part of the total drag energy is present in the wake. These steps are summarised in the table below.

Table 9.5: Wake percentage of total energy calculation

Variable	Value
Wake power [kW]	1 327
BL [kW]	6 763
Total [kW]	8 090
Percentage wake [%]	16.40

The left side of the equation Equation 9.7, is calculated using an estimated drag value of 18 kN from the CFD analysis. Converting this to power, the drag is multiplied by the free stream velocity at cruise, equal to 225 m/s. Multiplying this value by the earlier found wake energy percentage of 16.40% results in a total energy present in the wake of 664.19 kW. This is significantly lower than the initial value of 1 327 kW found using the integral relation. However, using the estimate that only 60% of this wake energy could be re-energised by the propeller, this results in a value of 796.03 kW for the inlet wake energy. All in all, the wake energy calculations have proved to not be representative of the actual energy present in the wake of the fuselage. For these reasons only a 200 kW reduction in shaft power is assumed in the simulations as an increased performance gain. In reality the gain is likely to be higher, as the velocity differences from the CRotor analysis are not fully accurate, the pressure differences were not taken into account and because of the axi-symmetrical velocity profile that was assumed. A detailed analysis of the performance gain due to boundary layer ingestion proves to be difficult but is a topic for further investigation to properly understand the potentials of using this propulsive concept.

9.5. Additional propeller mechanisms

The propeller requires mechanisms for both contra-rotating and variable pitch features. Additionally, the requirement of stopping the propeller during take-off and landing, requires a gyroscope and brake system installed in the propeller hub. The purpose of this section is to briefly describe the necessary integrated propeller systems. Eventually, as the A320appu progresses to later design stages, a more detailed analysis should be performed regarding all the described propeller mechanisms.

9.5.1. Propeller gyroscope and brakes

The propeller system requires a gyroscope-brake system to ensure the safe stopping of the propeller during take-off and landing. Taking into account risk **PR-05: The propeller stopping mechanism fails and propeller hits the ground during take-off and/or landing**, this is an important component since propeller-strikes are more likely as a result of the large diameter. The purpose of the gyro is to identify the angular position of the blades so that they can be safely stopped at the correct position, since without this information, a propeller-strike becomes much more likely. Additionally, this system ensures the safe stopping of the propeller during flight phases in which the aircraft is close to the ground and performs a yaw or roll movement, since this can cause one of the propeller blades to be closer to the ground than under normal circumstances. The gyro allows the blades to be stationed in a position where the probability of a propeller-strike is minimised.

A number of gyroscopes exist, all differing in the accuracy with which an angle can be measured. For space- and aircraft-applications⁹ a Hemispherical Resonator Gyroscope (HRG) is used. This high accuracy device is extremely reliable, accurate and is already applied in commercial aircraft application systems. Additionally, it can be very compact. The aforementioned reasons justify why the HRG is well applicable in the A320appu. Multiple gyroscopes can also be installed for added reliability.

The propeller brake system can use simple press-brakes since the propeller and engine can be decoupled on demand as a result of the turbine being freely mounted. The brake system is best located before the contra-rotating mechanism to directly bring both propellers to a stand-still. The propeller angles should be measured and verified with the gyroscope data to ensure the propellers are stopped in the correct orientation. An additional cooling mechanism should be applied to ensure the redundant heat does not damage nearby subsystems.

⁹<https://bit.ly/2Za8md7>, retrieved on 19-06-2020

9.5.2. Contra-rotating mechanism

The contra-rotating propeller will use a co-axial gear system. A co-axial gear system uses a single input shaft connected to two independent output shafts.

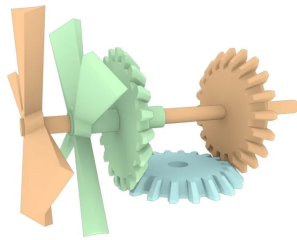


Figure 9.10: The co-axial contra-rotating gear mechanism¹⁰



Figure 9.11: Helical gears in a perpendicular configuration¹¹

As can be seen in [Figure 9.10](#), the co-axial gear system is using three perpendicular gears. To decrease wear, lubricants will be introduced into the gear system. Eventually, helical gears, displayed in [Figure 9.11](#), are utilised as these mesh better together than conventional gears. Moreover, helical gears produce less noise and experience less wear. Additionally, helical gear are stronger than spur gears since more teeth are in contact at the same time. Ultimately, with sufficiently accurate manufacturing helical gears can virtually become wear and maintenance free. All aforementioned benefits justify the choice for using an helical.

9.5.3. Variable pitch mechanism

As decided upon earlier, the propeller will use a variable pitch mechanism. The applied variable pitch mechanism uses a similar helical gear set-up as in [subsection 9.5.2](#). The entire system will rotate by changing the centre gear angle. Hence, the pitch of all blades can be, simultaneously, adjusted by the same angle. Both the forward and aft propeller will utilise the same variable pitch mechanism displayed in [Figure 9.12](#).

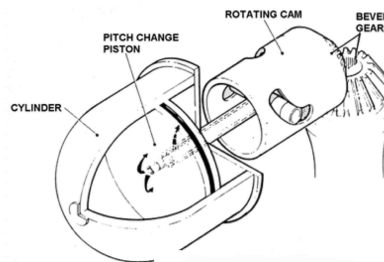


Figure 9.12: Hydromatic propeller variable pitch mechanism¹²

A hydromatic pitch control mechanism is utilised. The propeller hub, visualised as a cylinder in [Figure 9.12](#), contains a fluid which can be pressurised to push the pitch change piston. Subsequently, the rotating cam will be pushed and rotate the gears, annotated as bevel gears in [Figure 9.12](#), which are connected to the propeller blades.

9.6. Structural integrity of the propeller

The structural integrity of the propeller has been confirmed by use of a Python programme. The simulation software considers thrust, drag and centrifugal forces and aerodynamic twist moments exerted on the propeller. The purpose of the numerical simulation is to visualise the total stress encountered over the propeller blade in spanwise direction. By allowing variable sheet thicknesses and materials a lightweight propeller structure can be configured. Additionally, varying cross-sections can be implemented in the programme. The cross-section data is provided to the programme by extrapolating propeller characteristic from CRotor into a .txt file. The first analyses revealed the experienced stresses to be substantially high. To address this issue, a more elaborate evaluation of composite materials has been added to the simulation. This additional analysis allows composite materials, such as carbon fibre, to be used which potentially provide a lightweight material choice. This section aims to describe programme logic, limitations, verification and validation and ultimately results of the propeller structural analysis.

¹⁰<https://bit.ly/384vIVn>, retrieved on 18-06-2020

¹¹<https://bit.ly/3i9xQjA>, retrieved on 18-06-2020

¹²<https://bit.ly/3eCDVmK>, retrieved on 18-06-2020

9.6.1. Assumptions and the blade model

Below, assumptions regarding the propeller structural simulation have been stated:

- The cross-section is infinitely rigid in its own plane, i.e. the cross-section does not deform
- The cross-section remains normal to the deformed axis of the beam
- The airfoil can be modelled as a rectangular thin-walled box with chord length as width and maximum thickness as height
- The sheet thickness remains constant when the cross-section experiences forces
- No creeping or deformation due to a change in temperature is experienced
- The moment caused by the centrifugal force is neglected since the airfoil is simplified to a thin-walled rectangular box
- The propeller blades' gravitational pull are considered negligible compared to the thrust-, drag-, centrifugal and torque-loads exerted on the propeller

As the blade geometry varies in the spanwise direction, a number of different rectangular cross-sections are evaluated. Eventually, the propeller is divided into sixteen distinct cross-sections. This number of sections was chosen to ensure a significant change in chord length and sheet thickness over the spanwise direction. Every distinct segment experiences its own forces and moments which are detailed in [subsection 9.6.2](#). The blade sections and the structural nodes are visualised in [Figure 9.13](#). Note that in reality, sixteen blade sections are configured in the simulation model.

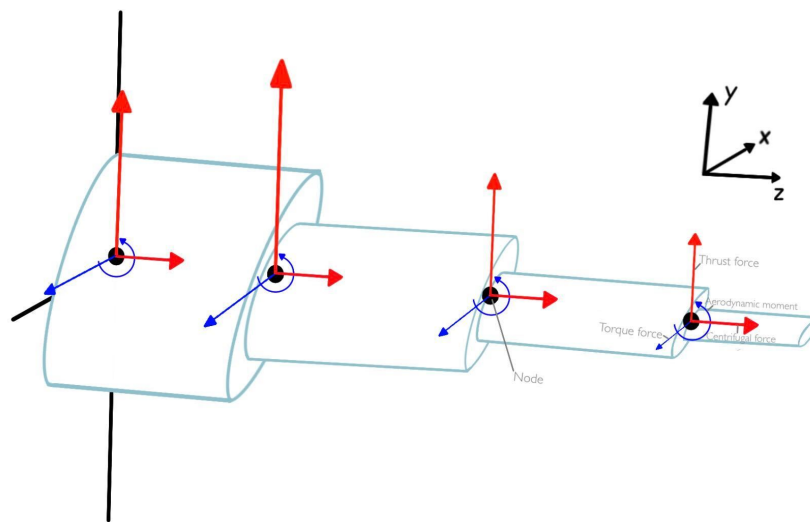


Figure 9.13: A front view of the propeller, displaying the different blade sections

9.6.2. Exerted forces and moments on the propeller blade

[Figure 9.14](#) and [Figure 9.15](#) visualise the generalised loads on the propeller. The two figures merely give a general overview of the exerted forces on the propeller, i.e. the forces are not to scale and its locations are not correct. In reality, the thrust, torque (or drag) and aerodynamic twist are distributed forces and moments of the propeller blade in spanwise direction. This distribution is not constant and is included in the programme by consulting the moments at each of the 16 blade segments. The induced moments are cumulative. In other words, the first node experiences the largest moment, the second a slightly smaller moment and so on. The moments at 16 distinct nodes are conveniently supplied by the CROTOR simulation.

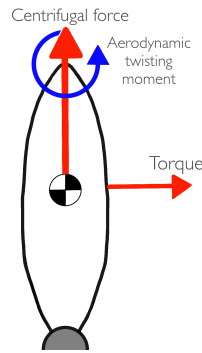


Figure 9.14: Front view of the propeller with generalised centrifugal, aerodynamic twisting and torque loads

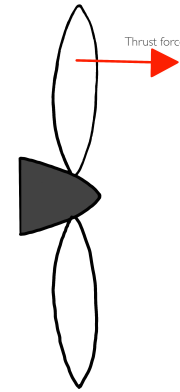


Figure 9.15: A side view of the propeller, displaying the generalised thrust load

9.6.3. Programme logic

A flow diagram of the considered simulation is displayed in Figure 9.16. Firstly, CRotor data and sheet thickness data is required as input. Following this, the CRotor data is converted into matrices which is used as input. The matrices also include information on the varying cross-section geometry of the blade. Using the geometrical data and sheet thickness and material, the centrifugal force can be calculated. This centrifugal force is a result of the blade mass, centroid location and rotational velocity. This relation is given in Equation 9.11. Following the determination of the centrifugal force, distributed force and moment values are inserted into the *SectionProperties*¹³ Python package which calculates the Von Mises stress throughout the structure. This is an iterative process and is repeated for all sixteen spanwise blade segments. Important to notice is that the Von Mises stress theorem only returns correct results for isentropic materials. In case anisotropic materials are implemented, the Tsai-Hill analysis is applied. The Tsai-Hill simulation uses the stresses calculated by the *SectionProperties* Python package. The last consideration during the stress calculations is the propeller pitch angle β . This angle is different for every blade segment and is taken into account to provide a more accurate stress and failure estimation. Following the stress calculations, the script returns the maximum stress in both the forward and aft propeller. Additionally, a plot visualising the Von Mises stress distribution over both propellers in spanwise direction is provided.

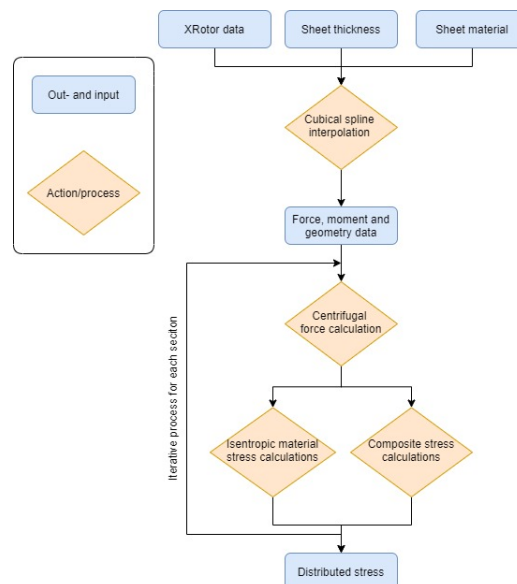


Figure 9.16: Flow diagram associated with the structural analysis Python programme

9.6.4. Results of the propeller structural analysis

The structural analysis is performed for the flight envelope in which the highest loads are experienced by the propeller. The flight phase with the highest load is climb-out in which the thrust equals 26.88 kN. Aided by the moments, forces and geometry, supplied by CRotor, the propeller structural analysis is assessed. As one can

¹³<https://sectionproperties.readthedocs.io/en/latest/index.html>, licensed under the MIT license, date retrieved: 09-06-2020

expect, the imposed stresses on the propeller root are rather high. Therefore, the propeller blade root section's geometrical parameters have been multiplied by a factor of 1.15 for both the forward and aft propeller. As only the root section is changed, it is assumed that the aerodynamic performance of the propeller does not change. The chord and height values for the aft and front propeller are displayed in Figure 9.17 and Figure 9.18, respectively. Additionally, the forward and aft propeller pitch angles are visualised in Figure 9.19.

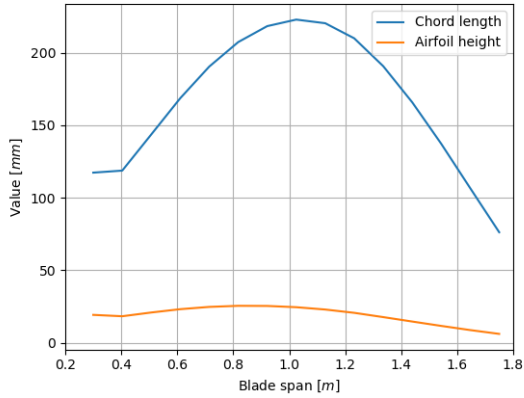


Figure 9.17: Height and chord length forward propeller

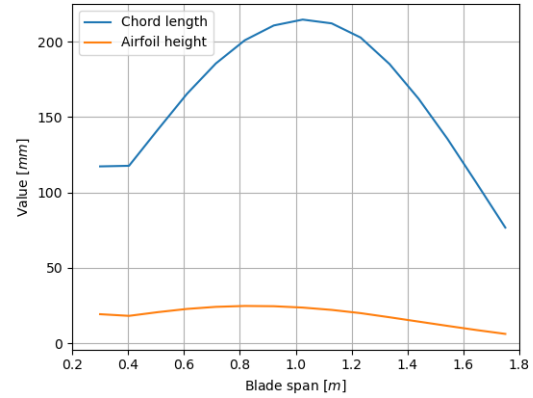


Figure 9.18: Height and chord length aft propeller

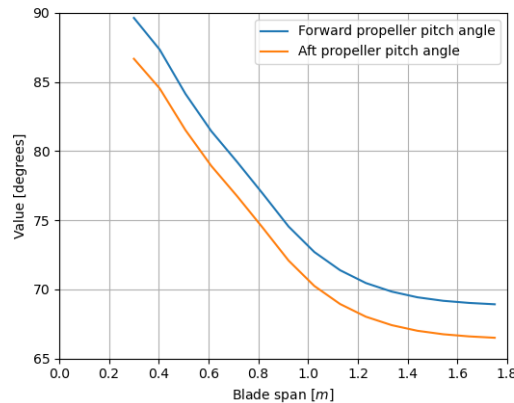


Figure 9.19: The propeller pitch angles for both the aft and forward-propeller

The CRotor data-file also contains the induced moments at each node. Eventually the moments, combined with the shear and normal forces will generate the load case. The right-handed coordinate system given in Figure 9.13 is used in the following structural calculations. The induced moments are plotted over the blade span in Figure 9.20 and Figure 9.21. Since the propeller experiences the largest moments and forces at the root, the sheet thickness is supposed to be larger at the root than at the tip. As the production of sheets requires a thickness of at least ≈ 1 mm, a parabolic sheet distribution is applied. This sheet thickness distribution is visualised in Figure 9.23. As the entire geometry and load distribution has been determined, the Von Mises stresses can be calculated. The Von Mises stress analysis of an isentropic material for both propellers are displayed in Figure 9.22. Additionally, the Von Mises stress distribution in the xy-plane of the aft and forward propeller root are displayed in Figure 9.25 and Figure 9.24, respectively.

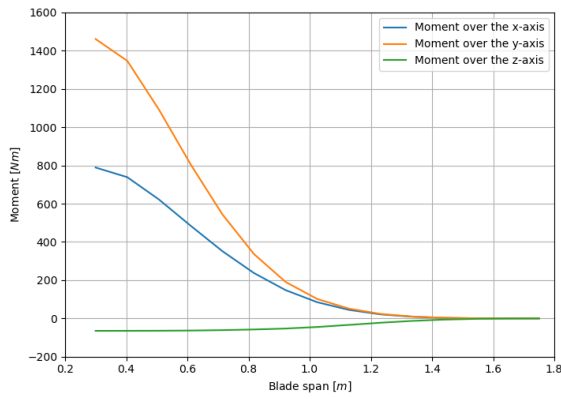


Figure 9.20: Induced moments forward propeller

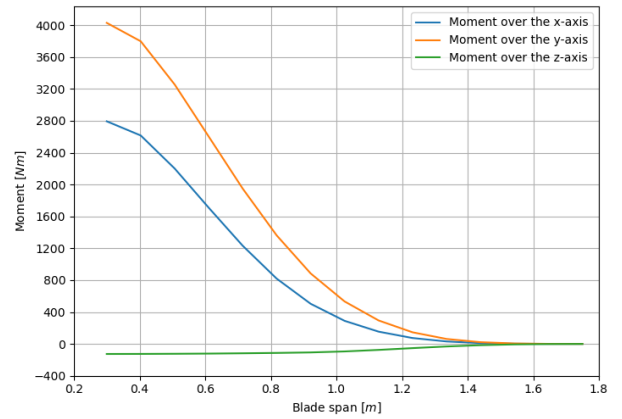


Figure 9.21: Induced moments aft propeller

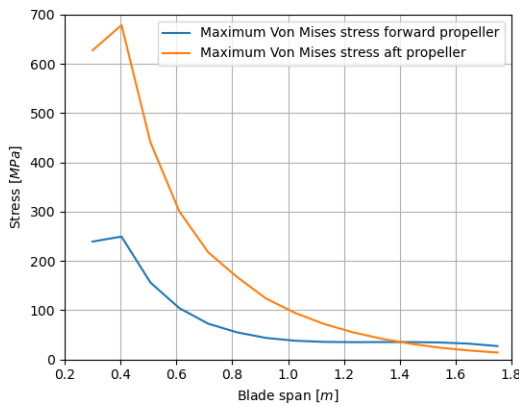


Figure 9.22: The Von Mises stress over the blade span for both forward and aft propeller

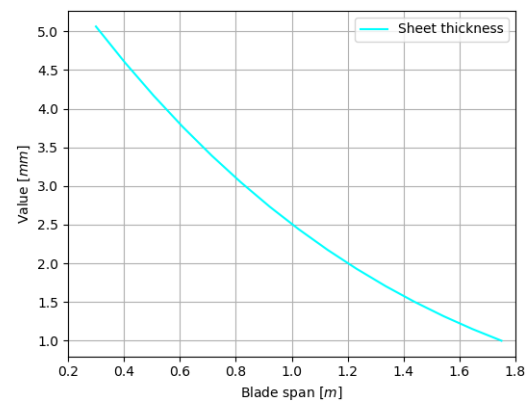


Figure 9.23: Forward and aft propeller sheet thickness

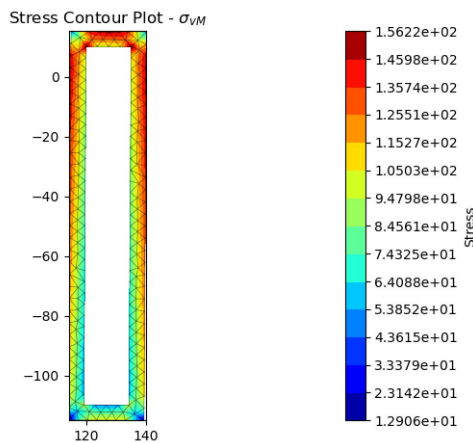


Figure 9.24: Von Mises stress in the xy-plane for the forward propeller in [MPa], cross-section width on the x-axis and height on the y-axis, both in [mm]

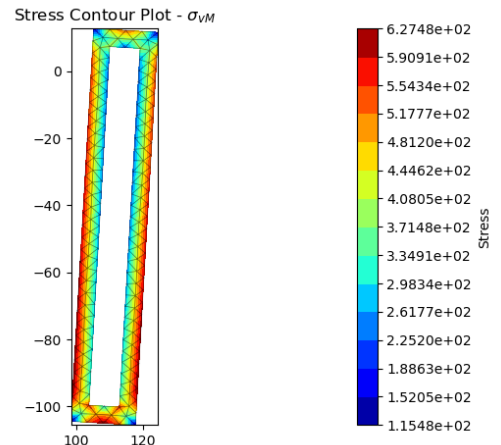


Figure 9.25: Von Mises stress in the xy-plane for the aft propeller in [MPa], cross-section width on the x-axis and height on the y-axis, both in [mm]

Stress analysis

Evidently, from Figure 9.22, the stresses experienced by the aft propeller are the most extreme. Since these stresses clearly surpass the yield strength of aluminium, which is 276 MPa¹⁴ and taking a safety factor of 20% into account the maximum allowed stress is 184 MPa, a material is needed with a higher yield strength. As the imposed stress is a factor ≈2 too high, the mere addition of stringers will not be sufficient. Also, solidifying the entire propeller does not provide a feasible solution since the centrifugal forces will become significantly higher due to the increased mass. Thus, the Standard Carbon Fibre composite was chosen as the propeller material due to its strength in both longitudinal and traverse direction. The material characteristics are summarised in

Table 9.6. Another observation which can be made with regard to Figure 9.25, is the absence of a compressive force. This phenomena can be explained by considering that the centrifugal force is significantly high at the root of the propeller blade. The centrifugal force imposes a surplus of tensile stress which compensates for the compressive forces and moments. However, further along the propeller the compressive stress will play a more significant role due to the decreasing centrifugal force. This will be elaborated on later whilst looking at the optimum composite fibre orientation angle.

Table 9.6: The material properties of the composite Std CFRP¹³

Property	Value
Ult. Tensile Strength 0°	600 [MPa]
Ult. Comp. Strength 0°	570 [MPa]
Ult. Tensile Strength 90°	600 [MPa]
Ult. Comp. Strength 90°	570 [MPa]
Ult. In-plane Shear Strength	90 [Mpa]
Density	1 600 [kg/m ³]

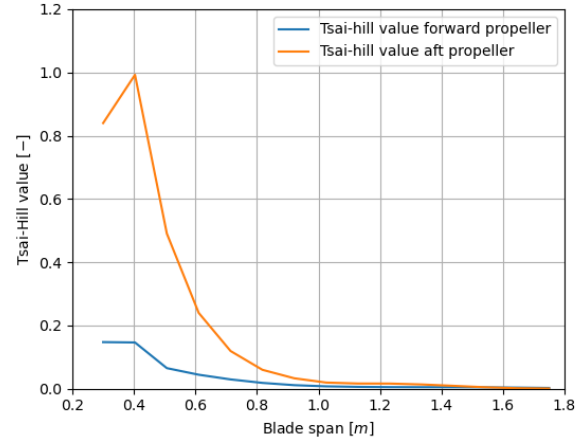


Figure 9.26: The Tsai-Hill values along the blade span for both propellers

As stated before, the Tsai-Hill analysis is necessary to properly assess composite structures. Summarised, if the Tsai-Hill returns a value larger than one, the structural integrity of a structure cannot be confirmed. A more elaborate explanation of the Tsai-Hill analysis can be found in section 11.9. The result of the Tsai-Hill analysis can be seen in Figure 9.26. Since none of these values surpass one, the composite propeller blade’s structural integrity can be considered to be confirmed. Since the density and geometry of the propeller are known, the mass can be calculated to be 2.2 kg per propeller blade. Even though this might seem rather light, this number can be justified by remembering that the propeller has a thickness of 5 to 1 mm. Additionally, the composite’s density is low compared to conventional materials such as aluminium (2 710 kg/m³ versus 1 600 kg/m³)¹³.

Composite fibre orientation

As composites are unidirectional, their orientation with respect to a datum is rather important. For this analysis, the z-axis in Figure 9.13, is taken as datum, i.e. the line along with the angle equals 0°. The Tsai-Hill analysis, previously added to analyse composite structures, is used to calculate the optimum angle fibre orientation. This angle is an average value. In other words, the average fibre angle of each section should equal the optimum fibre angle. The optimum average fibre angles of the forward and aft propeller are displayed in Figure 9.27.

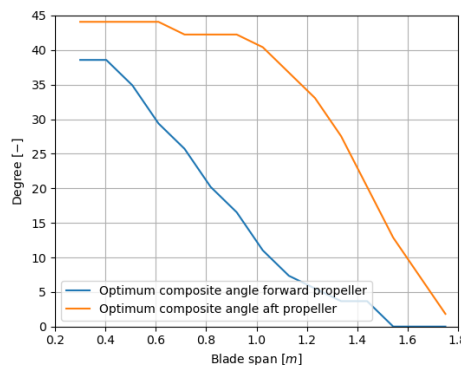


Figure 9.27: The optimum average angle of both propellers’ composite fibre orientation

It can be observed that the optimum average fibre equals roughly 45° at the root of the blade and slowly decreases to zero. This is mainly due to the accumulating shear forces which provide a substantial shear stress near the root. The shear stress compared to the normal stress becomes smaller as one progresses over the

¹⁴<https://bit.ly/2Nvmjwz>, date retrieved: 17-06-2020

blade in spanwise direction. The decreasing shear- versus normal-stress explains the decreasing optimum fibre angle.

To summarise, the used propeller thickness is displayed in Figure 9.23. Additionally, the composite Standard Carbon Fibre Fabric is used to provide a lightweight propeller design. The carbon fibre's properties are summarised in Table 9.6. Eventually, the weight of each propeller blade for both forward and aft will be 2.2 kg.

9.6.5. Programme verification and validation

Evidently, programme verification and validation is important to see whether the simulation returns the correct results. Verification is performed by comparing the script to a theoretical model. Simulation validation is completed by comparing the script output to previously performed experiments.

Verification

As explained in 9.6.3, the simulation essentially calculates the Von Mises stress in spanwise direction. The Von Mises stress is the total stress; shear, bending and normal stresses over multiple axes, experienced by a structure. The mathematical formulation of the Von Mises stress is detailed in Equation 9.8¹⁵. The Tsai-hill definition and method is verified in subsection 11.8.2, which is assumed to be applicable to the propeller analysis. Considering the programme logic, both the centrifugal force and the Von Mises stress equations need to be verified. A number of unit tests are performed to verify the simulation. Furthermore, the sign convention displayed in Figure 9.28 is used to establish positive (tensile) stresses in the positive quadrant of the xy-plane.

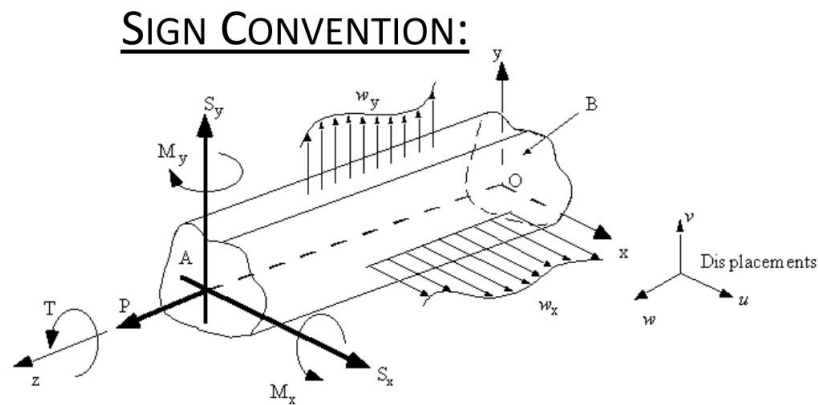


Figure 9.28: Sign convention used in the verification procedure of the Python script

$$\sigma_{\text{Von Mises}} = \sqrt{0.5[(\sigma_{xx} - \sigma_{yy})^2 + (\sigma_{yy} - \sigma_{zz})^2 + (\sigma_{zz} - \sigma_{xx})^2 + 6(\tau_{xy}^2 + \tau_{yz}^2 + \tau_{zx}^2)]} \quad (9.8)$$

The script verification will be assessed by running the script with a certain predefined geometry and experienced load. For this same geometry and arbitrary load, the theoretical Von Mises stress will be calculated. Afterwards, the values are compared to assess whether the programme is performing in a just manner. Also, a small number of unit tests is performed to compare intermediate results. The hypothetical blade data and loading is stated in Table 9.7.

¹⁵https://en.wikipedia.org/wiki/Von_Mises_yield_criterion, retrieved on 22-06-2020

Table 9.7: Values used in script verification

Blade details	Section 1	Section 2
Start of section	0% blade span	50% blade span
M_x	1 200 [Nm]	900 [Nm]
M_y	900 [Nm]	600 [Nm]
Width, b	0.2 [m]	0.1[m]
Height, h	0.2 [m]	0.1 [m]
Sheet thickness, t	0.005 [m]	0.005 [m]
r_{hub}	0.0 [m]	
r_{blade}	1.5 [m]	
RPM	1 000 [1/min]	
$\rho_{\text{aluminium}}$	2 710 [kg/m ³]	

As evident from [Table 9.7](#), the second blade section starts halfway the blade span. Two varying moments over the x- and y-axis are induced on the propeller blade. The Von Mises and centrifugal stress at the root of the blade are considered. Even though the moments and varying geometry at the second blade segments have no significant meaning, they are included to see whether the simulation is able to use the correct data.

As can be seen in [Equation 9.8](#), the unknowns are the σ_z , σ_x and σ_y . As clearly no shear forces are present, the shear stress variables equate to zero in [Equation 9.8](#). For a rectangular thin walled beam the moments of inertia are:

The equations for moment of inertia were taken from literature. Due to the presence of multiple symmetry axes, the product of Inertia, I_{xy} , is zero. Furthermore, $I_{xx} = I_{yy}$ since the height and width are equal for both cross-sections. This results in $I_{xx} = I_{yy} = 2.437 \cdot 10^{-5} \text{ m}^4$ and $I_{zz} = 6.1520 \cdot 10^{-4} \text{ m}^4$. The equations for normal stresses were once again taken from literature. Conveniently, the M_z and I_{xy} are zero. Additionally, the x, y coordinates at which maximum stress is experienced are located at $x = 0.1 \text{ m}$ and $y = 0.1 \text{ m}$, since those are the most extreme x - and y -values. Furthermore, the z -value is zero since the stresses are assessed at the root of the blade. Eventually, the x - y -plane will experience a tensile, positive stress (a right-handed coordinate system is used). The aforementioned data simplifies the stress equations to:

$$\sigma_z = \frac{(M_x I_{yy}) \cdot y + (M_y I_{xx}) \cdot x}{I_{xx} I_{yy}} \quad (9.9) \quad \sigma_x = \sigma_y = 0 \quad (9.10)$$

This yields $\sigma_z = 8\,490\,852 \text{ Pa}$. Comparing the theoretical to the analytical output, it can be concluded that the offset between both is negligible small. The next step is to notice that σ_z has another component, namely the centrifugal force and induced normal stress. The centrifugal force is defined positive as displayed in [Figure 9.13](#). This force can be calculated by [Equation 9.11](#).

$$F_{\text{centrifugal}} = \frac{mV^2}{r} \quad (9.11) \quad V = \text{RPM} \frac{2\pi r}{60} \quad (9.12)$$

In [Equation 9.11](#) the r quantifies the distance from the centre of the entire propeller to the centroid of the blade. Difficulties are mainly imposed by calculating the centroid, \bar{x} , location. Furthermore, the velocity, V , also depends on the centroid location. The velocity is dependent on the RPM as formulated in [Equation 9.12](#). Calculating the centroid is performed by using [Equation 9.13](#). The centre of the propeller is taken as the datum from which \bar{x} is measured.

$$\bar{x}_{\text{centroid}} = \frac{\sum_{i=1}^n m_i x_i}{\sum_{i=1}^n m_i} \quad (9.13)$$

The centroid for the first section is located at $0.5 \cdot 0.75 = 0.375 \text{ m}$. The second section has its centroid located at $0.75 + 0.5 \cdot 0.75 = 1.125 \text{ m}$. The centroid for the theoretical propeller, using data retrieved from [Table 9.7](#), is located at:

$$m_i = \frac{R_{\text{blade}}}{\text{number of sections}} \cdot (4 \cdot b_i \cdot t - 4_i \cdot t^2) \cdot \rho_{\text{aluminium}}$$

$$m_1 = 7.93 \text{ kg}; m_2 = 3.86 \text{ kg}$$

$$\bar{x}_{\text{centroid}} = \frac{7.9268 \cdot 0.375 + 3.8618 \cdot 1.125}{7.9268 + 3.8618} = 0.621 \text{ m}$$

Consecutively, the theoretical centrifugal force can be calculated to be:

$$V = 1000 \cdot \frac{2\pi \cdot 0.6207}{60} = 64.998 \text{ m/s}$$

$$F_{\text{centrifugal}} = \frac{(7.9268 + 3.8618) \cdot 65.0^2}{0.621} = 80240 \text{ N}$$

Comparing the numerical and theoretical results, the error is negligible small. Ultimately, the normal stresses in the x-y-plane can be calculated with aid of $\sigma_z = \frac{F}{A}$. Since all the bending and normal stresses in the y-z- and x-z-plane equal zero, the Von Mises stress equals σ_z . The sum of the two centrifugal and bending stresses is $20\,574\,329 + 8\,490\,852 = 29\,064\,954 \text{ Pa} = \sigma_z$. The numerical simulation returns a stress value of $29\,065\,181 \text{ Pa}$. The error is calculated to be $1 - (29\,064\,954) \cdot (29\,065\,181)^{-1} = 0.00000779 \cdot 100 = 0.000779\%$. This percentage is negligible, hence the simulation is verified. The verification results and values are summarised in [Table 9.8](#).

Table 9.8: Theoretical and numerical values with associated errors

Induced stress	Script output [MPa]	Theoretical value [MPa]	Error in %
Bending stress	8,490,852	8,490,852	0
Centrifugal stress	20,574,329.17	20,574,329.15	$1 \cdot 10^{-7}$
Von Mises stress	29,065,181	29,064,954	$7.79 \cdot 10^{-4}$

The errors presented in [Table 9.8](#) are rather small. This can be explained by considering that the *SectionProperties* Python module uses almost the exact same equations as the theoretical approach. The negligible small errors can be blamed on rounded arithmetic implemented in computers.

Validation

Programme validation is performed by comparing the current structural loading and calculation to a previously performed research by *Y.A.P. Teeuwen* [67]. This thesis was successfully defended at the Technical University of Delft. Hence, its content can be considered valid. The aforementioned research focuses on Propeller Design for Conceptual Turboprop Aircraft. Although the specifics, such as engine and aircraft type, might differ, confirming the propeller's structural integrity was performed in a similar manner. The aforementioned thesis considers a similar load case as the simulation software described in [section 9.6](#), with the addition of the centrifugal moment. Similarly, the blade has been divided into a number of sections which all experience their own load. This research justifies the observation that maximum stresses are experienced at the blade root. Additionally, as the thesis uses the exact same equations for stress calculations, the structural simulation discussed in this report is correct. Therefore, the simulation software can be assumed to be validated.

9.6.6. Programme limitations

The main limitations of the numerical model are:

- The airfoil is modelled as a rectangular box, in actuality the geometry and with that moments of Inertia are different
- The calculations do not include fatigue cycles
- The centrifugal moment is neglected
- Vibrations are not assessed

The aforementioned limitations immediately provide potential points of improvement for future versions of the simulation software.

9.7. Conclusion

The purpose of the propeller design was to find a propeller configuration which meets all requirements whilst providing a significantly high efficiency. A number of design options have been considered. Especially the airfoil choice along the blade in spanwise direction proved to provide substantial efficiency gains. The simulation software CRotor and XFLR5 were used to determine airfoil and propeller performance, respectively. Eventually a contra-rotating, variable pitch, variable RPM propeller system was configured which meets all requirements. The forward- and aft-propeller main geometrical characteristics and airfoil distribution are displayed in [Tables 9.9](#) and [Table 9.10](#). Additionally, the propeller is visualised in [Figure 9.29](#).

Table 9.9: Propeller geometrical characteristics

Variable	Forward propeller	Aft propeller
Number of blades [-]	3	3
Radius [m]	1.75	1.75
RPM 5-11 km [-]	1 000	1 000
RPM 0-4 km [-]	1 400	1 400
Efficiency [%]	80	92.6

Table 9.10: The airfoil distribution along the propeller blade in spanwise direction

r/R	Airfoil
0.000 - 0.274	MH112mod
0.274 - 0.400	MH113mod
0.400 - 0.580	MH114mod
0.580 - 0.770	MH115mod
0.770 - 0.988	MH117mod
0.988 - 1.00	MH120mod

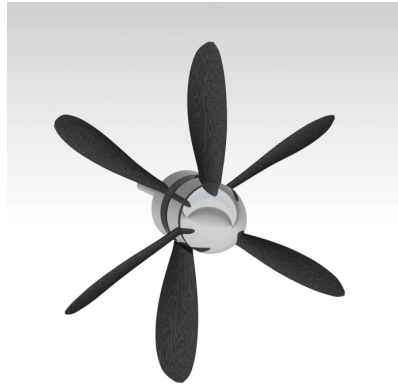


Figure 9.29: A CATIA render of the propeller

As determined by a statistical mass estimation, the entire propeller system mass will be 172.4 kg. The propeller blade's structural integrity has been confirmed by a newly designed structural simulation. The simulation indicated that the use of Standard Carbon Fibre provided a lightweight solution. Additionally, by using a boundary layer ingestion configured propeller, 200 kW of power is recycled from the fuselage wake energy. This provides a significant efficiency gain which means the propeller provides the same amount of thrust with a lower shaft power input. This efficiency gain has not been taken into account in [Table 9.9](#).

9.8. Recommendations

Due to limited resources and time, a number of assumptions and simplifications has been made during the propeller design phase. Some of these limitations are discussed, such as those of the structural model and the constant velocity inlet used in CROTOR instead of a velocity profile. These limitations immediately provide a basis for an improved design process. A more advanced analysis tool will significantly increase the reliability of the design. Also, a more advanced structural analysis simulation might decrease the propeller weight. Specific design aspects that were touched upon but not further examined include the implementation of sweep. Sweep would greatly increase the operating Mach number that can be achieved. Additionally, configuring two different radii for the forward and aft propeller should be evaluated and considered.

Fuel System Design

In order for the engine to function on hydrogen due diligence is required to design a fuel system that allows for storage of the hydrogen and that lays out the infrastructure that distributes the fuel to the combustion chamber. For the A320appu, a cryogenic pressure vessel that stores liquid hydrogen was found as the optimal solution.

In this chapter, the numerical model in [section 10.1](#) for tank design and the input properties in [section 10.2](#) are initially described to introduce the subject. This is followed up by the description of the the designed fuel tank, starting with the thermal design, [section 10.3](#), then the mechanical design, [section 10.4](#), and geometric design, [section 10.5](#). Furthermore the connection between the storage and the engine is described in fuel distribution system, [section 10.6](#), which includes the pipes, pump and the heat exchanger designs. In continuation, sections discussing the performed sensitivity analyses , verification and validation methods are [section 10.7](#) and [section 10.8](#), respectively. Finally a conclusion, [section 10.9](#), for the fuel system and recommendations, [section 10.10](#), are given to wrap up the chapter with a discussion.

10.1. Numerical model

This section provides a brief overview of the design logic and the code used during tank design. As presented in [Figure 10.1](#) the four main input data are hydrogen mass, venting pressure, temperature, and outer radius. In addition, each section has its own parameters which may be tweaked easily if necessary. The final output is the tank geometry.

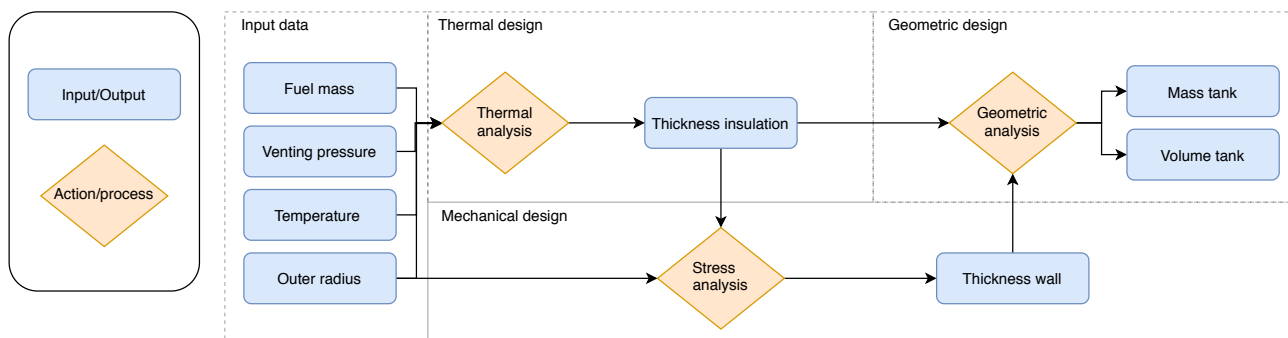


Figure 10.1: Hydrogen tank code flow chart.

First, the tank is analysed on thermal performance. Here, it is assumed that the inner and outer wall have negligible contribution to the total thermal resistance network due to high conductivity. This assumption avoids an iterative process where the thermal design is dependent on the mechanical design and vice versa. Furthermore, there are many different configurations that can meet the boil-off requirement. Therefore, instead of designing the insulation system based on the requirement, a tool has been developed to verify the requirement for an arbitrary insulation system. As output, the thermal analysis provides a valid insulation system as output with its known thickness. Secondly, the stress analysis is performed with the insulation thickness and outer radius as input variables. The load cases determine the thickness needed to support the hydrogen tank. Also, fatigue loading cycles have been taken into account in the tank wall design. As a result, the total wall thickness and configuration is found. Finally, the outputs of the stress and thermal analysis are used to generate geometric properties of the tank. The code is designed such that the volume requirement for LH_2 is always met. Consequently, the length of the tank extends when the thickness of the wall increases. Hence, the mass, volume, and length of the tank are affected. The new geometry is then checked on whether it fits in the aft cargo hold.

10.2. Input data

There are four main input parameters for the numerical code: fuel mass m_{H_2} , venting pressure p_{vent} , temperature T_{amb} and T_{H_2} , and the outer radius r_o . The hydrogen fuel mass follows from the 400 kg requirement needed for propulsion and power generation. Consequently, the tank volume can be calculated after determining the density at the venting pressure for which Equation 10.1 is used. The part containing p_{vent} in the brackets comes from regression analysis using values in Table 10.1. All other values have been provided here as well. The venting pressure is simply a design choice and was set to 3 bar. Furthermore, the starting pressure, p_o , was found to be 1.72 bar [42]. For the tank walls, an ambient pressure at 3 km altitude was used to get a cabin pressure equivalent to be used as a reference to calculate the pressure differential that the outer tank wall experiences, such that $p_{amb@3km} = 70\,109\,Pa^1$. In Equation 10.1, p_{vent} must be converted to bar. With ρ_{mean} the required tank volume can be determined and is equal to $V_t = m_{H_2}/\rho_{mean} = 6.24\,m^3$.

$$\rho_{mean} = (\phi_{LH_2} \cdot \rho_{LH_2} + (1 - \phi_{LH_2})\rho_{GH_2}) \cdot (-0.034p_{vent} + 1.03) \quad (10.1)$$

One of the two main requirements for the fuel system regards the energy content of the APPU system versus the A320neo. **FTD-Sys-21**: The amount of energy stored in H2 shall not exceed 15% of the energy content in kerosene. The energy content could be checked by calculating the energy stored in the 19 tonnes of kerosene and the 0.4 tonnes of hydrogen. This gives the energy content E_{H_2} of the hydrogen as stated in Equation 10.2. With this checked, requirement **FTD-Sys-21** has been met.

$$E_{H_2} = \frac{119.87[\text{MJ/kg}] \cdot 400[\text{kg}]}{119.87[\text{MJ/kg}] \cdot 400[\text{kg}] + 43.2[\text{MJ/kg}] \cdot 19000[\text{kg}]} = 5.52\% \quad (10.2)$$

Table 10.2: Input values of the tank design model

Table 10.1: Parameters and values for the mean density calculation [65].

P_vent [bar]	Mean Density	Parameters	Value
1.0	1.000	ϕ_{LH_2} [-]	0.97
2.0	0.950	ρ_{LH_2} [kg/m ³]	70.9
3.0	0.915	ρ_{GH_2} [kg/m ³]	0.09
4.0	0.89	p_{vent} [Pa]	$3 \cdot 10^{-5}$
5.0	0.86	ρ_{mean} [kg/m ³]	64.1

Input data	Value
m_{H_2} [kg]	400
ρ_{mean} [kg/m ³]	64.1
volume [m ³]	6.24
T_{amb} [°C]	45
T_{H_2} [°C]	-252.87
p_{vent} [Bar]	3.0
p_o [Bar]	1.72
$p_{amb@3km}$ [Bar]	0.70108

Furthermore, T_{amb} follows from requirement **FTD-Sys-23** where an ambient temperature of 45°C is stated. For T_{LH_2} , it is assumed that it starts at the boiling temperature of liquid hydrogen which is $T_{LH_2} = -252.87^\circ\text{C}$. Finally, the outer radius has been determined based on the height of the cargo hold discussed in chapter 3. Some margin has been taken into account and therefore the outer diameter is slightly less than 1 243 mm. In summary, the input values are presented in Table 10.2.

10.3. Thermal design

The purpose of this section is to assess the thermal performance of the insulation system. In aircraft applications it is required to store liquid hydrogen for longer periods of time. Therefore, an effective and lightweight insulation must be designed. The numerical model used to determine the thermal performance is heavily dependent on the input data discussed in section 10.2. As output this section provides an insulation system that meets the 48 hours boil-off requirement.

10.3.1. Boil-off requirement

The requirement for boil-off, one of the major concerns in LH₂ tanks, is driving in the design of the hydrogen tank. Extensive research has been done and is currently on-going in improving the thermal performance of cryogenic tanks. In this report, the definition of the boil-off time is the time at which the hydrogen tank must be vented. The internal pressure will rise due to heat leakage until it is stabilised by a pressure relief system. As mentioned in section 10.2, the tank is designed to withstand an internal pressure of 3 bar, hence, $p_{vent} = 300\,000\,Pa$. Another function of the tank is to store 400 kg of hydrogen. Therefore, requirement **FTD-Sys-23** may be rephrased to: *The tank shall store 400 kg of liquid hydrogen at an ambient temperature of 45°C for 48 hours without reaching the venting pressure of 300 000 Pa.*

¹<https://www.mide.com/air-pressure-at-altitude-calculator>, date retrieved 02-06-2020

10.3.2. Model assumptions

A number of assumptions are listed below for the thermal analysis of the hydrogen tank. Furthermore, the elliptical tank configuration 2 in section 3.3 has been replaced by a cylindrical shape in order to decrease complexity.

- *Steady state heat transfer is assumed.* Hence, the insulation system may be over designed since heat flow will reduce for a lower temperature difference.
- *Thermal performance is assessed in 1D.* The temperature varies radially.
- *Temperature is assumed constant and uniform across the 1D analysis.* In reality, there will be a gradient.
- *The spheroid is modelled as a perfect sphere.* Consequently, uncertainties are introduced due to the difference of between the areas of these shapes.
- *Calculations are based on solid conduction only.* However, a 10% increase in heat transfer is used to take into account the effects of radiation.
- *Inner and outer structural wall, which are made of high conductivity material, are assumed to have negligible contribution to the total thermal resistance network.* This mostly affects the radial position of the insulation system which produces slight different results.

10.3.3. Heat transfer

For the thermal design, radiation is not omitted and therefore a 10% increase in heat transfer rate is taken into account, noted by $f_{rad} = 1.1$. As stated by Fourier's law of heat conduction, the rate at which heat is transferred through a material depends on the temperature difference, geometry of the tank, and the thermal properties of the material [38]. In essence, it is proportional to the thermal potential difference divided by the thermal resistance imposed by the material through which the heat flows. If these properties are known, a model can be created that approximates the environment in which the hydrogen tank operates.

It is assumed that the internal temperature of the tank starts at the boiling temperature of hydrogen, T_{H_2} , and that the tank is subjected to an ambient temperature, T_{air} . In terms of geometry, the tank consists of a cylinder with two (half) spheroids at both ends. However, for the thermal analysis it is assumed that the caps are both perfect spheres as mentioned in subsection 10.3.2. Furthermore, the thermal properties are dependent on the type of material used for the wall and insulation. A schematic of the problem can be viewed in Figure 10.2. For a one dimensional case the problem is simplified to Equation 10.3 and Equation 10.5 for both the cylindrical and the spherical shape. The total heat flow is then the sum of the heat flow through the two shapes as shown in Equation 10.7 [38]. Furthermore, h_i (LH₂) and h_o (air) are 1000^2 and 5^3 W/m²K.

$$q_{cyl} = -\frac{kA}{\Delta x} \Delta T = \frac{(T_{air} - T_{H_2}) \cdot f_{rad}}{Rth_{cyl}} \quad (10.3) \quad Rth_{cyl} = \frac{1}{h_i A_c} + \frac{1}{2\pi L_{cyl}} \sum_{i=1}^n \frac{\ln(r_{i+1}/r_i)}{k_i} + \frac{1}{h_o A_c} \quad (10.4)$$

$$q_{sph} = -\frac{kA}{\Delta x} \Delta T = \frac{(T_{air} - T_{H_2}) \cdot f_{rad}}{Rth_{sph}} \quad (10.5) \quad Rth_{sph} = \frac{1}{h_i A_c} + \frac{1}{4\pi} \sum_{i=1}^n \frac{1}{k_i} \left(\frac{1}{r_i} - \frac{1}{r_{i+1}} \right) + \frac{1}{h_o A_s} \quad (10.6)$$

$$q_{tot} = q_{cyl} + q_{sph} = \frac{(T_{air} - T_{H_2}) \cdot f_{rad}}{Rth_{tot}} \quad (10.7) \quad Rth_{tot} = \left(\frac{1}{Rth_{cyl}} + \frac{1}{Rth_{sph}} \right)^{-1} \quad (10.8)$$

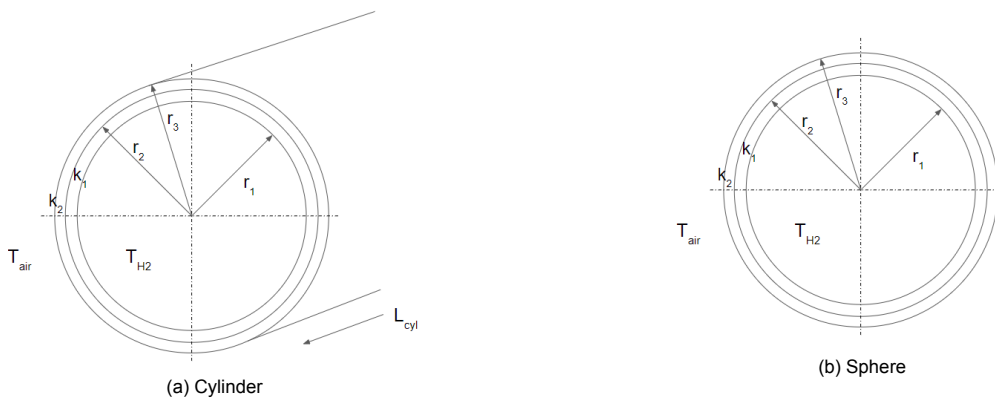


Figure 10.2: The cylindrical and spherical shapes of the tank.

²https://www.researchgate.net/publication/282555385_Film_Boiling_Heat_Transfer_Properties_of_Liquid_Hydrogen_in_Natural_Convection

³<https://www.sciencedirect.com/topics/engineering/convection-heat-transfer-coefficient>

Both q_{cyl} and q_{sph} are dependent on the internal temperature of the tank which varies when reaching the venting pressure. However, the start temperature is set to the boiling point of LH_2 . Due to this condition, the hydrogen tank finds itself in the liquid to vapour phase change. It is assumed that the temperature stays constant and that only the entropy of the system changes due to incoming heat flow. Therefore, the system is regarded at steady state, that is, the heat flow does not change over time.

10.3.4. Insulation

In this section, the design of the insulation system is explained which is essential for cryogenic storage applications. As discussed in Mital's review on hydrogen tanks [46], an insulation system has to be designed for four critical functions, which have been listed below.

1. The insulation system must minimise boil-off while keeping additional mass to a minimum.
2. The insulation system must prevent atmospheric gasses to condensate and solidify onto the tank.
3. The insulation system must not fail due to cyclic loading of LH_2 .
4. The insulation system must have low thermal conductivity and low density.

A lower thermal conductivity results in a higher thermal resistance as seen in Equation 10.4 and Equation 10.6. As a result, the heat flow through the material can be reduced based on Equation 10.3 and Equation 10.5. Figure 10.3 gives an overview of different materials that may be selected. First, a material is selected based on low conductivity and density from Figure 10.3a as mentioned in the list of functions. It can be seen that Flexible Polymer foam and Aerogel are suitable materials for insulation purposes while keeping in mind that the density of Aerogel is a magnitude bigger. However, their thermal distortion must be considered as well to avoid high induced stresses due to cyclic loading of LH_2 . When observing Figure 10.3b, Aerogel has a lower thermal expansion coefficient compared to Flexible Polymer Foams. Therefore, Flexible Polymer Foams perform better in terms of density but worse when looking at thermal expansion.

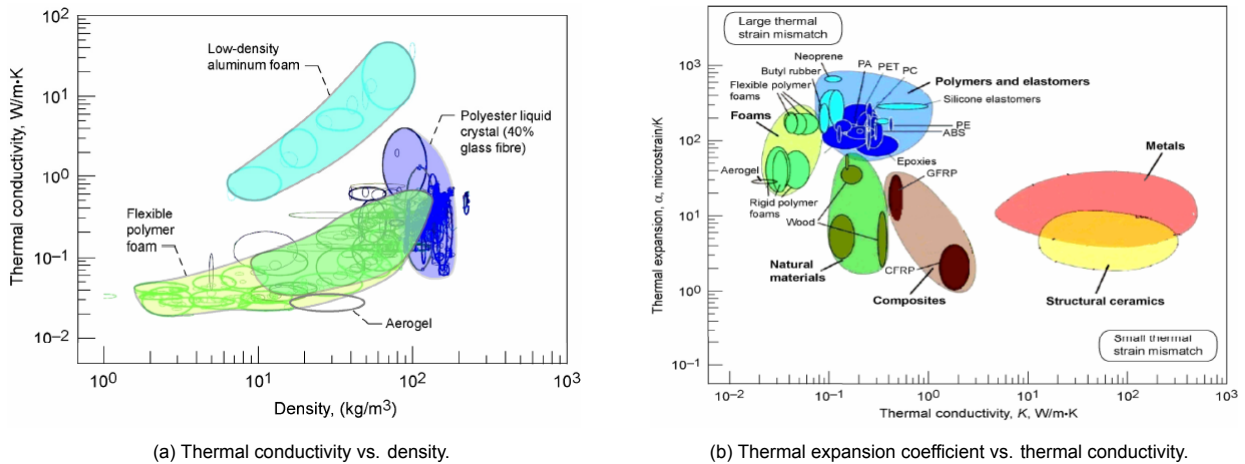


Figure 10.3: Overview of materials for insulation design [4].

The internal pressure is related with Equation 10.9 where $\rho^* = \rho_g / (\rho_g - \rho_l)$ [65]. This is based on a model suggested by Lin et al. [42]. However, because requirement **FTD-Sys-23** applies to a tank without mass leaving the system, $\dot{m}_{out} = 0 \text{ kg/s}$. Thus, Equation 10.9 may be rewritten to Equation 10.10 in order to find a first estimate on the heat transfer rate through the insulation system. Here, t_{req} is in fact the required boil-off time and p_{des} the venting pressure which is the maximum allowable pressure that the tank may be exposed to before it is vented. A first preliminary value for q_{des} in Equation 10.11 is found for a specific number of parameters. Note that the energy derivative, $\phi = [\rho(\partial u / \partial p)_\rho]^{-1}$. This means that in case the tank wall lets through more than 92.45 W the boil-off requirement is not met.

$$\frac{dp}{dt} = \frac{1}{V_t} \left[\rho \left(\frac{\partial u}{\partial p} \right)_\rho \right]^{-1} [\dot{Q} - \dot{m}_{out} \Delta h_v (x + \rho^*)] \quad (10.9)$$

$$q_{des} = \dot{Q} = \frac{V_t p_{des} - p_o}{\phi t_{req}} \quad (10.10)$$

$$q_{des} = f(V_t, \phi, p_o, p_{des}, t_{req}) = f(6.24, 0.05, 1.72 \cdot 10^5, 3.0 \cdot 10^5, 172800) = 92.45 \text{ W} \quad (10.11)$$

Different configurations have been tried to find a heat transfer rate which is lower than the maximum allowable heat flow q_{des} . The thermal performance of flexible polymer foam and Aerogel are investigated. This has

been done by varying their thicknesses in the thermal resistance network. Two layers, each 5 mm thick and of the same material were considered. It is known that the thermal conductivity of a material depends on the temperature in which it operates. Different values could be found for Aerogel which were $10.0 \cdot 10^{-3}$ at 78K and $13.0 \cdot 10^{-3}$ at 220K [22]. However, different values for the thermal conductivity of foam could not be found. However, having the same k-values resulted in very similar numbers and therefore it was deemed sufficiently accurate for the purpose of this analysis.

The values for r_i and r_{i+1} in Equation 10.4 and Equation 10.6 change depending on the thickness. In Figure 10.4, the thickness represents the total thickness of the tank wall in millimetres. In case only Foam or Aerogel is used, there does not exist a combination of thermal conductivity and thickness that has sufficient thermal resistance to let through a heat flow lower than $q_{des} = 92.45 \text{ W}$. The lowest heat flow values for foam and Aerogel are 1 278 W and 680.1 W, respectively. Here, the overall thermal conductivity of the foam is $21.0 \cdot 10^{-3}$ [7]. Furthermore, the lowest heat flow value may be achieved for a thickness close to 240 and 250 mm which results in a tank length longer than the available 9.8 m, including the bulk cargo, in the A320neo [1]. Thus, it is concluded that only using foam or Aerogel is not sufficient for the design of the insulation system. For this reason, an additional insulation layer must be added that has lower thermal conductivity properties.

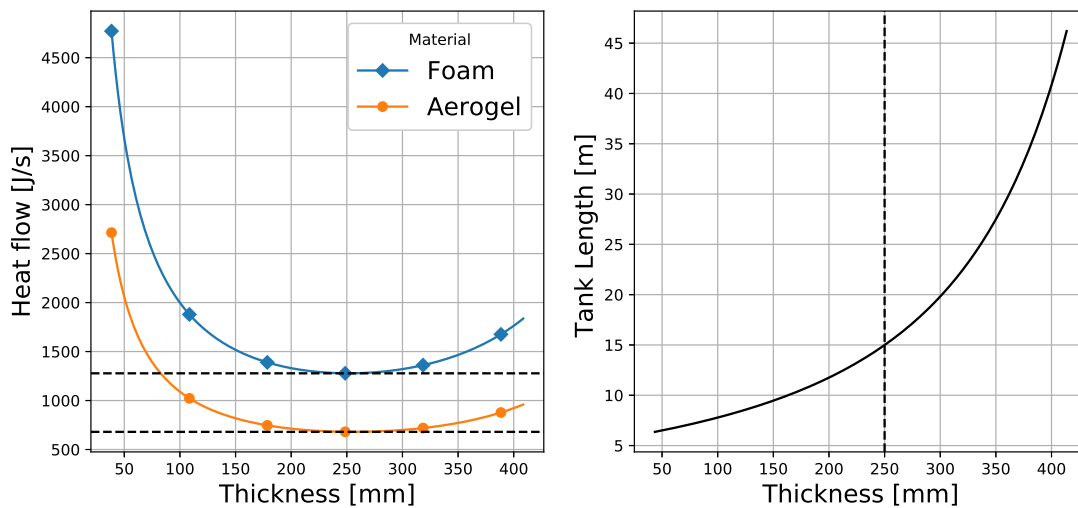


Figure 10.4: Heat flow and tank length due to thickness of foam & Aerogel material.

Multilayer insulation

Often essential for cryogenic applications are multilayer insulation (MLI) systems which can achieve much lower thermal conductivities compared to flexible polymer foam or Aerogel [46]. For this reason, the possibilities of adding an MLI system into the total insulation design has been investigated. MLI systems consist of a spacer and a reflector stacked upon each other. The spacer is often made of a thin fibreglass, polyester, silk, or plastic layer. On the other hand, the reflector is made of Mylar or Aluminium foil with a thickness of 6-7 μm . Furthermore, MLI systems perform best in high vacuum (HV) conditions, but can also operate in soft vacuum with higher thermal conductivity. J.E. Fesmire, from the *Cryogenics Test Laboratory at the Kennedy Space Center*, presented in his paper a number of MLI systems including its properties [31]. The tests were performed for boundary temperatures between 78K and 293K using a cylindrical calorimeter. For one of the configurations, the results have been summarised in Table 10.3 for a 15.5 mm thick MLI system.

Table 10.3: Properties of a 15.5 mm Mylar/Net (15.5, 40, 2.6) multilayer insulation system [31].

CVP [millitorr]	WBT [K]	K_e [mW/m K]
0.02	293	0.031
0.1	293	0.040
1.0	293	0.072
10	293	0.469
100	293	3.24
1040	293	8.08

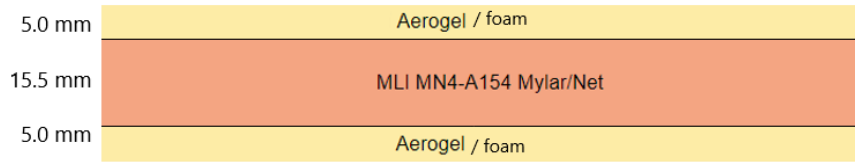


Figure 10.5: Preliminary schematic of the insulation system.

The thermal conductivities shown in Table 10.3 were used to calculate the performance of the total insulation system presented in Figure 10.5. Here, the two layers may either be made of foam or Aerogel. The results for Aerogel are plotted in Figure 10.6. Since the only difference for this analysis is the thermal conductivity, same results have been found in case foam is used. Their difference is negligible because the thermal performance is mostly determined by the MLI system. The bold black line shows the 48 hour requirement of hydrogen storage without boil-off. Furthermore, graphs have been plotted using Equation 10.12 which is a combination of Equation 10.7 and Equation 10.10 to find the boil-off time. All parameters stay constant except for the thermal resistance, R_{th} , which changes for different thicknesses and conductivities. However, even though these combinations are presented, one can only be certain of the performance at a 15.5 mm thickness obtained from Fesmire’s paper [31]. This is shown in Figure 10.6 by the horizontal dotted line.

One of the disadvantages of using an MLI system is that high vacuum must be maintained in order to preserve the thermal performance of the system. Therefore, when designing the MLI system, it is desirable to increase the vacuum pressure as much as possible for a certain insulation thickness. Hence, the additional line for $k = 17.2 \cdot 10^{-5} \text{ W/mK}$ allows an increase in thermal conductivity until it reaches the boil-off time requirement. This point is chosen such that the boil-off time of the total insulation system takes into account a 10% safety factor over the 48 hours requirement. In case the MLI system can be designed such that it has $k = 17.2 \cdot 10^{-5} \text{ W/mK}$, the boil-off time of the system becomes 52.8 hours.

$$t_{boil} = \frac{p_{des} - p_o}{T_{air} - T_{H_2}} \frac{R_{th} \cdot V_t}{\Delta U \cdot f_{rad}} \tag{10.12}$$

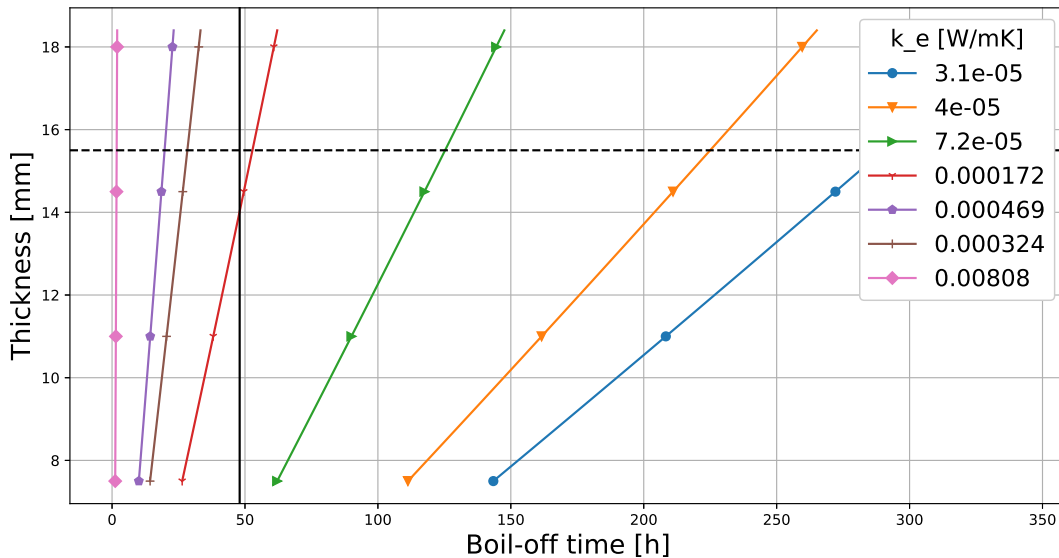


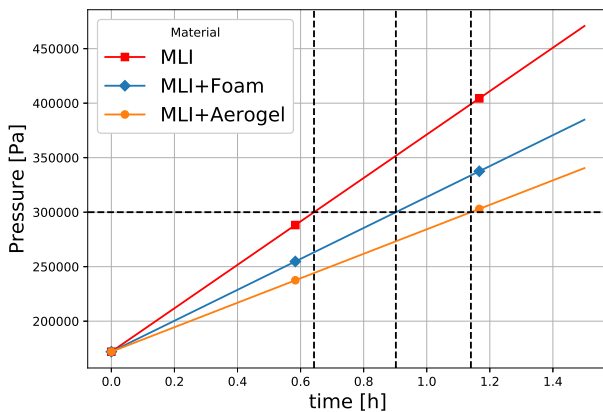
Figure 10.6: Performance of total insulation system for different MLI thermal conductivities plotted in a thickness vs. boil-off time diagram.

10.3.5. Flexible polymer foam vs. Aerogel

Both flexible polymer foam and Aerogel may be used to protect the MLI system and to safeguard the tank in case of vacuum loss within the MLI system. However, based on weight, safety, and cost only one is chosen for the insulation system. First, it was found that the thermal conductivity of MLI increases to $17.5 \cdot 10^{-3} \text{ W/mK}$ upon loss of high vacuum. This value corresponds to a CVP of 768 585 *millitorr* (102 470 *Pa*) [31]. Therefore, the model is changed to this new k -value to analyse the thermal performance. The results are presented in

Figure 10.7. Here, the insulation systems containing MLI with either foam or Aerogel are compared with each other. The lowest available thickness of Aerogel is 5 mm [30] and the same is chosen for foam for comparison. From Figure 10.7 it is concluded that the combination of MLI and Aerogel perform best in terms of boil-off time. The additional two layers of Aerogel extend the time from 0.64 to 1.14 hours, an increase of 77.4%. In case of foam, it is increased from 0.64 to 0.9 hours which is 40.4%. Thus, in terms of boil-off time Aerogel performs better.

The total mass of the tank wall for either foam or Aerogel is calculated as well. In Table 10.4, the densities of the different materials have been provided for this calculation. The density of Aerogel is roughly 3x more compared to Foam. Therefore, the tank will have more mass. However, with respect to the total mass this is expected to be a small increase in percentage. Since this difference is small it is justifiable to choose Aerogel for its lower thermal conductivity.



Material	ρ [kg/m ³]	t [mm]
Aerogel	91	5 (2x)
MLI	53	15.5
Foam	32	5 (2x)

Table 10.4: Insulation system material properties.

Figure 10.7: Duration in reaching venting pressure upon performance loss in MLI system.

10.3.6. Thermal design output

The output of the thermal performance analysis is a 25.5 mm thick insulation system that consists of three layers. The multilayer insulation system is surrounded by two layers of Aerogel each 5 mm thick as shown in Figure 10.8. In terms of thermal performance, the designed insulation system is able to store 400 kg of hydrogen for 52.8 hours without boil-off which is 10% more than the required boil-off time of 48 hours. However, it is slightly over designed according to the numerical model to take into account any discrepancies and uncertainties. Risk HT-03 Passive cooling is insufficient for 48 hours of safe storage from Table 7.1 is mitigated by having the 10% contingency in the insulation layer. Furthermore, upon performance loss of the MLI the insulation system is able to store the hydrogen for 1.14 hours without having to initiate the pressure relief system.

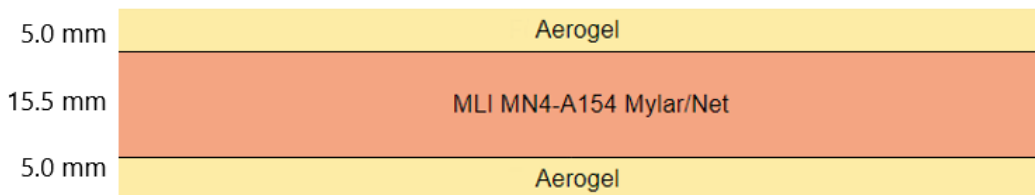


Figure 10.8: Final insulation system of the hydrogen tank.

10.4. Mechanical design

The mechanical design is based on extensive literature that exists for pressure vessel design in conjunction with sources that are focused on the aircraft applications and concepts for enabling cryogenic storage of liquid hydrogen. Four steps were performed for the mechanical analysis:

1. Identify the functions of the structure and define its load cases
2. Investigate and utilise pressure vessel design rules
3. Verify design thickness for limiting allowable stress dictated by load cases
 - Fatigue assessment for cyclic loading

4. Examine structural and material interfaces

- Temperature effects
- Sloshing
- Support structure

The tank design structure consists of an outer tank wall, insulation layers and an inner tank wall. Each layer has its own function and purpose. The outer tank wall serves as a fairing that keeps the layers intact and protects it from outside loads. The insulation layers address the heat flow in to the system. Lastly, the inner tank wall addresses the cyclic loading due to pressure and temperature.

A reference value for the allowed stress is $\sigma_{allowed} = \sigma_Y \cdot e_w$ [49], where the joint efficiency was taken as a 0.7 value for a metal tank wall. For current analysis the safety factor (SF) was set at 1.5 in order to accommodate a burst or proof pressure of 1.5 times the venting pressure, the set internal pressure for which the pressure vessel is designed, resulting in an allowable design stress $\sigma_{allowed} = \sigma_Y \cdot 0.67$. The safety factor could be adjusted if the tank design will be made more of a higher complexity or experimental data of the materials or structures is lacking to make proper judgement of a optimal safety factor before the product is appropriately tested. The approach for each of the steps are discussed briefly in the respective sections and a summary Table 10.5 is provided in the overall fuel tank design section to display the in and outputs that are used in the mechanical model.

Table 10.5: Inputs and outputs of mechanical analysis

	Δp [bar]	r [mm]	σ_a [MPa]	E [GPa]	Minimum, t [mm]	Producible, t [mm]
Outer tank wall	1.3	609.5	N/A	$E1 = 18.4;$	2.2	2.0
	1.3	609.5	N/A	$E2 = 36.7$	2.2	2.0
Inner tank wall	3.0	581.8	$\sigma_Y/SF = 193;$	72	2.3	3.0
	3.0	581.8	$\sigma_f = 64$	72	2.7	3.0

Description inputs and outputs table

In the table the different input parameters for the design rule equations and the fatigue design hoop stress equations are provided. The results of this are in the column describing minimum thickness. The producible thickness denotes a rounded off thickness to account for manufacturability and small defects and imperfections introduced during production. Note that for the composite outer wall this thickness has been downscaled instead of upscaled. This has to do with the outer fairing primarily existing as a outer layer for protection and that it is inherently slightly oversized to carry the delta pressure of 1.3 bar. The outer wall in particular normally is a stiffened panel and thus will decrease in thickness and mass during further iterations, with additional geometry added to counter critical buckling stresses as primary design load case [3]. In this case for simplifications the acquired thickness has been rounded down to 2.0 mm.

10.4.1. Load cases

First and foremost the boundary conditions for which the mechanical design will bring stiffness and stability to the fuel tank have to be analysed.

Applying standard pressure vessel design methodologies will work to an extent, though it does not necessarily take into account a tank which is designed to be mobile - it will experience acceleration loads due to movements of the aircraft -and will to some degree have a changing environment. To make sure the fuel tank will act in even the most extreme cases, the structure needs to be proven for various load cases. Concisely this means that for any of these load cases the pressure vessel will not deform plastically or lose its function in some way when applying any of the worst case, extreme loads. This can be summarised in an equation where all stresses due to external forces, temperature stresses and stresses due to pressure differentials need to be lower than the material's specific ultimate stress by safety factors K_i and for the allowable stresses by safety factor SF.

$$K_1 \cdot \sigma_{external} + K_2 \cdot \sigma_{thermal} + K_3 \cdot \sigma_{pressure} \leq SF \cdot \sigma_{allowed} \leq \sigma_{ult} \quad (10.13)$$

As a basis for the load cases that are valid for the pressure vessel, primarily a study on cryogenic pressure vessel design criteria for aerospace applications by NASA in 2007 has been taken as a reference. An overview of these load cases are summarised in the table below.

Table 10.6: Load cases of the mechanical analysis

Load case	Value	Note
Nominal acceleration load [N]	2 025	$(m_{tank} + m_{fuel}) \cdot 0.3 \cdot g$
Extreme acceleration load [N]	30 379	$(m_{tank} + m_{fuel}) \cdot 4.5 \cdot g$
Internal pressure inner tank wall [Pa]	300 000	p_{vent}
Δp outer tank wall [Pa]	129 900	$(p_{vent} - 1 \cdot 10^5) - p_{amb@3km}$
ΔT inner tank wall [°C]	297.87	$T_{amb} - T_{H2}$

Primarily important here is the load case for the pressure differential over the tank wall and the cyclic loading due to the tank being drained of its fuel after most of its flights during operation. The pressure loading is what drives the design of the tank walls. For the inner tank wall it is the internal pressure and for the outer tank wall buckling due to outer pressure. [3] The design of the support structure is driven by the acceleration loads that act on the fuel tank. The total analysis of these load cases could not be achieved in the timespan of the DSE project. Instead focus is put in the cyclic loading that drive the tank wall design such that a tank design could be derived and an initial sizing for the fuel system could be made.

10.4.2. Design rule equations

A series of assumptions and simplifications had to be made such that a first iteration of the mechanical design could be performed:

- The structure experiences a biaxial stress field
- The tank is a cylindrical vessel with ellipsoidal endcaps of a 2:1 ratio
- A thin walled approximation is applied; the thickness of the cross section is less than 10% of the radius of the cross section.
- Weld efficiency is 0.70, the lower bound limit
- The inner and outer tank wall are unstiffened panels
- No connecting rod is implemented between the inner and outer tank walls
- The structure does not include nozzles or small openings
- Insulation does not carry any loads
- Insulation layers do not exercise a pressure drop of vacuum near to the boundary of the outer tank wall, instead a approximate pressure drop of one bar is used to model the pressure differential between the tank walls.

The material choices that have been made for the analysis are derived from literature. For the inner tank wall Al2219 is referenced to be an optimal choice [13]. Next to that, for the composite outer tank wall it is advised to use a carbon-epoxy material [3]. All material properties are taken from the aerospace materials database of the Granta Design CES EduPack software [63]. For aluminium-2219 this database was restricted to Al2219-T185 and for the carbon-epoxy laminate an altered High Strength Epoxy/HS carbon fibre unidirectional prepreg is used for the analysis in a one to two ratio of plies in 0 and 90 degrees angle, respectively, by applying the rule of mixtures.

Inner tank wall

The thickness t of the pressure vessel skin is calculated from the thin walled hoop stress, Equation 10.14, in which the internal pressure of the tank is represented by P , r as the radius of the tank and σ_θ is the hoop stress, the normal stress in circumferential/tangential direction. The axial stress in longitudinal stresses is half the size of the hoop stress and is therefore not a limiting factor for the design thickness for the thickness of a cylinder. Note that for a sphere or ellipsoidal head the axial and tangential normal stresses are equal and both follow Equation 10.15.

$$t = \frac{p \cdot r}{\sigma_\theta} \quad (10.14)$$

$$t = \frac{p \cdot r}{2 \cdot \sigma_z} \quad (10.15)$$

For a more realistic result with respect to the general hoop stress equation, a modified equation derived from the American Society of Mechanical Engineers (ASME) Boiler and Pressure Vessel Code (BVPC) hoop stress formula for cylindrical shells has been used [13].

$$t_h = \frac{p_{des} \cdot d_0 \cdot K}{2 \cdot \sigma_a \cdot e_w + 2 \cdot p_{des} \cdot (K - 0.1)} \quad (10.16) \quad K = \frac{1}{6} \left[2 + \frac{a}{c} \right] \quad (10.17)$$

In this equation the parameters are the same as for the thin walled hoop stress Equation 10.14, with the exception of the joint or weld efficiency e_w and the constant K , which is typically a number between 0.7 and 1.0⁴. The

⁴<https://www.pveng.com/joint-efficiency/>, date retrieved: 02-06-2020

joint efficiency indicates the effect of the seam introduced in the manufacturing process of a metal pressure vessel, which introduces a stress concentration. A value of 0.7 is chosen such that a conservative thickness will be retrieved. The constant K value depends on the ratio of the major to minor axes of the ellipsoidal head geometry that is being considered. With a being the value of the semi-major axis of the ellipsoid and c the value for the semi-minor axis of the ellipsoid, in case of an oblate spheroid.

Outer tank wall

Class II pressure vessels design rules for cylindrical shells under uniform pressure have been used to design the composite fairing that forms the outer tank wall. The application of this equation asks for the tensile moduli in the biaxial directions, i.e. longitudinal and tangential (circumferential) directions: E_1 and E_2 [5]. The next two equations are modified stress equations for longitudinal and circumferential stresses and are stiffness based. This is illuminated in that the outer tank wall needs to be designed for stability for which stiffness is primarily important [3].

$$t_1 = \frac{p \cdot r}{2 \cdot (0.001 \cdot E_1)} \quad (10.18)$$

$$t_2 = \frac{p \cdot r}{0.001 \cdot E_2} \quad (10.19)$$

Analogous to the relation for hoop stresses in spherical shells under pressure, the ASME equivalent is as follows [5]:

$$t = \frac{p \cdot r}{2 \cdot (0.001 \cdot E_{1,2})} \quad (10.20)$$

These values are retrieved by using a laminate that has twice the amount of fibres in tangential than in longitudinal direction, such that the thickness is optimised for both directions for the respective normal stresses. This approach is performed only for preliminary analysis. In practice it is better to have additional plies (around 10% volume ratio of the laminate) in off-axis angles to account for additional stresses and to follow composite design guidelines [16]. For instance a [0, 45, -45, 90] laminate, with fibres oriented in biaxial angles but also intermediate (45,-45) angles could suffice. Additionally, locating 45 and -45 together with 90 degree angled plies toward the exterior surface of the laminate is beneficial for the allowable stress due to buckling. These are considerations that should be taken in the next design phase for the composite fairing [16].

10.4.3. Fatigue assessment

Subsequent loading cycles are carried by the inner tank wall which has a considerable impact on the life time of the fuel tank. Calculations on the static internal pressure do not incorporate the cyclic loading due to pressurisation cycles of the tank by repeatedly draining and filling the tank in its lifetime. Aircraft in the new generation of the A320 family are designed for $N = 60\,000$ cycles⁵. Due to maintenance difficulties of the current fuel tank design iteration and the related inability to remove the tank easily, the full life time of A320 family aircraft is what the inner tank wall has to be designed for. To attest this number for fatigue assessment, the cycles are multiplied by 8 to make a proper approximation of the fatigue life of the inner tank wall; resulting in $N_{life} = 0.48$ million cycles. This number 8 stems from the standard deviations of experimental data which are retrieved from aluminium alloy test specimens [56].

The stress life curve and its derived fatigue life curves are dependent on loading type and material properties. This already determines the shape of the stress life curve. The fatigue life curve is in addition also influenced by the properties of the structure that is investigated. To allow for adjusting the slope to retain a good approximation for the fatigue of the structure, division by the stress concentration factor K_t to account for critical, peak stresses is performed. In order to setup the fatigue life curves the ratio of the amplitude stresses has to be known and the limiting ultimate stress has to be identified such that the maximum fatigue stress can be properly defined. In addition the value of K_t has to be established to modify the slope between the upper and lower allowable stress limits. The upper limits of the stress life and the design fatigue life are the following relations:

$$\sigma_a = \sigma_{ult} \quad (10.21) \quad \sigma_a = \sigma_f \sim 0.32 \cdot \sigma_{ult} \quad (10.22)$$

The lower limits of the stress life and the design fatigue life are the the following relations:

$$\sigma_a = 0.5 \cdot \sigma_{ult} \quad (10.23) \quad \sigma_a = \sigma_f \sim \frac{0.32 \cdot \sigma_{ult}^2}{1.32 \cdot \sigma_{ult} \cdot K_t} \quad (10.24)$$

These empirical relations to obtain the minimum thickness for maximum fatigue stress are obtained from the book *Fatigue of Structures and Materials*, written by J. Schijve [56]. Since the tank is loaded from 0 to max, the

⁵<https://bit.ly/2Bk53YP>, retrieved on 17-06-2020

amplitude stress has factor $R = 0$ and the σ_a at the point for the fatigue design is twice the amplitude stress: $2 \cdot \sigma_a = \sigma_f$. Moreover, the tension-tension fatigue that the tank wall experiences results in $\sigma_{ult} = \sigma_Y$ being the critical stress that reaches σ_f , the stress at which the structure fails. The inner tank wall pressure vessel is modelled as a notched structure which introduces a peak stress factor of $K_t = 2.5$. [2]. This accounts for the peak stress at the crown of the ellipsoidal heads.

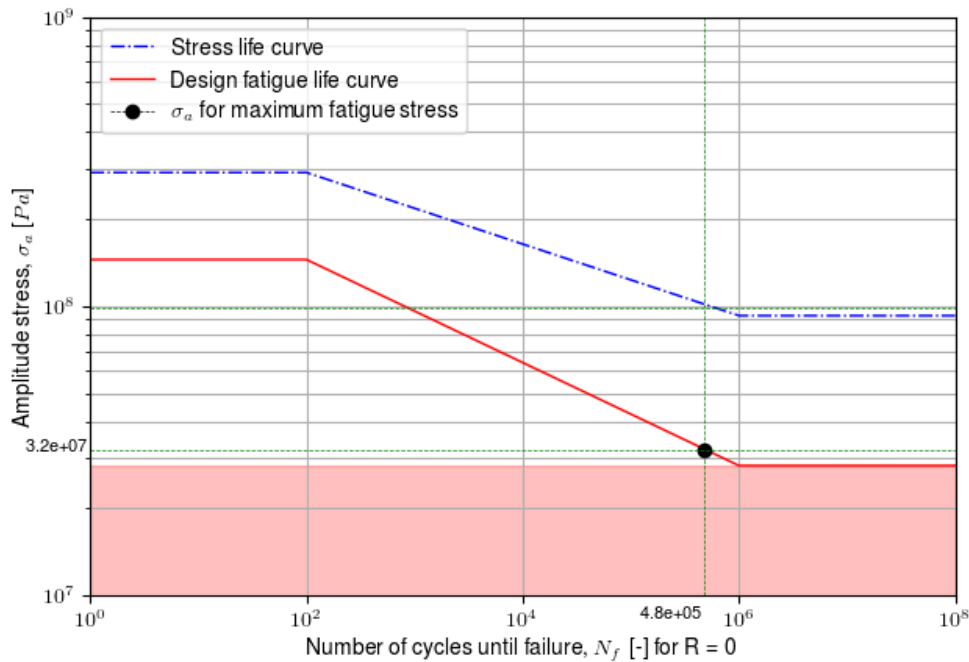


Figure 10.9: Fatigue life of a notched structure made of Al2219-T185

Finally from the fatigue life plot the σ_a at $N_{life} = 0.48$ million cycles can be read, which denotes a value of $\sigma_a = 32$ MPa; $\sigma_f = 2 \cdot \sigma_a = 64$ MPa. Thus failure due to cracks will be at a stress of 64 MPa.

$$t = \frac{p \cdot r}{\sigma_f} \quad (10.25)$$

In order to retrieve the related minimum thickness for maximum fatigue stress the hoop stress equation is used in Equation 10.25.

Liner

The fatigue design of the inner tank wall makes the inner tank wall design mechanically sound. What does need to be taken into account, still, is oxidation due to surface contact with hydrogen and hydrogen accumulation through the material. This can alter the material properties of the inner tank wall which reduces the fatigue life and the maximum fatigue stress.

A good solution to prevent such deteriorating phenomena is by installing a liner material as a chemical resistant barrier between the hydrogen and the tank wall surfaces. Another method might be to utilise a liner-less composite inner tank wall that has sufficient protection to function in cryogenic conditions. The latter has not been thoroughly tested yet in combination with liquid hydrogen and research is well underway. ⁶

10.4.4. Temperature effects

The temperature difference has a big influence on the material properties of a material of the inner tank wall. In cryogenic conditions specifically the yield strength of the material will increase, but also its brittleness. This could have negative implications for the ductility and the toughness of the material that has to be looked into. However, the chosen Al2219-T185 is an aluminium alloy which implicates that it does not have a ductile to brittle transition. It is a material suited for cryogenic conditions and will increase in fracture-toughness at a decreased temperature⁷. Thermal stresses that might be inflicted upon the structure due to thermal strain, however, has to be looked into, preferably by applying a FEM analysis of the whole structure.

⁶<https://www.compositesworld.com/articles/carbon-composite-liner-less-pressure-tank-handles-cryogenic-temps>, date accessed: 30-06-2020

⁷<http://www.totalmateria.com/Article23.htm>, retrieved on 22-06-2020

10.4.5. Sloshing

Sloshing is a principle which frequently occurs within liquid storage tanks when the liquid substance stored in the tank is subjected to external inputs or excitations. This results in a higher possibility of an increase in internal tank pressure, due to enhanced vaporisation or condensation of the liquid/gas interface. Eventually, this can result in unexpected increases or decreases in tank pressure for which it has not been designed, resulting in an increased possibility of accidents.

The principle of sloshing can only occur in partially filled tanks. When the shape of the storage tank, and the amount of fluid in it, is of sufficient magnitude, the large liquid movement also generates acute hydrodynamic stresses, which could then cause instabilities and a breakdown of the structure. To prevent this, research has been put into designing solutions to stop this unwanted behaviour of the fluid. This resulted in upgraded designs of tanks which include anti-sloshing baffles that prevent pipe intake from the abrupt fuel starvation. Anti-sloshing baffles make use of the principle of hydrodynamic resistance of geometries and shapes. By increasing the hydrodynamic resistance of a fluid, unwanted sloshing can be prevented.

Since normally, anti-sloshing baffles are designed using CFD programmes, the team decided to not put extra effort into the specific design and geometry of the baffles, and just mention the existence of the baffles within the tank. The team opted, for a number of porous baffles placed at equal spaced distances, for which the final fuel-flow over the porous baffle is equal to a maximum of two times the maximum fuel flow.

10.4.6. Support structure

The external loads due to acceleration of the fuel tank are carried by the support structure. Most important is that the support structure translates most loads to normal and shear stresses over a large contact area and avoids point loads, which will increase normal stresses due to bending. The tank is a cylindrical vessel which as opposed to a spherical design is more prone to bending stresses. Additionally the structure will not be part of the airframe. Instead it will be attached to a six point support structure which attaches to the airframe [14]. This enables the tank to be attached or detached to the airframe without the necessity to redesign the airframe or cargo compartment to fit the fuel tank.

10.5. Geometry

With the total thickness known the geometry of the tank is determined. This is done by first examining the cylindrical shape. This design is for the more detailed design extended with spherical heads and analysed for reference values. There are however concerns with perfect circular heads that will not experience the same strain for the same pressure compared to its cylindrical counterpart. This can be negated by having a different major to minor axis ratio that is bigger than one. A good ratio is two, 2:1, which already shows a more optimal deformation of the cylindrical section with respect to the end caps.

Because the mass requirement, hence volume, is fixed, any thickness added to the tank will result in extending the tank to maintain this number. This is the reason why this step is done the last as shown in the flow chart, Figure 10.1. The exact volume of both caps of the tank are known and therefore the volume needed in the cylinder is calculated using Equation 10.26, Equation 10.27, and Equation 10.28 where $r_i = r_o - t$ and c is the length of the oblate spheroid. So, output L_{cyl} depends on the thickness of the tank wall. This approach is only valid for a tank length of at least the size of the two endcaps. In short form: $l_{tank} \geq 2 \cdot r_o$.

$$V_{cylinder} = V_{LH2} - V_{spheroid} \quad (10.26)$$

$$V_{spheroid} \approx \frac{4\pi}{3} r_i^2 c \quad (10.27) \quad l_{cyl} = \frac{V_{LH2} - \frac{4\pi}{3} r_i^2 \cdot c}{\pi r_i^2} \quad (10.28)$$

In Figure 10.10 the proportions of the tank are visible for the outside layer of the tank. The radius of the outside layer is kept the same as this is limited by the space available in the cargo hold, while the other layers are built inwards to retrieve the geometry in radial direction.

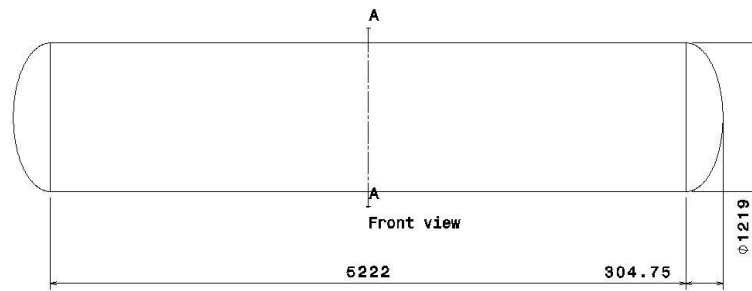


Figure 10.10: Tank geometry schematic with values given in millimeters.

Then, with L_{cyl} , r_o , and r_i known the mass of the tank is calculated. First, the area of each layer is found and multiplied times the thickness in order to find the volume. The area of the spheroid is expressed in Equation 10.30 where $e^2 = 1 - c^2/r_o^2$ with $c = 304.75 \text{ mm}$ which is half of the radius⁸. Here, t and ρ are the thickness and density of each individual layer presented in Table 10.7. Note that Aerogel (inner) and Aerogel (outer) have slightly different masses due to their different radial position. The total mass is then simply the sum of all the masses. Finally, the total length of the tank is $L = L_{cyl} + 2 \cdot c$.

$$m_{layer} = 2\pi r t \cdot L_{cyl} \cdot \rho \quad (10.29) \quad m_{spheroid} = \left(2\pi r_o^2 + \pi \frac{c^2}{e} \ln \left(\frac{1+e}{1-e} \right) \right) \cdot t \cdot \rho \quad (10.30)$$

Table 10.7: Tank wall properties.

Layer	ρ [kg/m ³]	t [mm]	m [kg]
CFRP	1750	2	66.88
Aerogel (o)	91	10	10.42
MLI	53	15.5	14.60
Aerogel (i)	91	10	10.02
Al2219-T185	2840	3	186.25
Total			288.16

10.6. Fuel distribution system

Now that the tank itself has been designed, a connection between the tank and the engine has to be designed. This connection consists of a valve, pump, pipe lines and a heat exchanger. Each part will be discussed and designed for the A320appu and finally a layout of the connection will be discussed and illustrated. First the inputs and desired outputs of the system are listed down below which will be used to decide and design the distribution system.

Inputs

- Pressure in tank: 3 bar
- Fuel flow: 0.100 kg/s (see subsection 10.6.1)
- Temperature of fuel in tank: 20K
- State of fuel: liquid

Outputs

- Pressure at CC: 28 bar
- Fuel flow: 0.100 kg/s
- Temperature of fuel at CC: 288K
- State of fuel: gaseous

10.6.1. Fuel lines design

This design requires two types of fuel lines, one transporting liquid hydrogen and the other one transporting gaseous hydrogen. For the liquid hydrogen pipe, it is needed to insulate to make sure that it will stay liquid while the gaseous hydrogen does not need any insulation as it will be at ambient temperature. First the liquid hydrogen line will be discussed and after that the gaseous line.

To determine a initial diameter of the fuel line, the incompressible Bernoulli equations are used. This equation is used for low-viscosity fluids meaning that this can be used for liquid hydrogen. For this initial sizing is assumed that liquid hydrogen is incompressible to simplify the problem.

$$\rho g h_{surface} + p_{surface} = \frac{1}{2} \rho v_{exit}^2 + \rho g h_{exit} + p_{exit} \xrightarrow{\text{simplify}} v_{exit} = \sqrt{2g\Delta h} \quad (10.31)$$

⁸<https://mathworld.wolfram.com/OblateSpheroid.html> retrieved 17-06-2020

$$\dot{m}_{exit} = \rho A_{exit} V_{exit} \quad d_{exit} = 2 \sqrt{\frac{A_{exit}}{\pi}} \quad (10.32)$$

In Equation 10.31 a simplification is shown which is possible with the assumption that the pressure in the tank is equal to pressure in the pipe line. This means that the pressure can be taken out of the equation and rewriting the remaining equation results in an expression for the exit velocity. Using the exit velocity an required diameter can be calculated using Equation 10.32. The height of the surface is chosen to be 97% of the total height of the tank, as it was chosen to fill the tank not completely. The location of the exit is assumed to be 10 cm above the bottom of the tank. With a datum on the bottom of the tank are the heights determined. The mass flow is assumed to be 0.1 kg/s to have a contingency factor on top of the required fuel flow of 0.095 kg/s. This value is obtained from the subsection 8.3.5 where the required mass flow was calculated.

Table 10.8: Summary of calculations for exit diameter.

Parameter	Value	Unit
Density (ρ)	70.9	kg/m ³
Gravitational acceleration (g)	9.81	m/s ²
Height exit (h_{exit})	0.10	m
Height surface ($h_{surface}$)	1.14	m
Exit velocity (V_{exit})	4.52	m/s
Mass flow fuel (\dot{m}_{exit})	0.10	kg/s
Area exit (A_{exit})	$3.10 \cdot 10^{-4}$	m ²
Diameter exit (d_{exit})	0.02	M

Table 10.9: Summary of calculations for gaseous hydrogen fuel line.

Parameter	Value	Unit
Density (ρ) ⁶	2.422	kg/m ³
Area exit HE (A_1)	$7.85 \cdot 10^{-3}$	m ²
Velocity exit HE (V_1) ⁷	132.34	m/s
Mass flow fuel (\dot{m})	0.10	kg/s
Diameter GH ₂ line (d_2)	0.14	m
Area GH ₂ line (A_2)	$1.54 \cdot 10^{-2}$	m ²
Velocity GH ₂ line (V_2)	67.5	m/s

Summarised in Table 10.8, all calculations have been performed and this resulted in a diameter of two centimetres. This value will be used for the liquid hydrogen fuel line's inner diameter. This value is compared to a similar fuel system design to verify if the value is in the right order of magnitude. In this design, they determined a inner diameter of 2.46 cm, meaning that the value seems reasonable and is verified [14].

However the gaseous hydrogen fuel lines need to be designed separately due to the large difference in density with liquid hydrogen. The inner diameter of the fuel line will be based on the exit diameter of the heat exchanger. In the heat exchanger, the phase of the fuel is changed from liquid to gaseous. The heat exchanger will be further discussed in subsection 10.6.3. The exit diameter of the heat exchanger is equal to 10 cm, so this value will be used as the initial diameter to calculate the area for the Bernoulli equation for conservation of mass. As hydrogen is assumed to be incompressible, Equation 10.33 can be utilised to determine the fuel velocity as well as the fuel line inner diameter. As the fuel flow stays constant, the flow can be slowed down by increasing the area of the fuel line. As the initial velocity is quite high, it is desired to slow this flow down. The inner diameter is assumed to be 14 cm. By making the diameter of the fuel line 4 cm bigger, the flow velocity is reduced by a factor of two.

$$\dot{m}_1 = \dot{m}_2 \rightarrow \rho A_1 V_1 = \rho A_2 V_2 \quad (10.33)$$

Now that both the fuel lines inner diameter is determined it is time to determine all the materials that will be used for the pipe lines, namely the inner and outer layer and the insulation.

The inner pipe material of the liquid hydrogen pipe is chosen to be the same as the inner tank wall, Al2219-T81. The reasoning behind this is that this material does not become brittle with low temperatures and can withstand the stresses induced by the pressure as discussed when designing the inner tank wall. Then the insulation is chosen to be closed cell foam with a thickness of 3.8 cm. The reason for this insulation is that it is needed to keep the liquid in cryogenic conditions before it flows into the heat exchanger. The outer pipe wall is chosen to be made of Al6061 with a thickness of 0.04 cm. The decision on the insulation and outer wall has been made due to the fact that it has been confirmed that this is sufficient as it is used in a similar reference design [14].

As the liquid hydrogen fuel line is designed, it is time to move onto the gaseous hydrogen fuel line. This will be utilised after the fuel has been through the heat exchanger and needs to be transported to the combustion chamber. Since this fuel line carries gaseous hydrogen at ambient temperature, there is no need for a insulation layer. This results in the need for a different pipe design. The inner diameter remains the same, however the

⁶<https://bit.ly/2BEC2XM>, retrieved on 19-06-2020.

⁷This value is based on Equation 10.33 with the initial flow velocity of Table 10.8 and a constant area.

material choice will change. For the gaseous hydrogen lines a stainless steel is chosen, since it has very high resistance against corrosion, oxidation and vibrations as well as high creep and rupture strengths. This is very beneficial for a fuel line since it will be very hard to rupture and the performance of the line will not decrease quickly. Another important aspect is permeability, which needs to be minimised. When gaseous hydrogen and air mix it can ignite which would have catastrophic consequences. To minimise the permeability, the stainless steel is integrated into an elastomer composite which then functions as a barrier⁸. For the initial design of a gaseous hydrogen lines, a thickness elastomer is assumed to be 2.0 mm. Due to limited research in thin, lighter gaseous hydrogen lines no detailed design decision could be made. The current line thicknesses have been determined by calculating the hoop stress in the lines with Equation 10.34 and compare the calculated hoop stress with the yield strength of the materials. Knowing the inner diameter of the lines as well as the pressure inside of the lines, initial thicknesses could be inserted to calculate the hoop stress.

$$\sigma_{w_{liquid}} = \frac{Pd}{2t} = \frac{30 \cdot 10^5 \cdot 0.02}{2 \cdot 0.001} = 30 \text{ MPa} \quad \sigma_{w_{gas}} = \frac{Pd}{2t} = \frac{30 \cdot 10^5 \cdot 0.14}{2 \cdot 0.002} = 105 \text{ MPa} \quad (10.34)$$

From this calculation resulted that both inner fuel lines can withstand the hoop stress easily, since the hoop stress is almost a factor 10 smaller than the yield stresses of both materials, which are between 200-290 MPa. Eventually a thickness of 1 mm is decided upon for the liquid hydrogen line and 2 mm for the gaseous hydrogen lines because the analysis done here is not very detailed so there is a high contingency factor. An illustration for the initial design showing the material choice and thickness of both fuel lines can be found for liquid hydrogen in Figure 10.11a and for gaseous hydrogen in Figure 10.11b.

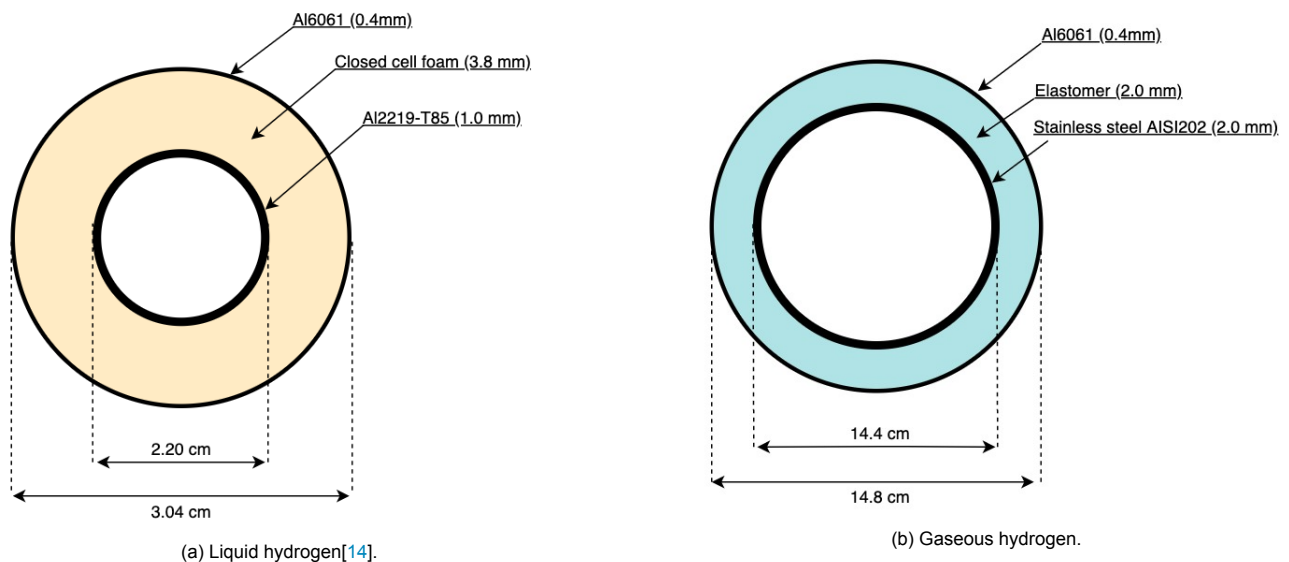


Figure 10.11: Fuel line design

With the geometry known, a initial mass estimation can be performed. For this mass estimation the elastomer 'high density Polyethylene has been chosen for reference[20]. The required length has been determined by evaluating the distance between the tank and the engine and adding a contingency factor to it. As it is easier to keep gaseous hydrogen in fuel lines than liquid hydrogen due to the cryogenic conditions, it is decided that the liquid hydrogen fuel line is as short as possible. As it still has to travel through a pump and arrive at the heat exchanger, a total length for the liquid hydrogen fuel line is chosen to be 3 m of the required 15 m, meaning that the gaseous hydrogen line will be 12 m. With the complete geometry and the material densities, a weight is determined in Table 10.10. The total fuel lines weight is equal to 3.44 + 101 = 104.44 kg.

⁸<https://bit.ly/3g4T8wW>, retrieved on 12-06-2020

Table 10.10: Mass of LH_2 and GH_2 fuel lines [14][20].

Material	Density [kg/m^3]	Volume m^3	Weight [kg]
Al6061 LH_2	2 700	$1.1 \cdot 10^{-4}$	0.31
Closed cell foam LH_2	2 785	$9.2 \cdot 10^{-4}$	2.57
AL2219-T815 LH_2	2 840	$1.9 \cdot 10^{-4}$	0.56
Total weight LH_2 line, 3 [m]			3.44
Elastomer(High density Polyethylene) GH_2	970	$9.1 \cdot 10^{-4}$	10.67
Al6061 GH_2	2 700	$1.8 \cdot 10^{-4}$	6.04
Stainless steel AISI202 GH_2	7 900	$8.9 \cdot 10^{-4}$	84.58
Total weight GH_2 line, 12 [m]			101

10.6.2. Pump selection

Liquid hydrogen is a fuel with very low viscosity, meaning that selecting a pump has to be done with care. The purpose of the pump is to make sure that the pressure and mass flow are changed sufficiently to provide the desired fuel flow at the right pressure into the combustion chamber. There are two main types of pumps; positive displacement pumps and rotodynamic pumps. In this case one of each category is evaluated. The positive displacement pump(PD) is a vane pump and the rotodynamic pump is a centrifugal pump⁹. The vane pump is chosen because it is the PD pump that performs best with very low viscosity and the centrifugal pump is also known for increased efficiency with lower viscosity fluids¹⁰. To choose which pump is used, both pumps are evaluated on different categories, as seen in Table 10.11.

Table 10.11: Comparison between centrifugal and vane pump¹¹

Characteristic	Centrifugal pump	Vane pump
Operating pressure	Low pressures	High pressures
Pressure efficiency	One optimal pressure	Higher pressure, more efficient
Viscosity efficiency	Lower values	Extremely low values
Maintenance/cost	Low	High
Capacity	High	Low

Next to viscosity, there are other parameters that influence the choice between the pumps. As already mentioned, there is also a desired pressure increase indicating that the pump should be able to perform under high pressures. Knowing this, the operating pressure and efficiency have been added to evaluate the two pumps. To see if the pump would be able to process the desired fuel flow, the characteristic capacity has added to the list as well. Not only performance but also cost and maintenance are important to evaluate when choosing a pump, since there is a budget and complexity desired to be minimised. Both pumps are illustrated below in Figure 10.12a and 10.12b. The illustration of the vane pump it can be seen that the pressure increases over with the colour indication which is caused by the decreasing area of the sections in the pump. The picture centrifugal pump shows the flow of the fuel and the is increased in the impeller which rotates.

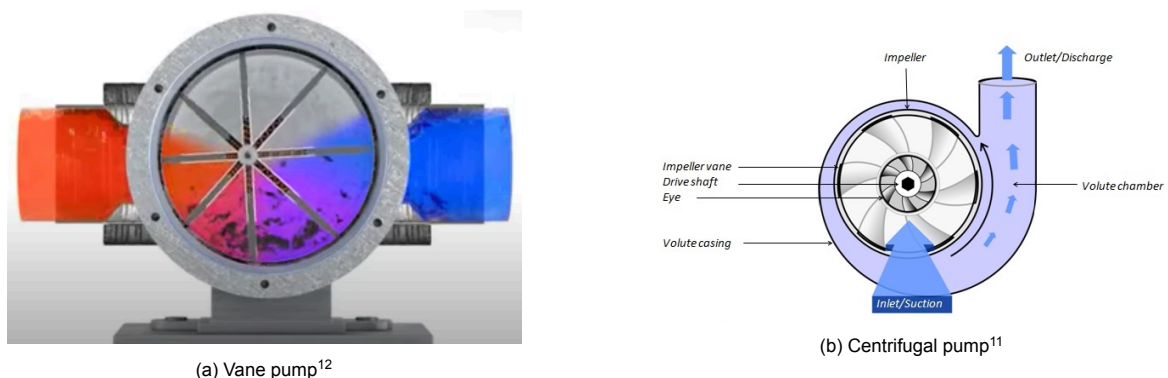


Figure 10.12: The two evaluated pumps' schematic cross-section.

⁹<https://bit.ly/2ViFX8c>, retrieved on 08-06-2020

¹⁰<https://bit.ly/2YCl2dO>, retrieved on 09-06-2020

¹¹<https://bit.ly/2BHWGGi>, retrieved on 08-06-2020

Using this table and knowledge of the required mass flow rate and properties of the liquid hydrogen, it can be concluded that a vane pump is the best choice. The reason for this is that the viscosity value is extremely low ($1.4 \cdot 10^{-5} \text{ Pa}\cdot\text{s}$ at 20K), while centrifugal pumps can only endure a viscosity 10 times larger as a minimum. Another reason is that the pressure is required to be in the range of 30–40 bar, which means that the efficiency of a centrifugal pump would decrease significantly. Even though the maintenance and cost are higher, the other characteristics weigh out the cost and time needed for a vane pump. An initial mass estimation of the vane pump is based on the required pressure and mass flow and is equal to 20 kg^{13} . However, an important aspect has not been addressed yet, which is the temperature range at which both pumps can operate. Due to the limited resources, there was no estimation possible to which would be more suitable. Both pumps need extra measures to make sure it would be able to operate in cryogenic conditions.

10.6.3. Heat exchanger

With the fuel being adjusted to the desired pressure and fuel flow, the only step that needs to be taken is that the fuel needs to become gaseous. This means that heat needs to be added to the fuel, which is possible when utilising a heat exchanger. A heat exchanger is a system in which two substances flow and exchange heat with one another. There are many different types of heat exchangers that could be chosen, however it has been decided to design a heat exchanger for liquid hydrogen based on a design for a natural gas heat exchanger by K.G. Fohmann [34]. This complete section is based on this master's thesis. This method has been verified and validated in the thesis which is the reason this method has been chosen.

In this master thesis is the complete design process discussed that to come up with a preliminary design for a heat exchanger. For this design are various assumptions made and most of them are listed below.

- Steady-state operating conditions
- No heat transfer to surroundings
- Only lateral heat conduction is taken into account
- Constant overall heat transfer coefficient
- Constant heat capacity
- Constant physical properties along heat exchanger
- No flow maldistribution
- No heat sources or sinks
- Constant sectional fluid properties
- Constant mass flow
- Only liquid hydrogen is absorbing heat during evaporation
- Constant temperature during evaporation

There are multiple type of heat exchanger discussed, tubular, plate-type, extended surface and regulators. After evaluating all four different types, it was determined that a tubular heat exchanger was most suitable for the application, more specifically a shell-and-tube heat exchanger. The main reason for this is they function very well with high temperature and pressure differences between fluids and environment. A shell-and-tube heat exchanger has two substances moving along each other, the fuel in one or multiple tubes and the cooling/heating substance flows between the shell and tube(s). This can be seen very clearly in Figure 10.13 where is indicated in which direction the substances flow.

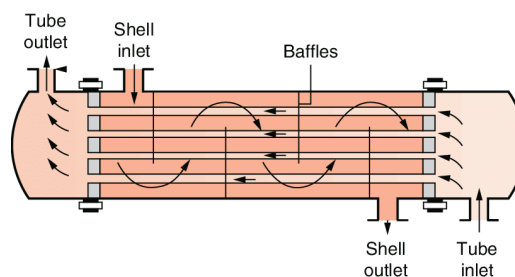


Figure 10.13: Example of a shell-and-tube heat exchanger cross-section [69]

For the shell-and-tube heat exchanger are also assumptions made to simplify the calculations even more. The assumptions are listed below.

- Pure counterflow
- One shell pass, one tube pass
- Multiple tubes parallel with one shell
- Fins will be added to the outside of the tubes
- Liquid hydrogen is the fluid in tubes and air is the fluid in the shell
- Only single flow in the heat exchanger

¹²<https://bit.ly/2VjSwv6>, retrieved on 10-06-2020.

¹³<https://eaton.works/2BdkwtG>, retrieved on 22-06-2020

A cross section of the heat exchanger is shown in Figure 10.14. In this figure are the tubes shown indicated with the red line, the fins are the blue lines connected to the tube and the blue dotted lines represent an artificial shell which are used to determine the heat flow on the outside of each tube to obtain a valid estimate of the heat flow of a multitube shell.

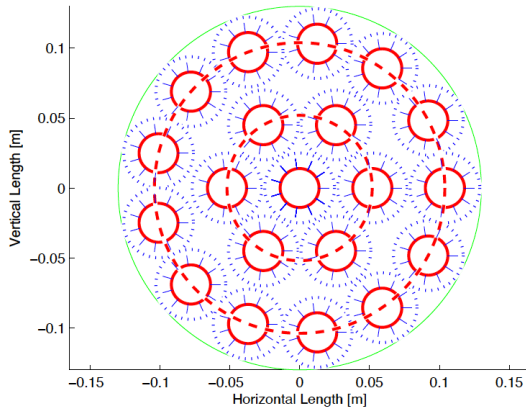


Figure 10.14: Cross section of designed heat exchanger [34]

Table 10.12: Geometry inputs for Equation 10.35

Parameter	Value	Unit
Radius tube (r_i)	0.013	m
Radius artificial shell (r_a)	0.052	m
Radius outer shell (r_o)	0.13	m
Length fins (l)	0.003	m
Amount of fins per tube (NO_{fins})	20	-
Thermal conductivity tube (k_t)	26	W/mK

To describe the heat flow in the heat exchanger, it is needed to determine the flow in both the tube and the shell. Next to this the thermal properties of the tube material need to be taken into account as well. Combining all this results in Equation 10.35 which calculates the total heat flow of the heat exchanger. Calculating this for every section and add this together results in the total heat flux.

$$UA = \left[\frac{1}{2\pi r_i \Delta x h_i + 2l \Delta x h_{fin} NO_{fins}} + \frac{1}{2\pi k_t \Delta x} \ln \left(\frac{r_o}{r_i} \right) + \frac{1}{2\pi r_o \Delta x h_o} \right]^{-1} \quad (10.35)$$

With the heat flux calculated after adding a section, this value can be used to fill in Equation 10.36 which can be compared to the value calculated in Equation 10.37 [38]. To calculate the heat transfer multiple characteristic values of liquid hydrogen are needed to be obtained from reference data. The data needed to be obtain are listed in Table 10.13.

Table 10.13: Input data to calculate heat flux and heat transfer¹⁵

Parameter	Value	Unit
Specific heat (c_p)	8373.6	J/kgK
Mass flow (\dot{m})	0.10	kg/s
Temperature inlet air	450	K
Temperature inlet LH ₂	20	K
Temperature outlet air	288	K
Temperature inlet LH ₂	288	K

$$\dot{q} = UA \Delta T_{lm} \quad \Delta T_{lm} = \frac{(\Delta T_I - \Delta T_{II})}{\ln(\Delta T_I / \Delta T_{II})} \quad (10.36)$$

$$\Delta T_I = T_{air,i} - T_{LH_2,o} \quad \text{and} \quad \Delta T_{II} = T_{air,o} - T_{LH_2,i}$$

$$\dot{q} = \dot{m}_{LH_2} c_{pLH_2} \Delta T_{LH_2} \quad (10.37)$$

The only variables that are missing at the moment are the heat transfer coefficients. There are three different coefficients used to calculate the heat flux which are the inner (h_i), outer (h_o) and fin (h_{fin}) heat transfer coefficient. These coefficient have been estimated using the results of the natural gas heat exchanger. Then the total heat transfer required is calculated with Equation 10.37 and compared to the heat transfer of the length calculated at that moment. The length is then determined by checking if the heat transfer is equal to the required heat transfer as calculated in Equation 10.37.

To simplify the calculations, it was decided to only use single stage flow to determine the length, however it is still needed to take the two stage flow which is done by adding 10% to the calculated length of the heat exchanger. The length of the heat exchanger was calculated to be 1.37 m and with the contingency for the two phase flow the length is equal to 1.51 m. This is a reduction of length of almost one meter compared to the natural gas heat exchanger. The weight of the heat exchanger is estimated to be around 90 kg which is

¹⁵<https://www.bnl.gov/magnets/Staff/Gupta/cryogenic-data-handbook/Section3.pdf>, retrieved on 16-06-2020.

based on the weight estimation of the liquid natural gas heat exchanger. This makes sense because the heat transfer required for the liquid natural gas heat exchanger is four times larger than the one for liquid hydrogen¹⁶.

The air warming up the liquid hydrogen is obtained from the APPU compressors and is cooled down by the liquid hydrogen and will be utilised for the air conditioning. This way it is not needed to obtain bleed air from the main engines which results in less kerosene needed. The air from the compressor has a temperature of 450K and is cooled down to room temperature. This can then be used to circulate the cabin of fresh air, which required to be a mass flow of around seven grams of air per second per passenger¹⁷. This flow of air can be achieved with the designed heat exchanger, meaning that the air conditioning can be taken over completely from the main engines. The system used for this is in any other aspect the same as the one that is already inside the A320neo. There is only a diverging duct needed to decrease the pressure of the air to comply with the cabin pressure and air flow.

An illustration of the total fuel distribution system can be found in [section 10.9](#) along with the total mass of the distribution system.

10.7. Sensitivity analysis

The numerical model for both thermal and mechanical design are tested and discussed in this section. Through the means of a sensitivity analysis more information is given on the limitations and responsiveness of the code. First, the three main TPM for thermal design are evaluated and then mechanical design is covered.

10.7.1. Thermal design

From literature it is understood that the heat transfer across a material depends highly on its thermal conductivity and its thickness [38]. Therefore, a sensitivity analysis has been done on these key parameters to visualise the impact they have on the thermal design of the hydrogen tank. [Figure 10.15a](#) shows the relationship between boil-off time, thermal conductivity, and thickness. In this case, the numerical code assumes 1 layer of material with a certain thickness.

Logarithmic behaviour is observed which heavily depends on the thermal conductivity of the material. This is expected since $t_{boil} \propto Rth \propto 1/k$ according to [Equation 10.12](#) and [Equation 10.4](#). For a thickness of 40 mm, the boil-off time decreases from 2 250 hours to 1 150 hours when increasing k from 0.01 to 0.02 mW/mK. However, this decrease is much smaller when assessing the same Δk between 0.06 and 0.07. Therefore, in the limit the change in k has less effect on the boil-off time.

Also, the thicknesses have a remarkable influence on the boil-off time. First, the boil-off time at $k = 0.01$ increases as the thickness increases. However, at a certain point this behaviour reverses. For example, a thickness of 450 mm has a lower boil-off time than a thickness of 250 mm which has the highest value in [Figure 10.15a](#). Furthermore, it can be observed immediately that a thickness of 600 mm is the lowest performing thermal design. This phenomena is further investigated. [Figure 10.15b](#) plots the boil-off time as function of thickness for $k = 10^{-5}$, or $k = 0.01$ mW/mK. The shape of the graph describes indeed the behaviour of the boil-off time in [Figure 10.15a](#). At some point, increasing the thickness stops becoming beneficial. The reason for this behaviour is discussed later in [subsection 10.8.1](#).

The linear relation between thickness and boil-off time as seen in [Figure 10.6](#) may also be explained with [Figure 10.15b](#). Here, linear behaviour is observed between 1 mm to 50 mm. This explains why straight lines are seen in [Figure 10.6](#) as these have been calculated in a region between 7.5 mm and 18.5 mm. In case much higher boil-off times are required the numerical would have shown more curvature. Thus, the numerical model is sensitive to the domain in which boil-off time is calculated.

Finally, the code only works only for $0 < t < 609.5$ mm. If the thickness is equal to 0 there is no wall and hence no thermal resistance network. However, the code still calculates a thermal resistance because internal and external convection are always calculated even though there is no thickness. On the other hand, if the thickness equals 609.5 mm, maximum radius of the tank, a division by zero error is shown unsurprisingly. The $\ln(r_o/(r_o - t))$ term would then have a division by zero if $t = r_o$. Thus, it is concluded that the numerical model is either sensitive for these values or give unrealistic output.

¹⁶<https://cameochemicals.noaa.gov/chris/LNG.pdf>, retrieved on 15-06-2020

¹⁷<http://naca.central.cranfield.ac.uk/reports/arc/cp/1136.pdf>, retrieved on 19-06-2020

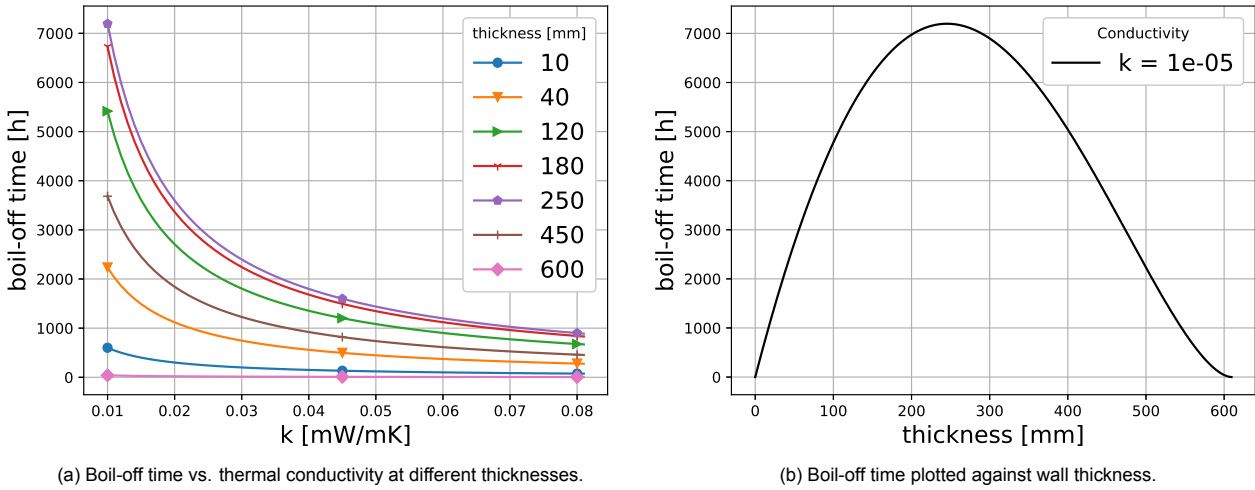


Figure 10.15: Boil-off time sensitivity analysis.

10.7.2. Mechanical design

For the tank wall analysis the design pressure is the most important design parameter. This pressure will be primarily carried by the inner tank wall, while the outer tank wall by design is related to the outside pressure primarily. The latter being held constant. This means that in Figure 10.16a only the thickness of the inner tank wall is intended to change significantly. The masses of both shells will change due to the additional cylinder length required by losing space in radial direction in the confined cargo compartment.

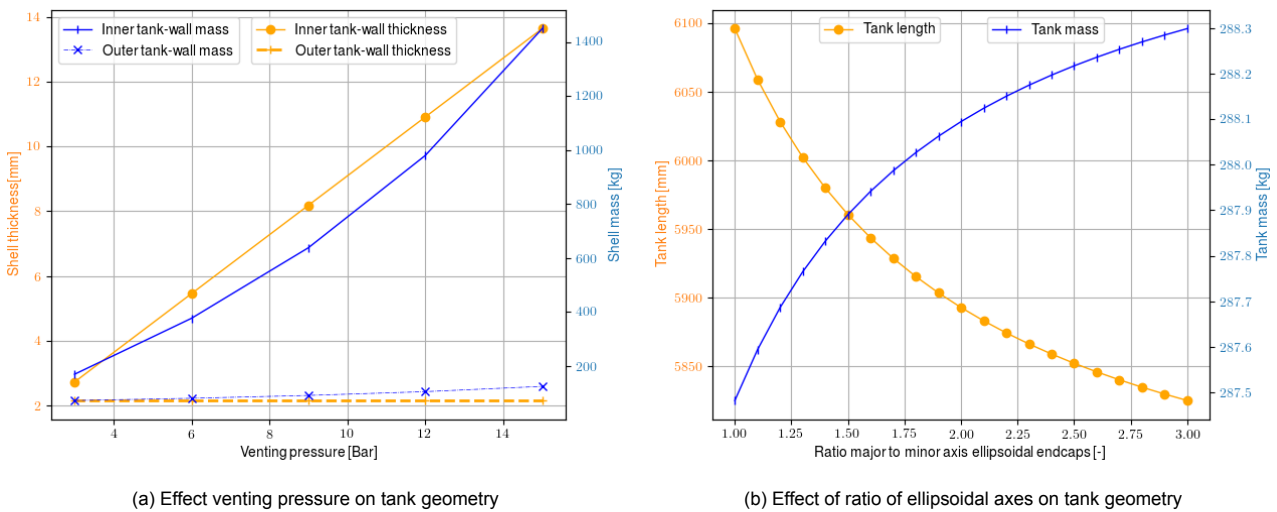


Figure 10.16: Relation mechanical design with geometry sensitivity curves

For the spherical heads it has been investigated that a ratio of 1.6 is the most effective cost and mass-wise for a pressure vessel with ellipsoidal heads [10]. This relation is visible in Figure 10.16b. Whereas to allow for a constant thickness of the pressure vessel it has been chosen for the current analysis to use the 2.0 ratio. Additionally it is better volume-wise as the cylindrical part of the tank will be longer for a constant required V_{H_2} . However it is not optimal, as due to the constant thickness, the tank will weigh much heavier, as the tank design will deviate from a more ideal spherical shape endcaps with a lower gravimetric density to an almost full cylinder with a higher gravimetric density. The relations in the plots show a expected result. This verifies the compatibility between the geometry and mechanical design parts of the numerical model.

10.8. Verification and validation

This section describes the verification and validation procedures performed during the tank design. First, verification is explained, and after that the validation is elaborated upon.

10.8.1. Verification

Arbitrary parts of the numerical code are tested and conclusion are drawn based on its behaviour. The results are presented and discussed in this section in order to verify the functionality of the model. The numerical model for both thermal and mechanical design are assessed.

Thermal design

In Figure 10.4, subsection 10.3.4, the heat flow for foam or Aerogel was plotted as function of the thickness. A minimum in the graph is clearly visible which happens at a maximum of the thermal resistance according to Equation 10.38 since everything else stays constant. Therefore, to verify this result a maximum must be found in the total thermal resistance.

$$q_{tot} = q_{cyl} + q_{sph} = \frac{(T_{air} - T_{H2}) \cdot f_{rad}}{R_{th_{tot}}} \quad (10.38) \quad R_{th_{tot}} = \left(\frac{1}{R_{th_{cyl}}} + \frac{1}{R_{th_{sph}}} \right)^{-1} \quad (10.39)$$

In Figure 10.17, the behaviour of the thermal resistance, excluding MLI, is plotted against the thickness. Indeed, a maximum can be found exactly at the same value for the thickness, around 250 mm. As the thickness, e.g. insulation, increases, so does the thermal resistance of the sphere. This is expected since all parameters for the sphere stay constant except the radii ratios, $1/r_i - 1/r_{i+1}$, which increases. This causes $R_{th_{cyl}}$ to go up continuously until the numerical model gives a *math domain* error for a thickness bigger than the maximum radius of the tank. Also, as $R_{th_{sph}}$ increases, the smaller $1/R_{th_{sph}}$ becomes and, therefore, the less it contributes to the total thermal conductivity which explains why $R_{th_{cyl}}$ and $R_{th_{tot}}$ are close to each other and why they show a converging behaviour. Furthermore, according to Equation 10.39 the total thermal resistance should always be lower than the thermal resistance of the cylinder which can indeed be seen in Figure 10.17.

In order to store the required 400 kg, the tank volume must stay constant. Hence, any thickness added results in elongating the tank to maintain this requirement. The numerical model takes this into account. In fact, this relationship has already been plotted in Figure 10.4. As stated in Equation 10.4, $R_{th_{cyl}}$ depends on L_{cyl} which changes as the thickness increases. A maximum is expected since at some point the addition of insulation material stops being beneficial because the change in cylinder area starts to overcome the $\ln(r_{i+1}/r_i)$ term. To verify this, the length of the cylinder has been set to a constant value. The plot showed similar behaviour as sphere's thermal conductivity, $R_{th_{sph}}$. Thus, it is concluded that the numerical model functions properly for it is intended to do.

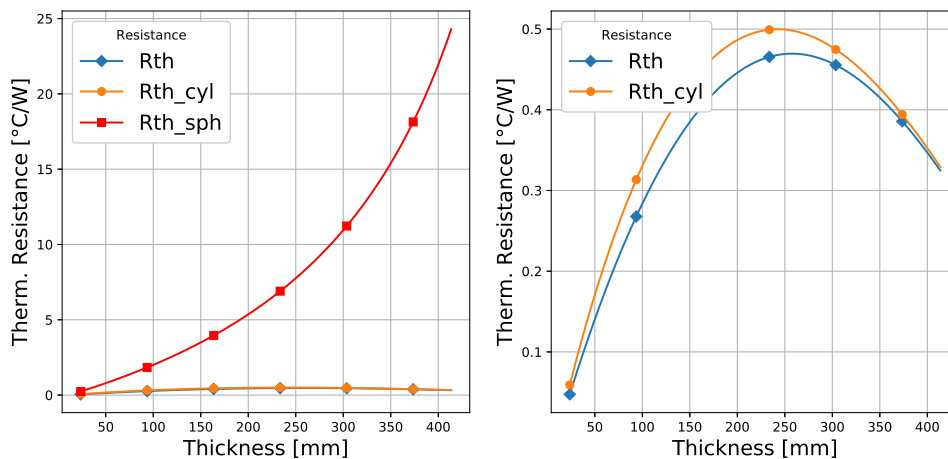


Figure 10.17: Thermal resistance of the cylinder, sphere, and total tank plotted against thickness.

Now that the thermal resistance and subsequently the heat flow has been verified, the pressure vs. time plot is further investigated. A configuration with a higher heat leakage should reach the venting pressure sooner since more heat is entering the tank per time unit. Figure 10.18 plots this relationship again. The heat flows are shown in Table 10.14. The values confirm that the pressure-time plot acts accordingly. The MLI configuration reaches the boiling time, or venting pressure, sooner than the other two configurations while having the highest heat leakage. Also, this is expected since the MLI only is less thick than those other designs. In case of the other two configurations, both have the same thickness and therefore the only parameter that dictates the performance is their thermal conductivity. The k-value for Aerogel is smaller and, as a result, it is able to conduct less heat

per time unit. This result is seen back in Figure 10.18 since it is the configurations with the largest boiling time.

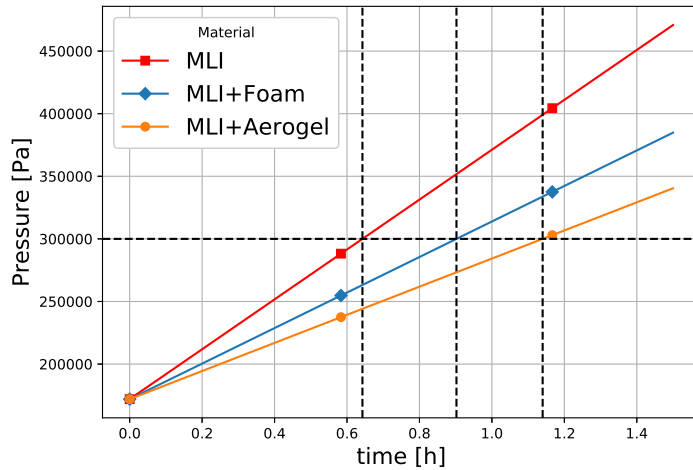


Figure 10.18: Duration in reaching venting pressure upon performance loss in MLI system.

Configuration	q [W]
MLI	5 118
MLI + Foam	3 312
MLI + Aerogel	2 817

Table 10.14: Tank wall material properties.

10.8.2. Validation

Experimental parameters and inputs are used to test the numerical model for both thermal and mechanical design. Their outputs are compared to the outputs obtained from papers to validate the numerical model. Furthermore, their discrepancies are discussed in order to fully understand the limitations of the model.

Thermal design

The paper by J.E. Fesmire is used to validate the numerical model [31]. 26 different MLI systems were tested on thermal performance with a CBT of 78K and a WBT of 293K using a cylindrical calorimeter. Throughout the experiment the temperatures were maintained constant in order to have steady state heat transfer. Consequently, the heat leakage Q , was measured with a mass flow meter for the different configurations. Using the one-dimensional Equation 10.40, the effective thermal conductivity of the MLI system was calculated.

$$k_e = \frac{Q \ln(d_o/d_i)}{2\pi L \Delta T} \quad (10.40)$$

Here, d_i is the inner diameter of the MLI system being tested which is always set at 167 mm. Furthermore, d_o is simply the outer diameter of the specimen which is dependent on its thickness. Therefore, $d_o = x + d_i$ where x is the thickness of the material. Recorded values have been provided for the warm boundary temperature which varied slightly during the experiment. The numerical values for heat flow were validated by giving the effective thermal conductivity as input, k_e , and obtaining Q_{num} as output with Equation 10.41. Then, Q_{num} is compared to the experimental values for Q as shown in Table 10.15.

$$q_{cyl} = -\frac{kA}{\Delta x} \Delta T = \frac{(T_{air} - T_{H2}) \cdot f_{rad}}{Rth_{cyl}} \quad (10.41) \quad Rth_{cyl} = \frac{1}{h_i A_c} + \frac{1}{2\pi L_{cyl}} \sum_{i=1}^n \frac{\ln(r_{i+1}/r_i)}{k_i} + \frac{1}{h_o A_c} \quad (10.42)$$

Only the cylindrical part of Equation 10.7 is taken for validation because the experimental setup is made of a cylinder. For this reason, Equation 10.41 is used to validate the numerical model. Hence, the validation is limited to the cylindrical shape of the hydrogen tank only. However, this part has the biggest surface area and is therefore the highest contributor to heat leakage. The data shown in Table 10.15 shows promising results for the accuracy of the numerical model. As can be seen from the series, 88.64% is the lowest acquired accuracy between two data points. On the other hand, the highest accuracy achieved is 99.50%. In general, the numerical model is said to be accurate. This claim is supported as well by the two regression lines in Figure 10.19. Furthermore, the accuracy for each data point has been calculated using Equation 10.43 where the absolute error percentage is subtracted from 100%.

$$accuracy = 100\% \cdot \left(1 - \frac{abs(Q_{num} - Q)}{Q}\right) \quad (10.43)$$

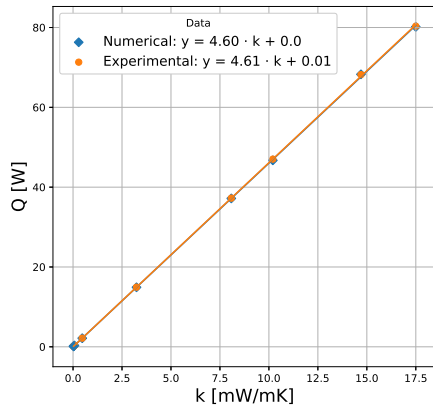
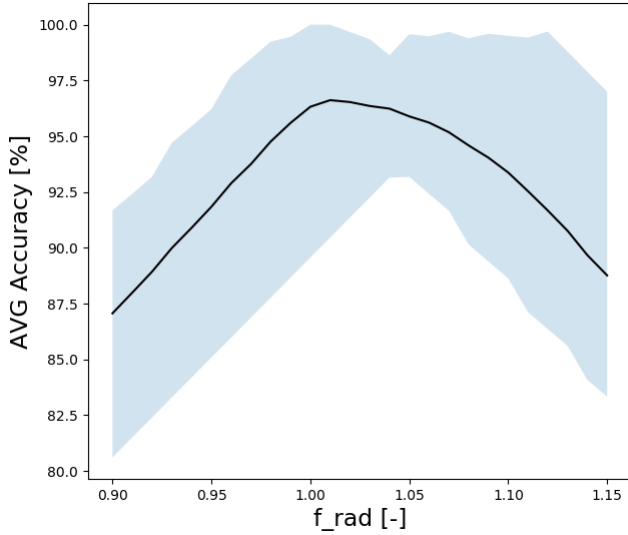


Figure 10.19: Heat flow vs. conductivity diagram for numerical and experimental heat flow data with regression line

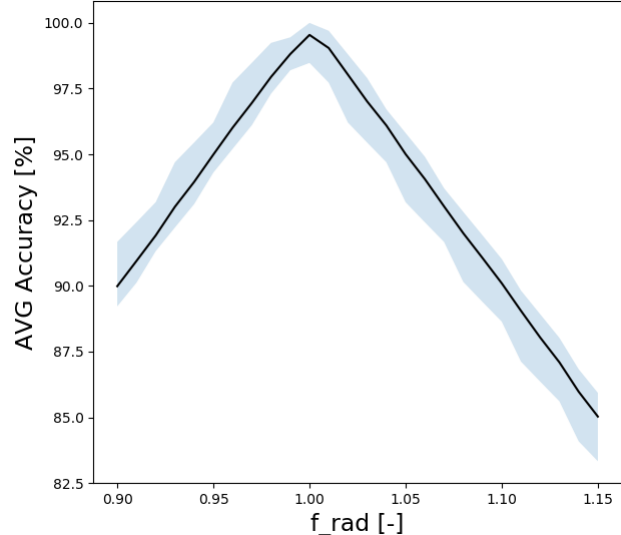
Input		Reference	Output	
WBT [K]	k_e [mW/mK]	Q [W]	Q_{num} [W]	Accuracy
294	0.029	0.132	0.143	88.64%
293	0.031	0.143	0.157	90.21%
293	0.04	0.183	0.202	89.62%
293	0.072	0.334	0.364	91.02%
293	0.469	2.162	2.367	90.52%
293	3.24	14.942	16.061	92.51%
293	8.08	37.248	38.885	95.69%
292	10.2	47.025	48.191	97.52%
295	14.7	68.199	68.543	99.50%
292	17.5	80.341	79.154	98.52%

Table 10.15: Numerical and experimental data for 15.5 mm Mylar/Net MLI system

The effective thermal conductivity k_e is a measure to determine the overall performance of the system. That is, the heat flow Q found experimentally does not only account for conduction, but also for all other forms of energy transfer. In this case, applying a correction factor to the heat flow would not be logical as it is already incorporated by k_e . Figure 10.20a shows the average accuracies with their corresponding minimum and maximum range in a series for different values of f_{rad} . It can be seen immediately that a highest average accuracy, 96.62%, is achieved for a value of $f_{rad} = 1.01$. This proves that the correction factor is not necessary when dealing with MLI due to the use of k_e . Consequently, Q_{num} is often overestimated in Table 10.15 when analysing an MLI layer. Another discrepancy found is that the numerical model takes into account convection resistances $1/h_i$ and $1/h_o$. When these are removed the spread reduces greatly as shown in Figure 10.20b. Here, the highest average accuracy is equal to 99.5% at $f_{rad} = 1.0$.



(a) With convection terms $1/h_i$ and $1/h_o$.



(b) Without convection terms $1/h_i$ and $1/h_o$.

Figure 10.20: Average accuracy of Q_{num} series plotted for different f_{rad} .

The thermal conductivities for Aerogel or foam are often given for conduction only. In that case, a correction factor, f_{rad} , would be more appropriate. It is unknown what the magnitude of f_{rad} should be exactly. However, a correction factor must be applied to take into account other forms of heat transfer. This is the reason why in subsection 10.3.4 $f_{rad} = 1.1$ is used in the numerical model to assess the total thermal performance of the tank. The implementation of this correction factor does not have catastrophic consequences because a higher value for heat leakage is found instead due to f_{rad} . In other words, it is likely that the insulation system is over designed, but that means that the boil-off time requirement is still met.

In conclusion, the numerical model is able to predict the heat transfer over the tank wall with great accu-

racy when using the effective thermal conductivity. Furthermore, it is found that there is room for optimising the model when calculating properties for an MLI system. This can be done by removing f_{rad} in case of MLI. However, removing f_{rad} does not apply to the other layers since these do not use an effective thermal conductivity. Unfortunately, validated data on different thermal networks could not be found to test the numerical model on multiple stacked layers. Therefore, the accuracy of the model remains inconclusive in this respect. Nevertheless, the numerical model shows good results for MLI systems and since these are main drivers for the total performance of an insulation analysis the numerical model is determined to be accurate enough for the A320appu project.

10.8.3. Mechanical design

The mechanical analysis performed in the numerical model is compared with the in-built model in CATIA. The same assumptions apply for the numerical model as for CATIA. Some actions are taken to get a comparable model in CATIA:

- Stress concentration at the crown of the ellipsoidal head, due to a created notch (notched structure)
- Constant thickness over the cylindrical and ellipsoidal shells
- Only the isotropic aluminium inner tank wall is considered
- Pressure differential over the tank wall $\Delta p = p_{vent}$

The CATIA model gives a resulting maximum stress of $\sigma_{max} = 64.4 \text{ MPa}$, which corresponds to $\sigma_a = 64 \text{ MPa}$ of the numerical model. Hence the deviation between the models is 0.625%.

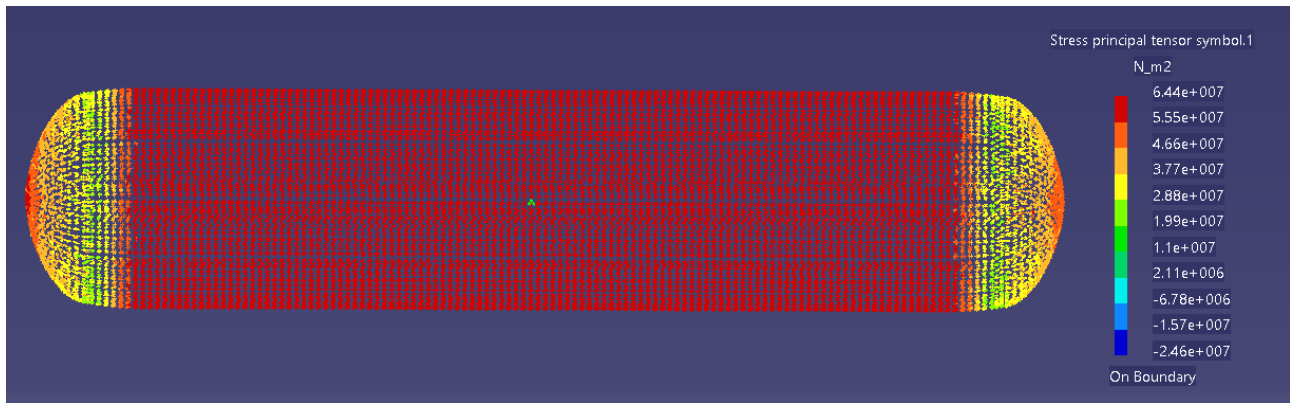


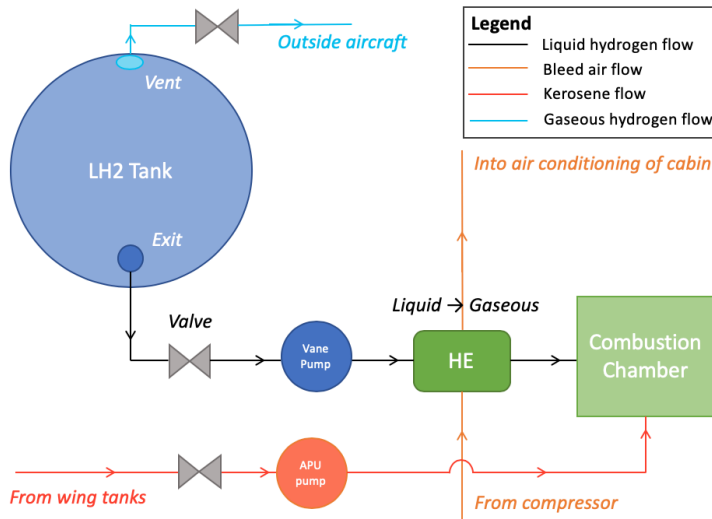
Figure 10.21

Furthermore with the CATIA model, the $p_{burst} = 1.5 \cdot p_{vent}$ has been configured to see whether the design fails for a SF of 1.5. The resulting $\sigma_{max} = 96.8 \text{ MPa}$. Therefore $\sigma_{max} = \sigma_Y / K_i = 290 / K_i$. Isolating the parameter K_i yields $K_i = 290 / 96.8 = 3$. This shows that due to the fatigue life design the pressure vessel retains a safety factor that is twice its intended value. Evidently this was already visible by taking the ratios of $(\sigma_Y) / (1.5 \cdot \sigma_f)$ out of Table 10.5. Overall, the results of the CATIA model validates the mechanical analysis model for the pressure load case of current fuel tank design.

10.9. Conclusion

The aim of this chapter is to design a thermally efficient and lightweight cryogenic tank to store 400 kg of hydrogen for 48 hours without boil-off. A numerical model has been developed to predict both the thermal and the mechanical behaviour of the tank. First, an insulation system is chosen that meets this requirement. Secondly, a stress analysis was performed on the inner and outer tank wall in order to assess the structural integrity of the tank. Finally, the thickness of the tank determined the geometric properties which was needed to built the CATIA 3D model shown in Figure 10.10.

After designing the cryogenic tank the fuel distribution system, which consists of a valve, pump, pipe lines, and a heat exchanger, was designed. Knowing the properties of each subsystem the total fuel distribution and storage were integrated as shown in Table 10.22. The specifications of the complete system are given in Table 10.16. Key properties are the total mass and the boil-off time which are 499 kg and 52.8 hours, respectively.



Properties	Value
m_{tank} [kg]	288
m_{dist} [kg]	210
m_{total} [kg]	499
V_{H2} [L]	6 240
V_t [L]	6 943
L_{tank} [m]	5.90
t_{tank} [mm]	30.5
\dot{m}_{fuel} [kg/s]	0.095
t_{boil} [h]	52.80
\dot{Q}_{leak} [W]	84.0

Table 10.16: Final tank properties

Figure 10.22: Complete fuel distribution system design

10.10. Recommendations

Due to lack of time and knowledge not all properties of the tank were able to be optimised. However, there are a number of recommendations for further design of the hydrogen distribution and storage system.

Firstly, in terms of thermal design, more analysis should be done on the interaction between the insulation material. Research shows that thermal expansion coefficient mismatches deteriorate the thermal performance of the insulation system. The A320appu project does not address this problem thoroughly since the numerical model does not take this into account. In case more is known about this problem a better decision can be made on material selection.

Secondly, the fuel distribution system requires more detailed analysis in order to accurately estimate its properties. Since this part of the total system is really specific in itself the amount of information online was limited. However, in the scope of the A320appu it serves its purpose as a preliminary design.

Thirdly, the possibilities of having separate tanks should be considered in the future for maintenance purposes. Due to the cylindrical shape of the tank it is assumed that maintenance may be done in the cargo hold itself. Therefore, it is currently fixed in the cargo hold. However, some airliners may prefer to have the option to remove the tank for inspection or when they do not need it for a specific flight. Hence, the idea of placing multiple tanks that may be removed individually should be investigated, f.i. multi-spheroids.

Another solution would be to use an elliptical shape which fits more efficiently in the cargo hold. Consequently, the length of the tank may be reduced and more cargo space is freed. This would mitigate the **HT-04** risk mentioned in chapter 7, Making these options available could give Airbus a strong competitive advantage on the market and would additionally enforce the hybrid brand of the A320appu.

The change in geometry of the tank will in effect change the mechanical analysis that needs to be performed. For an increasing complexity of the structure and for making further optimisations to the design more extensive numerical tools (FEM) should be used to properly model the fuel tank, for a combination of load cases as described in Table 10.6. From this analysis the design of the support structure, baffles, liner (or no liner) and connecting rods can ideally be determined. Extensive analysis is also required to retain the leak-before-burst condition that is one of the common designed failure modes for further design iterations and possibly modify the failure modes based on the most critical conditions for all the pressurised components in the fuel system.

Finally, as research on lightweight structures advances and more applications are possible for cryogenic storage, there will be more possibilities for the geometry of the tank and the fuel system can be more suitably optimised to obtain a lighter and more space efficient design. Nevertheless, as it concerns a fuel system with pressure vessel(s) it will always be required to make prototypes and test these in a dry-run, i.e. in a static, controlled environment, before the designs are proven for flight in the A320appu.

Empennage Design

The empennage of the A320appu has to be reconfigured to a T-tail configuration to allow better use of BLI, as explained in [chapter 3](#). This chapter proposes the initial design and geometry of the horizontal tail by investigating balance, longitudinal stability and control. The vertical tail is sized by looking at the lateral stability and control. Furthermore, a preliminary look is taken at the structural aspect of the empennage. At the end of the chapter, verification and validation of the used methods is performed, a conclusion of the whole analysis is given and recommendations for further analysis are proposed.

11.1. Requirements

The relevant driving requirements in regard to the the empennage are related to the stability and control and are the following:

FMP-Sys-09: The aircraft shall passively be statically and dynamically stable.

REG-Sys-40: The aircraft shall comply with CS 25 safety regulations.

To elaborate on the CS regulations, they refer to the ability to trim the aircraft (CS25.161), to maintain longitudinal and lateral stability (CS25.173, CS25.177 & CS25.181) and to ensure controllability during the critical flight conditions (CS25.143 to CS25.149, CS25.255 & CS23.221) [29]. Also the risk associated with these requirements is **FP-01**¹. Thus, the purpose of this chapter is to asses these requirements and risks.

11.2. CG estimations

To assess the stability and control of the aircraft, the CG range encountered during operations has to be known, more specifically the most FWD and most AFT CG are of interest. To obtain these values for the A320appu the following procedure was followed. First, the CG at OEW of the A320appu was estimated by retrieving the CG at OEW of the A320neo [1]. This value was adjusted by removing the moment contribution of the APU but adding the contribution of the added subsystems. Furthermore, a possible shift of the wing placement was taken into account. The mass breakdown of the APPU can be found in [Figure 11.1](#) and the resulting CG values can be found in [Table 11.1](#)².

Table 11.1: Mass and CG estimation of the A320appu .

	OEW [kg]	Moment arm [m]	Moment [kgm]	CG at OEW [x/c]
A320neo (OEW)	44 300	16.7	740 310	
Remove APU	-185	35.49	-6 566	
APPU subsystem				
New engine(s)	410	35.49	14 551	
S-duct	75.5	34	2 567	
Drivetrain	300	36.5	10 950	
Added propeller	173	39	6 747	
Fuel tank(s)	288	21.7	6 250	
Heat exchanger	90	26.2	2 358	
Fuel lines	100	27.5	2 750	
Wing group shift				
Wing group [9]	9 150	1	9 150	
Total	45 552	17.3	789 066	0.410

¹**FP-01:** The new empennage configuration does not support significant flight controllability

²For the calculation of the CG position some minor fuel distribution components weighing around 20 kg were neglected as it was difficult to determine their location and their impact considered negligible.

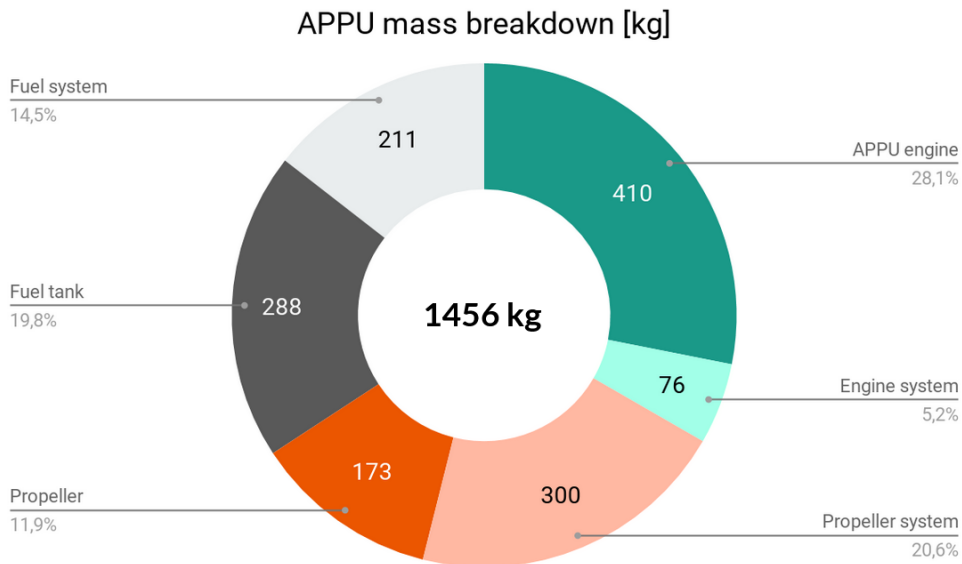


Figure 11.1: Mass breakdown of the APPU subsystem

Then, the aircraft is loaded by adding the cargo first, then the passengers, and lastly the fuel. The aircraft was assumed to be full and each passenger was assumed to weigh 86 kg including luggage. The A320neo is able to carry a maximum payload of 19 tonnes [1] so the remaining payload mass has been allocated to the cargo spaces, in proportion to their volume. Furthermore, the placement of the fuel tank in the aft cargo space is taken into account. The fuel mass of hydrogen was assumed to be 400 kg from chapter 8, and the remaining mass (12 tonnes) was allocated to kerosene fuel. For each loading sequence the worst case scenario was assumed, namely loading from the front to back and from the back to the front. This process is summarised by Figure 11.2 where the most aft and forward CG can easily be retrieved, which are used for further calculations. This CG range is encountered during loading and it is highly unlikely that during flight the same maximum and minimum CG is encountered. However, this overestimation is not corrected for and is considered as a safety margin for the eventual tail sizing.

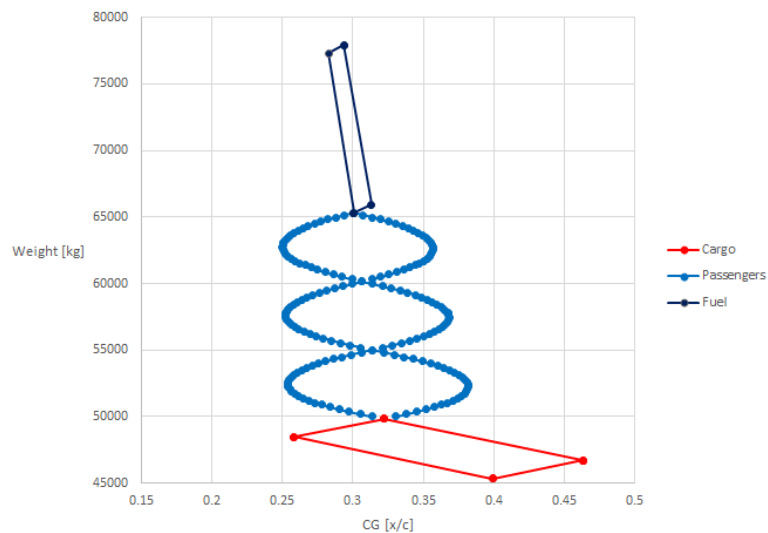


Figure 11.2: Loading diagram of the A320appu

11.3. Required horizontal stabiliser surface area

This section focuses on deriving the minimal necessary horizontal tail surface area to ensure longitudinal stability and control. For all calculations a trapezoidal wing is assumed where the root chord is placed on the top of the fin. To summarise, the following six points are investigated to initially size the horizontal stabiliser:

- Stick-fixed cruise
- Short period
- Recovery from deep stall
- Rotation at take-off
- Trimming at approach
- Trimming at stalling conditions

These six points are discussed one by one in the following sections, with first taking a look at the stability and then the controllability.

11.3.1. Stability

For the longitudinal stability, the critical condition for static stability was assumed to be the stick-fixed cruise condition as the A320appu uses irreversible controls, which makes the stick-free condition irrelevant. Furthermore, compatibility with the dynamic stability was assessed by investigating the short period. The phugoid was not considered because the period of this eigenmotion is generally large enough for the pilot to correct [64].

Stick-fixed cruise

The stability curve is derived by looking at steady-symmetric flight and ensuring that a change in angle of attack should result in a moment in the opposite direction. From this, and using a stability margin of 0.05 (the distance between the most aft CG and the neutral point), it produces Equation 11.1 [64, p 309].

$$\frac{S_h}{S} = \frac{1}{\frac{c_{L_{\alpha h}}}{c_{L_{\alpha A-h}}} \left(1 - \frac{d\epsilon}{d\alpha}\right) \frac{l_h}{c} \left(\frac{V_h}{V}\right)^2} \bar{x}_{c.g.} - \frac{\bar{x}_{ac} - 0.05}{\frac{c_{L_{\alpha h}}}{c_{L_{\alpha A-h}}} \left(1 - \frac{d\epsilon}{d\alpha}\right) \frac{l_h}{c} \left(\frac{V_h}{V}\right)^2} \quad (11.1)$$

The method to estimate the unknown aerodynamic coefficients (the lift rate coefficients, the aerodynamic centre and the downwash) is explained in Torenbeek [64] $\frac{V_h}{V}$ can be assumed to be 1, because there is little interference of the air reaching the horizontal stabiliser in a T-tail configuration. The mean aerodynamic chord is known as the wings of the A320appu are the same as the ones used in the A320neo. The tail arm l_h is influenced by the shift of the wing and calculated in section 11.4.

Short period assessment

The short period motion has not been considered as a driving parameter for the horizontal stabiliser as the civil requirements are qualitative of nature [64, p 319]. Nevertheless, it is investigated whether this eigenmotion is handled sufficiently during approach conditions. This is done, by comparing the time to halve amplitude of the short period to existing aircraft. Equation 11.2 to Equation 11.4 [64, p 320] have been used to compute the time-to-halve of the short period.

$$T_{\frac{1}{2}} = \frac{4 \ln 2}{L_{\alpha} \left(2 - \frac{c_m + c_{c_d} K_Y^2}{c_A}\right)} \quad (11.2)$$

$$\frac{c_m + c_{m\dot{\alpha}}}{c_{L_{\alpha}}} = -2.2 \frac{c_{L_{h\alpha}}}{c_{L_{\alpha}}} \frac{S_h}{s} \left(\frac{l_h}{\bar{c}}\right)^2 \left(1 + \frac{d\epsilon}{d\alpha}\right) \quad (11.3)$$

$$K_Y^2 = \frac{I_y g}{W \bar{c}^2} \quad (11.4)$$

I_y , the mass moment of inertia, has been determined to be 3 092 400 $kg \cdot m^2$ [47]. The weight used is the maximum landing weight. When the ultimate geometric values for the tail was inserted, the time to half amplitude ended up being 1.096 seconds. This is a typical value for a civil transport aircraft [64].

Recovery from deep stall

In T-tail configurations, the wake of the main wings and fuselage body can interfere with the horizontal stabiliser at very high angles of attack. This causes a reduction of the contribution of the tail plane to the longitudinal stability of 10% to 20% and can cause post-stall instability. For certification, the stall speeds must be demonstrated and safe recovery from deep stall is also required [64, p 53]. The exact interaction of the wake dynamics with the T-tail lift generation is complicated to assess and requires detailed aerodynamic analysis. For now, this effect is simply taken into account by including a 15% safety factor on the horizontal tail surface as dictated by the stability requirements [64, p 324].

11.3.2. Controllability

The controllability was evaluated by looking at the ability to produce enough down-force for sufficient pitch-up angular rotation at take-off. Additionally, trimming is not to be overlooked as it is one of the main functions of the horizontal tail. The considered critical conditions are trimming at approach speed with the flaps deployed and trimming at the point just before stall also with the flaps deployed.

Ensuring rotational capability at take-off

The horizontal tail must be able to provide enough down-force to induce sufficient angular velocity at the rotation speed. Equation 11.5 [64], can be used to compute the necessary horizontal tail volume and with given MAC and tail arm the surface ratio can be calculated.

$$\frac{S_h l_h}{S \bar{c}} = \frac{C_{L_{\max}}}{n_h n_q C_{L_h}} \left\{ \frac{C_{m_{a.c.}}}{C_{L_{\max}}} - \left(\frac{V_{S_1}}{V_R} \right)^2 \frac{x_g - z_T \sum T/W - x_{cg}}{\bar{c}} \right\} + \frac{C_L}{C_{L_h}} \left(\frac{x_q}{\bar{c}} - \bar{x}_{a.c.} \right) \quad (11.5)$$

where:

$$n_h = \frac{x_h - x_g}{l_h} \left(\frac{V_h}{V_R} \right)^2 \text{ and } n_q = 1 + \frac{C_{L_{h\alpha}} \bar{\theta}_R (x_h - x_g)}{C_{L_h} V_R}$$

z_T is the vertical distance between the centre of thrust of the engines and the CG. The angular velocity $\bar{\theta}_R$ is normally approximately equal to 3 deg/s³ but this has been increased to 5 deg/s to take some margin into account. Furthermore, the ratio $\frac{V_{S_1}}{V_R}$ can be assumed to be $\frac{1}{1.05}$ [64, p 325]. The calculation of the aerodynamic parameters is explained in more detail in Torenbeek [64].

Trimming at approach

When the aircraft descends, it has an upward pitching attitude and the flaps are deployed. This generally induces a major moment that has to be counteracted by the tail. From here a moment balance can be constructed [64], as shown in Equation 11.6.

$$\frac{S_h}{S} = \frac{1}{\frac{C_{L_h}}{C_{L_{A-h}}} \frac{l_h}{\bar{c}} \left(\frac{V_h}{V} \right)^2} \bar{x}_{cg} + \frac{\frac{C_{m_{a.c.}}}{C_{L_{Ah}}} - \bar{x}_{ac}}{\frac{C_{L_h}}{C_{L_{A-h}}} \frac{l_h}{\bar{c}} \left(\frac{V_h}{V} \right)^2} \quad (11.6)$$

It is assumed that the maximum (negative) lift coefficient the horizontal tail can produce is equal to -0.8. This is a common value for adjustable tails [64, p 325], which is going to be employed. The DATCOM method [64] is used to estimate all other aerodynamic parameters.

Trimming at stalling conditions

The aircraft should be able to reach stalling attitude according to CS25 [29]. For investigating if the aircraft is capable of trimming at this condition, Equation 11.7 [64, p 324] is used.

$$\frac{S_h l_h}{S \bar{c}} = \frac{C_{L_{\max}}}{n_h C_{L_h}} \left(\frac{C_{m_{a.c.}}}{C_{L_{\max}}} + \bar{x}_{c.g.} - \bar{x}_{a.c.} \right) \quad (11.7)$$

Just like Equation 11.5, with a given tail arm and MAC the necessary horizontal tail surface can be calculated.

11.4. Wing group placement

A common method [64] to reduce the required horizontal tail surface is to shift the wing such that the tail arm and the shift in centre of gravity becomes more favourable for the stability and control. When comparing the A320appu to the A320neo shifting the wing approximately 0.75 m backwards would result in the smallest horizontal tail. However, the shift is also constrained by the balance of the aircraft, see Figure 11.3, and sufficient ground clearance for the added propeller is needed, see Figure 11.4. To create extra space the wing group (and thus also the landing gear) is moved back approximately 1m to increase this ground clearance angle even though it is not optimal for the horizontal wing surface area. Furthermore, the landing gear has been extended by 0.35 m. Initial investigation suggests that the landing gear could be extended by a maximum of 0.5 m, because there seems to be enough spacing between the middle of the fuselage and the first encountered non-structural element, in this case the anti-shock body [21]. The ground clearance angle for the A320appu has then be determined to be 12.7°. This is a reduction compared to the the A320neo which has an angle of 13.1° with fully extended landing gears [21]. It is deemed acceptable as this is similar number and still much more than the clearance angle of the Airbus A321, which is 11.2° with fully extended main landing gear⁴.

³<https://bit.ly/3eF7tj0> retrieved on 15/06/2020

⁴<https://bit.ly/3eFVAtf>, retrieved on 15-06-2020

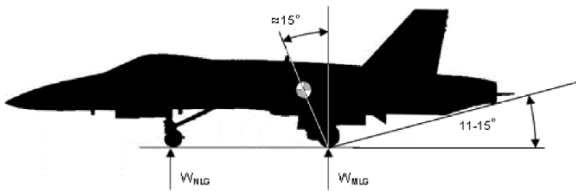


Figure 11.3: Tip back angle of an aircraft [37]

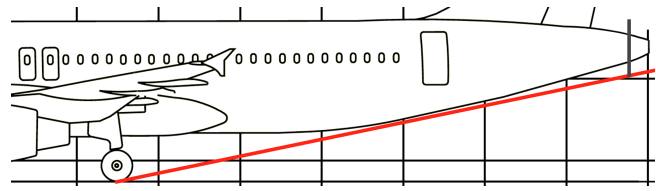


Figure 11.4: Ground clearance angle of propeller [21]

11.5. Horizontal stabiliser geometry

The constraints in regard to the surface area of the horizontal tail and the wing placement have been set. These are used to determine the ultimate geometry of the horizontal stabiliser. This geometry is a trapezoid and can thus be defined by using four parameters, namely the root chord length, the tip chord length, the quarter chord sweep angle and the span. The logic by which they were determined is as follows:

- The root chord length is restricted by the tip chord length of the vertical tail.
- A larger sweep angle is preferred as this postpones the critical mach number. However, this does also increase the required surface area.
- Limiting the span reduces the bending moment and is therefore favourable from a structural point of view but a larger span increases the aspect ratio which increases the lift slope.

In summary, the horizontal tail was designed for a similar $\frac{S_h}{S}$ to the A320neo with an as large as possible sweep angle and small as possible span and root chord. Figure 11.5 shows the interaction between the geometric parameters, the required tail area and how the iteration process was performed until an acceptable initial design has been found. Table 11.3 shows the last iteration; that is the input parameters, the assumptions that have been made and the final geometric parameters. The intermediate DATCOM parameters are shown in Table 11.2.

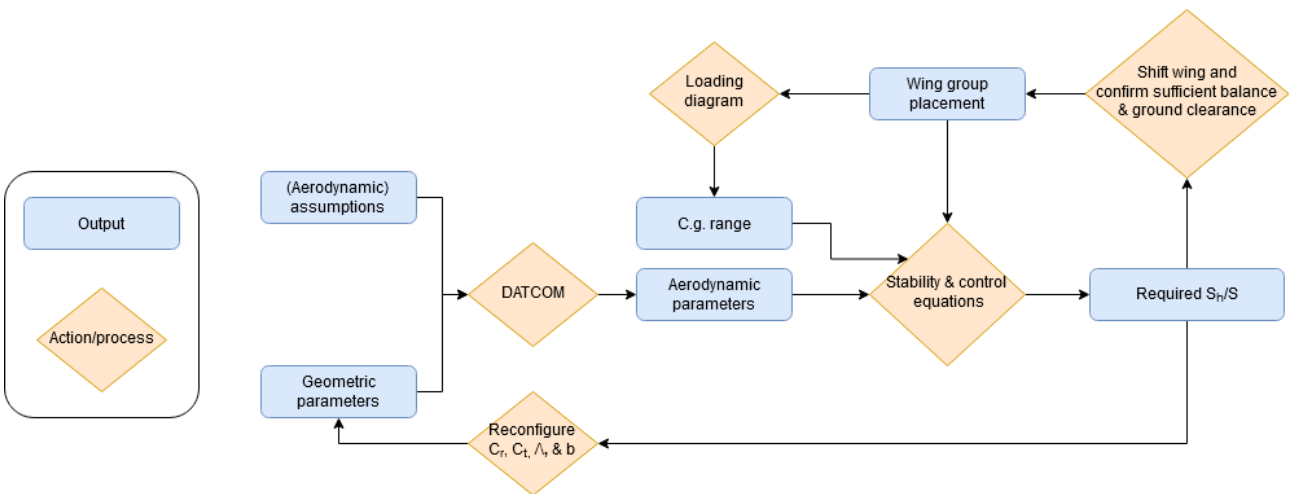


Figure 11.5: Design procedure to determine the horizontal stabiliser geometry

Table 11.2: Results of aerodynamic parameters in different flight configurations when using the DATCOM method of Torenbeek [64]

	Cruise	Approach	At rotation point	Stall
Mach [-]	0.78	0.27	0.22	0.18
C_L [-]	-	2.0	2.8	2.8
$C_{L\alpha_{A-h}}$ [-]	6.88	5.38	5.42	5.35
$C_{L\alpha_h}$ [-]	4.73	-	3.75	4.73
$C_{m_{ac}}$ [-]	-	-1.05	-1.00	-1.06
\bar{x}_{ac} [-]	0.24	0.15	0.15	0.15

Table 11.3: Parameters of the final iteration for the horizontal tail

Horizontal tail geometric parameters		Assumptions for DATCOM estimation	
Area (trapezoidal) [m ²]	36.98	Aerodynamic	
Span [m]	12.75	$\frac{V_h^2}{V}$ [-]	1
Taper Ratio [-]	0.55	η_h landing & take-off [-]	0.97
Lambda -0.25 ht [deg]	22	η_h cruise [-]	0.95
Tail arm [m]	16.6	Speed of sound sea level [m/s]	343
Tip chord length [m]	2.0	Speed of sound 10 km [m/s]	295.5
Root chord length [m]	3.8	$C_{L,max}$ [-]	2.8
A_h [-]	4.40	$C_{Lh,max}$ [-]	0.8
Actual $\frac{S_h}{S}$ [-]	0.2678	c_{m0} (NACA 0012) [m]	-0.014
Main wing & fuselage geometric parameters		$\frac{d\epsilon}{d\alpha}$ (cruise) [-]	0.00335
MAC [m]	4.19	Engines	
XLEMAC [m]	15.6	T/W [-]	0.34
Taper ratio [-]	0.27	b_n [m]	2.224
Tip chord length [m]	1.64	l_n [m]	3.4
Root chord length [m]	6.07	z_t [m]	1.975
Area (trapezoidal) [m ²]	138.1	Flaps	
Span [m]	35.8	$\frac{S_{wf}}{S}$ [-]	0.78
Fuselage diameter [m]	3.95	c'/c [-]	1.1
Lambda -0.25 [deg]	25	μ_1 [-]	0.27
A [-]	9.3	μ_2 [-]	1.03
Wetted Area [m ²]	122.4	μ_3 [-]	0.031
I_{yy} [m ⁴]	3 092 400	Results	
Placement of horizontal tail [m]	33.77	Required $\frac{S_h}{S}$ [-]	0.262
Placement of landing gear [m]	18.6	$T_{\frac{1}{2}}$ [seconds] (at approach)	1.096

11.6. Required vertical stabiliser surface area

The vertical stabiliser can be analysed separately from the horizontal and is mainly responsible for ensuring lateral stability, safe crosswind landings and control with an engine failure. Generally, when using wing mounted engines, the last criteria (control with engine failure) is critical. Assessing crosswind landings accurately requires more detailed (wind tunnel) data because the control derivatives need to be known with great precision to produce accurate results [64]. Furthermore, this criteria is generally not critical for wing mounted engines. Therefore this criteria is not being investigated. The same is true for assessing the lateral stability; thus for now, only control during engine failure is looked at. Since the A320appu does incorporate an s-duct close to the vertical stabiliser, this will interfere with the airflow going across the vertical tail. However since the duct is so small the effect of the duct is assumed to be negligible.

11.6.1. Aspect ratio and T-tail configuration effects

The vertical tail has more variation in shapes than the horizontal tail but here it is also modelled as a standard trapezoid wing, as shown in Figure 11.6. Normally the aspect ratio of the vertical tail can be calculated by dividing the span squared by the area. However, the placement of the horizontal stabiliser on the fin can alter the effective aspect ratio as shown in Figure 11.7. In the case of a T-tail configuration the effective aspect ratio is 1.6 times the geometric aspect ratio. Note that for now a dorsal fin is also included in the A320appu vertical stabiliser in order to postpone stalling of the vertical tail to higher angle of attacks. This is included as contingency but can be removed later if deemed unnecessary.

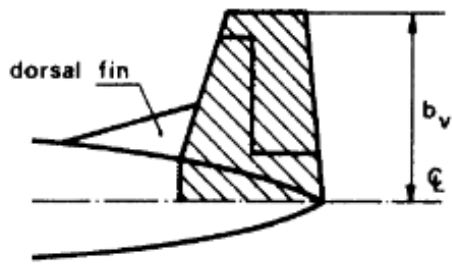


Figure 11.6: Definition of vertical tail area [64, p 331]

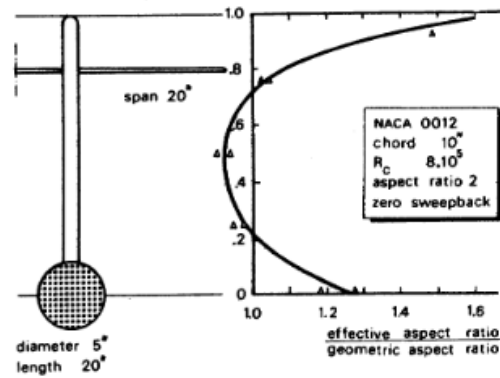


Figure 11.7: Effective aspect-ratio of the fin in combination with the horizontal stabiliser [64, p 53]

11.6.2. Engine failure

While the A320appu has an auxiliary propulsion unit at the back which can be used to create thrust without a yawing moment, the certification will be for a twin engine jet, so this factor has to be ignored. The possible critical moments for engine failure are during cruise and during take-off just after V1 when the take-off is not to be aborted anymore. There is a coupling effect in cruise between roll and yaw but not during take-off as roll and yaw has to be avoided to remain on the runway. Because of this interaction, it is hard to say which one of the two is critical thus both are investigated.

Engine failure during cruise

To assess the engine failure during cruise, Figure 11.8 has been used. $\Delta T_e y_e$ is the yawing moment induced by the engine thrust T_e times y_e , which is the lateral distance between the engine and the CG. The C_L has been calculated at cruise altitude and V_{mca} using Equation 11.8.

$$L = W \cos(\phi) \tag{11.8}$$

Where a bank angle of 5 degrees was assumed as that is an imposed limitation on the bank angle [64, p 333]. In the case of the A320appu it is possible to use a negative sideslip angle and compensate this with a bank angle roll suggesting that for the vertical tail size the take-off condition is critical. Then the horizontal tail surface can be calculated by dividing the resulting term from the graph by $\eta_v = \frac{V}{V_v}$ and $C_{Y_v \beta}$ which was estimated using the DATCOM method[64].

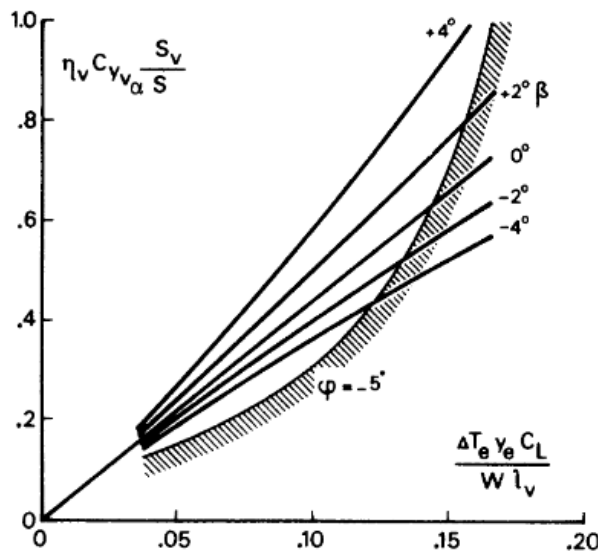


Figure 11.8: Roll and sideslip effects on vertical tail sizing [64, p 335]

Engine failure during take-off

The induced engine moment during take-off has to be compensated completely by the rudder deflection as no sideslip or bank angle can be present in order to remain on the runway. It is assumed that the lateral force is then only induced by the vertical tail because of the rudder deflection meaning $S = S_r$. Furthermore the control derivative has been linearised to ease calculations, thus $C_Y = C_{Y_{\delta_r}} \delta_r$. Using this assumption a moment equilibrium can be set up, as seen in Equation 11.9:

$$\Delta T_{ey_e} = \frac{1}{2} \rho V_v^2 S C_Y l_v = \frac{1}{2} \rho V_v^2 S_r C_{Y_{\delta_r}} \delta_r l_v = \frac{1}{2} \rho V_v^2 \frac{S_r}{S} \frac{S_v}{S} S C_{Y_{\delta_r}} \delta_r l_v \tag{11.9}$$

$C_{Y_{\delta_r}}$ can be calculated using Equation 11.10. More information on the meaning of the variables can be found in [53, p 462].

$$C_{Y_{\delta_r}} = C_{Y_{v_\beta}} (k' K_b) \left(\frac{c_{l_\delta}}{(c_{l_\delta})_{theory}} \right) (c_{l_\delta})_{theory} \frac{S_v}{S} = C_{Y_{v_\beta}} C_1 \frac{S_v}{S} \tag{11.10}$$

C_1 is a constant summarising the relation between $C_{Y_{\delta_r}}$ and $\frac{S_v}{S}$. Rewriting Equation 11.9 by inserting Equation 11.10 and rearranging yields Equation 11.11:

$$\frac{S_v}{S} = \sqrt{\frac{2 \Delta T_{ey_e}}{\rho V_1 \left(\frac{V_v}{V}\right)^2 \frac{S_r}{S} C_{Y_{v_\beta}} C_1 \delta_{r_{max}} l_v}} \tag{11.11}$$

11.7. Vertical stabiliser geometry

The determination of the vertical tail geometry follows a similar process as for the horizontal tail. Again, the initial constrain comes from the required tail surface area. Since the wing is modelled as a trapezoid, the remaining four design parameters are the root chord length, the tip chord length, the quarter chord sweep angle and the span. The length of the tip chord of the vertical tail should be larger than the root chord length of the horizontal tail. The same criteria as in section 11.5 are used, however the span has an extra limitation to ensure structural integrity. The T-tail configuration introduces additional structural problems in regard to flutter and/or divergence and thus, the aspect ratio is limited to approximately 1.2 [64]. In summary, the vertical tail was designed for a minimal $\frac{S_v}{S}$ with an as large as possible sweep angle of at least 30° and an as small as possible span and root chord. Figure 11.9 shows how the iteration process was performed until an acceptable initial design has been found. Table 11.4 shows the last iteration; that is the assumptions that have been made, intermediate parameters from the DATCOM/Roskam method and also the final geometric parameters.

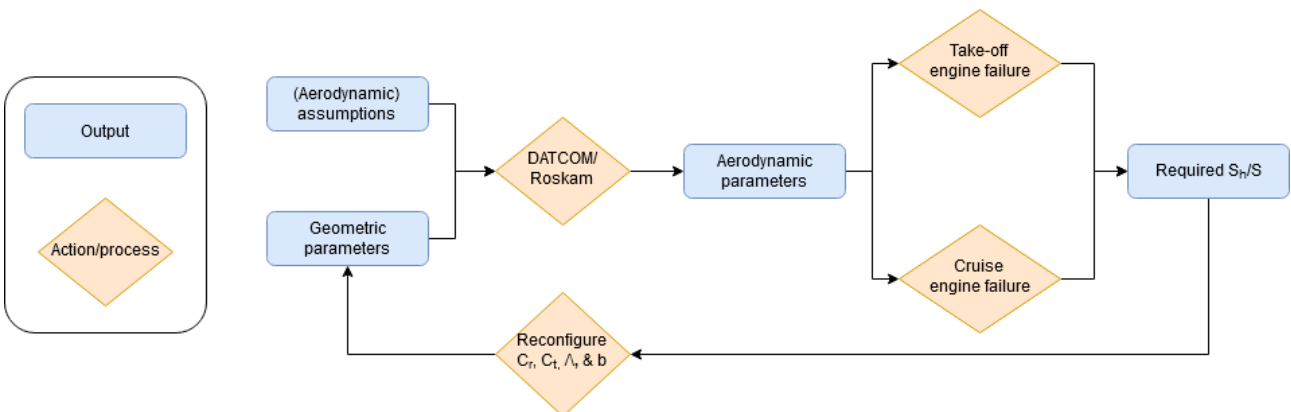


Figure 11.9: Design procedure to determine the horizontal stabiliser geometry

Table 11.4: Final geometric parameters of the vertical tail, the assumptions made for the calculations and the intermediate aerodynamic coefficients

Geometric parameters		Aerodynamic (& other) assumptions	
Area (trapezoidal) [m ²]	24.75	$\frac{V_h^2}{V}$ [-]	0.9
Height [m]	5.5	η_v [-]	0.95
Taper Ratio [-]	0.8	Speed of sound sea level [m/s]	343
Lambda -0.25 -vt [deg]	34	Speed of sound at 11000m [m/s]	295.5
Tail arm [m]	16.4	Mach at V_1 [-]	0.262
Tip chord length [m]	4.0	Stall mach during cruise [-]	0.331
Root chord length [m]	5.0	k' [-]	1.2
Actual $\frac{S_v}{S}$ [-]	0.179	K_b [-]	1
$A_{v,eff}$ [-]	1.195	$\frac{c_{l\delta}}{(c_{l\delta})_{theory}}$ [-]	0.92
$A_{v,geometric}$ [-]	1.22	$c_{l\delta,theory}$ [-]	4.2
Wing area [m ²]	138.082	$V_1 \frac{m}{s}$	90
$\frac{S_v}{S}$ [-]	0.182	V_{mca} at sea level [m/s]	56.59
Estimated (aerodynamic) coefficients		Sideslip angle [deg]	-5
$C_{y_{v,theta}}$ at sea level [-]	2.036	One engine thrust [N]	55
$C_{y_{v\beta}}$ at 10000m [-]	2.041	Engine moment arm [Nm]	5.9
V_{mca} at 10000m [m/s]	97.815	Weight (MTOW) [N]	735 750
C_L at mca [-]	2.78	Max rudder deflection [deg]	25
$\eta_v C_{y_{v\beta}} \frac{S_v}{S}$ [-]	0.23	$\frac{S_v}{S_r}$ [-]	0.27
Required $\frac{S_v}{S}$ [-]	0.178		
C_1 [-]	0.106		

11.8. Structural considerations

T-tail configurations are notoriously problematic in regard to their structural integrity. The stresses in the vertical tail are high because it has to carry the load from the horizontal tail to the fuselage. Furthermore, there can also be unfavourable aeroelastic effects (flutter) and divergence when loads with specific frequencies are introduced. This chapter discusses a critical static load case for both the horizontal and the vertical tail. Namely, at maximum airspeed with maximum lift coefficient as that induced the highest lift forces. Furthermore, a preliminary look into the modal analysis of the vertical tail is made in order to compute the natural frequencies and assess if the displacements are so large that they can cause unfavourable (aeroelastic) effects. The A320neo empennage is composed of a mix of composite materials. The main reason is because composites provide a lightweight and strong structure which is more resilient against the aforementioned aerodynamic and structural loads. The same rationale is adapted in the A320appu design. Primarily, only carbon fibre reinforced plastic is considered and applied.

11.8.1. Horizontal tail

While generally the load case of the horizontal tail in a T-tail configuration is the same as in a conventional configuration, the size of the T-tail is larger. Thus, the loads, and most importantly the bending moment at the root of the horizontal tail, are larger. These additional stresses are investigated in this section and a preliminary design of the structural elements in the horizontal tail is proposed.

Load case, cross section modelling and stresses

The horizontal tail has been investigated for the load case shown in [Figure 11.10](#). The cross section has been modelled as a thin walled rectangle containing different stiffener elements, namely a front and back spar and a variable amount of stringers. The highest forces are experienced at the section where the horizontal tail is fastened to the vertical tail as there the highest bending moment is present. In an effort to homogenise the stresses and save weight, the load carrying part of the horizontal tail is modelled as a square frustrum. In this way both the chord thickness and chord length vary along the span. The root and tip chord length have already been determined in [section 11.5](#), where the load carrying structure is assumed to be the same dimensions and the width of the section is still open to change. Using the *Sectionproperties* module on Python⁵, the cross sections are constructed discretely along the span of the horizontal tail. Subsequently, the load

⁵<https://sectionproperties.readthedocs.io/en/latest/> retrieved on 15/06/202

cases determined in Figure 11.10 are applied to retrieve the (2D) stress distributions, as seen in Figure 11.11. However in order to determine what the dimensions and thicknesses of the stiffening elements need to be, the failure mode for composite structures need to be determined. Note, Figure 11.10 does not show a top view but the same kind of geometry is assumed in both directions. Additionally, Figure 11.11 shows an exaggerated thickness to make the plot more readable; for the calculation a thickness of 5 [mm] was used.

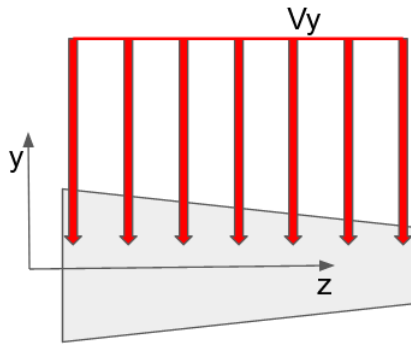


Figure 11.10: Front view of considered loading case of the horizontal tail

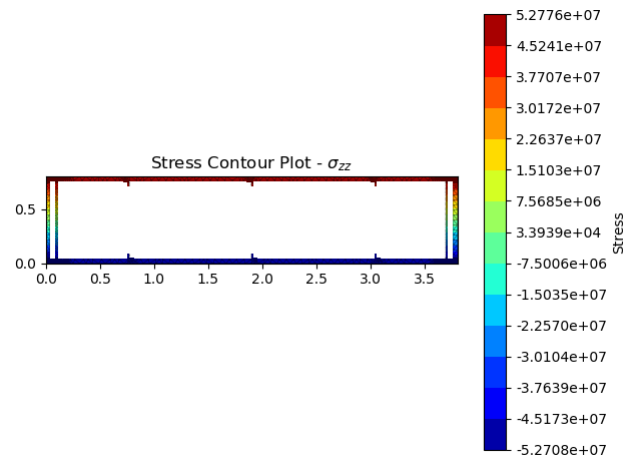


Figure 11.11: Normal stresses on the cross section at the root of the horizontal tail. $V_y = 27.3 \text{ kN/m}$

Failure analysis

Fibre-reinforced polymer composites are orthotropic materials as their strength parallel to their fibres is stronger than their strength orthogonal to their fibres. In order to incorporate this behaviour of composites the Tsai-Hill failure criteria, see Equation 11.12 has been used as a failure criterion for both compression and tension. The ultimate strength along the fibres (longitudinal) is denoted by σ_L , orthogonal to their fibres denoted by σ_T and shear strength τ_{LT}

$$\left(\frac{\sigma_L}{\sigma_{L,U}}\right)^2 - \frac{\sigma_L\sigma_T}{\sigma_L^2} + \left(\frac{\sigma_T}{\sigma_{T,U}}\right)^2 + \left(\frac{\tau_{LT}}{\tau_{LT,U}}\right)^2 \geq 1 \tag{11.12}$$

were:

$$\begin{aligned} \sigma_L &= \sigma_z \cos(\theta)^2 + 2\tau_{xy} \sin(\theta) \cos(\theta) \\ \sigma_T &= \sigma_z \sin(\theta)^2 - 2\tau_{xy} \sin(\theta) \cos(\theta) \\ \tau_{TL} &= -\sigma_z \sin(\theta) \cos(\theta) + \tau_{xy} (\cos(\theta)^2 - \sin(\theta)^2) \end{aligned} \tag{11.13}$$

The angle of the fibres is noted by θ and can be varied in as preferred.

Of course the failure depends on the specific material that is used which in this case is going to be standard carbon fibre unidirectional (CFUD). As can be seen in Table 11.5 has excellent strength both in compression and tension while having a lower density than aluminium.

Table 11.5: Material properties of 120°C fibre/epoxy resin carbon fibre unidirectional (CFUD) cure, with a fibre content of 60%⁶

Variable	Value
$\sigma_{L,U}$ tension [MPa]	1 500
$\sigma_{L,U}$ compression [MPa]	1 200
$\sigma_{T,U}$ tension [MPa]	50
$\sigma_{T,U}$ compression [MPa]	250
$\tau_{LT,U}$ [Mpa]	70
ρ [kg/m ³]	1.6

Structural elements

According to the Tsai-hill criteria the horizontal tail has very little chance of failing in strength even with a safety factor of 20% taken into account. This can be seen in Table 11.12 where the criteria along the span of the

⁶http://www.performance-composites.com/carbonfibre/mechanicalproperties_2.asp, retrieved on 18-06-2020

horizontal tail is shown. The optimum fibre angle ended up being around 40 degrees which has been computed with the numerical model⁷. The spikes in the shear strength are caused by imperfections in the mesh, causing high shear flow concentrations at the corners and at the connections of the different elements. For now this has not been corrected by smoothing the cross sections as these stress concentrations are also to be expected in reality, although optimisation can be achieved by curving the corners and connections. This indicates that weight can be saved by reducing the amount of structural elements in the tail or reducing the thickness of these elements. For now this iteration is not performed yet and the geometry as shown in Figure 11.11 is not adjusted. The reason for this is that the assessed failure criteria is not sufficient in order to finalise the design. While strength was assessed, often it is the stiffness that is the limiting factor. Thus this initial design of the horizontal tail should be investigated further in regard to these aspect in a later design stage.

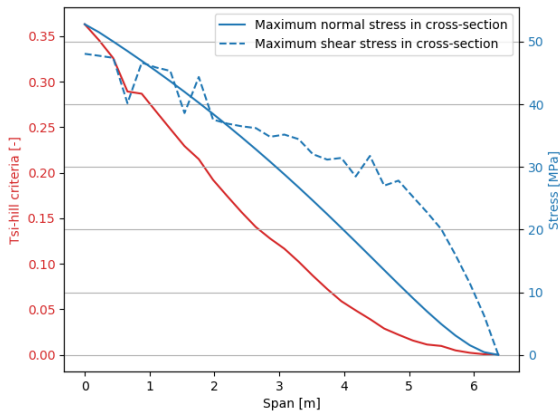


Figure 11.12: Tsai-hill criterion vs maximum normal and shear stress along the span of the wing discretised in 15 sections

Table 11.6: Structural support of the horizontal tail wing box

	Skin	Spars	Stringers
Number	-	2	3
Thickness [m]	0.005	0.005	0.005
Length [m]	3.9-2	0.1 (spar cap)	0.05
Width [m]	0.8-0.2	0.8-0.2	0.05

11.8.2. Vertical tail

The load case of the vertical tail in a T-tail configuration is different from a conventional configuration because of the added axial force that has to be transferred from the horizontal tail to the fuselage. Carrying the load itself is not the only problem as a major compressive force might lower the natural frequency and compromise the integrity of the structure. A preliminary investigation in both problems is performed in this subsection.

Static load case and cross section modelling

The considered loading case for the vertical tail is shown in Figure 11.13. Here, the exact same modelling approach has been used as for the horizontal tail but with different chord lengths, taken from section 11.7. When applying $N = 348 \text{ kN}$ and $V_y = 110 \text{ kN}$, the resulting stresses in the structure were so low that a thin box ($t = 5 \text{ mm}$) without any stiffening elements would be sufficient to carry the resulting stresses (approximately 20 MPa). This means that strength is not the limiting factor for the design of the vertical tail and thus a preliminary look is taken at how the stiffness plays a role.

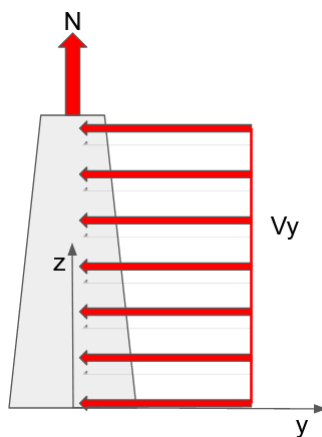


Figure 11.13: Front view of considered loading case of the vertical tail

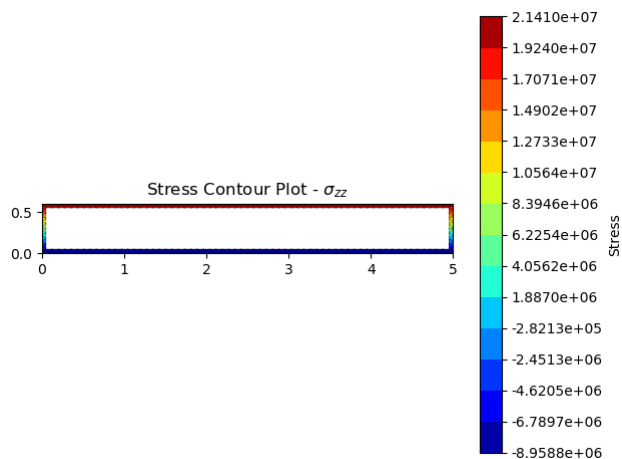


Figure 11.14: Normal stresses on the cross section at the root chord of the vertical tail⁸

⁷Note that in reality the mirrored loading case occurs as well, for which the optimal angle would be -40 degrees.

Modal analysis

The reason that T-tails are particularly prone to flutter is due to coupled interaction between the vertical tail and the horizontal tail. The deflections of the vertical tail can cause the elevator to respond unfavourably creating an amplifying system. To investigate this effect detailed analysis on the aerodynamics of the elevators and bending of the vertical tail are required. This is saved for a later design stage, however, in order to perform a preliminary investigation of this phenomenon, the goal for now is twofold. First, the natural frequencies of the vertical tail is estimated as these are to be avoided at all cost and secondly, the deflections along the beam are computed as these need to be minimised in order to limit the effect of flutter. To find the natural frequency of the vertical tail a finite element mesh was created as shown in [Figure 11.15](#). This splits up the vertical tail in n elements and $n + 1$ nodes, each with a different stiffness, mass, inertia and cross-sectional area but a constant length l .

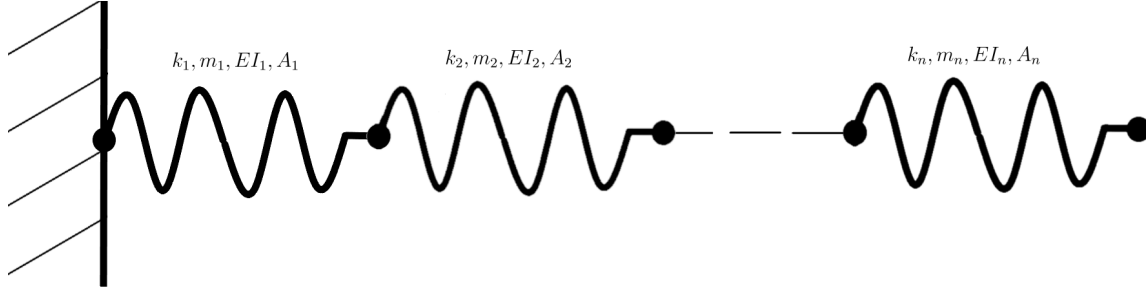


Figure 11.15: Discretisation of vertical tail, modelled as cantilever beam with varying inertia, stiffness, mass and cross-sectional area.

The equations of motion for this system can be written as [Equation 11.14](#) [55].

$$M\ddot{z} + (K + NK_{geo})\dot{z} = F(t) \quad (11.14)$$

where M is the global mass matrix, N the axial force (negative for compression positive for tension), K the global stiffness matrix and K_{geo} the geometric stiffness matrix. A node has four degrees of freedom; two displacement values (z_1, z_2) and two slope angles (θ_1, θ_2), one displacement and one slope per node. When assuming that the transverse displacement is a cubic function and the boundary conditions of [Equation 11.15](#) are applied, it can be shown that four admissible shape functions are as in [Equation 11.16](#) [55] [23].

$$\begin{aligned} z = 0 &\rightarrow w(0) = w_1 & \phi_1 &= 1 - 3\left(\frac{z}{l}\right)^2 + 2\left(\frac{z}{l}\right)^3 \\ z = 0 &\rightarrow \frac{\partial w(0)}{\partial x} = \theta_1 & \phi_2 &= z - 2l\left(\frac{z}{l}\right)^2 + l\left(\frac{z}{l}\right)^3 \\ z = l &\rightarrow w(l) = w_2 & \phi_3 &= 3\left(\frac{z}{l}\right)^2 + 2\left(\frac{z}{l}\right)^3 \\ z = l &\rightarrow \frac{\partial w(l)}{\partial x} = \theta_2 & \phi_4 &= -l\left(\frac{z}{l}\right)^2 + l\left(\frac{z}{l}\right)^3 \end{aligned} \quad (11.15) \quad (11.16)$$

Then the local mass matrix of element l , being the element between the two adjacent nodes, is a 4x4 matrix because of the four degrees of freedom with the terms as in [Equation 11.17](#) [23]:

$$m^{(l)} = \rho \begin{bmatrix} \int_0^l \phi_1 \phi_1 A(z) dz & \int_0^l \phi_1 \phi_2 A(z) dz & \int_0^l \phi_1 \phi_3 A(z) dz & \int_0^l \phi_1 \phi_4 A(z) dz \\ \int_0^l \phi_2 \phi_1 A(z) dz & \int_0^l \phi_2 \phi_2 A(z) dz & \int_0^l \phi_2 \phi_3 A(z) dz & \int_0^l \phi_2 \phi_4 A(z) dz \\ \int_0^l \phi_3 \phi_1 A(z) dz & \int_0^l \phi_3 \phi_2 A(z) dz & \int_0^l \phi_3 \phi_3 A(z) dz & \int_0^l \phi_3 \phi_4 A(z) dz \\ \int_0^l \phi_4 \phi_1 A(z) dz & \int_0^l \phi_4 \phi_2 A(z) dz & \int_0^l \phi_4 \phi_3 A(z) dz & \int_0^l \phi_4 \phi_4 A(z) dz \end{bmatrix} \quad (11.17)$$

For the local stiffness matrix and geometric stiffness matrix a similar symmetric matrix can be set up. Row i and column j of the 4x4 matrices can be found by [Equation 11.18](#) for the local stiffness matrix and [Equation 11.19](#) for the local geometric stiffness matrix.

$$k_{i,j}^{(l)} = \int_0^l \phi_i'' \phi_j'' EI(z) dz \quad (11.18)$$

$$k_{geo_{i,j}}^{(l)} = \int_0^l \phi_i'' \phi_j'' dz \quad (11.19)$$

To convert the local matrices to global matrices the local matrices were assembled in such a way that they are placed on the diagonal of the global matrices while adding the 2x2 overlapping parts, as shown on [Figure 11.16](#) for the mass matrix.

⁸Note that the thickness has been exaggerated to make the plot more readable, for the calculations $t = 5 \text{ mm}$ has been used.

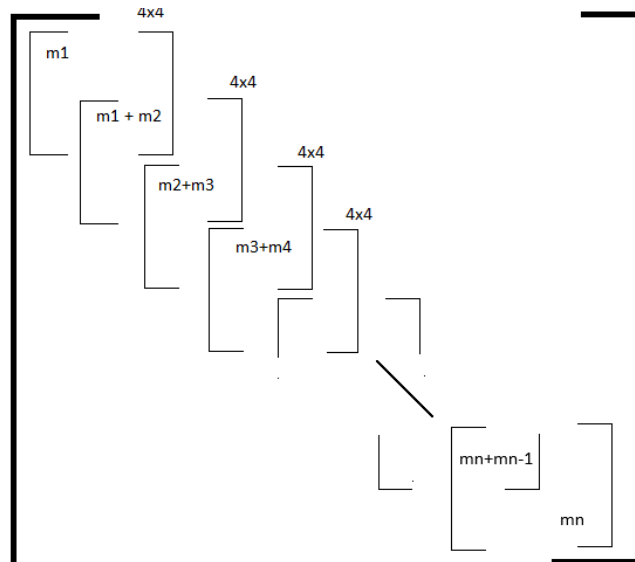


Figure 11.16: Assembling local mass matrices to create the global matrix

The same can be done to create the global stiffness and geometric stiffness matrix. The only thing left to do before being able to solve Equation 11.14 for the eigenvalues is to impose the boundary conditions. This is done by removing the first and second columns and rows from the global matrices. This corresponds to the conditions of a cantilevered beam as the displacement and the slope angle of the first node are zero. Then, by solving Equation 11.20 for the natural frequency, f_n , the value can be determined.

$$(K - PK_{geo}) = (2f_n\pi)^2 M \tag{11.20}$$

Given the previous global matrices the deflections in a static loading case can simply be found by applying Equation 11.21, where F is the global (static) force vector.

$$U = (K - K_{geo})^{-1}F \tag{11.21}$$

For this, the global force matrix needs to be assembled by the local force vectors for element l the local (shear) force vector and local moment, when the loads and moments on node i are V_{y_i} and M_i respectively, is as equation Equation 11.22.

$$f^l = [V_{y_l}, M_i, V_{y_{l+1}}, M_{l+1}] \tag{11.22}$$

Assembling this vector in the same way as shown in Figure 11.16, but this time in 1D, yields the global force vector. The lowest found natural frequency is equal to **76 Hz** and the transverse displacements can be found in Figure 11.17, where the sign is dependent on the direction of the shear force and is arbitrarily negative in this case.

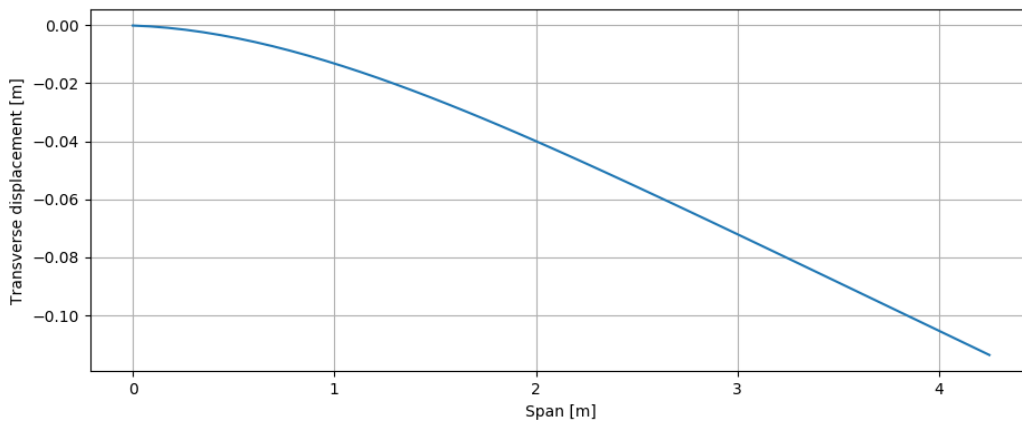


Figure 11.17: Transverse displacement along the span of the vertical tail

While the transverse displacement seem to high to be able to keep it as is, it becomes apparent from section 11.9 that the accuracy of the model is questionable. The reasons for these inaccuracies might be caused by improper

discretisation along the length or that the assumed frustrum geometry is not representative of the tail. Therefore, the structural elements of the vertical tail are not yet determined after the aforementioned analysis and more enquires about the vibrations should be made at a later design stage.

11.9. Verification and validation

The following section looks at the verification of the Tsai-hill criteria and the validation of the stress distribution and the displacements.

11.9.1. Verification

The python module has already extensively been verified in [subsection 9.6.5](#) thus in this section only the Tsai-hill criterion is looked at.

Tsai-hill

The algorithm calculating the maximum Tsai-hill criterion is verified by simply calculating one case by hand and comparing the values. The highest Tsai-hill value in the horizontal tail load case should be found when looking at the highest stress value as found in [subsection 11.8.1](#) (52.71 MPa), while there is no shear stress to relieve this stress in the transverse direction when using an angle, which in this case is set to 38.57°, inserting it in [Equation 11.12](#) and [Equation 11.12](#) using the ultimate values from [Table 11.5](#) and a safety factor of 1.2, yields:

$$\begin{aligned}\sigma_L &= 52.71 \cos(38.57) = 32.22 \\ \sigma_T &= 52.71 \sin(38.57) = 20.48 \\ \tau_{TL} &= -52.71 \sin(38.57) \cos(38.57) = -25.68\end{aligned}\quad (11.23)$$

$$1.2 * \left[\left(\frac{32.22}{1500} \right)^2 + \left(\frac{20.38}{50} \right)^2 - \frac{32.22 * 20.38}{1500^2} + \left(\frac{-25.68}{70} \right)^2 \right] = 0.363 \quad (11.24)$$

This value is indeed the same as shown in [Table 11.12](#) at the root of the horizontal tail.

Natural frequency

The simple [Equation 11.25](#) can be used to calculate the natural frequency of a system with constant mass and stiffness. For a rod the stiffness is equal to $k = \frac{3EI}{l^3}$ [23]. When inserting the same values for the Young's modulus and the average values for the mass and inertia along the discretisation (112 GPa, 113 kg and 0.00456 m⁴), it results in a natural frequency of 67 Hz. While there is still about a -11% discrepancy between the values, this can be attributed to making the assumption of a rod.

$$\omega = \sqrt{\frac{k}{m}} \quad (11.25)$$

However it is important to keep in mind that the effect of the compressive force is not yet taken into account by [Equation 11.25](#), while it is in the model, from which you would expect an even lower natural frequency.

11.9.2. Validation

While the stress distributions have been verified, it is not yet sure if the model does actually represent the actual vertical tail. To validate the model, it is compared to a CATIA simulation in the following to sections, with regard to stress, displacements and natural frequency.

Stress distributions

To validate the stress distribution and the displacements for a static load case, a load case similar to [Figure 11.13](#) was applied with $N = 348 \text{ kN}$ and $V_y = 26.8 \text{ kN/m}$. However, now the vertical tail was assumed to be from aluminium as CATIA does not allow for composite structures. The cross section in the middle of the vertical tail ($z = 2.125$) was investigated in regard to the maximum Von Misses stress. The model of [subsection 11.8.2](#) predicts a maximum Von Misses stress of 9.6 MPa at the cross section. The same vertical tail was analysed in CATIA, as shown in [Figure 11.18](#), which provided a value of 11.3 MPa. A difference of 17.7%. This discrepancy can mostly be attributed to the difference of geometry of the vertical tail in the CATIA model and the square frustrum that was used in the model. However with discrepancies this large, it is not possible to validate the used model.

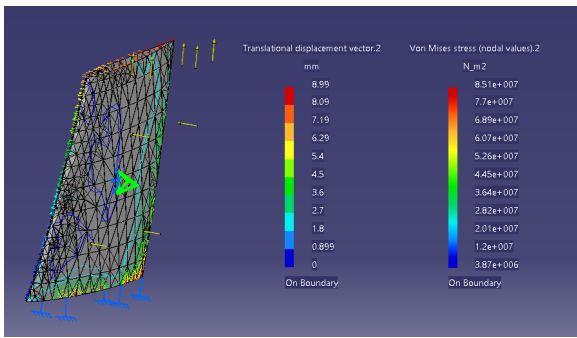


Figure 11.18: Von Mises stresses and displacements of the vertical tail as calculated by CATIA.

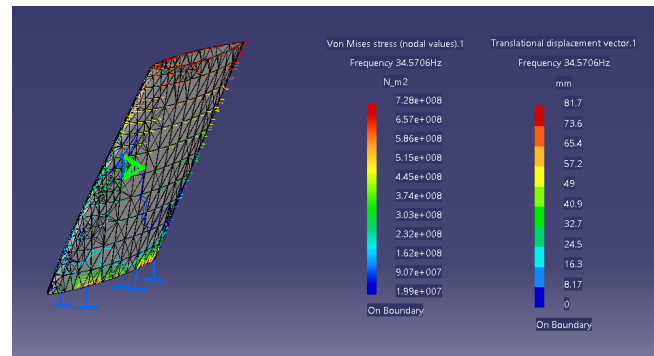


Figure 11.19: First eigenmotion of the vertical tail shown in CATIA including the induced stresses and displacements.

Natural eigenfrequencies & transverse displacement

In order to validate the modal analysis as performed in subsection 11.8.2, a vibrational analysis of the same vertical tail, but from aluminium instead of composite, was performed in CATIA of which the result is shown in Figure 11.19. The first eigenfrequency as calculated by CATIA ended up being 34.6 Hz versus 42.1 Hz as predicted by the model of subsection 11.8.2, a difference of 18%. Furthermore the larger the modes the less accurate the model becomes as it overshoots the frequencies compared to the predicted values from CATIA (247 Hz vs 113 Hz, and 683 Hz vs 129 Hz for the 2nd and 3rd modal frequencies). Therefore, while this tool can be used to determine an initial lowest eigenfrequency, it must be kept in mind that the tool seems to over-predict the values. The transverse displacement at the tip of the vertical tail seems to have a similar inaccuracy where the displacement predicted by the model is equal to 12.1 cm while CATIA of 9.0 cm. All in all though, the discrepancies are assumed to be large to use them to design the structural elements of the vertical tail and more investigation is needed.

11.10. Conclusion

The analysis of this chapter yielded a preliminary design for the empennage. The stability and control aspect was investigated and provided the values of Table 11.7 for the outer geometry of the horizontal and vertical tail.

Table 11.7: Summary of horizontal and vertical tail properties

	Horizontal tail	Vertical tail
Area (trapezoidal) [m ²]	36.98	26.95
Span [m]	12.75	5.125
Lambda -0.25 ht [deg]	22	34
Tip chord length [m]	2	4
Root chord length [m]	3.8	5.8
Geometric A [-]	4.4	1.12
Actual $\frac{S_h/v}{S}$ [-]	0.268	0.182

The structural aspect was also taken into consideration but there are severe limitations to the analysis the consequences of induced vibrations. This has not been successfully assessed yet and has to be looked at later design stages. However, for now it can be stated that the current empennage complies with the requirements regarding the stability and control. namely requirement FMP-Sys-09⁹ and REG-Sys-40¹⁰.

11.11. Recommendations

The analysis for the empennage is far from complete. There are a lot of aspects still to be investigated. A few important considerations that were encountered during the performed analysis but which were not yet assessed due to limitations in time, data and/or expertise are given here.

11.11.1. Stability & Control

The following recommendation are with regard to assessing the stability and control of the aircraft.

⁹The aircraft shall passively be statically and dynamically stable

¹⁰The aircraft shall comply with CS 25 safety regulations.

Out of trim manoeuvres

During normal flight operations, the aircraft will deviate from trim conditions to perform manoeuvres. The controllability of these manoeuvres need to be ensured by a proper tail size. However this investigation is kept for a later design stage since there are a lot of manoeuvres that have to be kept into account, while most of them will not be the limiting criteria [64].

Crosswind landings

An airline should be able to perform landings under severe weather conditions. Heavy crosswinds cause a yawing moment that the vertical tail should be able to counteract. The reason it is not investigated now is that to calculate the necessary tail surface, detailed knowledge of multiple control derivatives has to be known as the result is very sensitive to the exact values of these control derivatives. Furthermore for wing mounted engines, the controllability during one engine failure is often limiting [64]. In a next design stage, it should be checked if the aircraft does also comply to this requirement.

Lateral stability

While the longitudinal stability was taken under consideration, the lateral stability is not. Again, engine failure is most often the limiting factor and assessing the lateral stability is a complicated procedure [64]. Thus for now this is left untouched but at a later moment, the dynamic lateral stability should be investigated by looking at the eigenmotions of the plane and the static lateral stability should be ensured during normal flight operations.

11.11.2. Structural analysis

The following recommendations concern the structural analysis of the empennage.

Failure modes

At the present moment, only the Tsai-hill criterion is used in regard to the failure in the composite design. In reality predicting the failure of composites is complicated and is not captured by only one criterion. Later, more investigation needs to be done in regard to more specific failure criteria and the failure modes of the composite tail.

Modal analysis

The current modal analysis is not in itself accurate enough to be able to determine the required stiffness of the tail. Furthermore, the response to vibrational forces and other dynamic elements, e.g. the interaction of the displacement of the vertical tail and the lift distribution of the horizontal tail, should be looked at in more detail.



A320appu Analyses

Complete Aircraft Performance Analysis

The A320appu is designed to ensure that many performance parameters are the same or improved compared to the design of the A320neo. Due to a different configuration, different weights the various performance requirements are all analysed individually, mainly examining its deviation from the A320neo performance. In [section 12.1](#) the requirements related to aircraft performance are listed and briefly discussed. The requirements are analysed and validated in [section 12.2](#). The chapter is concluded with the electrical- and hardware-software block diagrams. These describe how power and data flows through the aircraft, in order to power all subsystems and to have the APPU system perform optimally.

12.1. Requirements

The following requirements are related to the aircraft performance, most of all the ranges achieved and requirements related to the take-off, landing and climb of the aircraft.

- FMP-User-01:** The aircraft shall have the same range as the Airbus A320neo WV055.
- FMP-User-01.1:** The aircraft range at maximum payload and maximum take-off weight shall be 4500 *km*.
- FMP-User-01.2:** The aircraft range at maximum fuel and maximum take-off weight shall be 6250 *km*.
- FMP-User-01.3:** The aircraft ferry range shall be 7900 *km*.
- FMP-Sys-05:** The landing distance of the aircraft shall not increase more than 5% from the total landing distance of the Airbus A320neo WV055 at the same weight and altitude.
- FMP-Sys-06:** The take-off distance of the aircraft shall not increase more than 5% from the total take-off distance of the Airbus A320neo WV055 at the maximum take-off weight and altitude.
- FMP-Sys-07:** The climb angle during initial climb of the aircraft shall not decrease by more than 5% from the climb angle of the Airbus A320neo WV055 at the maximum take-off weight and altitude.
- FMP-Sys-08:** The climb rate during initial climb of the aircraft shall not decrease by more than 5% from the climb rate of the Airbus A320neo WV055 at the maximum take-off weight and altitude.

12.2. Performance analysis

In this section the performance of the complete A320appu is analysed. The performance consists of the range of the aircraft, and its flight characteristics, such as take-off performance and maximum climb angle. First, the flight profile is explained. Next, the process of creating the payload-range diagrams is elaborated with a verification method included. The section is concluded with an analysis on the landing, take-off and climb performance.

12.2.1. Flight profile

The typical mission for which the A320appu was designed for is that of a mission from Amsterdam to Lisbon, at a cruising altitude 36 000 *ft*. The take-off manoeuvre and climb out together with taxi are part of the Landing Take-off (LTO) cycle up to 3 000 *ft*. After this a climb phase takes place taking the aircraft to an altitude of 36 000 *ft*. From here the cruise phase initiates rising slightly to the cruise altitude. The length of this mission is just under 1 000 *nm*, a distance of 1 900 *km*. The typical mission duration for which is designed is around this number. Other mission analysis done for single aisle aircraft are often in this range or slightly lower.

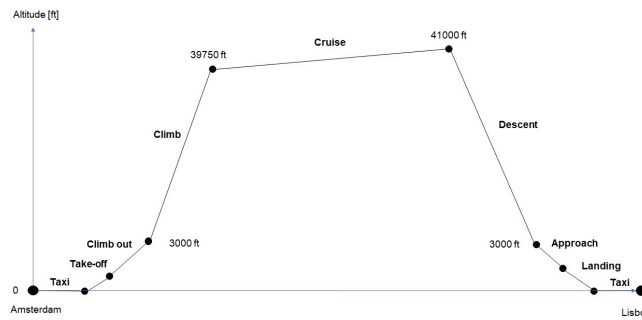


Figure 12.1: Flight profile of a typical mission

12.2.2. Payload-Range diagrams

Payload range diagrams are of importance for airliners. They give a quick overview of the potential of an aircraft and thus an indication for what profitable missions are. First the procedure for constructing a payload range diagram is explained, followed by the assumptions made. After that, the results are shown. The results consist of the payload range diagram and a diagram showing the possible CO₂ savings for a certain distance, when comparing the A320appu to the A320neo. Next, the simulation is verified by comparing the simulation results to the results obtained by using the Breguet Range Equations. A typical payload range diagram consists of three ranges:

- The harmonic range, at maximum PL at MTOW
- Range at maximum fuel at MTOW
- The ferry range, at maximum fuel and no PL

Having a large harmonic range is the most important for airlines, since flights are more profitable when the maximum amount of payload is taken. The quickest way to construct the diagram is by determining the three ranges. Simply insert the amount of payload and fuel for each point into the analysis, calculate the maximum distance, put them in the graph and connect them with straight lines. In this analysis however, it is desired to also obtain the CO₂ saved for a certain mission distance. Hence, the ranges for numerous fuel amounts are calculated. When the MTOW was exceeded, payload was removed. If the fuel tanks were full, further payload was removed. The APPU system was always utilised to its full potential, up to the point where not enough hydrogen was available. From that moment on the APPU contribution was decreased such that it could just manage with the available hydrogen.

For this analysis it was assumed reserve fuel had to be taken into account. Enough fuel had to be left at the end of the descent to cruise for an extra 45 minutes. For the Breguet range analysis it was assumed that the L/D was constant. The Breguet equations are different for jet aircraft compared to propeller aircraft. However, the A320appu is both. It was assumed for this analysis that first all hydrogen meant for the cruise phase was used, and then the kerosene. Also, as normally aircraft do not have to divert or loiter for a significant time, the loiter phase is done entirely on kerosene. The fuel fractions for the LTO phases were taken from J. Roskam [52] and modified slightly to better match the calculated LTO fuel usages.

Simulation

The simulation code used in [chapter 8](#) was used in this analysis as well, with some minor modifications. The program was not used to optimise for 20% savings, but to find the minimal fuel required for a certain range. This is in order to ensure that real world operations are reflected, where also just the right amount of fuel is taken on board, including fuel for a 45 minute cruise as reserve. The iteration loop started with a low amount of fuel and at a small range, slightly smaller than the distance already flown in the climb and descent phases. It ran the mission for that distance and calculated the fuel used. If this fuel used was larger than the amount of kerosene taken on board, the simulation was run again, but now with more fuel. This continued until enough fuel was taken on board. After this the code increased the distance by Δd and started the same loop again. All these loops are graphically shown in [Figure 12.2](#).

At some point the contents of the hydrogen tank were not sufficient anymore to supply the APPU engine with fuel throughout the mission at the thrust setting chosen. When this was encountered, the thrust setting was decreased and the simulation run again. This process was repeated until the hydrogen was sufficient for the mission. Fuel could simply be added up until the harmonic range. However, when the MTOW was exceeded, this could not be done further. After the harmonic range the program took out payload mass, and added kerosene, and ran the simulation again, until the kerosene requirement was met and the MTOW not exceeded. Once the fuel tank was full, the amount of kerosene was kept the same, and payload was further removed,

again until the range requirement was met. Once all payload was removed the ferry range was known, the results were plotted and the program stopped.

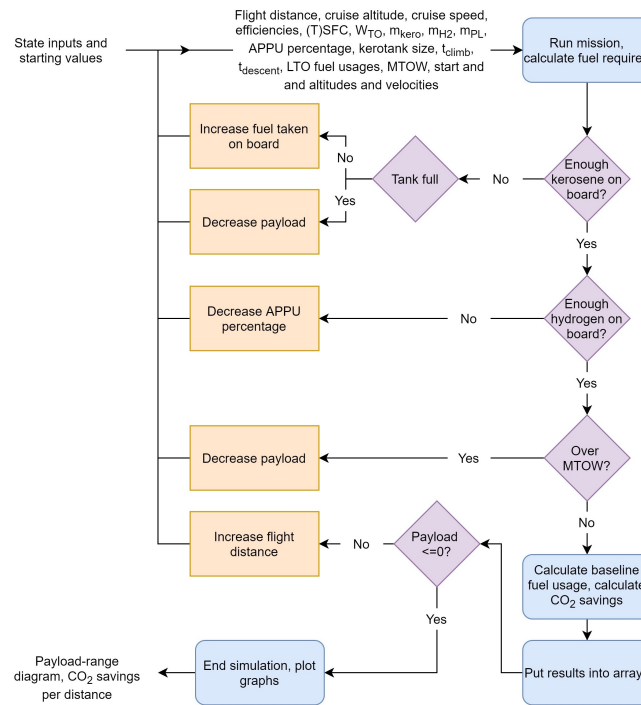


Figure 12.2: Payload-Range diagrams code flow chart

Breguet equation

As a verification method, the range was also computed using the Breguet range equations, Equation 12.1 and Equation 12.2.

$$R_j = \left(\frac{V}{g * c_j} \right) * \left(\frac{L}{D} \right) * \ln \left(\frac{W_B}{W_E} \right) \quad (12.1)$$

$$R_p = \left(\frac{\eta_p}{g * c_p} \right) * \left(\frac{L}{D} \right) * \ln \left(\frac{W_B}{W_E} \right) \quad (12.2)$$

Here R is the range in meters where the subscripts j and p stand for jet and propeller respectively. V is the true airspeed, g is the gravitational acceleration and c_j is the TSFC in cruise. η_p is the propeller efficiency and c_p is the power specific fuel consumption. L/D is the lift to drag ratio, which is taken to be constant here, at 17.5. Lastly, W_4 is the aircraft weight at the beginning of the phase, and W_5 is the aircraft mass at the end of the phase. The difference between the two is then the fuel that is used in that particular phase.

A preliminary estimate of the total range from the simulation was 6 100 km. To get the distance that is travelled in the cruise phase, the distance travelled in the climb and descent have to be known first. Table 8.2 shows the beginning and end velocities of all phases. All accelerations were assumed to be linear, so the distance travelled can simply be deducted from multiplying the time with the average velocity. It was found that the horizontal distance travelled in the climb was 180 km and during the descent was 211 km giving a combined distance of 392 km. The hydrogen is utilised fully during the mission, so all that is available for propulsion in the cruise phase is used. Subtracting the hydrogen required for other phases and for subsystem power generation, 195 kg is left for propulsion. The values in Table 12.1a were used as inputs for Equation 12.2:

Table 12.1: Breguet equation inputs.

(a) Inputs for cruise and final range

Variable	Value
η_p [-]	1
g [m/s ²]	9.81
c_p [kg/J]	$2.525 \cdot 10^{-8}$
L/D [-]	17.5
W_B [kg]	77 715
W_E [kg]	77 520

(b) Inputs for final mass

Variable	Value
V [m/s]	231.5
g [m/s ²]	9.81
c_j [kg/Js]	$14.6 \cdot 10^{-6}$
L/D [-]	17.5
R_j [km]	5 533
W_B [kg]	77 520

This resulted in a hydrogen cruise range of 177.5 km. Knowing the climb, descent and hydrogen cruise ranges, the final range can be obtained, and equals 5 533 km. The end mass is unknown and, therefore, Equation 12.1 is rewritten to the following:

$$W_E = W_B * \exp - \left(\frac{R_j * V}{g * c_j} * \frac{L}{D} \right) \quad (12.3)$$

Using the parameters from Table 12.1b, this resulted in an end mass of 63 747 kg. This gives a mass difference of 13 773 kg, the amount of kerosene used. In order to determine whether the kerosene available for the cruise is sufficient, also the reserve fuel has to be calculated. There has to be enough fuel left at the end of the cruise to be able to cruise for another 45 minutes. At 231.5 m/s this equals 625 km. Equation 12.3 is used again to obtain the end mass, but with 625 km as range and 63 662 kg as the begin mass. Note that this is 85 kg less than the previous end mass. This is because 85 kg are subtracted from the hydrogen that is consumed by the subsystem power generation during the cruise phase. The resulting end mass and mass difference are 62 271 kg and 1 391 kg respectively. Combining the previous results, the kerosene available for regular cruise is obtained and found to be 13 787 kg, 14 kg less than what was required. This difference is considered negligible. This means that the simulation is verified, because the results coincide with those of the Breguet range analysis.

Simulation results

Table 12.2 shows the final result of the simulation. These are graphically shown in Figure 12.3 and Figure 12.4. These graphs also show the potential CO₂ savings for each range. What is remarkable, is that the harmonic range of the APPU running on kerosene is larger compared to when it runs on hydrogen. This is due to the limited capacity of the hydrogen tank, which forces the contribution of the APPU to the thrust to decrease. At a range of 6 000 [km] the APPU contributes only around 2-3% if it runs on hydrogen, while it is still above 15% if it runs on kerosene. The result is that at long ranges the A320appu acts almost as an A320neo, with less payload and more dry mass. In Figure 12.4b, it can be seen that the higher efficiency of the APPU leads to a 8-11% CO₂ reduction. The higher savings at short ranges are due to the savings in the LTO cycle. This CO₂ reduction means less kerosene is burned, and this is used to increase the range. However, if the APPU barely contributes, it cannot provide these improvements, which is the case if the APPU runs on hydrogen.

12.2.3. Landing, take-off and climb

An aircraft's aerodynamic design is highly influenced by the performance it is able to achieve. In the A320appu design process, several other requirements were leading when sizing the empennage for instance and other design choices were mainly related to minimising the changes to the A320neo design.

Take-off distance

The changes to the A320neo design are thus minimised. This results in the MTOW, the wings and the main engines being completely the same. Because of this, the maximum take-off distance is not different for the A320appu.

Landing distance

The landing distance of an aircraft consists of:

1. Air distance - the distance the aircraft flies from an altitude of 50 ft until touch down.
2. Ground roll - the distance travelled from touch down until the aircraft has come to a halt.

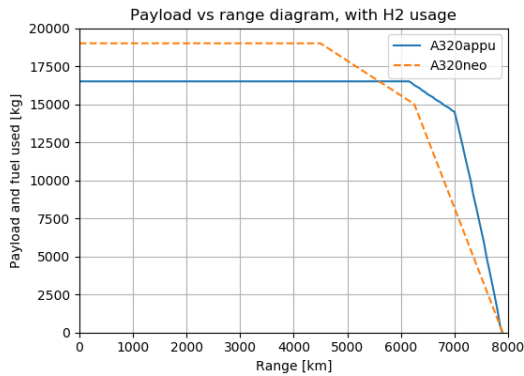
From the functional analysis of the entire aircraft system it is assumed that the aft propeller is not running during the entire landing phase, from an altitude of 50 ft until the aircraft has stopped completely. The landing distance of the A320appu will vary from that of the A320neo because of its additional operational empty weight and its different configuration. Due to the shifted wing and altered CG, the moment balance is different as well. This results in the horizontal stabiliser of the A320appu having to generate more negative lift than that the A320neo. A worst case scenario is assumed in this analysis; the aircraft is operating at stall right before landing. This means that the main wing cannot compensate for the increase in downforce by increasing its C_L , and thus the aircraft will have to fly faster. Flying faster, however, will increase the required stopping and thus landing distance. According to requirement **FMP-Sys-05**, the landing distance may not increase by more than 5%, so this problem has to be quantified.

It has been calculated that the A320neo and A320 appu generate 67.2 kN and 73.2 kN of downforce with their horizontal stabiliser, respectively. Also the MLW of the A320appu is larger, 69 250 kg instead of the A320neo's 67 400 kg. Combining these two factors results in the wing of the A320appu having to generate 3.31% more lift. This increases the stall speed by $\sqrt{3.31\%} = 1.82\%$. Equation 12.4¹ shows that the landing

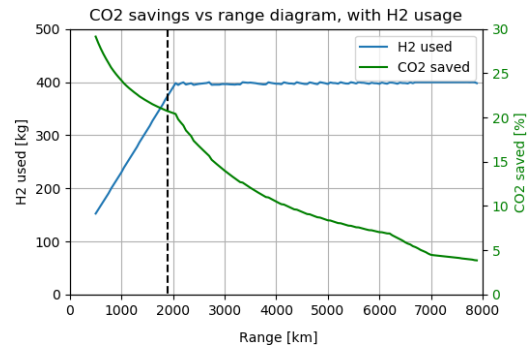
¹R. Vos, J.A. Melkert, ADSEE slides, A/C Preliminary Sizing (T/W-W/S diagram), TU Delft

distance required is quadratically proportional to the landing speed, hence the landing distance is increased by 3.31% which is below the 5% requirement.

$$s_L = 0.5847 * V_{sland}^2 \tag{12.4}$$

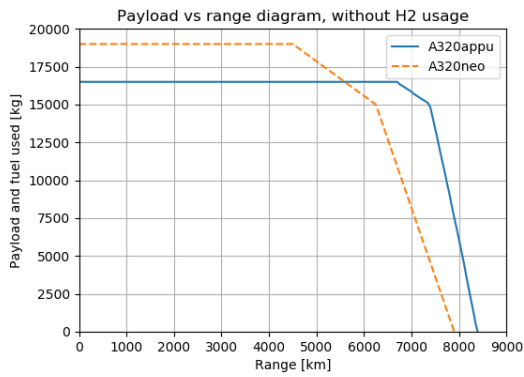


(a) Payload-range diagram for the A320appu with hydrogen usage

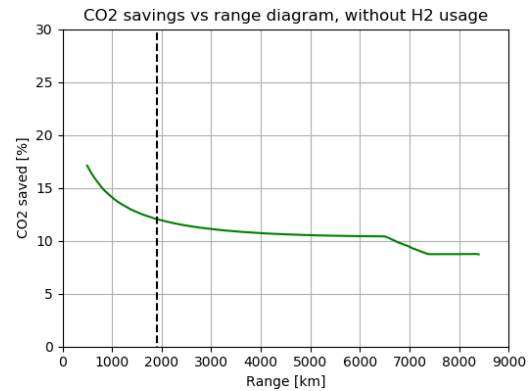


(b) CO₂ savings-range diagram for the A320appu with hydrogen usage

Figure 12.3: Payload-range and CO₂ savings-range diagrams for the A320appu with hydrogen usage



(a) Payload-range diagram for the A320appu without hydrogen usage



(b) CO₂ savings-range diagram for the A320appu without hydrogen usage

Figure 12.4: Payload-range and CO₂ savings-range diagrams for the A320appu without hydrogen usage

Table 12.2: A320appu ranges

Type of mission	A320appu range [km]
Harmonic range	6 150
Max fuel @ MTOW range	7 000
Ferry range	7 870

Climb rate and climb angle

The rate of climb of an aircraft is calculated using the following formula:

$$ROC = \frac{P_a - P_r}{W} = \frac{TV - DV}{W} \tag{12.5}$$

In which P_a is the available power and P_r is the required power. The equation is true under the assumption that the change in velocity is zero and the flight path angle remains constant. Examining the rate of climb and requirement **FMP-Sys-08** which states that the climb rate is not to decrease by more than 5%, the thrust must thus cancel out the additional drag associated with the A320appu design. The OEW of the A320appu differs from that of the A320neo, however, in designing for similar aircraft performance one was able to design for the same MTOW by altering the payload and fuel weights. By not changing the MTOW the performance remains the same. Moreover, the A320appu is able to deliver more thrust than the A320neo during climb and with the BLI for the propeller the fuselage’s wake energy will be ingested and utilised decreasing the overall drag of the aircraft. Because of an increased thrust and overall decrease in drag, the rate of climb performance will

improve. The climb angle under which the A320appu is able to climb is also different than that of the A320neo. The relation that described the climb rate angle is as follows.

$$\sin\gamma = \frac{T - D}{W} = \frac{ROC}{V} \tag{12.6}$$

Again the second relation only holds for a constant flight velocity. For the climb angle the same reasoning holds as for the rate of climb of the aircraft.

12.3. Electrical block diagram

The generation and distribution of electrical power is shown in Figure 12.5. In general, the A320appu will maintain the same electrical subsystems architecture as the A320neo. Therefore, there is not much difference in that respect. Nevertheless, the electrical block diagram (EPS) is presented to highlight a number of key points where the A320appu differs. Electrical power is generated from two sources: the APPU and the main engines. The A320appu shall utilise the APPU as primary source for electrical power and, in case of emergency or failure, the main engines shall act as a back-up source. Both APPU and main engines drive their own generator which produces electricity for main engine start-up, avionics, and cabin systems [60].

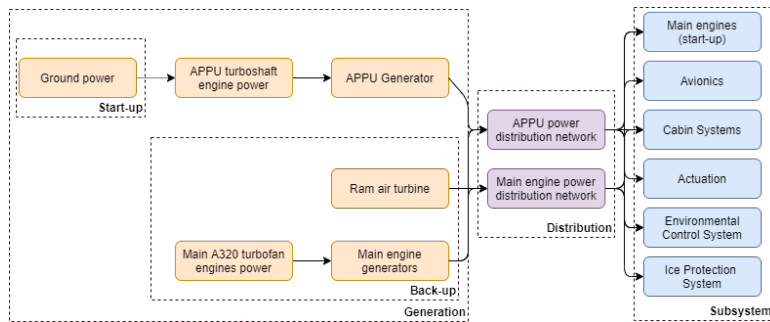


Figure 12.5: Electrical block diagram of the A320appu.

12.4. Hardware-Software block diagram

Figure 12.6 describes the data flow from certain hard- and software components, categorised in inputs and in outputs. Only data flows relevant to the APPU system are shown. Figure 12.7 gives a detailed visual of one of the feedback loops in the system.

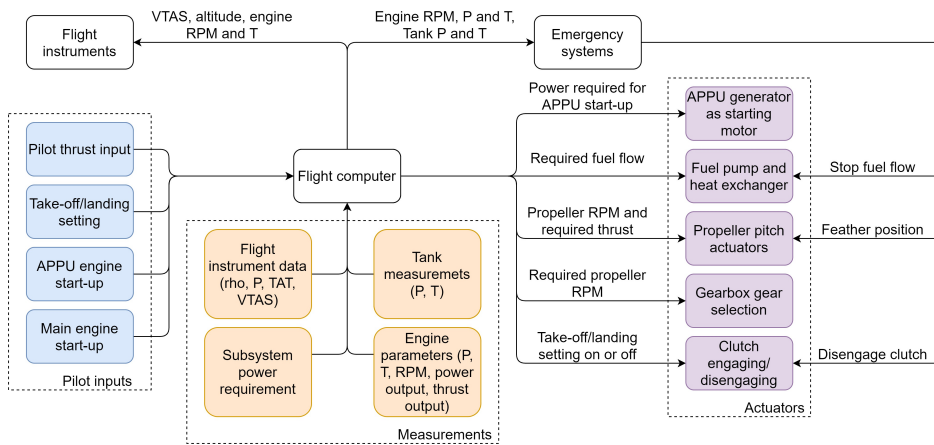


Figure 12.6: Overview of the hardware-software relations

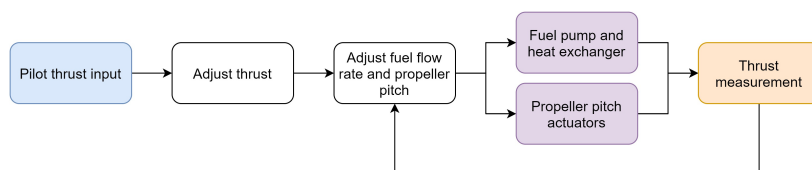


Figure 12.7: Detailed view of a feedback loop between hardware and software components

Sustainability Analysis

The main motivation of this project is to lower the emissions of CO₂, and other greenhouse gasses such as NO_x, CO, unburnt hydrocarbon, and soot. The CO₂ reduction has been quantified earlier in this report. However, the LTO emissions are also of great importance because of their impact on the local environment. For this reason, these emissions are quantified in this chapter and compared to the LTO emissions of the A320neo. For residents near airports noise emissions of aircraft become similarly as important. For this reason, noise produced by the A320appu is also investigated.

13.1. Requirements

Stated below are the requirements applicable to this analysis.

- SUST-User-24:** The CO₂ emission should be at least 20% lower than A320neo for a typical mission.
- SUST-User-25:** The NO_x, CO, unburnt hydrocarbon and soot emission for the LTO cycle should be reduced by at least 50% when compared to A320neo for a typical mission.
- SUST-Sys-26:** The noise pollution of the renewed aircraft shall not exceed the noise emissions of the A320neo by more than 5%.

13.2. LTO analysis

Emissions in the Landing and Take-Off cycle are of relevance for the local air quality. Therefore, it is important to limit the emission of these gasses by aircraft. Over the years the International Civil Aviation Organisation (ICAO) has put increasingly tighter restrictions on NO_x emissions from aircraft engines. The A320neo uses the LEAP-1A26, which already has one of the lowest NO_x Emissions Index (EI) of all certified turbofan engines. On top of this, as shown in [section 13.1](#), it is desired that these emissions in LTO are cut in half. This section explains what emissions are taken into account, followed by how they are formed. Next, the problem is quantified, both for the A320neo and the A320appu. Lastly, the results are summarised.

13.2.1. LTO gas emissions

As already mentioned in requirement **SUST-User-25**, nitrous oxides (NO_x), carbon monoxide (CO), unburnt hydrocarbons (HC) and soot are considered. The equivalence ratio is the ratio between the current fuel-to-air ratio (f/a) and the stoichiometric f/a . The stoichiometric f/a is the ratio where there is just the right amount of air to burn all the fuel. For example, if hydrogen is the fuel, with a stoichiometric f/a there are two H₂ molecules present for every O₂, generating two water molecules and leaving no unburnt H₂ molecules or unused O₂ molecules. Soot, HC and CO are created by incomplete combustion. These exhaust gasses contain carbon-atoms which have not fully reacted with the oxygen in the air. Soot is formed in case too much fuel is added compared to the mass flow of air due the equivalence ratio being too high. HC and CO are on the other hand formed when the equivalence ratio is too low. The carbon-atoms in the exhaust gasses originate from kerosene combustion. However, if hydrogen is used as a fuel source, these gasses disappear due to absence of carbon-atoms. As a result, greenhouse gasses such as soot, HC and CO are practically non existent during hydrogen combustion. Moreover, there is a benefit of having less CO₂ emissions with respect to producing slightly more H₂O, namely, the lifetime of H₂O is considerably smaller than CO₂ which makes it negligible for the green-house effect.

However, this does not apply to NO_x emissions. These are formed at high temperatures through the reaction of nitrogen and oxygen contained in the air which exist in the combustion chamber. Therefore, this happens regardless of the type of fuel used and therefore NO_x is emitted during both hydrogen and kerosene combustion.

13.2.2. Emissions analysis

First, the LTO emissions of the considered gasses are quantified for the A320, except for soot because this is relatively unknown and, hence, little data is available. However, soot is not produced during hydrogen combustion for reasons mentioned before. Consequently, the calculated savings would increase even more if soot emissions are considered as well. The ICAO has a database with data on emissions for a large variety of engines¹. Table 13.1 shows the EI per gas and per LTO phase. The EI has to be multiplied with the fuel consumed in that phase in order to get the total emissions, so the fuel usage for both the A320neo and the A320appu are given. Finally the emissions are calculated².

Table 13.1: EI for the LEAP-1A26 engine and LTO fuel consumptions and total LTO emissions for the A320neo and A320appu (main engines only)

LTO phase	HC EI [g/kg]	CO EI [g/kg]	NO _x [g/kg]	A320neo fuel usage [kg]	A320neo total emissions [kg]	A320appu fuel usage [kg]	A320appu total emissions [kg]
Take-off	0.02	0.22	18.77	71.82	1.114	51.2	0.9733
Climb-out	0.02	0.27	11.16	186.12	2.131	136.6	1.564
Approach	0.04	2.74	8.67	116.16	1.330	30.3	0.3469
Taxi/idle	0.28	21.4	4.63	274.56	7.224	50.2	1.321
Total				648.66	11.83	268.3	4.205

In this calculation, however, the emissions from the APPU engine are not taken into account yet. It is assumed in the analysis that the APPU engine runs on hydrogen. Since there are no operational hydrogen burning turboshaft engines for aviation yet, there is no data on the EI for this type of engines. However, NASA has found an equation [45], Equation 13.1, that allows to calculate the EI for given combustion chamber conditions. It has to be noted that the values used in this equation are not in SI units. The pressure is in pounds per square inch (PSI) and the temperature is in Fahrenheit (°F).

$$EI_{NO_x} = A' \cdot P_{in}^{0.594} \cdot e^{\frac{T_{in}}{350}} \cdot (f/a)^{1.6876} \cdot \left(100 \cdot \frac{\Delta P}{P}\right)^{-0.56} \quad (13.1)$$

P_{in} and T_{in} are the pressure and temperature at the beginning of the combustion chamber respectively. A' is a constant specific to the fuel injector used in the research by NASA, lean direct injection (LDI) fuel injectors. This type of fuel injectors is well suited for low NO_x emitting engines, hence it is assumed the APPU turboshaft engine will also utilise this technology. $\frac{\Delta P}{P}$ represents the pressure losses in the combustion chamber. This is taken to be 2%³.

As to verify whether this equation was actually applicable and gave accurate results, the NO_x EI of the APPU if it were to run on kerosene was also calculated. Take-off conditions and power setting were used. The increase in f/a was simply calculated using the ratio between the LHV's of hydrogen and kerosene. The resulting NO_x EI was 16.53 g/kg, which is in the same order of magnitude as the NO_x EI of the LEAP-1A26 engines at take-off. This indicates that Equation 13.1 is applicable for this analysis. Below in Table 13.2 the resulting NO_x EI for the APPU engine for the different LTO phases are shown. Remarkably, the EI of approach is higher than the EI of climb-out. This is because, eventhough the total thrust during approach is much lower, the thrust of the APPU is roughly the same.

In climb-out, the APPU contributes 15% to the total thrust, which is 85% of maximum thrust. During approach the APPU provides half of the total thrust, which is only 30% of the maximum thrust. In short, the EI are similar because the APPU provides similar power. The fuel usage per phase is also given, and lastly the total NO_x emissions for the APPU engine in LTO are calculated. The results from the analysis are summarised in Table 13.3. The A320appu number is the sum of the total value given in Table 13.1 and the total value in Table 13.2. It can quickly be seen that the requirement of 50% savings has been met with quite some margin.

¹<https://www.easa.europa.eu/domains/environment/icao-aircraft-engine-emissions-databank>, retrieved on 10-06-2020

²<https://bit.ly/2YC9BCx>, retrieved 08-06-2020

³This can be considered an optimistic value, and might need to be increased in later design stages

Table 13.2: APPU NO_x EI, hydrogen usage and total NO_x emissions in LTO per phase

LTO phase	NO _x EI [g/kg]	Hydrogen usage [kg]	Total emissions [g]	Trust as fraction of total [-]	APPU contribution [-]
Climb-out	3.277	11.6	38.14	0.85	0.15
Approach	3.387	19.1	64.80	0.3	0.5
Taxi/idle	0.424	14.5	6.14	0.07	1.0
Total		45.2	109.0		

Table 13.3: LTO emissions and savings summarised

Variable	Value
A320neo LTO emissions [kg]	11.83
A320appu LTO emissions [kg]	4.31
Emissions reduction [%]	63.53

13.3. Noise

Aside from gas and particulate emissions, a source of pollution that is important to consider in aviation is noise. Noise analysis for the APPU is limited by expertise and insight, and is thus completed in a rudimentary manner. The relevant requirement for the APPU is **SUST-Sys-26**, dictating that the alterations made to the A320neo should not lead to its noise level being more than 5% higher in decibel. To examine any changes in noise level, the base A320neo and its noise level is considered. After this, the effect of the APPU propeller and engine is considered to determine the total level of the A320appu.

13.3.1. A320neo noise

The base noise for the A320neo is taken from [28]. While the highest level of noise is the approach EPNL, the APPU is at a low power in approach, or the propeller is switched to a feathered pitch in a Y-shape before landing. The APPU is operating at its highest power in climb, so the lateral EPNL level is considered. Taken for the VW055 of the A320-251N, the level is 85.7 *dB*.

13.3.2. APPU propeller noise

The aft propeller of the A320appu is the most significant contributor to the overall increase in sound. Estimating noise with empirical methods is considered out of the scope of the project. The determination of noise levels is thus done using XRotor, as the program was also used for the design of the propeller in [chapter 9](#). The noise of the propeller is simulated at the point at climb-out at the end of LTO, the highest-power point of the engine simulation and propeller thrust.

The highest noise level is taken from the simulation as 73 *dB*. However, this is for just one of the propellers. Thus, the total noise of the propeller is taken to be a sum of two propellers of 73 *dB*. Furthermore, the simulation does not account for turbulent airflow, which is expected to add to noise. For this reason, a factor of 2 increase in the overall noise level is taken. This leads to a total propeller noise level of 79 *dB*. There are two additional contributions to noise which has not yet been analysed. One contribution is from the penalised thermal components of an open rotor with respect to a ducted fan, as there will be no absorption into the lining of a shroud in its proximity. In other words, thermal radiation will not be adequately absorbed into the aircraft, which should be investigated. The second contribution is from the additional harmonics regarding the contra-rotating blades. The blades will interact which will have an additional penalty on noise levels that are produced with respect to a single propeller blade.

13.3.3. APPU engine noise

The APPU is a turboshaft engine. As its energy goes into driving the shaft rather than propelling the exhaust, the exhaust noise is considered negligible to the total noise level. Considering the internals of the engine, there are other noise sources. Combustion, as well as turbines, are sources of noise. However, the APPU engine is less than a third as powerful as the main engines, reducing its noise emission in comparison. Furthermore, the placement in the tail cone leads to shielding of much of the engine noise; these factors lead to these noise sources, too, being negligible.

13.3.4. Overall aircraft noise

To determine the aircraft's total noise level, the base A320neo noise is summed with the estimated propeller noise level. This leads to a final noise level of 86.5 *dB*, a 0.93 % decibel increase from the base A320neo's level.

Operations and Logistics Concept Description

With the complete aircraft designed, it is time to look into how this aircraft will operate between the existing aircraft. To develop a good opinion on this, the operations and logistics are analysed for multiple aspects. First the liquid hydrogen operations and logistics will be discussed and after this the airport operations and logistics are mentioned.

14.1. Liquid hydrogen operations & logistics

This section will discuss the operations and logistics that are required for implementing a new fuel into the already existing procedures. A new fuel brings new opportunities and challenges. Both will be discussed, starting with the refuelling system of the A320appu. After that the logistic required to provide liquid hydrogen to the A320appu will be discussed.

14.1.1. Fuelling operations

The procedure to refill the liquid hydrogen tank is illustrated in [Figure 14.1](#) and shows a large resemblance with a kerosene dispenser. There is however a difference between the figure and the A320appu refuelling which is the location of the tank. In [Figure 14.1](#) is the tank located in the tail cone while in the A320appu the tank is located in the aft cargo hold. This means that the dispenser and the hoses itself will not differ but the location of the refuelling will.

The refuelling procedure can be explained using the figure. In the figure it can be seen that liquid hydrogen is fuelled into the tank and the gaseous hydrogen that has been created inside the tank is taken out to make sure the tank can be completely filled with the optimal amount of liquid hydrogen which is 97% of the tank's volume. The gaseous hydrogen is captured and can be used to fuel ground vehicles that work on gaseous hydrogen or could be returned to the hydrogen power plant to liquify again. A vacuum pump is used to fuel the liquid hydrogen into the tank to force the liquid in the right direction, while the helium bottles are used to remove all gaseous hydrogen from the tank that was left from a previous mission[15].

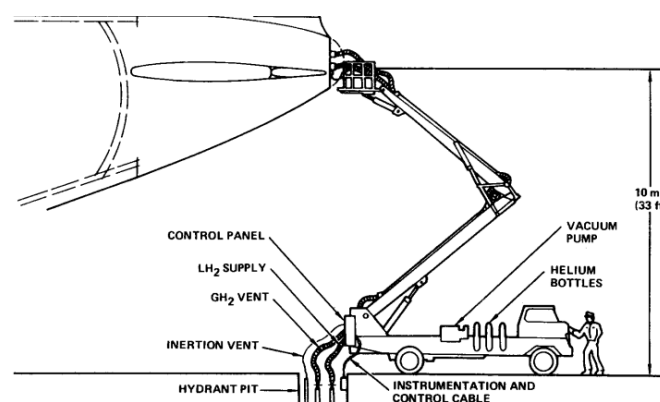


Figure 14.1: Fuelling procedure for liquid hydrogen[15].

Now that the system that will be utilised is known, it is time to determine the fuelling time needed to completely fill the tank. Liquid hydrogen does not fuel as fast as kerosene due to lower volumetric density of liquid hydrogen. However this is not a difficulty for the A320appu since hydrogen is only used in a small amount. With the

vacuum pumping fuelling system a fuelling speed of 450 l/min can be achieved while with kerosene a speed of 900 l/min can be reached [19]. To satisfy requirement **FTD-Sys-22¹**, it is needed to analyse the drainage of the hydrogen tank. The viscosity of liquid hydrogen is 100 times smaller meaning that the liquid hydrogen is a very thin liquid which drains faster than kerosene. Next to this is also the fact that much more kerosene is taken on a flight than hydrogen which means that the draining of liquid hydrogen will be faster than kerosene.

In [Figure 14.1](#), a hydrant pit is described where the liquid and gaseous are supplied utilising underground piping. This is however initially not installed as the liquid hydrogen can also be delivered by truck. This decision has been made because of the difficulties that arise when designing and placing an underground hydrogen fuel network. One of these difficulties is that there are frequent leaks due to corrosion between pipe and soil. Another difficulty is the placement of these pipes which would mean that the whole airport has to be under construction which would obstruct the normal operations of the airport. Since the A320appu only uses a small fraction of liquid hydrogen as fuel, this drastic redesign of the airport is not viable [27]. The logistics of the liquid hydrogen supply will be discussed in the next section.

14.1.2. Liquid hydrogen logistics

When bringing the A320appu into service, it is very important to have an overview of the availability of liquid hydrogen at every airport. In the early stage of the usage of the A320appu, it is possible to obtain liquid hydrogen from existing liquefaction capacity close to the airports. The reason for this is that the amount of liquid hydrogen will initially be quite low, since only 400 kg of liquid hydrogen is needed per flight and the amount of flight utilising liquid hydrogen will be low in the beginning. The liquified hydrogen will be brought to the airport with trucks. This is one of the reasons that the introduction of this new fuel is done preferably at airports that have an existing liquefier nearby [59]. The delivered liquid hydrogen can be stored at the airport and smaller trucks can be filled and drive to the gate where hydrogen refuelling is needed. This preliminary logistics concept is illustrated with a flowchart which can be seen in [Figure 14.2](#)

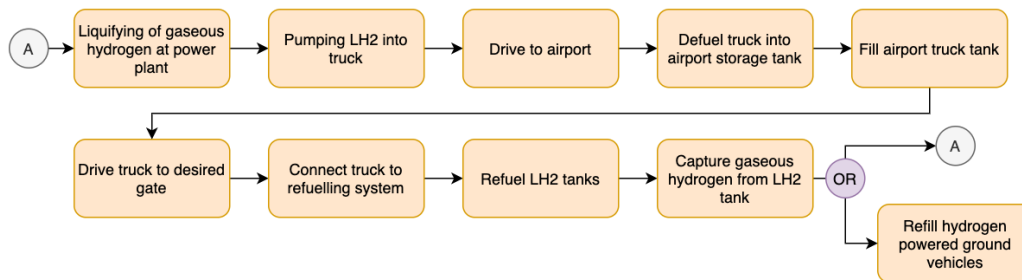


Figure 14.2: Flowchart of the liquid hydrogen logistics

Having the constraint on availability of LH_2 limits the locations where the A320appu can operate as desired. In the last few years, more and more hydrogen filling stations have been built in developed regions (North America, Europe and Japan/China), see [Figure 14.3](#). This means that the A320appu will operate mostly in these regions in the first years of operating. With the knowledge obtained from the market analysis in [chapter 4](#), it can be observed that the regions with high aviation growth coincide with the regions in [Figure 14.3](#). This overlap is very beneficial for bringing the A320appu in service because these regions are most interested in buying new aircraft to handle the growth of aviation, reducing emission at airports and they have the right hydrogen infrastructure to use as a starting point.

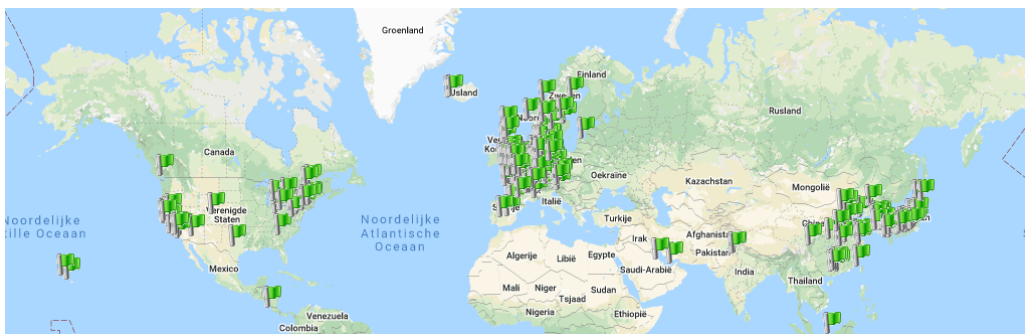


Figure 14.3: Locations of hydrogen filling stations in operation²

¹The hydrogen tank shall be able to be drained in same amount of minutes as the kerosene tanks.

Since the A320appu is a short to medium range aircraft, the proposed regions are sufficient to use as a starting network. The reason for this is that the regions perform a lot of short to medium range flights so many airport in the starting regions are able to provide sufficient liquid hydrogen which is beneficial for the local emissions and the region coincides with the range of the A320appu. However the problem of not having stations in other parts of the world needs to be resolved to be able to use the A320appu's full potential all around the world.

14.2. Airport operations and logistics

Not only the fuelling logistics, but also the logistics at the airport need to be re-evaluated. The liquid hydrogen fuelling service needs to be implemented in the ground operations. The current layout is illustrated in Table 14.4. The figure shows that there are already many different types of equipment used simultaneously. For the A320appu new equipment needs to be added, such as the fuelling dispenser for the liquid hydrogen. However, adding equipment might have influence on the ground operations. Analysing the changes in ground operations and with that the turnaround time will be done in the next section.

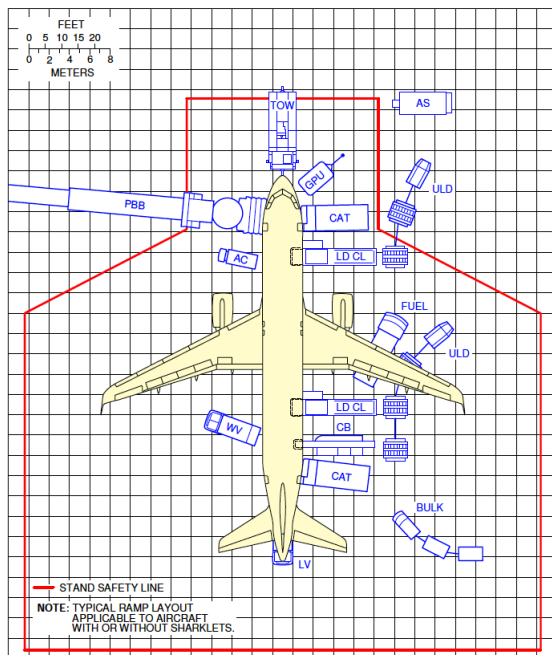


Figure 14.4: A Typical Ramp Layout of the A320neo at a gate [1]

Table 14.1: Legend of Ground Support Equipment

Abbr.	Meaning
AC	Air Conditioning Unit
AS	Air Start Unit
BULK	Bulk Train
CAT	Catering Truck
CB	Conveyor Belt
FUEL	Duel Hydrant Dispenser or Tanker
GPU	Ground Power Unit
LDCL	Lower Deck Cargo Loader
LV	Lavatory Vehicle
PBS	Passenger Boarding Bridge
TOW	Tow Tractor
ULD	Unit Load Device Train
WV	Portable Water Vehicle

14.2.1. Turnaround time

The most important variable for airlines is the turnaround time. This can be explained by the logic that the turnaround time influences the profit of an airline quite substantially. Having a low turnaround time is beneficial, since it is then possible to perform more missions per day, which means more profit. The turnaround time is the interval needed between flight to perform all ground operations, such as reservicing and refuelling. The turnaround time is dependant on multiple factors. They are gathered below in bullet points. These factors are for the A320neo and do not include additions/changes needed for the A320appu [1].

- Passenger Handling; deplaning and boarding.
- Cargo unloading and loading
- Refuelling
- Cleaning
- Catering
- Ground Handling/General Servicing

With the A320appu the current procedures of the A320neo as seen in Figure 14.4 are still performed, however the APPU influences these procedures. The refuelling and ground handling will differ because of the additional tank and using only the APPU for all ground manoeuvres. To calculate the turnaround time the first step is to see which servicing activities are performed at which moment of the turnaround time. There are two types of servicing, there is full servicing which means that all ground support will be executed. There is however a shorter version which is used throughout the day between missions, since on short-medium range flights it is not needed to for example refill the water tank. This is beneficial for the airlines because the turnaround time can then be shortened meaning that more missions can be performed per day.

²<https://www.h2stations.org/stations-map/?lat=49.139384&lng=11.190114&zoom=2> retrieved on 08-05-2020

The A320neo has a turnaround time with full servicing of 44 minutes and the shortened version has a turnaround time of 22 minutes. The difference lies in the fact that there is no refuelling, waste water and portable water servicing. The reason for this is that the kerosene tanks can take extra fuel with them during the first mission that can be used for the next mission and water tanks will not be full after one mission. Taking the extra fuel sounds like it would only cost money since it makes the aircraft heavier what results in more fuel used, however it could be that the fuel at the destination is much more expensive and this way is more profitable. Another cause of the shortened servicing is that the cleaning and catering are done less extensive meaning that it will be done faster. And also the passenger deplaning and boarding is done much faster by utilising the front and the back door.

However for the A320appu, an additional service needs to be performed. The refuelling of the hydrogen tank needs to be done with the full servicing and also for the shortened servicing. The hydrogen tank does not have the capacity to bring extra liquid hydrogen that can be used for the mission after the current one. From this can be concluded that hydrogen can only be fuelled for one mission and always needs to be refuelled. The fuelling time for liquid hydrogen can be calculated using the fuelling speed of 450 l/min and the required amount of litres to be fuelled, which is 6 240L as mentioned in section 10.5. Dividing 6 240 by 450 results in a fuelling time of 14 minutes. Looking at Figure 14.6 it can be seen that the refuelling of kerosene takes around 16 minutes, meaning that it is possible to perform both refuelling procedures simultaneously.

The only constraint left is the question if the refuelling dispenser can fit next to all the other ground operations equipment. Based on Figure 14.4 a new ground operations diagram with the changes implemented can be found in Figure 14.5. In this figure the fuelling dispenser and truck are displayed instead of the aft cargo loader to show that it is possible to perform the fuelling simultaneously on time and space perspective. From this can be concluded that the full servicing turnaround time will not increase and will remain at 44 minutes as shown in Figure 14.6. This also means that risk OP-05³ will not be a difficulty.

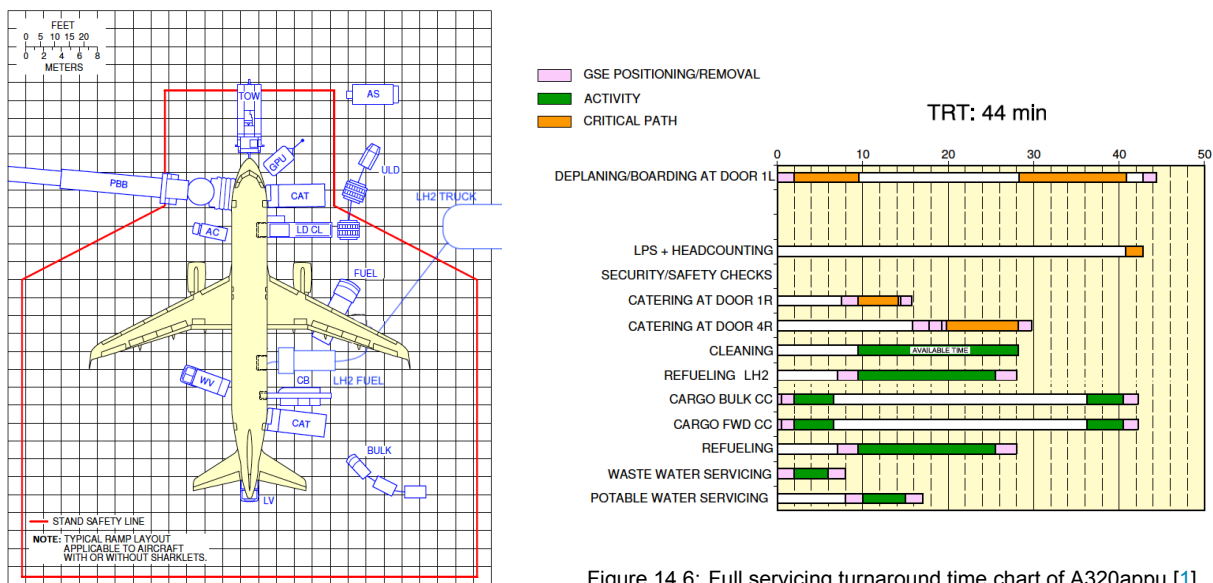


Figure 14.6: Full servicing turnaround time chart of A320appu [1]

Figure 14.5: Ramp layout of A320appu at a gate [1]

Analysing the shortened turnaround time, it can be seen that placement is not a problem as discussed before, however the optimal way of reservicing is that nothing else is performed while fuelling. This is however not possible in the shortened version of reservicing because in this schedule is reuelling not taken into account. This could mean that the turnaround time of the shortened servicing increases. However, due to the extra space available because of the absence of the kerosene fuelling dispenser, it might be possible to refuel while the bulk cargo hold is still being loaded. This needs to be looked into because if this is not possible it is still a option to let the APPU run on kerosene to keep the turnaround time as low as possible. This is a operational choice for the airlines utilising the aircraft. The shortened turnaround is illustrated in Figure 14.7 and has a turnaround time of 22 minutes, so half the full servicing turnaround time.

³OP-05: Refuelling takes significantly longer than current aircraft kerosene refuelling, see chapter 7.

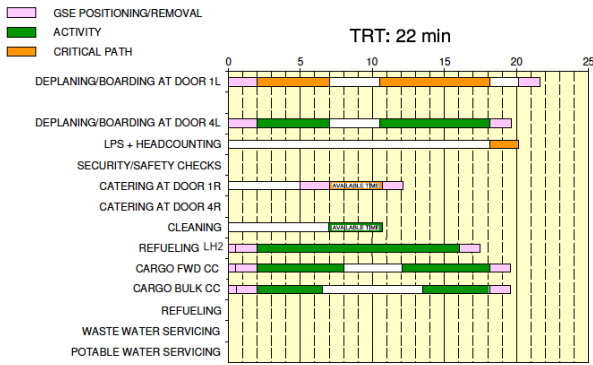
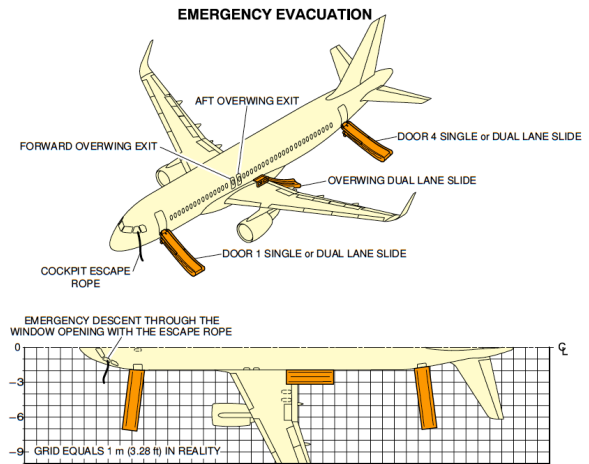


Figure 14.7: Shortened turnaround time chart of A320appu [1]



NOTE:
 - LH SHOWN, RH SYMMETRICAL.
 - DIMENSIONS ARE APPROXIMATE.

Figure 14.8: Emergency evacuation plan A320neo/appu [1]

Another important question to ask is if the additional tank will decrease safety during flight. One important example is the evacuation plan of the aircraft. What requirement **OPS-Sys-32** states is that the evacuation plan should not change due to the additional hydrogen tank. This can be analysed by looking at Figure 14.8. In this figure, it can be seen that all the six emergency slides are not placed around the aft cargo hold where the tank is, meaning that the aircraft evacuation plan will not be obstructed by the tank.

Not only the reservicing differs from the A320neo, but also the ground operations such as push back and taxiing. Normally a taxi bot will push the aircraft back and will place it in such a way that the aircraft can taxi to the runway. However with the A320appu, the propeller will be utilised by reversing the pitch and using reversed thrust to push back from the gate. When the aircraft is in the right position, the propeller will be placed in a forward thrust position and will be used to taxi to the runway instead of the main engines. The main engines are started just before the runway by the APPU to minimise kerosene usage during the ground phase.

RAMS Characteristics

RAMS is a abbreviation of Reliability, Availability, Maintainability and Safety. RAMS has developed into an important aspect of aerospace design, it is an recognised management and engineering discipline that emphasises important aspects of a design that initially might be neglected. In [Figure 15.1](#), the correlation between all four term is illustrated. It can be seen that these characteristics influence each other. All four characteristics will be discussed, starting with safety followed by maintainability and finally the reliability and availability are concluded.

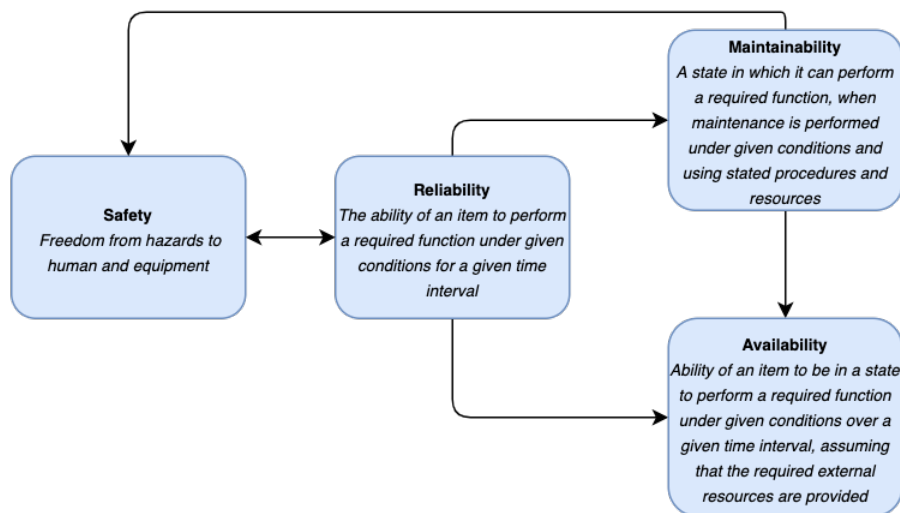


Figure 15.1: Correlation between RAMS characteristics [36]

15.1. Safety

As the A320neo is known as a very safe aircraft, it is needed to ensure this as well with the addition of the APPU system. This needs to be analysed and to make sure most aspects are discussed a list of requirements regarding safety has been created. The requirements related to safety of the A320appu are listed below. The final two requirements are related to the CS25 regulations.

- OPS-Sys-29:** The aircraft hydrogen refuelling system shall be safe to operate.
- OPS-Sys-30:** The aircraft hydrogen storage system shall be safely separated from the passenger cabin.
- OPS-Sys-33:** The propeller shall not cause considerable risk or danger for ground crew.
- OPS-Sys-39:** The aircraft shall be safe during all flight operations.
- REG-Sys-40:** The aircraft shall comply with CS 25 safety regulations.
- REG-Sys-40.1:** The Auxiliary Power Unit shall comply with CS 25 subsection J: 'AUXILIARY POWER UNIT INSTALLATION'.

15.1.1. Hydrogen safety

The safety of hydrogen can be seen from many perspectives, for the design it can be divided in subsystems of the hydrogen fuel system. The subsystems are the cylindrical tank itself, the fuel lines, fuel pump and the refuelling system. The tank has been designed to make sure that no hydrogen will escape the tank for at least 48 hours, however to increase safety multiple systems can be installed. A few examples are listed below.

- Leak detection system
- Fire detection system
- Ventilation system
- Emergency stop system

The leak detection system should be in contact with the ventilation system in the cargo hold. In the event of a leak, the hydrogen immediately becomes gaseous as it escapes the tank and needs to be vented away to make sure that it cannot ignite. This is why there has to be a well functioning ventilation system, as well as a fire detection system for when ignition occurs inside the aircraft. Leakage is caused by cracks in the tank, which means that air can also enter the tank which is very dangerous. However there is already prevention for this as there is a outer aluminium layer that serves as protection when there is an inner layer crack and vice versa [14].

There are two types of fuel lines for each state of the fuel, gaseous and liquid. The liquid hydrogen fuel line is designed with the same approach as the hydrogen tank. The fuel line also has a insulation layer to make sure that the cryogenic condition remains inside the line. Leakage in the fuel line works the same way as for the tank, however to make sure that the fuel feed will be halted, an emergency system needs to be implemented that will close the valve as soon as a leak is detected. For the gaseous hydrogen line another procedure is needed. The hydrogen is gaseous meaning that there are no cryogenic conditions which makes the fuel line design simpler. However, an elastomer layer is added to prevent air penetrating into the line, as this could cause ignition of the gaseous hydrogen. A crack in the line would not immediately mean that there is a leak due to the elastomer, but if there is a leak, this will be detected and the ventilation system will increase the ventilation making sure that the hydrogen is ventilated outside of the aircraft.

The final subsystem to discuss is the refuelling system. This system consists of a truck delivering the liquid hydrogen and a dispenser carrying a vacuum pump, helium bottles and two fuel lines as explained in [subsection 14.1.1](#). In this situation is safety very important to make sure that all ground personnel or passengers are not in imminent danger. The safety steps for the fuel lines will be the same as described for the lines inside of the aircraft. The helium bottles are used to clean out the fuel lines and tank such that there will be no dust or frozen air inside which could obstruct the fuel flow or could react with the hydrogen. Another measure that can be taken is choosing the ground under which fuelling takes place. Since hydrogen reacts with a lot of materials but not with concrete, a good safety measure is to choose this as surface to ensure safety for the ground crew as it will not ignite as soon as it hits the ground and can be ventilated [48].

The fuel truck delivering the liquid hydrogen is part of the infrastructure that needs to be implemented at the airport, as described in [subsection 14.1.2](#). For this infrastructure, safety measures are needed as well, which is why placing the liquid hydrogen storage tank has to be done carefully. The tank should be stored at a sufficient distance from the gates, the runway and the surrounding buildings to make sure that all these building will not be damaged in case of a explosion. The distance is determined by multiple variables such as storage pressure and detection time. To make sure that these distances do not need to be larger, safety measures could be applied to the storage tank(s). This can be done in various ways such as having enough spacing between the tanks, minimum pipework, well designed pressure relief system, well chosen materials and prevention on overfilling. Another measure that can be taken is having a good system to prevent leaks from igniting and spreading, such as a water and foam spray system.

15.1.2. Propeller safety

Open functional propellers are dangerous, both during operations and failure. An advantage of the A320appu propeller is its location. The centre of tail cone is located at a height of 5.3 *m*, measured from the ground for the A320neo. As the tail cone height does not change for the A320appu, the propeller blade tips will not reach any lower than $5.3 - 1.75 = 3.55$ *m*. Additionally, the landing gear is extended and the propeller hub height is slightly heigher than the A320neo tail cone. Consequently, the propeller is located even higher than the 3.55 *m* mentioned before. Therefor, a collision with an individual is unlikely.

Furthermore, propeller blade failure could occur in which a propeller blade might detach from the hub. This could happen due to a tailstrike, hub mechanism failure or a collision with a foreign object such as a bird strike. Conventional propeller aircraft impose regulations on the surrounding subsystems to be able to perform after damage from a loose propeller blade has been imposed. As the A320appu propeller is located at the tail of the aircraft, a detached propeller blade will not pose any real risks. The design utilises a counter-rotating propeller with six blades in total for which there are no maintenance regulations set up yet. To develop initial maintenance procedures, it is needed to first look into the types of damage that could occur. A list with possible causes of failure are listed below.

- Misalignment
- Cracks
- Dents
- Lightning strike
- Foreign object strike
- Overspeed
- Fire/Heat damage

Looking at these failure modes, it can be seen that some are left out. For example corrosion on the A320 appu propeller will not be a failure mode because the propeller is made from a composite material M55UD. Others like pitting and nicks are not included for the same reason. However there are still enough failure modes to take into account.

Ultimately, the chance of foreign objects being sucked into the propeller is rather small since the propeller solely uses the air stream which flows over the fuselage. However, in the case loose material is being blown up by the main engines, foreign objects could enter the propeller system. The safety of passengers or crew will not be compromised. However, the foreign object might be propelled into an unpredictable direction and harm or damage external objects or personnel.

15.1.3. APPU engine safety

The last system that is adapted is the APU engine, which will now provide shaft power and becomes a APPU engine. The APPU engine will intake free air stream which is taken from the top of the fuselage with the use of a s-duct. This differs from the APU, where air is taken in at the bottom of the tail cone. By placing the inlet above the fuselage, the risk of taking in foreign objects decreases making the inlet safer. Another difference is that the APU is designed to be used when the main engines stop working, while the APPU works throughout the flight and the main engines become the back-up. This means that the aircraft is now more dependant of the engine which means safety becomes more important. The engine will utilise hydrogen as its main fuel but can easily switch to kerosene when needed. The change of fuel does not cause any problems for the engine and makes the engine more safe with a redundant fuel type during flight. Other safety aspects such as uncontained engine failure are discussed in [section 8.8](#).

Due to the resemblance of the new engine with the APU, a good way to make sure that the engine is safe is to use the CS-25 regulations on a APU as a baseline and to add to those safety measures. In this document are various things discussed such as flammability, air intake and exhaust system and bleed air duct system [29]. By making sure that the changes of the engine still comply with the regulations makes sure that the engine is safe enough to operate.

15.2. Maintainability

Maintenance is the ability of a system to be maintained, the ease, accuracy, safety and economically feasible. This is a design characteristic and can be divided into two categories; time and man-hours. For time elapsing are four different terms. The first one is Mean Time To Repair (MTTR), which entails the interval needed to repair a system to be able to operate again. The second term is the Mean Preventive Maintenance Time (MPMT) which is the time needed to perform preventive maintenance. The third one is Mean Time To Maintain (MTTM) and refers to the time required for both preventive and corrective maintenance. The final term is Mean Down Time (MDT) which is related to the logistic delay apart from the active maintenance. However, these terms can be influenced by the second category being the man-hours. By increasing the amount of labour-hours the time required will decrease, but the maintenance cost will increase so there is a need to find a equilibrium between the two [36].

Table 15.1: Type of maintenance checks for aircraft¹

Level	Interval [FH]	Description	Ground time [h]	Man-hours
A	120-150	Visual examination of airframe, power plant, avionics and accessories	8	60
B	750	A check plus selected operational check, fluid servicing, lubrication and open inspection panels	24	200
C	3 000	A and B checks plus detailed inspection airframe, engines and accessories, heavy lubrication, corrosion prevention and flight controls calibration.	72	3 000
D	20 000	A, B and C checks plus removal cabin interior for detailed structural inspection and rebuild	21 days	10 000

¹<https://bit.ly/3i6G63F>, retrieved on 19-06-2020.

For aircraft maintenance there are four types of checks, each indicated with a letter. These levels are used to divide the inspections into four different intervals instead of many different intervals, meaning that the aircraft should be brought into maintenance many more times which would decrease the flight hours. The four checks can be found in [Table 15.1](#). Since this design is an addition to the existing A320neo, the maintenance will only be discussed regarding the systems that have been changed/added. The rest of this section will the propeller, APPU engine and liquid hydrogen fuel system be discussed. The section about the propeller design is based on a document of the FAA called 'Aircraft propeller maintenance [33].

15.2.1. Propeller maintenance

For all the mentioned failures are multiple ways to inspect this. Inspection is not always needed but there are some situations after which it is rushed. One example is after a suspected impact, such as a bird or runwaylight. Another example is when the aircraft is struck by lightning or suspected. There are three levels of inspection; pre-flight inspection, detailed inspection and teardown inspection which is inspired by the levels for airframes. The pre-flight and detailed inspection can be compared to the levels A and B mentioned in [Table 15.1](#).

Pre-flight inspection is done using visual inspection since this can be done without difficulty. While inspecting visually, changes in surface can already be spotted and can indicate that there might be damage. This can be done by looking at the complete propeller to see if there are cracks or fasteners missing as well as feeling the surface of the propeller for indents. For composites, use a thorough visual inspection combined with a coin tap which can track down delamination, repair damage or debonds. This is a relatively easy and cheap method of inspection and can detect various damages.

Detailed inspection is done in an interval chosen by the manufacturer which is most of the time fixed. For the propeller this would be the time interval of level B, meaning ones per 750 flight hours. For this type of inspection is disassembly and special equipment needed as it will look into more detail to the blades and other parts of the propeller. Not only look for damage like dents but also for fatigue in the spinner and the connectors such as fasteners. The A320appu propeller has variable pitch and variable speed, meaning that there are two additional systems that need to be inspected. For the variable pitch, inspect the connections and cables. For the variable speed is a gear box utilised, which requires detailed inspection as well.

The third level of inspection is the teardown inspection, which is needed when there are problems discovered during one of the other inspections. Teardown inspection is only performed when requested and does not have a constant interval. For this inspection, the complete propeller is disassembled and inspected in a very detailed manner. Inspection procedures as penetrant, ultrasonic and magnetic particle inspection are used, which is all performed in a repair station with special equipment. At the end it is decided if the propeller is discarded, parts can be reused or the complete propeller is again airworthy.

15.2.2. APPU engine maintenance

As described in the safety section, the APPU engine has much resemblance with the APU engine which indicates that the new engine can be maintained in a similar manner. Visual inspection can be performed to see if there are any obstructions in the duct or at the exhaust of the engine. To have a valid indication of when detailed maintenance of level B, C or even D is needed a few indications can be utilised. Two examples are measuring the exhaust temperature to indicate the quality burn inside the engine as well as measuring the specific fuel consumption. It is needed to keep in mind that both hydrogen and kerosene can be used in this engine for which the temperature and consumption will be different which might result in a different maintenance interval then when the engine only uses kerosene [32].

15.2.3. Liquid hydrogen fuel system maintenance

Storing liquid hydrogen comes with its difficulties. However, it is also necessary to make sure that all subsystems maintain their quality. This is where maintenance steps in, however there are no documented maintenance procedures developed yet. Therefore, this section will address the aspects that need to be inspected.

The first part of the system is the hydrogen tank itself, which holds 400 kg of liquid hydrogen throughout the flight. Compared to kerosene, hydrogen is a much more flammable fuel which results in the logic that there should be smaller maintenance interval for the hydrogen tank. To make sure that the tank does not need to be inspected extensively at every interval, multiple systems are used that check the status of the design, such as a leak and fire detection system. Inspecting these systems is a lot more easy since this can be done inside of the aircraft. As the tank does not take up the complete aft cargo hold, it is possible to perform inspection on the tank inside of the aft cargo hold. This means that for visual inspection as well as for checking up on systems that are monitoring the tank that the tank does not need to be taken out. There are as mentioned leak and fire

detection systems, but there is also a system that can measure the heat flow which can be used as a indication of the quality of the insulation that can be utilised. These checks can be done as a level A inspection as they can be performed quite fast and easy while they still give a good indication of the condition of the tank.

Next to the indicators, the openings in the tank can be checked; the valves for venting and fuelling as well as the outer layer of the tank for any damage or other things such as dust that could obstruct the fuel flow. As a level C maintenance procedure, the tank should be inspected from the inside to make sure that there is no damage on the inside as well.

15.3. Reliability and availability

Reliability is defined as the probability that a system will function as desired for a given period of time and under certain operational conditions. Reliability of a system is most of the time dependant on other systems, meaning the reliabilities influence each other. This can be seen from two perspectives; series and parallel. Additionally, a system's complexity influences reliability. If the system complexity decreases, it reliability inherently increases. This section will discuss all aforementioned phenomena to assess the reliability of the total system.

15.3.1. System complexity

The appu contains a number of components which all increase system complexity. Especially the propeller configuration introduces an increase in system complexity. The novel contra rotating, variable pitch, variable RPM and BLI propeller requires extensive research. Also, the addition of a mid-take-off or -landing stopping mechanism, combined with a gyroscope to apprehend a tail strike increases complexity significantly. Unfortunately, more complex systems tend to be less reliable. The correlation between reliability and complexity is explained by considering that every component has each own reliability factor. The total system reliability can be found by multiplying all reliability factors. Hence, a larger number of components equals a decreased reliability.

15.3.2. Parallel reliability

Parallel reliability encompasses systems in which components are performing in a parallel configuration. For a parallel coupled system, both components need to fail in order for the entire system to fail. The A320appu has a number of parallel coupled systems such as the BLI propeller and two fuel systems. The former considers the propeller located on the aft of the fuselage and the two main engines which could compensate for a propeller failure. The latter is correlated to the fact that the APPU can use both kerosene and hydrogen as fuel. A drawback associated with using merely kerosene is that the range is slightly reduced compared to the A320neo. This has mainly to do with a slightly smaller amount of kerosene in the A320appu compared to the A320neo.

Several factors of the design are more correlated and its functions are placed in a 'series' network. In such a network all components must operate for the system to function properly. In the A320appu, the larger part of the auxiliary unit functions are in series. Apart from the fuel systems, which have two separate systems, from the engine to the propeller blades the systems are interrelated. Once the fuel is provided to the system, in order to provide thrust, the following components all have to operate properly: engine, gearbox and propeller. Failure of any of these systems thus have disastrous consequences for the functionality of the APPU and thus the reliability of the aircraft.

15.3.3. Availability

The availability of the aircraft is highly related to its reliability and maintenance intervals. The system availability is related to the operational state of the aircraft, which is related to both the reliability and the maintainability of the aircraft. If the described maintenance intervals turned out to be underestimated the availability of the aircraft reduces. The reliability factors that influence the availability are the failures occurrence and the hazard rate. If these are high this in turn results in a lower availability.

Another important availability parameter of the A320appu design that influences its effectiveness is the availability of hydrogen fuel. As discussed in the design's relation to sustainable development, these goals are only achieved when liquid hydrogen is available as a fuel and airports have adapted their infrastructure to accommodate an aircraft such as the A320appu [36].

Cost Estimation

When designing an aircraft, a cost estimation has to be performed at an early stage to ensure costs are within budget. The Life Cycle Cost (LCC) is the total cost of an airplane program incurred during the airplane life cycle. The total airplane life cycle consists of six consecutive phases, running from planning and conceptual design all the way to disposal of the aircraft. For a preliminary cost estimation, the LCC is broken down into four cost sources, which are shown below. These four cost sources will be explained in the upcoming sections to provide a clear overview of the costs related to the aircraft. At the end of the section their profit and return on investment will be discussed.

1. Research, Development, Test and Evaluation Cost (C_{RDTE})
2. Acquisition Cost (C_{ACQ})
3. Operating Cost (C_{OPS})
4. Disposal Cost (C_{DISP})

From Roskam [54] it is given that the LCC can be expressed as:

$$LCC = C_{RDTE} + C_{ACQ} + C_{OPS} + C_{DISP} \quad (16.1)$$

Since the acquisition cost of the aircraft consists of the manufacturing cost and the profit obtained, Equation 16.1 can be rephrased as:

$$LCC = C_{RDTE} + C_{MAN} + C_{PRO} + C_{OPS} + C_{DISP} \quad (16.2)$$

Where, the profit cost of the manufacturer can be first estimated using a profit margin:

$$C_{PRO} = C_{MAN} \cdot \eta_{pro} \quad (16.3)$$

16.1. Research, Development, Test and Evaluation Cost Estimation

From requirement **OPS-User-28**¹, it is known that the total C_{RDTE} is expected to be at maximum around 5 billion euros. Research, Development, Test and Evaluation (RDTE) costs are broken down in Roskam [54] accordingly:

- | | |
|---|--|
| 1. Airframe engineering and design cost (C_{aed_r}) | 5. Test and simulation facilities cost (C_{tsf_r}) |
| 2. Development support and testing cost (C_{dst_r}) | 6. RDTE profit (C_{pro_r}) |
| 3. Flight test airplanes cost (C_{fta_r}) | 7. Cost to finance the RDTE phases (C_{fin_r}) |
| 4. Flight test operations cost (C_{fto_r}) | |

From this the total C_{RDTE} can be estimated using:

$$C_{RDTE} = C_{aed_r} + C_{dst_r} + C_{fta_r} + C_{fto_r} + C_{tsf_r} + C_{pro_r} + C_{fin_r} \quad (16.4)$$

To determine these individual cost fractions, the methods used as in [54] were applied. Since this cost estimation is performed at a fairly early stage of the design phases, these values will diverge more significantly from the actual cost due to contingency. It is however assumed that the development cost, or in other words C_{RDTE} , will not exceed the 5 billion euros as taken from the requirements. This assumption is valid, simply because the A320neo airframe is kept almost the same, and only minor adjustments were needed to make the A320appu. This will not require the 5 billion euros in RDTE capital, but for a first estimation, this value is assumed in further calculations.

¹**OPS-User-28**: The total development cost of the aircraft shall not exceed 5 billion euros.

16.2. Acquisition Cost Estimation

As already mentioned, the acquisition cost of the aircraft is determined by the production cost of the aircraft and the profit margin of the manufacturer itself. In day-to-day use the profit margin is also referred to as the operating margins, which is the profit of the manufacturer before taxes. Over the period of 2012 - 2019 (before the outbreak of COVID-19), the profit margin (net) of Airbus is given in [Figure 16.1](#)².

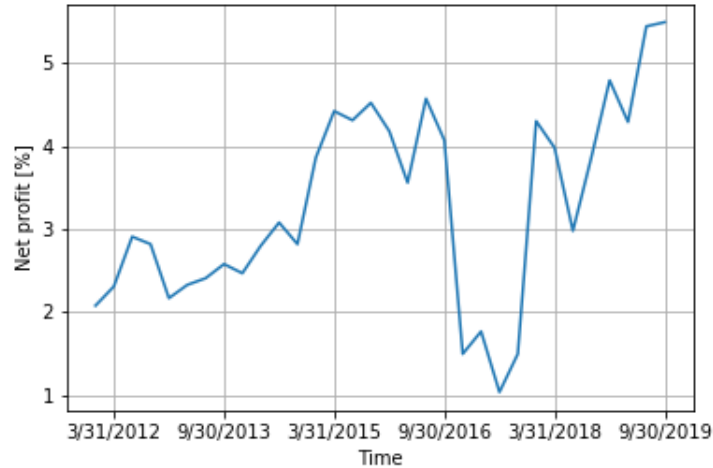


Figure 16.1: Net profit margin of Airbus over the past couple of years.

Using the methodology as described in Roskam, the total airplane program manufacturing cost can be broken down into the following components:

1. Airframe engineering and design cost (C_{aed_m})
2. Airplane production cost (C_{apc_m})
3. Production flight test operations cost (C_{fto_m})
4. Cost of financing the manufacturing program (C_{fin_m})

Empirical relations are known such that all the different cost fractions can be determined based on standard input parameters, similar for all aircraft. After having determined all the different cost fractions of manufacturing, the total manufacturing cost of the program can be estimated using:

$$C_{MAN} = C_{aed_m} + C_{apc_m} + C_{fto_m} + C_{fin_m} \quad (16.5)$$

The next step in determining the acquisition cost of the aircraft is to calculate the profit 'cost' of the aircraft program. For this a profit margin has to be determined in order to simply calculate the expected revenue. Since the profit cost is simply a function of the manufacturing cost, as prescribed in [Equation 16.3](#), a 50% profit margin was used to determine the profit cost of the aircraft program. Now having calculated all the cost fractions, the acquisition unit cost of the A320appu can be calculated using:

$$C_{A320appu} = (C_{man} + C_{pro} + C_{rdte})/N_{program} \quad (16.6)$$

In order to find all these values, the methodology as described in Roskam [54] was used. The values that were used to determine the individual cost components of the manufacturing cost are shown in [Table 16.1](#). As can be seen in [Table 16.1](#), a 50% contingency has been taken into account when determining the cost of the APPU itself, such that in later stages the cost budget will not overshoot. In determining the cost of the APPU, only the engine cost is used, since too little information at this stage of the design is known on the cost of the other subsystems of the APPU. In determining the manufacturing cost, it is assumed that the other costs are included in the 50% contingency.

²<https://bit.ly/3dAAYkN> retrieved on: 17/06/2020

Table 16.1: Input variables for the acquisition cost estimation

Variable	Value	Unit	Note
W_{amp_r}	68 865	[lbs]	Flowdown from empirical relation with MTOW
V_{max}	227	[KEAS]	From typical mission
$N_{program}$	4 688	[-]	Total projected number of A320appu built.
F_{diff}	1.8	[-]	Technology Readiness Indication: Technology not yet ready
F_{cad}	0.8	[-]	Acquaintance level with using CAD software
$N_{engines}$	2	[-]	Number of engines
N_{appu}	1	[-]	Number of appu's
$C_{mainengine}$	12 000 000	[\$]	Cost of the main engines, PW1000G
C_{appu}	1 300 000	[\$]	Cost of the appu, PW150
F_{int}	2 500	[\$/pax]	Assumed for jet aircraft
N_{pax}	180	[-]	Number of passengers, same as A320neo
R_m	50	[\$]	Hourly rate for manufacturing
R_r	60	[\$]	Hourly rate for research
$C_{ops/hr}$	3 000	[\$/hr]	Operating Cost for flight
T_{pft}	10	[-]	For jet transports
P_{ftoh}	4	[-]	
F_{fin_m}	0.15	[-]	Interest rate that cannot be used for investing, and is used for manufacturing.
F_{pro}	0.2	[-]	Gross profit margin
Cost Contingency Factor APPU	1.5	[-]	Cost contingency factor to account for inaccurate estimation of the cost of the APPU

Due to the fact that the source from which the cost estimation is used is from 1989, the data provided has to be updated to 2020. In other words this means that all cost related values have to be updated to current, 2020 Dollars. This is done using the Cost Escalation Factor Ratio (CEF-ratio), which is defined as:

$$CEF = CEF_{now} / CEF_{then} \quad (16.7)$$

This CEF-ratio is dependent on the inflation of the currency used to calculate the costs. In order to now fully determine the total manufacturing cost of the aircraft program all the different cost components have to be scaled up using the CEF-ratio such that:

$$Cost_{now} = Cost_{then} \cdot \frac{CEF_{now}}{CEF_{then}} \quad (16.8)$$

Since the manufacturing cost of the aircraft is dependent on the expected aircraft program size, the first step is to determine required program size. Following the current trend, Airbus is expected to maintain its 50% market share over the upcoming years. As described in [chapter 4](#), the aviation industry is expected to grow continuously, resulting in an increase of 40 000 aircraft by 2050. Assuming that the production rate of aircraft is constant over the period ranging from 2020 up until 2050, an average production rate of 1 333 aircraft per year is assumed. Since the EIS of the A320appu is aimed to be in 2035, in the period of 15 years (up until 2050), approximately 20 000 aircraft will be built. From this, Airbus will then have to produce 10 000 aircraft, as a result of its 50 % market share. From this, it is assumed that 25% will be the A320appu by 2035. This will increase to 50% by the end of 2050. Assuming a constant increase in market share of the A320appu, the total aircraft program of the A320appu is calculated to contain 3 900 aircraft.

Now having determined the total aircraft program, it is possible to determine the manufacturing cost per aircraft. To finalise the total cost per aircraft, other cost sources have to be added, such as C_{RDTE} . In order to do this, the total cost is assumed to consist of two components, C_{fixed} and $C_{variable}$. This way the total cost of the aircraft program can be determined using [Equation 16.9](#). This equation can be altered such that it can be used to calculate the total cost per aircraft built, [Equation 16.10](#). By increasing the program size, the total cost per aircraft built will plateau and hence converge to a constant value, $C_{variable}$, as expected from [Equation 16.11](#). By using the Roskam method, this can also be visualised as can be seen in [Figure 16.2](#). Here it can be seen the $C_{variable}$ is set equal to approximately \$73M, which is then equal to the manufacturing cost of the aircraft. By adding a fraction of the C_{rdte} to the manufacturing cost, the total cost of the aircraft can be determined.

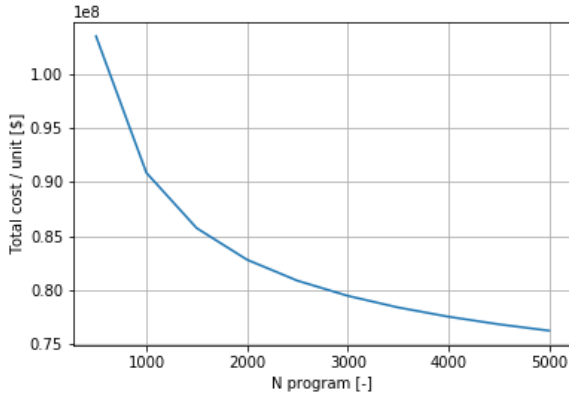


Figure 16.2: Total cost / unit

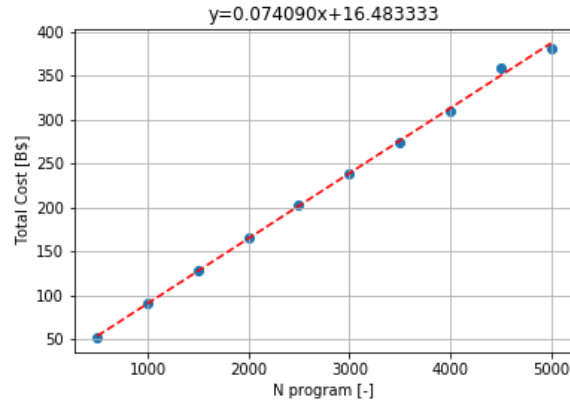


Figure 16.3: Total cost of the program

$$C_{tot} = C_{fixed} + C_{variable} \cdot N_{program} \quad (16.9)$$

$$C_{tot}/unit = \frac{C_{fixed}}{N_{program}} + C_{variable} \quad (16.10)$$

$$\lim_{N_{program} \rightarrow \infty} C_{tot}/unit = C_{variable} \quad (16.11)$$

16.3. Operational Cost Estimation

When looking from the airliners perspective, a clear overview of the operational cost of the aircraft helps to determine whether or not investing in the acquisition of new aircraft is feasible. An increase of the operational cost will either result in a lower profit margin per ticket sold, or to an increase in ticket price, which makes the airliner less attractive compared to other airliners. Therefore, the operational cost of the A320appu are determined using the method as prescribed in Roskam [54]. The operational cost of the aircraft is described as the summation of the Direct Operational Cost (DOC) and the Indirect Operational Cost (IOC) multiplied by the total number of nautical miles flown per aircraft as given by

$$C_{OPS} = (DOC + IOC) \cdot R_{blann} * N_{year} \quad (16.12)$$

Here N_{year} resembles the life cycle of the aircraft, which for the A320appu is assumed to be 20 years. The annual flight distance in nautical miles can easily be calculated by multiplying the block velocity (V_{bl}) times the annual block utilization (U_{annbl}). For the A320appu this has been calculated to be 1061394 nm, based on the average flight time of the typical mission Amsterdam to Lisbon. Since the IOC cost can be assumed to 90% of the DOC, only the DOC has to be determined. For this, the DOC has been broken down into the following parts:

1. DOC of flying (DOC_{flt})
2. DOC of maintenance (DOC_{maint})
3. DOC of depreciation (DOC_{depr})
4. Other DOC, consisting of fees, taxes, insurance and financial cost (DOC_{other})

Determining these values is fairly straightforward using the method as described by Roskam [54]. When calculating these values, the depreciation cost is very difficult to determine. The depreciation cost is dependent on the philosophy of the airliner, and for that a more sophisticated financial analysis has to be performed in order to determine it. Therefore, as a first assumption, the DOC_{depr} is assumed to be 0. By comparing the results with statistical data in a similar way (excluding DOC_{depr}), this assumption is valid. The most predominant cost factor in the DOC is the DOC_{flt} , due to the contribution of the aircraft fuel. The DOC_{flt} is determined using Equation 16.13:

$$DOC_{flt} = DOC_{crew} + DOC_{plt} + DOC_{ins} \quad (16.13)$$

First the methodology as described in Roskam [54], is used to verify and validate the numerical model with real life data. For that the input parameters are similar to that of a conventional A320neo, for which the operational

cost are known from statistical data³. The input parameters needed to determine the operational cost of the aircraft are taken from the flight envelope of the typical mission. As already mentioned in section 16.2, the data provided by the book of Roskam is fairly outdated, therefore some values had to be altered. As a second assumption, only the hourly rate take into account inflation and hence are dependent on the CEF-ratio. Inputting all the values of the A320neo on a typical mission, the following data is provided on the operational cost, for which a 90% additional cost of IOC is already added.

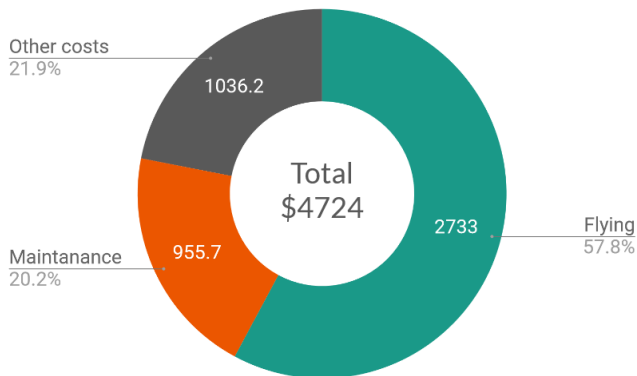


Figure 16.4: Operational cost in dollars per block hour using the method as described in Roskam [54]

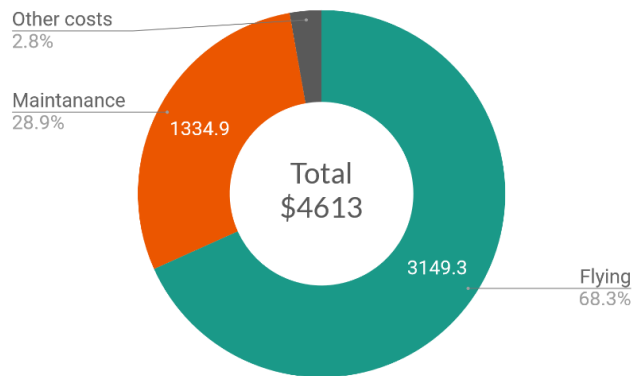


Figure 16.5: Operational cost in dollars per block hour using statistical data

As can be seen, there are some deviations in the specific cost components when comparing Roskam's method to statistical data. This deviation is mostly due to the fact that Roskam defines certain cost fractions different than the statistical data. The total operating cost per block hour using Roskam [54] overshoots the statistical data by 2.6%, which is assumed to be within the error margins that is preferred. Therefore, Roskam's method can now be altered by opting for the APPU design, which has an additional APPU and carries additional LH2, which has to be taken into account. The cost of LH2 on airports is expected to be 2\$/kg by 2035 [19]. Taken into account that approximately 400kg of hydrogen has to be taken for the typical mission, the fuel cost will increase significantly. Even though less hydrogen is taken, the effect of hydrogen on the operational cost is still significant. Furthermore, an extra engine in the form of an APPU has to be added. This will eventually result in the data as provided in Table 16.2. The total operational cost per block hour whenever the A320appu partially runs on hydrogen is equal to **5 447 dollars per block hour**, which is equal to a 15.3 percent increase in operational cost when comparing it to the A320neo (Roskam method).

Table 16.2: Overview of operational cost estimation methods

Operational cost [USD/blhr]	Roskam A320neo [USD/blhr]	Statistical data [USD/blhr]	Roskam A320appu no H ₂ [USD/blhr]	Roskam A320appu H ₂ [USD/blhr]
$C_{ops_{flt}}$	2 733.7	3 149.3	2 948.3	3 228.8
$C_{ops_{maint}}$	955.7	1 334.9	1 099.1	1 099.1
$C_{ops_{depr}}$	0.0	0.0	0.0	0.0
$C_{ops_{other}}$	1 036.2	128.8	1 081.0	1 120.1
$C_{opstotal}$	4 608.0	4 725.6	5 128.4	5 447.9

16.4. Disposal Cost Estimation

As the final cost source, the disposal cost of the aircraft has to be determined. From Roskam [54], the following equation is given to determine the disposal cost of the aircraft.

$$C_{disp} = 0.01 \cdot LCC \quad (16.14)$$

³https://www.planestats.com/bhsn_2014dec, retrieved on 19-6-2020

16.5. Life Cycle Cost

Having determined all the cost sources related to the aircraft, the total LCC can be determined per aircraft. By using Equation 16.2, the total life cycle cost per aircraft is estimated to be \$442M. A clear cost distribution can be seen in Figure 16.6, showing that the operational cost is the most predominant cost factor, as expected by Roskam [54].

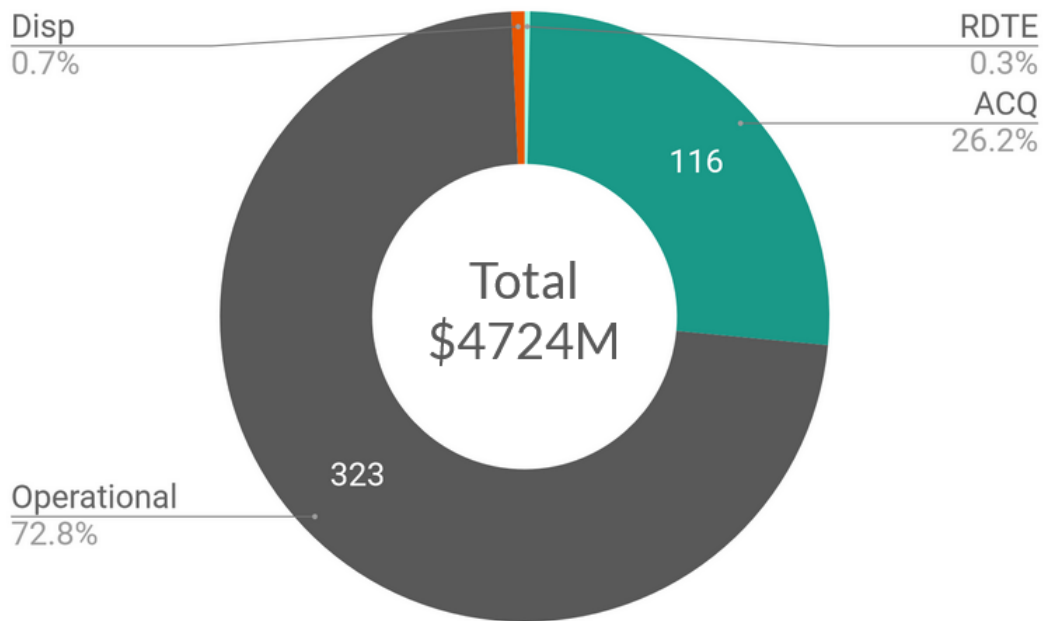


Figure 16.6: Pie chart showing the cost distribution of the LCC (in million dollars)

16.6. Profit and Return On Investment Estimations

Lastly, it is important to estimate the profit and Return On Investment (ROI) of the aircraft program, since the main goal of the manufacturer, Airbus, is to make the project as profitable as possible. Given the total cost of the aircraft program and the price for which the aircraft will be sold (acquisition cost), it is possible to determine the total Return On Investment (ROI) of the aircraft program. This is done by dividing the total incoming revenue by the total cost of the aircraft program. For a program size of 3 900, the total ROI is equal to **149%**. Furthermore the total profit of the program is then equal to **\$154B**.

Project Outlook

This chapter discusses the future planning of the A320appu project. The reasoning behind determining a project outlook is mentioned in [section 17.1](#). The overall outlook from post-DSE to entry into service of the aircraft is described using a Gantt chart in [section 17.2](#).

17.1. Entry into service

The requirement for the entry into service of the A320appu is the following:

- **OPS-User-27:** The entry into service of the aircraft shall be in 2035.

Originally the EIS was aimed to be in the year 2030. After consultation with one of the main stakeholders, the aircraft manufacturer Airbus, it was decided upon that this requirement was unrealistic. Due to the COVID-19 crisis of 2020, many modifications in the company's employer structure have taken place and uncertainties of developments of future aircraft have arisen. Due to this, the development phase of a new aircraft like the A320appu will be extended to a longer period, namely, up until 2035. In order to more specifically determine the entry into surface time of the aircraft, the Technology Readiness Level (TRL) is used¹. The TRL can be used to estimate the years to maturity, or in other words the years needed to successfully implement the technology into an aircraft. This can be seen in [Figure 17.2](#). A clear description of the TRL can be seen in [Figure 17.1](#).

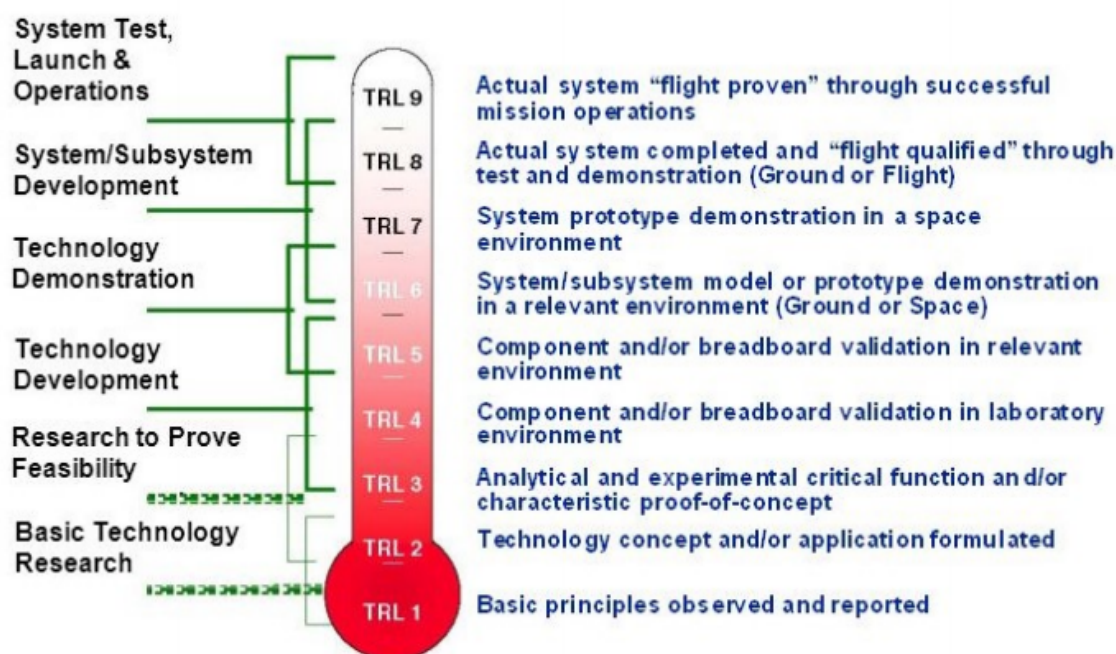


Figure 17.1: NASA Technological Readiness Levels

¹https://www.nasa.gov/directorates/heo/scan/engineering/technology/txt_accordion1.html, retrieved on 29-6-2020

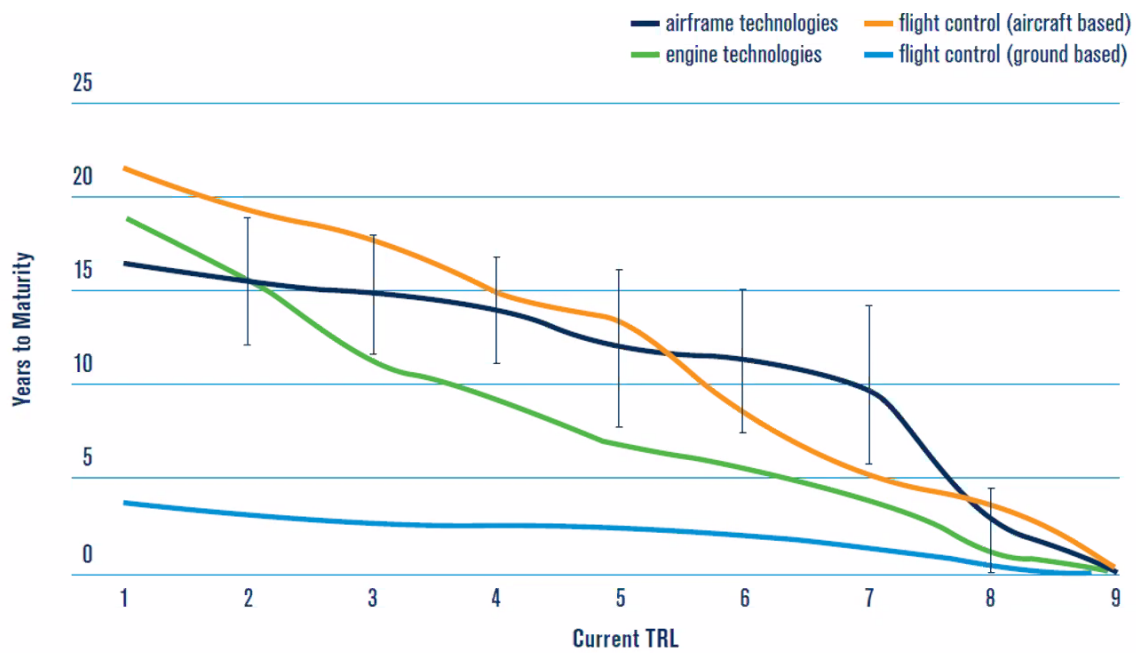


Figure 17.2: TRL with corresponding years to maturity [6]

Table 17.1: Technology Readiness Level of the A320appu

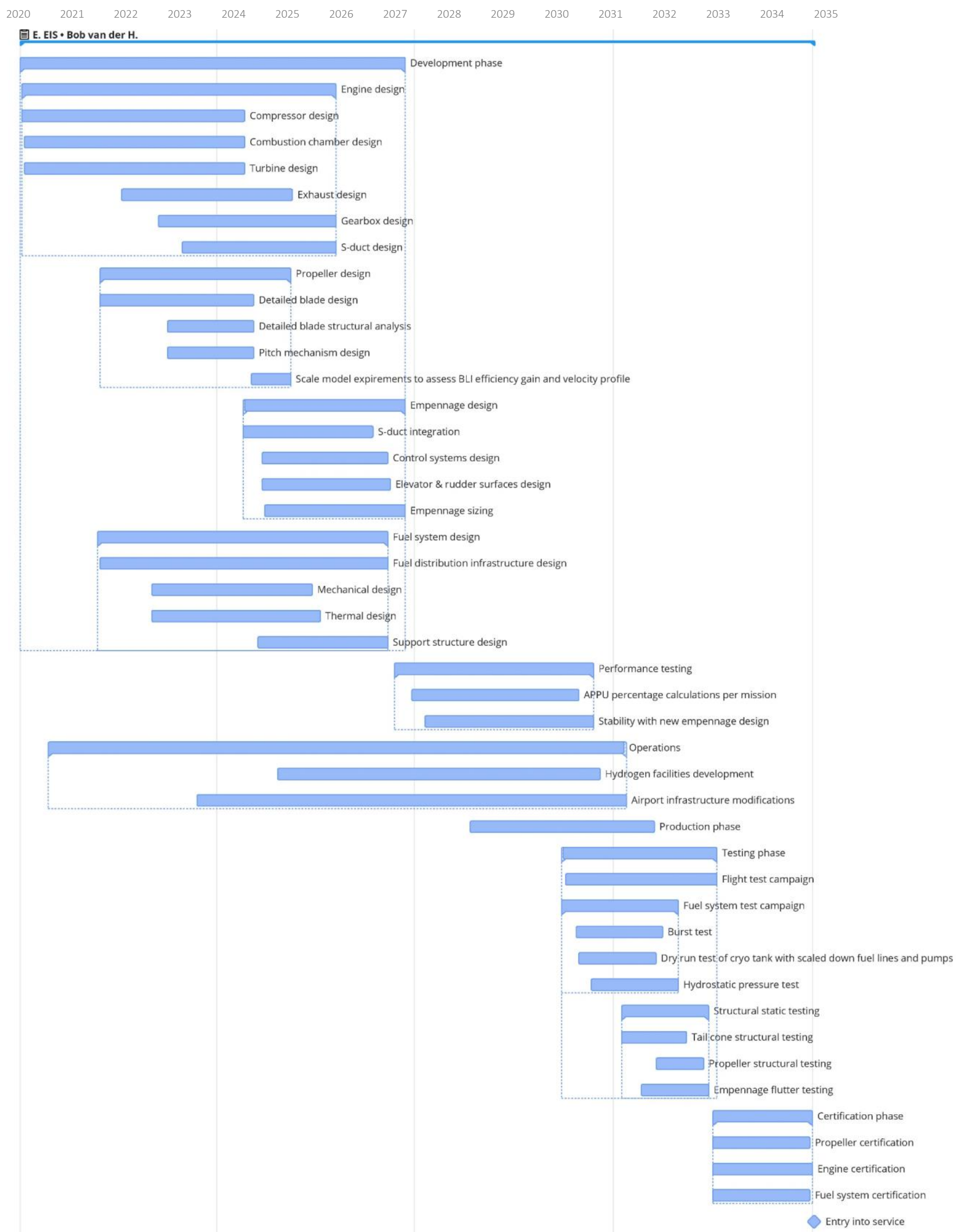
Technology	TRL	Years to maturity
Engine capable of running on both kerosene and hydrogen	TRL-4	8-11
T-tail	TRL-9	1-3
Contra-rotating propeller, variable pitch, variable RPM	TRL-7	3-4
Hydrogen tank	TRL-5	11-13
S-duct	TRL-8	3-4
Variable RPM, contra-rotating drivetrain including stopping mechanism	TRL-6	5-7

Table 17.1 highlights the most significant technologies present in the A320appu design that require analysis, including it is years to maturity. Here it can be seen that the EIS of 2035 is achieved, since no technology has years to maturity larger or equal than 15 years. The Technology Readiness Levels were determined by performing research on already existing aircraft technologies and finding similar concepts. This way a first order estimate on the TRL was determined. As can be seen, the T-tail and S-duct have the highest TRL simply because this technology is already (widely) implemented into existing aircraft, whereas dual fuel engines and contra-rotating propellers are not commonly used, therefore resulting in lower TRLs.

17.2. Project Gantt chart

All activities and steps to be taken to take this design from a university project to a large scale entry into service aircraft are listed and shown on a Gantt chart in Figure 17.3. The timeline is from the year 2020 to 2035. The tasks listed illustrate the different tasks associated with the A320appu design with regards to a regular aircraft timeline from development to entry into service. For instance, the testing phase include tests related to the hydrogen fuel system. Some of the tests that are to be performed during the testing phase have not been performed on aircraft yet. All these tests are related to the use of hydrogen as a fuel. Elaborate testing on this ensures a higher reliability of the aircraft in the end.

Figure 17.3: Project Gantt chart for 2020-2035.



17.3. Manufacturing, Assembly, Integration plan

By looking at all the different subsystems of the APPU system, a first iteration, basic production plan was designed which shows the basic flow-down from half fabricates up until the sub-assemblies and finally the APPU system. A more detailed production plan has to be decided upon in later stages of the design phase.

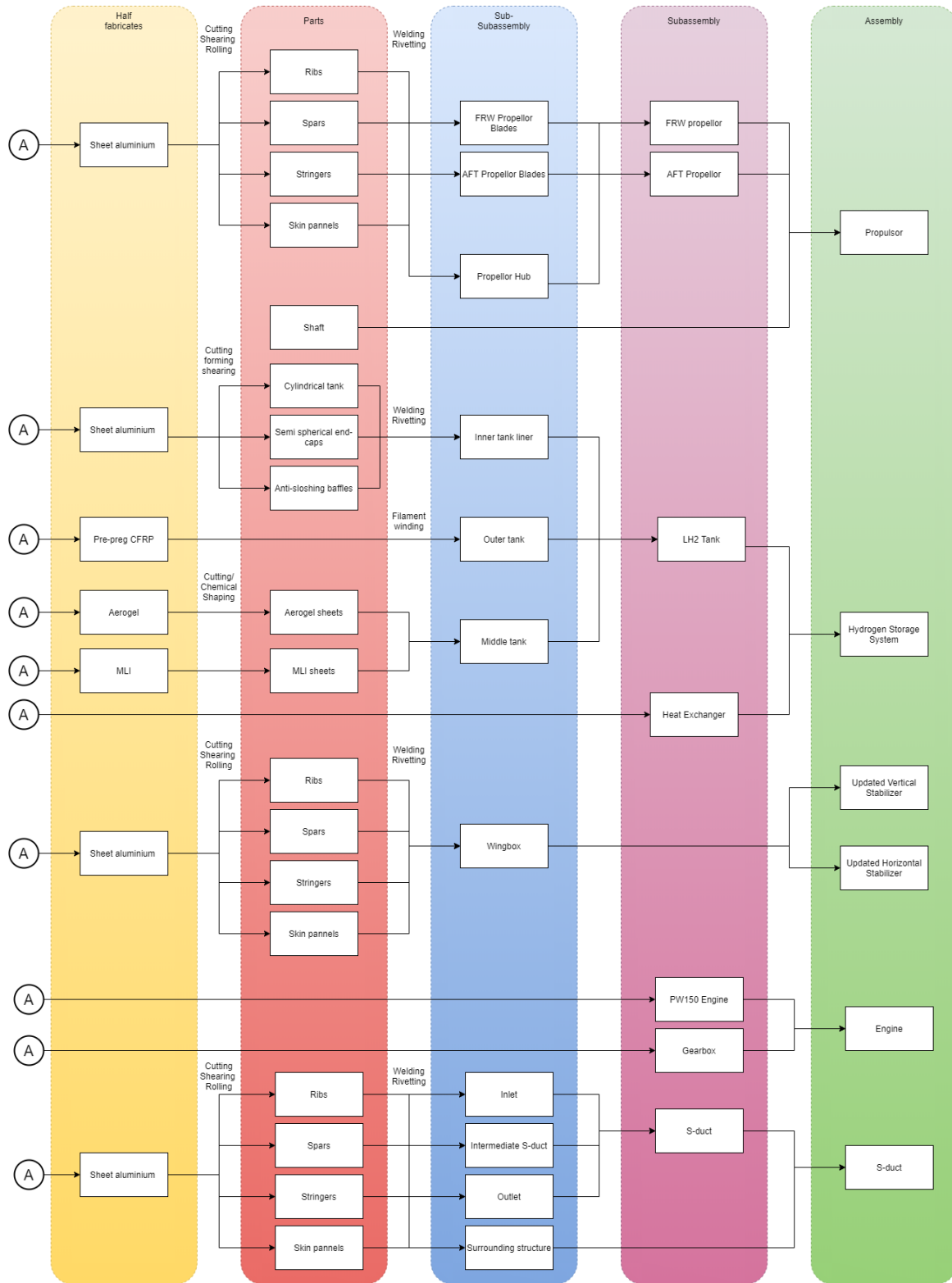


Figure 17.4: Production plan

Conclusion

The purpose of this report was to provide the design choice, argument the choices and present a final design configuration. Using information presented in previous design phases, a preliminary design was established. By integrating the design choices and providing additional subsystem details, the final design could be established. Aerodynamic, structural and mechanical analyses were necessary to guarantee the quality of the subsystems. Additionally, to meet the predetermined requirements, designs would be altered to provide a thorough design. Ultimately, the final design contained the following subsystem configurations:

- A multi-fuel (kerosene and hydrogen) engine located in the tail cone
- A boundary layer ingestion, contra-rotating, variable pitch, variable RPM and three-bladed propeller located at the tail cone
- A cylindrical tank located in the aft cargo hold

The design configuration proved to fulfil all predetermined requirement and can thus be concluded successful. A more comprehensive overview of all technical requirement can be found in [Table 18.1](#).

Table 18.1: Performance parameters for A320neo and A320appu

Parameter	A320neo	A320appu
OEW [kg]	44 300	45 757
MTOW [kg]	79 000	79 000
MPL [kg]	19 000	16 500
Kerosene tank capacity [L]	19 000	19 000
LH2 tank capacity [kg]	-	400
LTO kerosene [kg]	650	250
LTO H2 [kg]	-	50
APPU sea-level power [MW]	-	3.65
Cruise Mach [-]	0.78	0.78
Cruise altitude [m]	12 200	11 000
XLEMAC [m]	14.6	15.6
Harmonic range [km]	4 500	6 150
Maximum fuel range [km]	6 250	7 000
Ferry range [km]	7 900	7 870
Aquisition cost [\$M]	100	116
Kerosene required typical mission [kg]	5 786	4 625
LH2 required typical mission [kg]	-	350
Wing surface area [m ²]	126	126
Horizontal stabiliser surface (wetted) area [m ²]	31	37
Vertical stabiliser surface (wetted) area [m ²]	21.5	19.1
Landing distance increase [%]	0	3.31

Compliance matrix

All requirements are summarised in the compliance matrix. The table has the dual purpose of a last check if requirements are complied with and as a bookmark to easily navigate the report based on the requirement of interest. In the compliance matrix, "F" stands for *future design stages*.

Table 18.2: Compliance matrix

Requirement no.	Description	Satisfied	Section
FMP-User-01	Similar range to A320neo	Yes	12.2.2
FMP-User-01.1	4 500 km range at max payload	Yes	12.2.2
FMP-User-01.2	6 250 km range at max fuel	Yes	12.2.2
FMP-User-01.3	7 900 km ferry range	Yes	12.2.2
FMP-User-02	150 pax capacity	Yes	3.3
FMP-Sys-03	<5% decrease mach	Yes	8.3
FMP-Sys-04	<10% cruise altitude deviation	Yes	8.3
FMP-Sys-05	<5% increase landing distance	Yes	12.2.3
FMP-Sys-06	<5% increase take-off distance	Yes	12.2.3
FMP-Sys-07	<5% decrease climb angle	Yes	12.2.3
FMP-Sys-08	<5% decrease climb rate	Yes	12.2.3
FMP-Sys-09	Static & dynamics stability	Yes	11.3.1
POW-Sys-10	Power non-essential subsystems	Yes	8.2
POW-Sys-11	Emergency power to subsystems	Yes	8.2
POW-Sys-12	Main engines back-up	Yes	8.2
POW-Sys-13	Power for main engine startup	Yes	8.2
POW-Sys-14	APPU drives generator	Yes	8.4
PROP-User-15	APPU multi-fuel	Yes	2.1
PROP-Sys-16	APPU power for propeller	Yes	8.6
PROP-Sys-17	Thrust reversing	F	
PROP-Sys-18	BLI efficiency increase	Yes	9.4
PROP-Sys-19	Limit ground strike damage	Yes	9.3.5
PROP-Sys-20	Operate on H2 and kerosene	Yes	8.4.5
FTD-Sys-21	H2 energy content <15%	Yes	10.2
FTD-Sys-22	Equal drainage time	F	
FTD-Sys-23	48h boil-off time	Yes	10.3.6
SUST-User-24	<20% CO ₂ emissions	Yes	8.3
SUST-User-25	<50% LTO emissions	Yes	13.2.2
SUST-Sys-26	<5% increase in noise	Yes	13.3
OPS-User-27	EIS in 2035	Yes	17.1
OPS-User-28	<5B development costs	Yes	16.1
OPS-Sys-29	Safe refueling system	Yes	15.1.1
OPS-Sys-30	H2 storage safe separation	Yes	3.3
OPS-Sys-31	H2 tank fits in A320neo	Yes	3.3
OPS-Sys-32	Passenger evacuation plans unaffected	Yes	14.2
OPS-Sys-33	Ground crew propeller risks mitigated	Yes	15.1.2
OPS-Sys-34	Ground clearance	Yes	9.3.5
OPS-Sys-35	APPU airfield operations compatibility	Yes	14.2
OPS-Sys-36	Same airport gate usage	Yes	14.2
OPS-Sys-37	<10% increase in TaT	Yes	14.2.1
OPS-Sys-38	Tip-over limit	Yes	11.4
OPS-Sys-39	Aircraft safety	Yes	15.1
REG-Sys-40	Comply with CS 25 regulations		N/A, see 40.1 and 40.2
REG-Sys-40.1	APPU complies with CS 25, J	Yes	15.1
REG-Sys-40.2	Comply with CS 25 manoeuvrability	Yes	11.10
REG-Sys-41	Comply with airport regulations	Yes	14.2

A

Technical Drawings of the A320appu

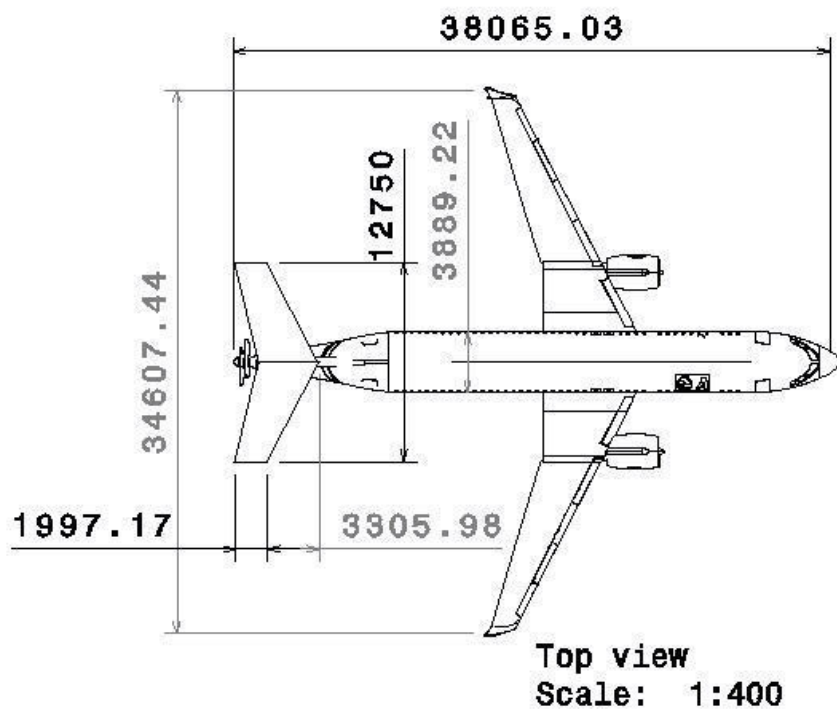
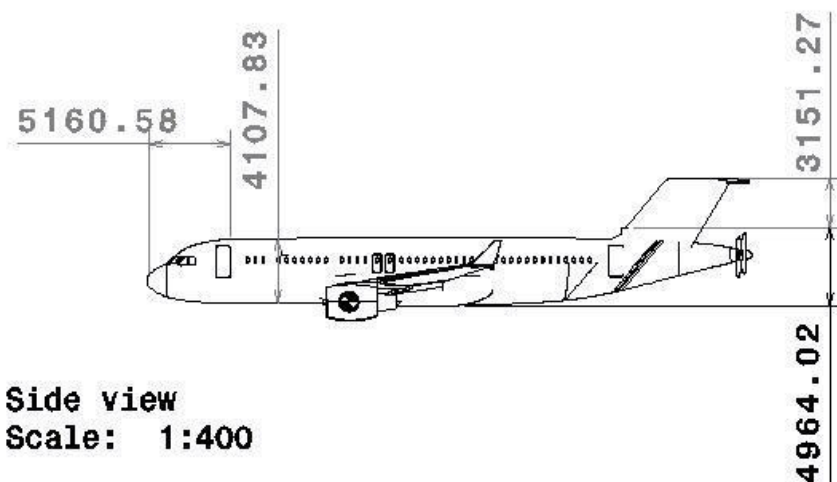


Figure A.1: Technical Drawing of the A320appu

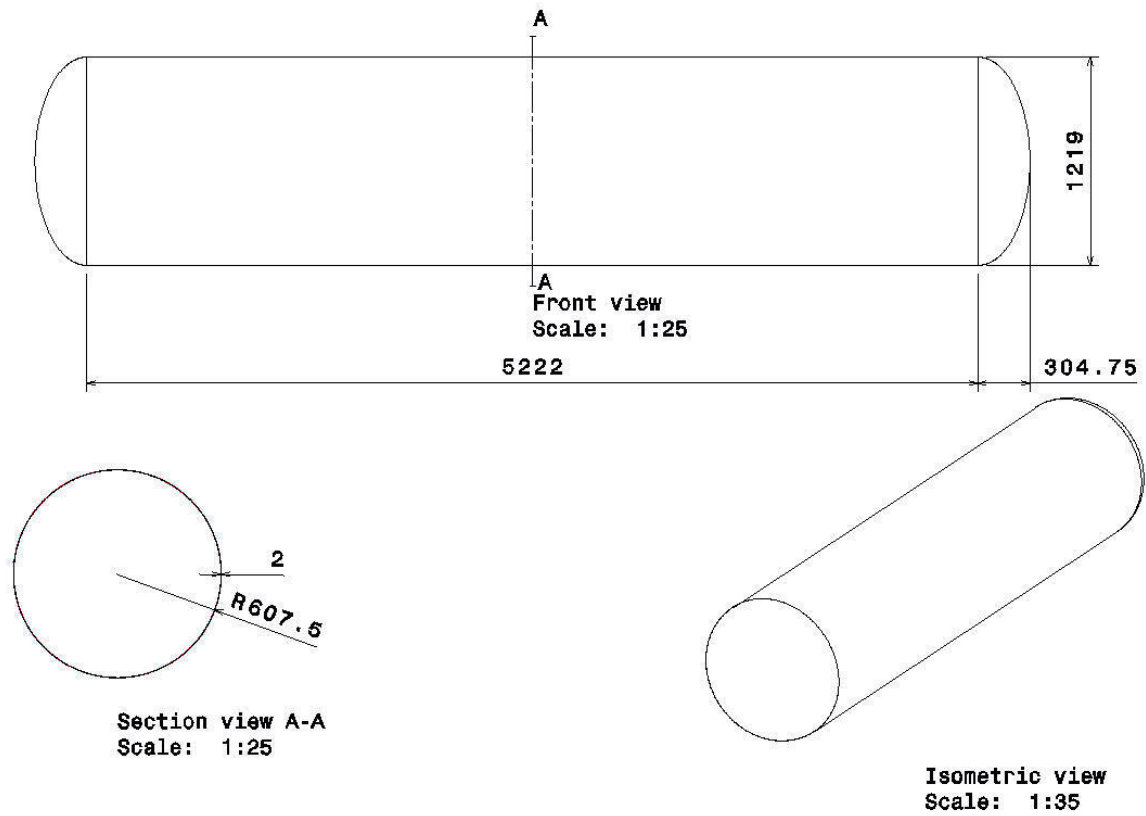
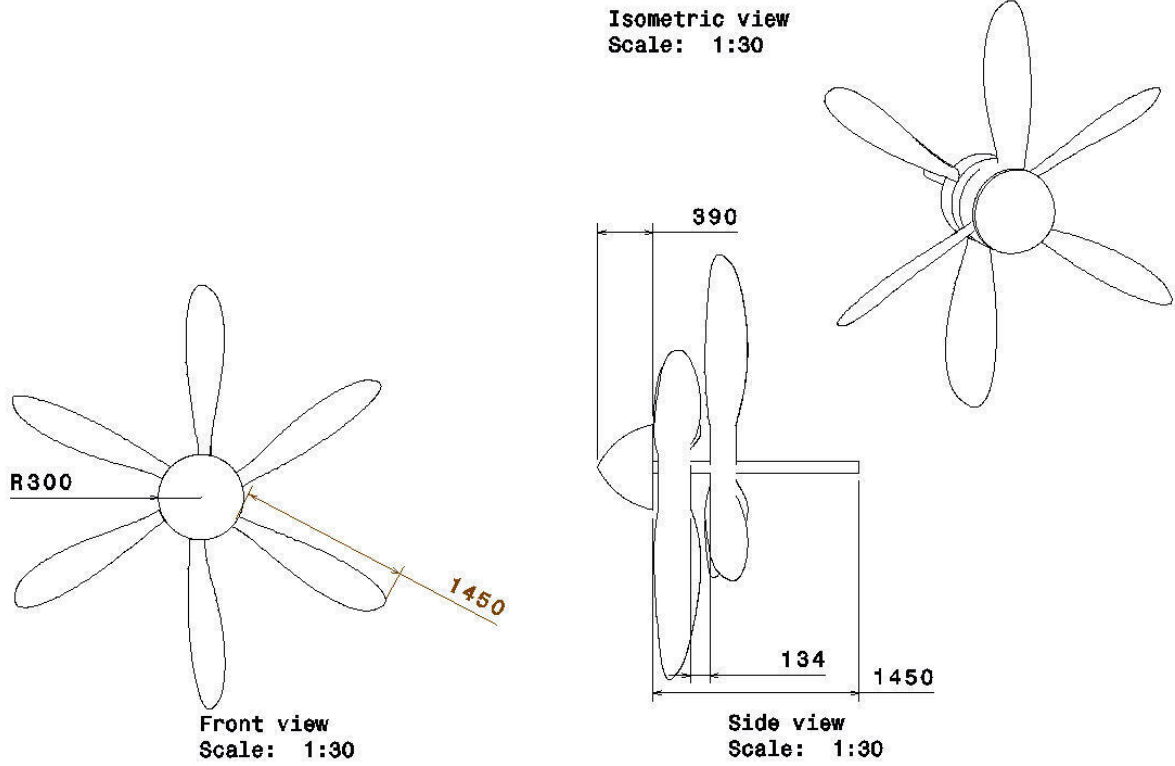


Figure A.2: Technical Drawing of the propeller and cryogenic tank

Bibliography

- [1] Airbus S.A.S., “A320 Aircraft Characteristics Airport and Maintenance Planning [online publication]”, 2020.
- [2] Alderliesten, R., “Introduction to Aerospace Structures and Materials”, *TU Delft Open*, 2018.
- [3] Arnold, S., Bednarczyk, B., Collier, C., and Yarrington, P., “Spherical Cryogenic Hydrogen Tank Preliminary Design Trade Studies”, *STI Report Series*, 2007, ,.
- [4] Ashby, M. F. and Cebon, D., “Materials selection in mechanical design”, *MRS Bull*, 2005, Vol. 30, No. 12, pp. 995.
- [5] ASME, “ASME Boiler and Pressure Vessel Code, Section X, Fiber-Reinforced Plastic Pressure Vessels”, *The American Society of Mechanical Engineers*, 2017.
- [6] Association, I. A. T., “Aircraft Technology Roadmap to 2050”, 2013, Vol. 1, pp. 18.
- [7] Augustynowicz, S., Fesmire, J., and Wikstrom, J., “Cryogenic insulation systems”, 1999, ,, *NASA*.
- [8] Aviation, G. E., “GE H-Series Turboprop Engines”, 2018, ,, *General Electric*.
- [9] Bai, C., Mingqiang, L., Zhong, S., Zhe, W., Yiming, M., and Lei, F., “Wing weight estimation considering constraints of structural strength and stiffness in aircraft conceptual design”, *International Journal of Aeronautical and Space Sciences*, 2014, Vol. 15, No. 4, pp. 383–395.
- [10] Barron, R., “Cryogenic Systems”, *Oxford University Press*, 1985.
- [11] Bensadoun, E., “Hydrogen Storage on board aeronef and ground infrastructure”, *Air Liquide*, 2015, ,.
- [12] Berens, T. M., Delot, A.-L., Chevalier, M., and van Muijden, J., “Numerical simulations for high offset intake diffuser flows”, In 52nd Aerospace Sciences Meeting, page 0371, 2014.
- [13] Brewer, G., “Hydrogen Aircraft Technology”, *CRC Press*, 1991.
- [14] Brewer, G., Morris, R., Davis, G., Versaw, E., and Cunnington Jr., G., “Study of fuel systems for LH2-fueled subsonic transport aircraft”, volume I and II, *Lockheed - California Company, Burbank (USA)*, 1978.
- [15] Brewer, G. D., “The prospects for liquid hydrogen fueled aircraft”, *International Journal of Hydrogen Energy*, 1982, Vol. 7, No. 1, pp. 21–41, *Elsevier*.
- [16] Campbell, F., “Structural Composite Materials”, *ASM International*, 2010.
- [17] Cavacece, M., Valentini, P. P., and Vita, L., “Mechanical Efficiency Analysis of a Cardan Joint”, 2004, ,, doi: 10.1115/DETC2004-57317.
- [18] Cho, J.-U. and Han, M.-S., “Strength and Fatigue Analysis of Universal Joint”, *Journal of manufacturing engineering & technology*, 2011, Vol. 20,.
- [19] Clean Sky 2 JU and FCH 2 JU, “Hydrogen-powered aviation; A fact-based study of hydrogen technology, economics and climate impact by 2050”, *Luxembourg: Publication Office of the European Union*, 2020, ,, [not yet published].
- [20] Cloud, A., “The permeability Characteristics of Silicone Rubber”, *Global Advances in Materials and Process Engineering*, 2006, ,, *Society for the Advancement of Material and Process Engineering*.
- [21] Coetzee, E., “Modelling and nonlinear analysis of aircraft ground manoeuvres”, *University of Bristol*, 2011.
- [22] Coffman, B., Fesmire, J., White, S., Gould, G., and Augustynowicz, S., “Aerogel blanket insulation materials for cryogenic applications”, In AIP Conference Proceedings, volume 1218, pages 913–920. American Institute of Physics, 2010.
- [23] Cook, R. D. et al., “Concepts and applications of finite element analysis”, *John Wiley & Sons*, 2007.
- [24] Dawood, F., Anda, M., and Shafiullah, G., “Hydrogen production for energy: An overview”, *International Journal of Hydrogen Energy*, 2020, ,, *Elsevier*.

- [25] DSE group 21, "Midterm Report; A320 Auxiliary Power and Propulsion Unit", 2020, Delft University of Technology.
- [26] Dubois, G. and Ceron, J. P., "Tourism/leisure greenhouse gas emissions forecasts for 2050: Factors for change in France", *Journal of Sustainable Tourism*, 2006, Vol. 14, No. 2, pp. 172–191, *Taylor & Francis*.
- [27] European Industrial Gases Association, "Hydrogen Transportation Pipelines; IGC Doc 121/04/E Globally Harmonised Document", 2004, ,.
- [28] European Union Aviation Safety Agency, "Type-Certificate Data Sheet For Noise No. EASA.A.064.3 for A320", January 2020, , [online publication].
- [29] European Union Aviation Safety Agency (EASA), "Certification Specifications and Acceptable Means of Compliance for Large Aeroplanes CS-25 Amendment 24 [online publication]", 2020.
- [30] Fesmire, J., "Aerogel Based Insulation Materials For Cryogenic Applications", *Cryogenics Test Lab, Kennedy Space Center*, 2018, ,.
- [31] Fesmire, J. and Johnson, W., "Cylindrical cryogenic calorimeter testing of six types of multilayer insulation systems", *Cryogenics*, 2018, Vol. 89, pp. 58–75, *Elsevier*.
- [32] Flight Operations Support & Services, "A320 Family Performance Retention and Fuel Savings", *Getting to Grips With*, 2008, , *Airbus*.
- [33] Flight standards Service Washington, D., "Aircraft propeller maintenance", *Federal Aviation Administration*, 2005, ,.
- [34] Fohmann, K., "Design of a Cooling System for the Hybrid Engine; Design of a heat exchanger for cooling bleed air with liquified natural gas.", Master's thesis, *Delft University of Technology*, 2015.
- [35] García, L., "Hydrogen production by steam reforming of natural gas and other nonrenewable feedstocks", In *Compendium of Hydrogen Energy*, pages 83–107. Elsevier, 2015.
- [36] Hamann, R. and van Tooren, M., "System Engineering & Technical Management Techniques Part II", *Delft University of Technology*, 2006, ,.
- [37] Heslehurst, R., "Undercarriage Lateral Tip-Over Criteria: A Parametric Study", *Journal of aircraft*, 2011, Vol. 48, No. 6, pp. 1825–1828.
- [38] Holman, J., "Heat transfer tenth edition", *The McGraw-Hill Companies. USA*, 2010.
- [39] Jansen, R. H., Bowman, C., and Jankovsky, A., "Sizing Power Components of an Electrically Driven Tail Cone Thruster and a Range Extender", 2016, , *NASA Glen Research Center*.
- [40] Koroneos, C., Dompros, A., Roumbas, G., and Moussiopoulos, N., "Advantages of the use of hydrogen fuel as compared to kerosene", *Resources, Conservation and Recycling*, 2005, Vol. 44, No. 2, pp. 99–113, *Elsevier*.
- [41] Kumar, V. M., "Physics of buoyant flows: from instabilities to turbulence", *World Scientific*, 2018.
- [42] Lin, C. S., Van Dresar, N. T., and Hasan, M. M., "Pressure control analysis of cryogenic storage systems", *Journal of propulsion and power*, 2004, Vol. 20, No. 3, pp. 480–485.
- [43] Lucas, J. R., O'Brien, W. F., and Ferrar, A. M., "Effect of BLI-type inlet distortion on turbofan engine performance", In *Turbo Expo: Power for Land, Sea, and Air*, volume 45578. American Society of Mechanical Engineers, 2014.
- [44] Lv, P. and Gangoli Rao, A., "Experimental Assessment of Boundary Layer Ingestion", *Delft University of Technology*, 2017, Slides.
- [45] Marek, C. J., Smith, T. D., and Kundu, K., "Low Emission Hydrogen Combustors for Gas Turbines Using Lean Direct Injection", 2005, ,pp. 3776.
- [46] Mital, S. K., Gyekenyesi, J. Z., Arnold, S. M., Sullivan, R. M., Manderscheid, J. M., and Murthy, P. L., "Review of current state of the art and key design issues with potential solutions for liquid hydrogen cryogenic storage tank structures for aircraft applications", 2006, ,.
- [47] Mutluay, T., "The Development of an Inertia Estimation Method to Support Handling Quality Assessment", Master's thesis, *Delft University of Technology*, 2015.

- [48] of the Desert, C., "Module 10: Maintenance and Fueling Facility Guidelines", *Hydrogen Fuel Cell Engines and Related Technologies*, 2001, ,.
- [49] Palanivelu, P. and Siva Prasad, P., "A Paper on Design and Analysis of Pressure Vessel", *International Journal of Engineering Research & Technology*, 2017, ,.
- [50] Ravinkanth, S., "A Effect of Elevator Deflection on Lift Coefficient Increment", *International Journal of Modern Engineering Research*, 2015, Vol. 5, No. 6, pp. 9–14, *International Journal of Multidisciplinary Educational Research*.
- [51] Rivard, E., Trudeau, M., and Zaghlib, K., "Hydrogen Storage for Mobility: A Review", *MDPI Materials*, 2019, ,.
- [52] Roskam, J., "Airplane Design: Part 1-Preliminary Sizing of Airplanes", *DARcorporation*, 1985.
- [53] Roskam, J., "Airplane Design: Part 6-Preliminary Calculation of Aerodynamic: Thrust and Power Characteristics", *DARcorporation*, 1985.
- [54] Roskam, J., "Airplane Design: Part VIII-Airplane Cost Estimation: Design, Development, Manufacturing and Operating", *DARcorporation*, 1995.
- [55] Şcedilakar, G., "The effect of axial force on the free vibration of an Euler-Bernoulli beam carrying a number of various concentrated elements", *Shock and Vibration*, 2013, Vol. 20, No. 3, pp. 357–367, *Hindawi*.
- [56] Schijve, J., "Fatigue of Structures and Materials", *Springer*, 2009, 2nd ed.
- [57] Scociety, R. A., "The influence of body geometry and flow condition on axisymmetric boundary layer at subcritical Mach number", 1979, ,.
- [58] Seddon, J., "Understanding and countering the swirl in S-ducts: tests on the sensitivity of swirl to fences", *The Aeronautical Journal*, 1984, Vol. 88, No. 874, pp. 117–127, *Cambridge University Press*.
- [59] Stiller, C. and Schmidt, P., "Airport Liquid Hydrogen Infrastructure for Aircraft Auxiliary Power Units", *Forschungszentrum Jülich GmbH, Zentralbibliothek*, 2010, , *Ludwig-Bölkow-Systemtechnik GmbH*.
- [60] Tan, S. C., "Electrically Assisted Propulsion & Power Systems for Short-Range Missions: Electrification of a Conventional Airbus A320neo", Master's thesis, *Delft University of Technology*, 2018.
- [61] Technology, A. W. . S., "Aerospace Source Book; Gas Turbine Engine Specifications", pages 128–143, *McGraw-Hill, Arlington, TX*, 2008, pages 128–143.
- [62] GasTurb GmbH, "GasTurb 12", 2020.
- [63] GRANTA Design, "CES EduPack 2019", 2019.
- [64] Torenbeek, E., "Synthesis of subsonic airplane design: An introduction to the preliminary design of subsonic general aviation and transport aircraft, with emphasis on layout, aerodynamic design, propulsion and performance", *Springer Science & Business Media*, 2013.
- [65] Winnefeld, C., Kadyk, T., Bensmann, B., Krewer, U., and Hanke-Rauschenbach, R., "Modelling and designing cryogenic hydrogen tanks for future aircraft applications", *Energies*, 2018, Vol. 11, No. 1, pp. 105, *Multidisciplinary Digital Publishing Institute*.
- [66] Xia, X., "Dynamic Power Distribution Management For All Electric Aircraft", Master's thesis, *Cranfield University*, 2011.
- [67] Y.A.P. Teeuwen, "Propeller Design for Conceptual Turboprop Aircraft", *Aerospace Engineering*, 2017, , *Delft University of Technology*.
- [68] Yin, F., Gangoli Rao, A., Bhat, A., and Chen, M., "Performance assessment of a multi-fuel hybrid engine for future aircraft", *Aerospace Science and Technology*, 03 2018, Vol. 77, , doi: 10.1016/j.ast.2018.03.005.
- [69] Zohuri, B., "Heat Exchanger Types and Classifications", pages 19–56, *Springer International Publishing Switzerland*, 09 2017, pages 19–56, ISBN 978-3-319-29834-4.